

University of Louisville

ThinkIR: The University of Louisville's Institutional Repository

Electronic Theses and Dissertations

12-2019

Oxygen deficient perovskites: effect of structure on electrical conductivity, magnetism and electrocatalytic activity.

Ram Krishna Hona
University of Louisville

Follow this and additional works at: <https://ir.library.louisville.edu/etd>

 Part of the [Inorganic Chemistry Commons](#)

Recommended Citation

Hona, Ram Krishna, "Oxygen deficient perovskites: effect of structure on electrical conductivity, magnetism and electrocatalytic activity." (2019). *Electronic Theses and Dissertations*. Paper 3336. <https://doi.org/10.18297/etd/3336>

This Doctoral Dissertation is brought to you for free and open access by ThinkIR: The University of Louisville's Institutional Repository. It has been accepted for inclusion in Electronic Theses and Dissertations by an authorized administrator of ThinkIR: The University of Louisville's Institutional Repository. This title appears here courtesy of the author, who has retained all other copyrights. For more information, please contact thinkir@louisville.edu.

OXYGEN DEFICIENT PEROVSKITES:
EFFECT OF STRUCTURE ON ELECTRICAL CONDUCTIVITY,
MAGNETISM AND ELECTROCATALYTIC ACTIVITY

By

Ram Krishna Hona
M.S., New Mexico State University, 2014

A Dissertation
Submitted to the Faculty of the
College of Arts and Sciences of the University of Louisville
in Partial Fulfilment of the Requirements
for the Degree of

Doctor of Philosophy in Chemistry

Department of Chemistry
University of Louisville
Louisville, Kentucky

December 2019

© Copyright 2019 by Ram Krishna Hona

All rights reserved

OXYGEN DEFICIENT PEROVSKITES:
EFFECT OF VACANCY ORDER ON ELECTRICAL CONDUCTIVITY,
MAGNETISM AND ELECTROLYTIC ACTIVITY

By

Ram Krishna Hona

A Dissertation Approved on

November 20th, 2019

by the following Dissertation Committee:

Dissertation Director – Dr. Farshid Ramezanipour

Dr. Mark Noble

Dr. Muriel Maurer

Dr. Ming Yu

DEDICATION

This dissertation is dedicated to my wife and my late mother.

ACKNOWLEDGEMENTS

I would like to express my sincere gratitude to my research advisor Prof. Dr. Farshid Ramezanipour for his continuous support in my Ph.D. study and for motivation and enthusiasm toward intense research. His amiable personality with all-time happy behavior and proper guidance kept me happy in all the time of research and during writing this thesis. I could not have imagined having a better advisor and mentor for my Ph.D. study.

I would like to thank my research and dissertation committee members, Dr. Robert. B. Buchanon, Dr. Mark Nobel, Dr. Muriel Maurer and Dr. Ming Yu. I would like to thank Dr. Arjun Kumar Thapa who guided me for collaborative work.

I would like to thank my TA supervisors, Dr. Richad Balwin, Dr. Aleeta M. Powe, Dr. Neal Stolowich for their guidance in my teaching assistantship during my entire PhD study.

I would like to thank my fellow doctoral students for their feedback, cooperation and of course friendship. In addition, I would like to express my gratitude to the staff of chemistry department for their cooperation in my study.

Last but not the least, I am grateful to my wife who has provided me through moral and emotional support in my life. I am also grateful to my other family members and friends who have supported me along the way.

Thanks for all your encouragement!

ABSTRACT

OXYGEN DEFICIENT PEROVSKITES: EFFECT OF VACANCY ORDER ON ELECTRICAL CONDUCTIVITY, MAGNETISM AND ELECTROLYTIC ACTIVITY.

Ram Krishna Hona

November 20, 2019

The present thesis deals with the synthesis and study of the physico-chemical properties of perovskite based oxide materials. Several novel oxygen deficient perovskites (ODP) have been synthesized by conventional solid state synthesis method. The novel compounds are $\text{CaSrFe}_2\text{O}_{6-\delta}$, $\text{CaSrFeCoO}_{6-\delta}$, $\text{Ca}_2\text{Fe}_{1.5}\text{Ga}_{0.5}\text{O}_5$, CaSrFeGaO_5 and $\text{BaSrFe}_2\text{O}_5$. Their magnetic, charge transport and electrocatalytic properties have been studied. Structural effect on electrical conductivity, magnetic and electrocatalytic properties have been studied in some series of ODPs.

$\text{CaSrFe}_2\text{O}_{6-\delta}$, $\text{CaSrFeCoO}_{6-\delta}$, $\text{Ca}_2\text{Fe}_{1.5}\text{Ga}_{0.5}\text{O}_5$ and CaSrFeGaO_5 have brownmillerite type orthorhombic structures with layered structure having alternate tetrahedral and octahedral layers which are connected to one another by corner sharing. These are vacancy ordered compounds. $\text{BaSrFe}_2\text{O}_5$ is vacancy disordered compound with cubic structure. Most of the studied materials exhibited G-type long range antiferromagnetic arrangement of magnetic moments.

During the study of charge transport property, compounds with structural order in a particular series show relatively less conductivity at room temperature and semiconductive nature and transition to metallic conductivity during temperature dependent conductivity measurement. Vacancy disordered compounds show relatively higher conductivity at room temperature and show mixed (semiconductive and metallic) conductivity during temperature dependent conductivity measurement.

The study of electrocatalytic properties revealed the relation with the conductivity and the structural order. The electrocatalytic activity toward oxygen evolution reaction is highly efficient if the material is highly conductive or highly ordered.

TABLE OF CONTENTS

CHAPTER 1. INTRODUCTION	1
1.1. Introduction to Solid State Chemistry	1
I. Solid state chemistry	1
II. Synthesis of solid state materials	2
III. Characterization methods of solid-state materials.....	3
i. Structure and phase purity identification	3
ii. Magnetic measurement	4
iii. Other techniques	5
iv. Physico-chemical property measurement	5
IV. Basics of diffraction	5
1.2. Introduction to Oxygen-Deficient Perovskites.....	10
I. Perovskite oxides	10

II.	Oxygen deficient perovskites (ODPs)	12
III.	Physical properties and possible applications	14
IV.	Role of A - and B – site cations	15
V.	Electrical conductivity of ODPs	16
VI.	Magnetism in perovskite oxides	17
VII.	Oxygen evolution reaction	19

CHAPTER 2. TRANSFORMATION OF STRUCTURE, ELECTRICAL CONDUCTIVITY AND MAGNETISM IN $AA'Fe_2O_{6-\delta}$, A=Sr, Ca and A'= Sr..... 21

Introduction	21
Experimental	23
Results and discussion	25
Crystal structure	25
Magnetic structure	33
Electrical Properties	36
Conclusion	43

CHAPTER 3. UNRAVELING THE ROLE OF STRUCTURAL ORDER IN TRANSFORMATION OF ELECTRICAL CONDUCTIVITY IN $Ca_2FeCoO_{6-\delta}$, $CaSrFeCoO_{6-\delta}$ and $Sr_2FeCoO_{6-\delta}$ 44

Introduction	44
Experimental	46
Results and discussion	48
Crystal structure	48
X-ray photoelectron spectroscopy	61
Electrical conductivities	65
Conclusion	73
CHAPTER 4. MAGNETIC STRIUCTURE OF CaSrFeCoO_5	75
Introduction	75
Experimental section	77
Results and discussion	78
Conclusion	86
CHAPTER 5. ELECTRICAL PROPERTIES OF ORDERED OXYGEN-DEFICIENT PEROVSKITE $\text{Ca}_2\text{Fe}_{0.5}\text{Ga}_{1.5}\text{O}_5$	87
Introduction	87
Materials and methods	90
Results and discussion	91
Crystal structure	91

Electrical properties	94
Conclusion	99
CHAPTER 6. ENHANCED ELECTRICAL PROPERTIES OF BaSrFe₂O_{6-δ} (δ=0.5): A DISORDERED DEFECT-PEROVSKITE.....	100
Introduction	100
Experimental.....	102
Results and discussion	103
Crystal structure	103
Magnetic properties	109
Electrical properties	111
Conclusion	115
CHAPTER 7. CHARGE-TRANSPORT PROPERTIES OF Ca₂FeGaO_{6-δ} AND CaSrFeGaO_{6-δ}: THE EFFECT OF DEFECT-ORDERED	117
Introduction	117
Experimental	120
Results and discussion	121
Crystal structure	121
Microstructure and X-ray photoelectron spectroscopy studies.....	125
Electrical properties	127
Conclusion	133

CHAPTER 8. DISPARITY IN ELECTRICAL AND MAGNETIC PROPERTIES OF ISOSTRUCTURAL OXYGEN-DEFICIENT PEROVSKITES $\text{BaSrCo}_2\text{O}_{6-\delta}$ AND $\text{BaSrCoFeO}_{6-\delta}$	134
Introduction	134
Experimental.....	136
Results and discussion	138
Crystal structure and crystallite morphology	138
X-ray photoelectron spectroscopy (XPS) and iodometric titration	141
Magnetic properties	142
Electrical conductivities	147
Conclusion	152
 CHAPTER 9. STRUCTURE-DEPEDANCE OF ELECTRICAL CONDUCTIVITY AND ELECTROCATALYTIC PROPERTIES OF $\text{Sr}_2\text{Mn}_2\text{O}_6$ and $\text{CaSrMn}_2\text{O}_6$	154
Introduction	154
Experimental	156
Results and discussion	158
Crystal structure	158
Electrical properties	161
Correlation between electrocatalytic activity and conductivity	164
Conclusion	167

CHAPTER 10. VARIATION IN ELECTRICAL CONDUCTIVITY OF $A_2Fe_2O_5$ (A=Sr, Ba)	168
Introduction	168
Experimental	169
Results and discussion	171
Crystal structure	171
Oxidation state of Fe	177
Magnetic properties	178
Electrical conductivity	180
Conclusion	185
CHAPTER 11. STUDY OF $Sr_2Fe_2O_{6-\delta}$ AS ANODE ELECTRODE IN Li-ION BATTERY.....	186
Introduction	186
Experimental	188
Results and discussion	189
Conclusion	199
CHAPTER 12. REMARKABLE OXYGEN-EVOLUTION ACTIVITY OF $Ca_{2-x}Sr_xFe_2O_{6-\delta}$	201
Supporting information	211
Material synthesis and characterization.....	211
Electrode preparation.....	211
Measurements of OER activity.....	212

REFERENCES.....	218
CURRICULUM VITAE.....	235

LIST OF FIGURES

Figure 1.1.1. Lattice planes formed by regular arrays of atoms in a crystal.....	7
Figure 1.1.2. Bragg's law in diffraction.....	8
Figure 1.1.3. Reciprocal lattice point.....	9
Figure 1.1.4. Ewald's sphere forming diffraction	10
Figure 1.2.1. Crystal structure of perovskite oxide. (a) Crystallographic unit cell and corner-sharing BO ₆ octahedra (cyan) are highlighted. The large white spheres are the A atoms. (b) View along the unit cell axis. Because of the cubic symmetry, the three axes are identical. (c) Coordination geometry around the A atom, which is 12-coordinated.	11
Figure 1.2.2. Crystal structure of CaSrFeCoO _{6-δ} (a) crystal structure showing unit cell with alternating (Fe/Co)O ₆ octahedra (cyan) and (Fe/Co)O ₄ tetra (pink) layers. The large white spheres are Sr atoms, the green spheres inside octahedra and tetrahedra are Fe and Co atoms and small red spheres are oxygen atoms. (b) A view along b axis to show the orientation of tetra next to each other in each layer. All atoms are removed for clarity. (c) shows the coordination geometry around the Sr atoms. Note that the Sr is 8-coordinated.....	14
Figure 1.2.3. Representation of electron hopping through Fe ³⁺ -O-Fe ⁴⁺ bond system	17
Figure 1.2.4. Super exchange by coupling two metals with unpaired d-electrons with an oxygen anion.....	18
Figure 1.2.5. Three different ordering schemes in antiferromagnetic perovskite oxides..	18
Figure 2.1. Rietveld refinement profile for powder X-ray diffraction data of Sr ₂ Fe ₂ O _{6-δ} in <i>I4/mmm</i> space group. Stars represent experimental data, red solid is the model, vertical tick marks show Bragg peak positions, and the blue line represents the difference plot.....	26
Figure 2.2. Crystal structure of Sr ₂ Fe ₂ O _{6-δ} . (a) and (b) show the alternating FeO ₆ octahedra (purple) and FeO ₅ square pyramids (green), viewed along the <i>a</i> and <i>c</i> axes, respectively. The large grey spheres are Sr atoms. (c) shows the coordination geometry around the Sr atoms. Note the presence of both 11 and 12-coordinated Sr atoms.....	26

Figure 2.3. Crystal structure of $\text{CaSrFe}_2\text{O}_{6-\delta}$. (a) The octahedral FeO_6 (purple) and tetrahedral FeO_4 (green) layers. Grey spheres represent Sr. (b) View from top to highlight the chain formation in the tetrahedral layer. The Sr atoms are omitted for clarity. (c) Coordination geometry of Sr atoms. Note that Sr is 8-coordinated.	28
Figure 2.4. Rietveld refinement profile for powder X-ray diffraction data of $\text{CaSrFe}_2\text{O}_{6-\delta}$, space group $Ibm2$. Black stars, red line, vertical tick marks and lower blue line represent the experimental data, structural model, Bragg peak positions and difference plot, respectively.	28
Figure 2.5. Scanning electron microscopy images of (a) $\text{Sr}_2\text{Fe}_2\text{O}_{6-\delta}$ and (b) $\text{CaSrFe}_2\text{O}_{6-\delta}$	29
Figure 2.6. X-ray photoelectron spectroscopy data for $\text{CaSrFe}_2\text{O}_{6-\delta}$	31
Figure 2.7. Powder X-ray diffraction data for the series of materials with varying Ca/Sr ratios.	32
Figure 2.8. Refinement of the crystal and magnetic structures using neutron diffraction data for $\text{CaSrFe}_2\text{O}_{6-\delta}$. The upper and lower tick marks represent the peak positions for crystal and magnetic structures, respectively.	34
Figure 2.9. The G-type antiferromagnetic order in $\text{CaSrFe}_2\text{O}_{6-\delta}$. Note that magnetic moments on each Fe site are aligned opposite to all nearest neighbors. The moments are oriented along the c -axis.	35
Figure 2.10. Magnetic Susceptibility data for $\text{CaSrFe}_2\text{O}_{6-\delta}$	36
Figure 2.11. (a) Total conductivity of $\text{Sr}_2\text{Fe}_2\text{O}_{6-\delta}$ and $\text{CaSrFe}_2\text{O}_{6-\delta}$ as a function of temperature. For $\text{Sr}_2\text{Fe}_2\text{O}_{6-\delta}$, the heating and cooling data (red and green) overlap. For $\text{CaSrFe}_2\text{O}_{6-\delta}$ hysteresis is observed between heating (black squares) and cooling data (blue circles). (b) Arrhenius plot of the total conductivity for $\text{Sr}_2\text{Fe}_2\text{O}_{6-\delta}$ (red stars) and $\text{CaSrFe}_2\text{O}_{6-\delta}$ (black circles).	39
Figure 2.12. Thermogravimetric analysis data for $\text{CaSrFe}_2\text{O}_{6-\delta}$ in air.	41

Figure 3.1. Crystal structure of $\text{CaSrFeCoO}_{6-\delta}$. (a) The crystallographic unit cell. The alternating $(\text{Fe/Co})\text{O}_6$ octahedra (cyan) and $(\text{Fe/Co})\text{O}_4$ tetra (pink) are highlighted. The large grey spheres are the A-site cations, $\text{Ca}^{2+}/\text{Sr}^{2+}$. (b) A view along the b axis (longest axis) to show the uniform orientation of tetrahedral chains. The A-site cations are omitted for clarity. (c) The coordination geometry around the A-site cation. There are 8 oxygens that are close enough to the A-site cation to be in its coordination sphere.....46

Figure 3.2. Rietveld refinement profile for powder X-ray diffraction data of $\text{CaSrFeCoO}_{6-\delta}$. Crosses represent experimental data, solid red line is the $Ibm2$ model, vertical tick marks show Bragg peak positions, and the lower line represents the difference plot.....50

Figure 3.3. Neutron diffraction Rietveld refinement profile for $\text{CaSrFeCoO}_{6-\delta}$. Magnetic reflections have been omitted. Crosses represent experimental data, solid red line is the $Ibm2$ model, vertical tick marks show Bragg peak positions, and the lower line represents the difference plot.51

Figure 3.4. Crystal structure of $\text{Sr}_2\text{FeCoO}_{6-\delta}$. (a) The crystallographic unit cell and corner-sharing $(\text{Fe/Co})\text{O}_6$ octahedra (cyan) are highlighted. The large grey spheres are the Sr atoms. (b) A view along the unit cell axis. Due to cubic symmetry, the three axes are identical. (c) The coordination geometry around the Sr atom, which is 12-coordinated....55

Figure 3.5. Rietveld refinement profile for powder X-ray diffraction data of $\text{Sr}_2\text{FeCoO}_{6-\delta}$ refined in $Pm-3m$ space group. Crosses represent experimental data, solid red line is the model, vertical tick marks show Bragg peak positions, and the lower blue line represents the difference plot.....56

Figure 3.6. Crystal structure of $\text{Ca}_2\text{FeCoO}_{6-\delta}$ featuring alternating $(\text{Fe/Co})\text{O}_6$ octahedra (cyan) and $(\text{Fe/Co})\text{O}_4$ tetrahedra (pink). The large grey spheres are Ca atoms. The crystallographic unit cell is highlighted using yellow lines. Note that the unit cell here is 2-times larger than that for the CaSr analogue.57

Figure 3.7. Rietveld refinement profile for powder X-ray diffraction data of $\text{Ca}_2\text{FeCoO}_{6-\delta}$ refined in $Pbcm$ space group. Crosses represent experimental data, red solid line is the model, vertical tick marks show Bragg peak positions, and the blue line represents the difference plot.....57

Figure 3.8. Scanning electron microscopy images for $\text{Sr}_2\text{FeCoO}_{6-\delta}$, $\text{CaSrFeCoO}_{6-\delta}$ and $\text{Ca}_2\text{FeCoO}_{6-\delta}$60

Figure 3.9. Powder XRD data for the series $\text{Sr}_{2-x}\text{Ca}_x\text{FeCoO}_{6-\delta}$, $x = 0 - 1$. The structural transition occurs above $x = 0.3$	60
Figure 3.10. Powder XRD data for the series $\text{Sr}_{2-x}\text{Ca}_x\text{FeCoO}_{6-\delta}$, $x = 1 - 2$. The structural transition occurs above $x = 1.2$	61
Figure 3.11. The Fe XPS spectra for $\text{Ca}_2\text{FeCoO}_{6-\delta}$, $\text{CaSrFeCoO}_{6-\delta}$ and $\text{Sr}_2\text{FeCoO}_{6-\delta}$	63
Figure 3.12. The cobalt XPS spectra for $\text{Ca}_2\text{FeCoO}_{6-\delta}$, $\text{CaSrFeCoO}_{6-\delta}$ and $\text{Sr}_2\text{FeCoO}_{6-\delta}$	64
Figure 3.13. Total conductivity of $\text{Sr}_2\text{FeCoO}_{6-\delta}$, $\text{CaSrFeCoO}_{6-\delta}$ and $\text{Ca}_2\text{FeCoO}_{6-\delta}$ as a function of temperature. For $\text{Sr}_2\text{Fe}_2\text{O}_{6-\delta}$, the heating (red) and cooling (black) data overlap. For $\text{CaSrFeCoO}_{6-\delta}$, the heating data are shown in green and cooling data in blue. For $\text{Ca}_2\text{FeCoO}_{6-\delta}$, the heating and cooling data are shown in pink and cyan, respectively.....	67
Figure 3.14. Thermogravimetric analysis of $\text{CaSrFeCoO}_{6-\delta}$ in air. An inflection in the data appears in the temperature range between the dashed lines. The inset shows the derivative plot.	70
Figure 3.15. Arrhenius plot of the total conductivity for $\text{Sr}_2\text{FeCoO}_{6-\delta}$ (black triangles), $\text{CaSrFe}_2\text{O}_{6-\delta}$ (red circles) and $\text{Ca}_2\text{Fe}_2\text{O}_{6-\delta}$ (green stars).....	72
Figure 4.1. Comparison between (a) perovskite and (b) brownmillerite structure. In brownmillerite, the oxygen vacancies are ordered. The difference in transition metal coordination geometry is highlighted. The A-site cations that reside in spaces between polyhedra have been omitted for clarity.....	77
Figure 4.2. Neutron diffraction refinement profile at 10 K for CaSrFeCoO_5 . The crosses are experimental data, the red line is the model and the lower grey line represents the difference plot. The upper and lower vertical tick marks locate the crystal and magnetic structure peak positions.	79
Figure 4.3. G-type antiferromagnetic order in CaSrFeCoO_5	79
Figure 4.4. Gaussian fit for (021) and (120) magnetic peaks, indicating (120)/(021) ratio of ~ 2.96	81

Figure 4.5. Fits for (021) and (120) magnetic peaks in neutron diffraction data using three different models with magnetic moments along *a* (intermediate), *b* (longest), or *c* (shortest) axis. As shown here, the model with moments along the *c*-axis leads to an excellent fit..82

Figure 4.6. Neutron diffraction refinement profile at 300 K for CaSrFeCoO₅. The crosses are experimental data, the red line is the model and the lower grey line represents the difference plot. The upper and lower vertical tick marks locate the crystal and magnetic structure peak positions.....83

Figure 4.7. Magnetic susceptibility data for CaSrFeCoO₅, as well as its Ca₂ and Sr₂ analogues. Images in a, b and c show the Ca₂, CaSr and Sr₂ compounds, respectively. Black squares show zero-field-cooled and red circles represent field-cooled data.85

Figure 5.1 Brownmillerite structure of Ca₂Fe_{0.5}Ga_{1.5}O₅.....88

Figure 5.2 Refinement profiles for Ca₂Fe_{0.5}Ga_{1.5}O₅ using (a) X-ray and (b) neutron diffraction.....92

Figure 5.3 SEM images of Ca₂Fe_{0.5}Ga_{1.5}O₅, showing good contact between the crystallites.....93

Figure 5.4 X-ray photoelectron spectroscopy data for Ca₂Fe_{0.5}Ga_{1.5}O₅.....94

Figure 5.5 (a) Electrical conductivity of Ca₂Fe_{0.5}Ga_{1.5}O₅ as a function of temperature. (b) Arrhenius plot and activation energies for Ca₂Fe_{0.5}Ga_{1.5}O₅95

Figure 5.6 AC impedance data for Ca₂Fe_{0.5}Ga_{1.5}O₅ at 200 °C. Three resistance-capacitance units indicate the bulk (left), grain boundary (middle) and electrode interface (right) resistance.....96

Figure 5.7 Thermogravimetric analysis for Ca₂Fe_{0.5}Ga_{1.5}O₅.....97

Figure 6.1. Rietveld refinement profiles for BaSrFe₂O_{6-δ} (δ=0.5): (a) X-ray and (b) neutron diffraction data.....104

Figure 6.2. Crystal structures of (a) BaSrFe₂O_{6-δ} (δ=0.5) and (b) CaSrFe₂O_{6-δ} (δ=1)....105

Figure 6.3. Scanning electron microscopy images of sintered pellets of (a) BaSrFe₂O_{6-δ} (δ=0.5) and (b) CaSrFe₂O_{6-δ} (δ=1).....107

Figure 6.4. X-ray photoelectron spectroscopy data for BaSrFe₂O_{6-δ} (δ=0.5).....108

Figure 6.5. Bulk magnetization data of BaSrFe₂O_{6-δ} (δ=0.5) (a) ZFCFC magnetic susceptibility data. The inset shows inverse of susceptibility versus temperature. (b) Isothermal magnetization data at 5 K and 400 K.....110

Figure 6.6. Electrical conductivity as a function of temperature for BaSrFe₂O_{6-δ} (δ=0.5) (red) and CaSrFe₂O_{6-δ} (δ=1) (green).....113

Figure 6.7. Thermogravimetric analysis data for BaSrFe₂O_{6-δ} (δ=0.5).....114

Figure 6.8. Arrhenius plot of the electrical conductivity for BaSrFe₂O_{6-δ} (δ=0.5) (red) and CaSrFe₂O_{6-δ} (δ=1) (green).....115

Figure 7.1. Rietveld refinement profiles for powder X-ray diffraction data of (a) Ca₂FeGaO_{6-δ} in *Pnma*, and (b) CaSrFeGaO_{6-δ} in *Ibm2* space group. Black crosses represent experimental data, the solid red line is the model, pink vertical tick marks show Bragg peak positions, and the lower blue line represents the difference plot. The arrows show the position of 131 peak, which is present for Ca₂FeGaO_{6-δ} and absent for CaSrFeGaO_{6-δ}. ..119

Figure 7.2. Rietveld refinement profiles for powder neutron diffraction data of (a) Ca₂FeGaO_{6-δ} in *Pnma*, and (b) CaSrFeGaO_{6-δ} in *Ibm2* space group. Black crosses represent experimental data, the solid red line is the model, pink vertical tick marks show Bragg peak positions, and the lower blue line represents the difference plot.....120

Figure 7.3. (a) Unit cell of Ca₂FeGaO_{6-δ}, *Pnma*. (b) Alternating octahedral and tetrahedral coordination geometry in Ca₂FeGaO_{6-δ}. The Ca atoms, located in spaces between polyhedra, are omitted for clarity. (c) Orientation of tetrahedral chains in two neighboring layers, which are opposite to each other in Ca₂FeGaO_{6-δ} (top view). The tetrahedral sites are primarily occupied by Ga and octahedral sites by Fe. The red and blue colors represent the two different orientations of tetrahedral chains.123

Figure 7.4. (a) Unit cell of CaSrFeGaO_{6-δ}, *Ibm2*. (b) Alternating octahedral and tetrahedral coordination geometry in CaSrFeGaO_{6-δ}. The Ca/Sr atoms, located in spaces between

polyhedra, are omitted for clarity. (c) Orientation of tetrahedral chains in two neighboring layers (top view). All tetrahedral chains have the same orientation in $\text{CaSrFeGaO}_{6-\delta}$124

Figure 7.5. Scanning electron microscopy images of $\text{Ca}_2\text{FeGaO}_{6-\delta}$ and $\text{CaSrFeGaO}_{6-\delta}$124

Figure 7.6. X-ray photoelectron spectroscopy data for (a) $\text{Ca}_2\text{FeGaO}_{6-\delta}$ and (b) $\text{CaSrFeGaO}_{6-\delta}$. The data for both materials show the same binding energies for Fe peaks.....126

Figure 7.7. Representative example of the Nyquist plot for $\text{CaSrFeGaO}_{6-\delta}$ at 25 °C. The semicircle can be fitted using two resistance-capacitance (RC) units, corresponding to the bulk ($R_1= 766 \Omega$, $CPE_1= 2.6 \times 10^{-8} \text{ F}$) and grain boundary ($R_2 = 3397 \Omega$, $CPE_2= 1.3 \times 10^{-7} \text{ F}$) 128

Figure 7.8. (a) Electrical conductivity of $\text{Ca}_2\text{FeGaO}_{6-\delta}$ (red) and $\text{CaSrFeGaO}_{6-\delta}$ (blue) as a function of temperature. (b) Arrhenius plots for electrical conductivity of $\text{Ca}_2\text{FeGaO}_{6-\delta}$ (red) and $\text{CaSrFeGaO}_{6-\delta}$ (blue).....128

Figure 8.1. Rietveld refinement profile for powder XRD data of a) $\text{BaSrCo}_2\text{O}_{6-\delta}$ and b) $\text{BaSrCoFeO}_{6-\delta}$. Black crosses represent experimental data, the solid red line is the cubic $Pm-3m$ model, pink vertical tick marks show Bragg peak positions, and the lower blue line represents the difference plot..... 139

Figure 8.2. Scanning electron microscopy images of $\text{BaSrCoFeO}_{6-\delta}$ (top) and $\text{BaSrCo}_2\text{O}_{6-\delta}$ (bottom).....140

Figure 8.3. X-ray photoelectron spectroscopy data. (a) shows the Co peaks for $\text{BaSrCo}_2\text{O}_{6-\delta}$. (b) and (c) show the Fe and Co peaks for $\text{BaSrCoFeO}_{6-\delta}$, respectively.143

Figure 8.4. Bulk magnetization data for $\text{BaSrCo}_2\text{O}_{6-\delta}$: (a) ZFC and FC magnetic susceptibility data. The inset shows inverse of susceptibility plotted against temperature. (b) Isothermal magnetization versus field, at 2K and 400 K..... 144

Figure 8.5. Bulk magnetization data for $\text{BaSrCoFeO}_{6-\delta}$: (a) ZFC/FC magnetic susceptibility data. The inset shows inverse of susceptibility versus temperature. (b) Isothermal magnetization data at 2K and 400 K.....145

Figure 8.6. Electrical conductivity of (a) $\text{BaSrCo}_2\text{O}_{6-\delta}$ and (b) $\text{BaSrCoFeO}_{6-\delta}$. The measurements were done in the same environment used for synthesis, namely in argon for $\text{BaSrCo}_2\text{O}_{6-\delta}$ and in air $\text{BaSrCoFeO}_{6-\delta}$. Heating data are shown in green and the cooling data in red.....149

Figure 8.7. comparison of the electrical conductivity for $\text{BaSrCo}_2\text{O}_{6-\delta}$ and $\text{BaSrCoFeO}_{6-\delta}$ both obtained in argon atmosphere.....150

Figure 8.8. Arrhenius plot for electrical conductivity of (a) $\text{BaSrCo}_2\text{O}_{6-\delta}$ and (b) $\text{BaSrCoFeO}_{6-\delta}$152

Figure 9.1. (a) Crystal structure and (b) Rietveld refinement profile from X-ray diffraction data for $\text{Sr}_2\text{Mn}_2\text{O}_6$, $P6_3/mmc$. Black crosses represent experimental data, the solid red line is the model, pink vertical tick marks show Bragg peak positions, and the lower grey line represents the difference plot.159

Figure 9.2. (a) Crystal structure and (b) Rietveld refinement profile from X-ray diffraction data for $\text{CaSrMn}_2\text{O}_6$, $Pm-3m$. Black crosses represent experimental data, the solid red line is the model, pink vertical tick marks show Bragg peak positions, and the lower grey line represents the difference plot.160

Figure 9.3. (a) Temperature dependent electrical conductivity and (b) Arrhenius plots for $\text{Sr}_2\text{Mn}_2\text{O}_6$ (blue circles) and $\text{CaSrMn}_2\text{O}_6$ (green triangles). The inset in (a) is a zoomed view of the increase in conductivity of $\text{Sr}_2\text{Mn}_2\text{O}_6$163

Figure 9.4. (a) Polarization curves for OER with mass activities for $\text{Sr}_2\text{Mn}_2\text{O}_6$ (blue) and $\text{CaSrMn}_2\text{O}_6$ (green). (b) Tafel slopes for $\text{Sr}_2\text{Mn}_2\text{O}_6$ (blue) and $\text{CaSrMn}_2\text{O}_6$ (green).....165

Figure 10.1. Rietveld refinement profile for powder XRD data of (a) $\text{Sr}_2\text{Fe}_2\text{O}_5$, with $Ibm2$ space group and (b) $\text{Ba}_2\text{Fe}_2\text{O}_5$ with monoclinic $P2_1/c$ space group. The solid red line shows the refinement model, black crosses represent experimental data, pink vertical tick marks show Bragg peak positions, and the lower blue line represents the difference plot.....271

Figure 10.2. Crystal structures of (a) $\text{Sr}_2\text{Fe}_2\text{O}_5$ and (b) $\text{Ba}_2\text{Fe}_2\text{O}_5$172

Figure 10.3. The coordination geometry of 7 crystallographically distinct Fe atoms and the connectivity of polyhedra in $\text{Ba}_2\text{Fe}_2\text{O}_5$. Red, green, blue and yellow polyhedra represent

tetrahedral, square pyramidal, pseudo square pyramidal and octahedral geometry, respectively (NS = not shared with other polyhedra).....176

Figure 10.4. Scanning electron microscopy images of $\text{Sr}_2\text{Fe}_2\text{O}_5$ (top) and $\text{Ba}_2\text{Fe}_2\text{O}_5$ (bottom).....177

Figure 10.5. X-ray photoelectron spectroscopy data for (a) $\text{Sr}_2\text{Fe}_2\text{O}_5$ and (b) $\text{Ba}_2\text{Fe}_2\text{O}_5$178

Figure 10.6. (a) Isothermal magnetization data, where black and red show $\text{Sr}_2\text{Fe}_2\text{O}_5$ magnetization at 5 K and 300 K, and blue and green represent the corresponding data for $\text{Ba}_2\text{Fe}_2\text{O}_5$. (b) Magnetic susceptibility data.179

Figure 10.7. Electrical conductivity of (a) $\text{Sr}_2\text{Fe}_2\text{O}_5$ and (b) $\text{Ba}_2\text{Fe}_2\text{O}_5$ in inert atmosphere. Blue circles and red stars represent the data obtained while heating and cooling, respectively. The inset in (b) magnifies the data in the temperature range 600 – 900 °C for $\text{Ba}_2\text{Fe}_2\text{O}_5$181

Figure 10.8. Thermogravimetric analysis data for (a) $\text{Sr}_2\text{Fe}_2\text{O}_5$ and (b) $\text{Ba}_2\text{Fe}_2\text{O}_5$182

Figure 10.9. Arrhenius plots for electrical conductivity of (a) $\text{Sr}_2\text{Fe}_2\text{O}_5$ and (b) $\text{Ba}_2\text{Fe}_2\text{O}_5$184

Figure 11.1. Crystal structure of $\text{Sr}_2\text{Fe}_2\text{O}_{6-\delta}$. (a) unit cell (b) side view and (c) Top view of the crystallographic structure which show the alternating FeO_6 octahedra (cyan) and FeO_5 square pyramids (purple). Sr atoms are removed for clarity.....190

Figure 11.2. Rietveld refinement profile for powder X-ray diffraction data of $\text{Sr}_2\text{Fe}_2\text{O}_{6-\delta}$ in $I4/mmm$ space group. Cross symbols represent experimental data, red solid is the model, vertical tick marks show Bragg peak positions, and the blue line represents the difference plot. Inset shows the peak bifurcation at higher 2θ angle.....191

Figure 11.3. SEM images of $\text{Sr}_2\text{Fe}_2\text{O}_{6-\delta}$191

Figure 11.4. X-ray photoelectron spectroscopy data for $\text{Sr}_2\text{Fe}_2\text{O}_{6-\delta}$193

Figure 11.5. Galvanostatic charge-discharge profiles of $\text{Sr}_2\text{Fe}_2\text{O}_{6-\delta}$ anode electrode at the voltage range of 3.0 -0.005 V with a current density of 25 mA/g for 1 st , 2 nd , 10 th , 20 th , 30 th , 40 th and 50 th cycles.....	195
Figure 11.6. Capacities versus cycle numbers of $\text{Sr}_2\text{Fe}_2\text{O}_{6-\delta}$ anode electrode at the voltage range of 3.0 -0.005 V with a current density of 25 mA/g.....	196
Figure 11.7. C-rate test of $\text{Sr}_2\text{Fe}_2\text{O}_{6-\delta}$ anode electrode at the voltage range of 3.0 – 0.005 V and different current densities of 25, 50, 100, 200, and 500 mA g ⁻¹ , respectively.....	197
Figure 11.8. Cyclic voltammetry of $\text{Sr}_2\text{Fe}_2\text{O}_{6-\delta}$ anode electrode scanned at the voltage range of 3.0 – 0.005 V with a scan speed of 1 mV s ⁻¹	198
Figure 12.1. Crystal structures of (a) $\text{Ca}_2\text{Fe}_2\text{O}_{6-\delta}$, (b) $\text{CaSrFe}_2\text{O}_{6-\delta}$, and (c) $\text{Sr}_2\text{Fe}_2\text{O}_{6-\delta}$. In (a) and (b), different colors represent different orientations of tetrahedral chains.....	203
Figure 12.2. (a) Polarization curves showing the OER activities, obtained using the conventional glassy carbon electrode setup. (b) Comparison of the activity of $\text{Sr}_2\text{Fe}_2\text{O}_{6-\delta}$ with state of the art materials RuO_2 and $\text{Ba}_{0.5}\text{Sr}_{0.5}\text{Co}_{0.8}\text{Fe}_{0.2}\text{O}_{3-\delta}$ (BSCF).....	205
Figure 12.3. Tafel slopes indicating the OER kinetics.....	207
Figure 12.4. Plot of $\Delta j = j_{\text{anodic}} - j_{\text{cathodic}}$ as a function of scan rate. The C_{dl} for each material is equivalent to half of the slope.....	208
Figure 12.5. (a) Polarization curves showing the OER activities of pure disks of catalysts. (b) Stability test for $\text{Sr}_2\text{Fe}_2\text{O}_{6-\delta}$ by performing 500 cycles.....	209
Figure S1. Rietveld refinement profiles using powder X-ray diffraction for (a) $\text{Ca}_2\text{Fe}_2\text{O}_{6-\delta}$, space group <i>Pnma</i> , (b) $\text{CaSrFe}_2\text{O}_{6-\delta}$, space group <i>Ibm2</i> , and (c) $\text{Sr}_2\text{Fe}_2\text{O}_{6-\delta}$, space group <i>I4/mmm</i> . Black symbols are the experimental data, red line represents the model, vertical tick marks show Bragg peak positions, and the lower blue line represents the difference plot.....	213

Figure S2. (a) The setup for testing the OER activity of catalysts disks, without glassy carbon electrode. (b) The entire measurement setup.....213

Figure S3. Cyclic voltammetry in non-faradic region to obtain double layer capacitance (Figure 4) for the three compounds (a) $\text{Ca}_2\text{Fe}_2\text{O}_{6-\delta}$, (b) $\text{CaSrFe}_2\text{O}_{6-\delta}$, and (c) $\text{Sr}_2\text{Fe}_2\text{O}_{6-\delta}$214

Figure S4. Polarization curve for $\text{Sr}_2\text{Fe}_2\text{O}_{6-\delta}$, obtained using the conventional glassy carbon setup, and with the addition of carbon black to the catalyst. Comparison to Figure 2 indicates that carbon black does not improve the OER activity.215

Figure S5. Tafel slopes for BSCF and RuO_2215

Figure S6. Plot of $\Delta j = j_{\text{anodic}} - j_{\text{cathodic}}$ as a function of scan rate for (a) BSCF and (b) RuO_2 . The C_{dl} for each material is equivalent to half of the slope.....216

LIST OF TABLES

Table 2.1. Refined structural parameters of $\text{Sr}_2\text{Fe}_2\text{O}_{6-\delta}$	27
Table 2.2. Refined structural parameters of $\text{CaSrFe}_2\text{O}_{6-\delta}$	29
Table 2.3. Room temperature conductivity and activation energies.....	37
Table 3.1. Refined structural parameters of $\text{CaSrFeCoO}_{6-\delta}$ using powder X-ray diffraction.....	52
Table 3.2. Refined atomic parameters of $\text{CaSrFeCoO}_{6-\delta}$ in <i>Ibm2</i> space group using neutron diffraction.....	53
Table 3.3. Comparison of space groups and unit cell parameters for $\text{Ca}_2\text{FeCoO}_{6-\delta}$, $\text{CaSrFeCoO}_{6-\delta}$ and $\text{Sr}_2\text{FeCoO}_{6-\delta}$	54
Table 3.4. Refined structural parameters of $\text{Sr}_2\text{FeCoO}_{6-\delta}$	56
Table 3.5. Refined structural parameters of $\text{Ca}_2\text{FeCoO}_{6-\delta}$	59
Table 3.6. Room temperature conductivity and activation energies.....	73
Table 5.1 The refined structural parameters for $\text{Ca}_2\text{Fe}_{0.5}\text{Ga}_{1.5}\text{O}_5$ from neutron diffraction. Space group: <i>Pnma</i> , $a = 5.3669(2)$, $b = 14.6214(5)$, $c = 5.5927(2)$, $R_p = 0.0744$, $wR_p = 0.0479$	92
Table 6.1. Refined structural parameters from neutron diffraction data for $\text{BaSrFe}_2\text{O}_{6-\delta}$ ($\delta=0.5$), space group <i>Pm-3m</i> , $a = 3.92851(4)$, $R_p = 0.041$, $wR_p = 0.033$	105

Table 6.2. Electrical conductivity, σ (S cm ⁻¹), and activation energies, E_a (eV), for increase in electrical conductivity up to 400 °C.	114
Table 7.1. Refined structural parameters for Ca ₂ FeGaO _{6-δ} from powder neutron diffraction. Space group <i>Pnma</i> , $a = 5.38902(9)$ Å, $b = 14.65164(22)$ Å, $c = 5.60081(9)$ Å, $R_p = 0.0405$, $wR_p = 0.0208$	130
Table 7.2. Refined structural parameters for CaSrFeGaO _{6-δ} from powder neutron diffraction. Space group <i>Ibm2</i> , $a = 5.6437(1)$ Å, $b = 15.0577(4)$ Å, $c = 5.4458(1)$ Å, $R_p = 0.0450$, $wR_p = 0.0216$	131
Table 7.3. Room Temperature Conductivity and Activation Energies.....	132
Table 8.1. Refined Structural Parameters for BaSrCoFeO _{6-δ} using powder X-ray diffraction data.....	139
Table 8.2. Refined Structural Parameters for BaSrCo ₂ O _{6-δ} using powder X-ray diffraction data.....	140
Table 8.3. Room Temperature Conductivity and Activation Energies.....	148
Table 9.1. Refined structural parameters for Sr ₂ Mn ₂ O ₆ using powder X-ray diffraction. Space group: <i>P6₃/mmc</i> , $a = b = 5.45233(8)$ Å, $c = 9.0856(1)$ Å, $R_p=0.030$, $wR_p= 0.038$, $\chi^2 = 1.790$	159
Table 9.2. Refined structural parameters for CaSrMn ₂ O ₆ using powder X-ray diffraction data. Space group: <i>Pm-3m</i> , $a = 3.7772(1)$ Å, $R_p = 0.051$, $wR_p = 0.064$, $\chi^2 = 1.406$	160
Table 9.3. Room temperature conductivity and activation energies.....	163
Table 10.1. Refined structural parameters for Sr ₂ Fe ₂ O ₅ using powder X-ray powder diffraction. Space group is <i>Ibm2</i> , and unit cell parameters are $a = 5.68023(6)$, $b = 15.5862(2)$, $c = 5.53425(6)$ Å.....	172
Table 10.2. Refined structural parameters for Ba ₂ Fe ₂ O ₅ using powder X-ray powder diffraction. Space group is <i>P2₁/c</i> and unit cell parameters are $a = 6.9772(1)$, $b = 11.7376(2)$, $c = 23.4575(4)$ Å, and $\beta = 98.7540(8)^\circ$	174
Table 10.3. Different coordination geometry and bond distances of Fe in Ba ₂ Fe ₂ O ₅ ...	175

Table 10.4. The connectivity of polyhedra in Ba ₂ Fe ₂ O ₅	176
Table 10.5. Room temperature conductivity and activation energies.....	184
Table 11.1. Refined structural parameters for Sr ₂ Fe ₂ O _{6-δ} from powder X-ray diffraction. Space group <i>I4/mmm</i> , <i>a</i> = 10.9301(2) Å, <i>b</i> = 10.9301(2) Å, <i>c</i> = 7.6958(2) Å, <i>R_p</i> = 0.0211, <i>wR_p</i> = 0.0299.....	190
Table S1. The refined structural parameters for Ca ₂ Fe ₂ O _{6-δ} from powder X-ray diffraction. Space group: <i>Pnma</i> , <i>a</i> = 5.40238(5), <i>b</i> = 14.7018(1), <i>c</i> = 5.57261(5), <i>R_p</i> = 0.013, <i>wR_p</i> = 0.018, χ^2 = 1.941.....	216
Table S2. The refined structural parameters for CaSrFe ₂ O _{6-δ} from powder X-ray diffraction. Space group: <i>Ibm2</i> , <i>a</i> = 5.6313(4), <i>b</i> = 15.181(1), <i>c</i> = 5.4695(4), <i>R_p</i> = 0.018, <i>wR_p</i> = 0.026, χ^2 = 1.604.....	217
Table S3. The refined structural parameters for Sr ₂ Fe ₂ O _{6-δ} from powder X-ray diffraction. Space group: <i>I4/mmm</i> , <i>a</i> = 10.9345(7), <i>b</i> = 10.9345(7), <i>c</i> = 7.6988(5), <i>R_p</i> = 0.022, <i>wR_p</i> = 0.031, χ^2 = 1.505.....	217

CHAPTER 1

INTRODUCTION

1.1. Introduction to solid states chemistry

I. Solid state chemistry

Solid-state chemistry, also known as material chemistry, is the study of the synthesis, structure, chemical, and physical properties and the application of solid materials particularly non-molecular solids. In general, the chemistry, structure and properties of the solid materials are interrelated. Thus, for a specific solid state chemistry, the study should be aimed at getting detailed knowledge of the three factors such as how the chemistry affects in the structure of a material and then how the structure affects the physical properties. One example of study of solid state chemistry is study of structure-property relation in perovskite oxide materials. Richard J. D. Tilley has well collected the works of structure-property relation in perovskite oxides.¹ They have been intensively studied for their dielectric, piezoelectric, and ferroelectric nature. Now the range of property-study has been extended to magnetic ordering, multiferroic properties, electronic conductivity, superconductivity, thermal and optical properties.¹ Perovskite oxides have wide range of structures from cubic SrTiO_3 to cation and anion deficient phases to hexagonal perovskites related to SrMnO_3 .¹ The chemical and physical properties of any members of these structural forms can be tuned to wide ranges by simply substituting A or B site cations. Next good example of structure-property relation can be found in a literature² which states the correlation between anti-ferromagnetic Neel temperature and structural destruction in

the series of rare earth ortho-ferrites (LnFeO_3 , $\text{Ln} = \text{La-Lu}$). The t value is below 1 for all LnFeO_3 leading to perovskite superstructure due to tilting of octahedra. The crystal structure will experience increasing tilt of the octahedra due to the decreasing effect of A cation radius down the lanthanide series. The interaction between B cations coupled with intervening oxygen ions results Antiferromagnetism.³ The effect of super-exchange leads to antiparallel alignment of the spins. The Neel temperature will become lower as the distortion increases causing more tilt. Thus, the Neel temperature can be correlated with the tilt of the octahedra. Thus, structural-property in solid state material can be revealed. So, a solid state chemist requires to have knowledge of structural – property relation to design a material of desired structure, property and application.

II. Synthesis of solid state materials

As is clear from the title “solid state chemistry”, generally no solution but high temperature (heat) is used to prepare a desired material. However, in some cases such as in coprecipitation and sol-gel method, solutions are used in the pre-stage of the synthesis and in subsequent steps, high heat is used to decompose the precursor compounds after drying. For perovskite oxides, conventional solid state method can normally be employed. In this process, the precursor compounds are mixed in stoichiometric proportions and mixed thoroughly. Since the solid state precursors require complete decomposition to form a completely new compound, multiple and high heating is required. In this case, the reaction takes place by ion diffusion at high temperature which is very slow process. Generally, perovskite oxides are synthesized from nitrates or carbonates. So, two stages of heating namely, calcination (low temperature) and sintering (high temperature) are accomplished to get a material of pure phase. This technique is commonly used to

investigate the chemistry induced structural changes and thermal stability of the structures. The detailed procedure for this method can be obtained in this thesis based articles.

III. Characterization methods of solid-state materials

i. Structure and phase purity identification

Once a sample is synthesized, its phase identification is first job to go ahead with other characterization procedures. A phase is a crystalline solid with a regular 3-dimensional arrangement of the atoms. Powder X-ray diffraction method is employed as a fast phase identification technique in solid state chemistry. The measured diffraction peak positions and intensities are like a fingerprint for a particular phase. The spacing of powder diffraction lines are dependent on the unit cell parameters for a crystalline compound. Phase purity is checked by comparison of the measured pattern with the entries in reference databases using a search-match algorithm. This is also known as qualitative phase analysis. The peak indexing is simplified by the computer programming during the comparison with the structure of another known compound. The powder pattern of a phase is confirmed by refinement process using certain computer programs such as Rietveld refinement using GSAS with EXPIGUI interface, Full prof fitting and Topaz fitting programs, where a known phase model is used for XRD data fitting.

The diffraction data may also be collected using neutrons. Neutron diffraction is a result of interaction of neutrons with nuclei and therefore scatters strongly with light atoms as well as heavy atoms and can easily differentiate between isotopes. X-rays interact with electron clouds and therefore scatter strongly from heavier elements with larger electron clouds. So, If a compound with elements of nearly similar atomic mass or with light elements is to be identified with exact composition and atomic positions, then neutron

diffraction is suggested. For example, we used neutron diffraction for $\text{Ca}_2\text{Fe}_{1.5}\text{Ga}_{0.5}\text{O}_5$ compound to find the atomic position of Fe and Ga elements in the crystal structure which X-ray diffraction could not explain.

ii. Magnetic measurement

Most materials have no permanent magnetic moment but a moment is induced in the presence of a field. The response is called magnetic susceptibility (χ). Usually magnetic susceptibility is measured to find the degree of material magnetization in an applied magnetic field. Mathematically, it is the ratio of magnetization M (magnetic moment per unit volume) to the applied magnetizing field intensity H.

$$\chi = \frac{M}{H} \quad (1)$$

Magnetic susceptibility, χ , is a function of temperature, T. So, it is commonly measured over a range of temperature. Magnetic field is also applied during susceptibility measurement. Generally, two measurements are performed for χ versus T: (a) Zero Field Cooled (ZFC) measurement where sample is first cooled in the absence of a field and then susceptibility is measured in the applied field as temperature rises. (b) Field Cooled (FC) measurement where sample is first cooled in the presence of a field and then susceptibility is measured in the same field as temperature rises. The data obtained from these two measurements, χ versus T may overlap or diverge from each other. The divergence shows the formation of magnetic domains induced by the applied field. the χ versus T plot appears as a smooth curve at low temperature region for a paramagnet. Any deviation from this behavior is an indication for the presence of a magnetically ordered state and the

temperature at which the deviation occurs is the magnetic transition temperature. Measurement of magnetization of a material as a function of the applied field, H, at constant temperature is also common. The magnetization is recorded during H rising and falling, both times. The M versus H graph is linear for a paramagnet, (as long as the saturation at high field and low T is not reached) and the data collected during both times, H value rising and falling will overlap. However, if there is any uncompensated magnetic moment in the system, divergence is observed for the data obtained for increase and decrease of H.

iii. Other techniques

Other techniques for characterization include scanning electron microscopy for microstructure analysis, X-ray Photoelectron Spectroscopy for oxidation state analysis, iodometric titration for oxygen content calculation.

iv. Physico-chemical property measurement

Temperature dependent oxygen absorption and desorption behavior of the materials is measured by thermogravimetric analysis using Ar gas. DC measurement and impedance spectroscopy study are performed for temperature dependent conductivity behavior analysis and conductivity mechanism of a material, respectively. CV measurement is performed for oxygen evolution reaction.

IV. Basics of diffraction

i. Bragg's law

X-rays are electromagnetic waves with a much shorter wavelength than visible light, typically on the order of 1\AA (1×10^{-10} m). When a beam of X-rays fall on a single particle, it scatters the incident beam uniformly in all directions. These scattered beams can add

together in a few directions to reinforce each other resulting a diffraction. The regular arrangement of atomic particles in a crystal system is responsible for the diffraction of the beams. X-ray diffractions were used in the identification of our material's crystal structures.

Crystals are regular arrays of atoms. These arrays form imaginary planes in the crystal system called crystal lattice. Lattice planes are crystallographic planes, characterized by the index triplet hkl , the so-called Miller indices. Parallel planes have the same indices and are equally spaced, separated by the distance d_{hkl} , (figure 1.1.1). There can be a number of sets of planes running in different directions in a crystal system, and they are named according to their orientation relative to the axes of the unit cell, the smallest repeated unit in the crystal system. For example, a set of planes, in an ideal cubic crystal system, running parallel to bc plane intercepts a axis but do not intercept b and c axes and can be expressed by Miller indices, hkl as $(1,0,0)$ planes. These planes are responsible for the constructive interference.

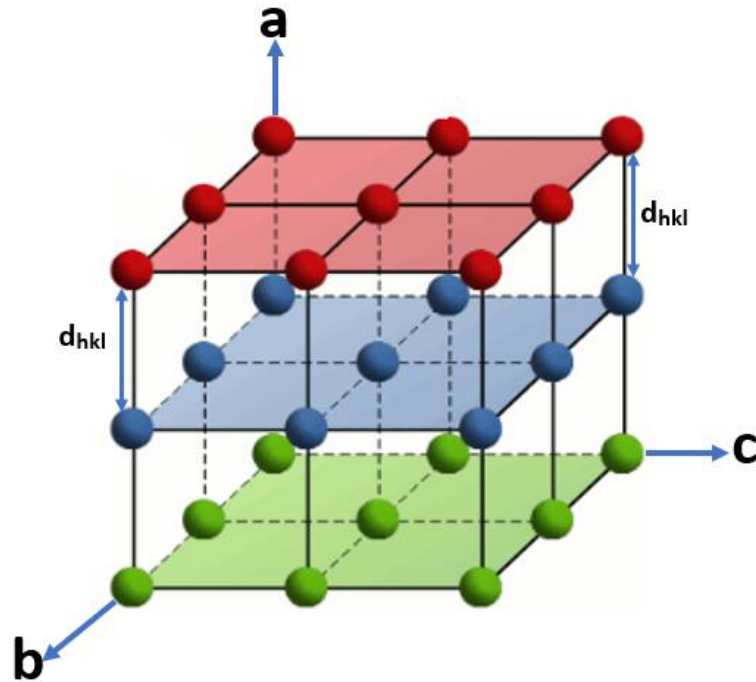


Figure 1.1.1. Lattice planes formed by regular arrays of atoms in a crystal

According to Bragg's law, when the waves are scattered from lattice planes separated by the interplanar distance d , the scattered waves interfere constructively and they remain in phase when the difference between the path lengths of the two waves is equal to an integer multiple of the wavelength. The path difference between two waves undergoing interference is given by $2d \sin \theta$, where θ is the scattering angle (as shown in figure 1.1.2).

Mathematically, it can be expressed as

$$n\lambda = 2d \sin\theta \quad (2)$$

When the diffraction meets the above condition, a constructive interference between the diffracted beams becomes possible to generate a diffraction. The diffraction data are commonly expressed as a function of 2θ where the diffraction peak at smallest 2θ corresponds to the largest d spacing.

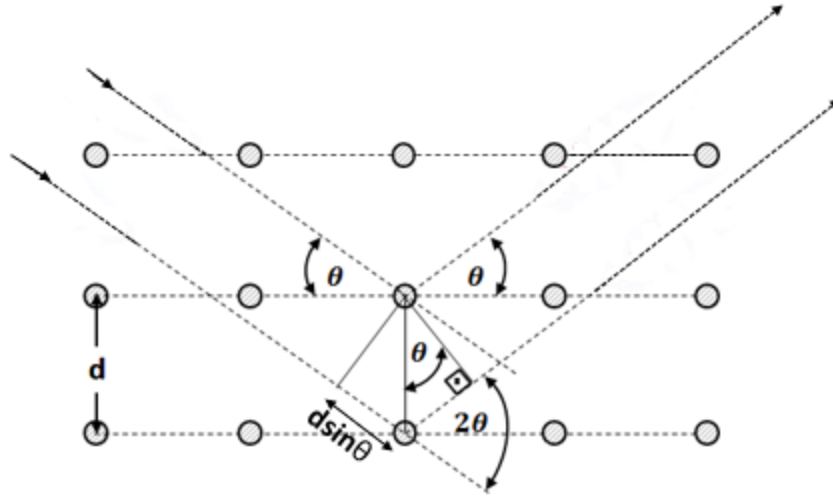


Figure 1.1.2. Bragg's law in diffraction

ii. Reciprocal lattices

To understand the reciprocal lattice, let us consider a unit cell of a cubic crystal (figure 1.1.3). Let us consider an arbitrary point A from which a normal \overrightarrow{AB} (vector) is drawn to a plane "bc". The distance of \overrightarrow{AB} should be reciprocal of d_{hkl} (distance between two bc planes) i.e. $\overrightarrow{AB} = \frac{1}{d_{hkl}}$. Every line drawn normal to all planes in all directions must have the distance equal to $\frac{1}{d_{hkl}}$. The planes can also be characterized by a vector $(\underline{\sigma}_{hkl})$ perpendicular to the normal vector \overrightarrow{AB} . Now, the lengths of the perpendicular vectors (\overrightarrow{AB}) are reciprocal to the interplanar spacings. The end points of these vectors (blue arrows in figure) also produce a periodic lattice that is known as the reciprocal lattice of the original direct lattice.

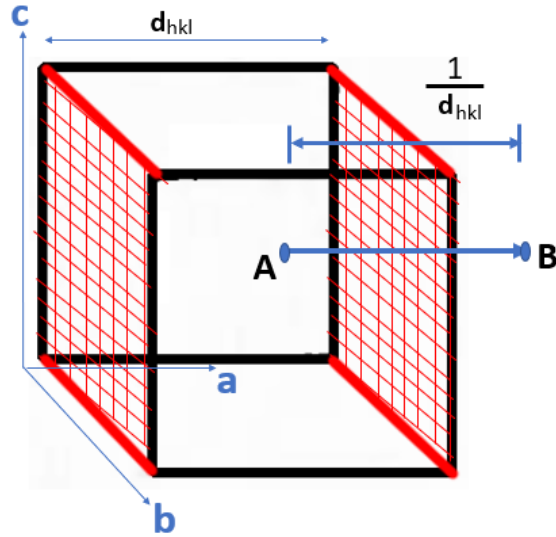


Figure 1.1.3. Reciprocal lattice point

If we consider a set of parallel planes hkl with the interplanar distance d_{hkl} and if we take one ($\underline{\sigma}_{hkl}$) with length $1/d_{hkl}$ from a set of vectors normal to the planes' family, then, $\underline{\sigma}_{hkl}$ represents the whole family of hkl planes having an interplanar spacing given by d_{hkl} .

iii. Ewald's sphere

The Ewald's sphere is the most useful tool to understand the occurrence of diffraction spots. It helps to visualize the properties of Bragg's law, $n\lambda = 2d \sin\theta$. It is an imaginary sphere of radius $1/\lambda$ surrounding a crystal (shown in figure 1.1.4). If we consider a real crystal in the center of the sphere, the origin of the reciprocal lattice lies in the transmitted beam at the edge of the Ewald sphere. Diffraction maxima (reflections, diffraction spots) occur only when the Bragg equation is satisfied and the Bragg's condition, $n\lambda = 2d \sin\theta$ is satisfied by the diffraction only when a reciprocal lattice point lies exactly on the Ewald sphere.

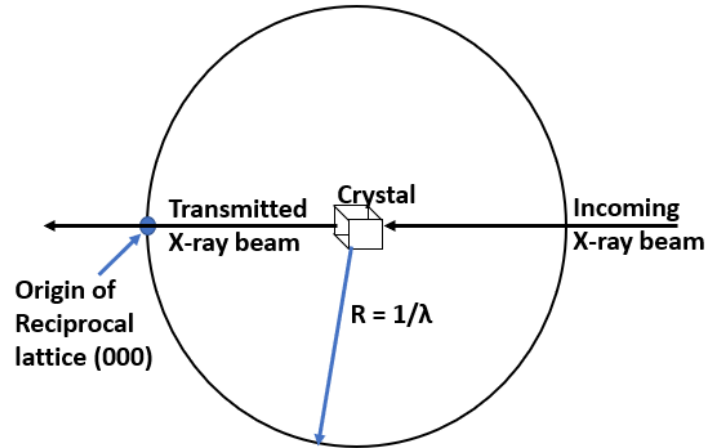


Figure 1.1.4. Ewald's sphere forming diffraction

1.2. Introduction to oxygen-deficient perovskites

Perovskites are a class of materials with similar structure and a myriad of exciting properties like superconductivity, magnetoresistance, catalysis and many more. They are easy to synthesize and are considered as the future of solar cells because their attractive structure makes them perfect for enabling low-cost, efficient photovoltaics. Since they have characteristics of mixed ionic and electronic conductivity, they can be applied as electrodes for fuel cells and hence they are also considered as future energy materials. They are predicted to play a role in next-gen electric vehicle batteries, sensors, lasers and much more.

I. Perovskite oxides

Oxide groups containing two or more different cations are called complex or mixed oxides. Many types of crystal structures are known for the oxides. One of them is perovskite structure. Perovskite oxides have the crystal structure similar to CaTiO_3 and it

is expressed in general chemical formula ABO_3 where A is generally alkaline earth metal or rare earth metal cations and B is transition metal or main p block metal cations (specifically group 13 metals). The ideal cubic-symmetry of perovskite structure has the B cation in 6-fold coordination surrounded by six oxide anions forming an octahedron. The A cation is surrounded by 8 octahedra with 12-fold cuboctahedral coordination. The size of A cations is bigger than B cations. The ideal structure of perovskite, which is illustrated in Fig. 1.1, is a cubic lattice.

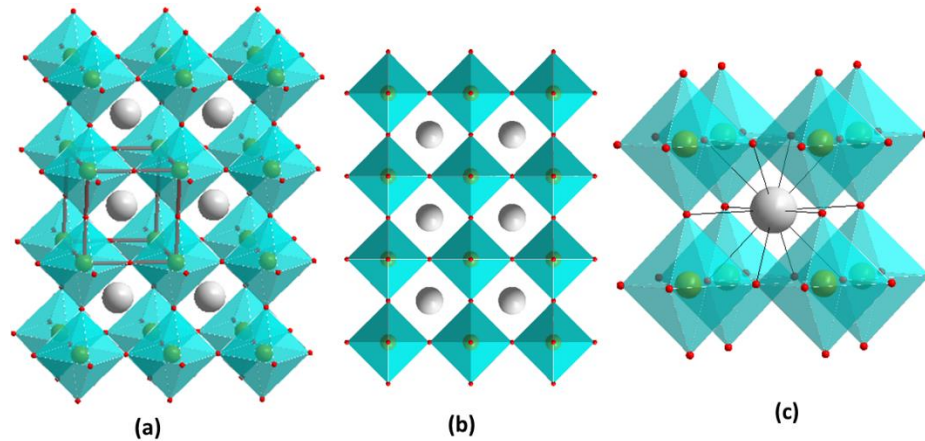


Figure 1.2.1. Crystal structure of perovskite oxide. (a) Crystallographic unit cell and corner-sharing BO_6 octahedra (cyan) are highlighted. The large white spheres are the A atoms. (b) View along the unit cell axis. Because of the cubic symmetry, the three axes are identical. (c) Coordination geometry around the A atom, which is 12-coordinated.

These ABO_3 oxides are regarded as purely ionic crystals where the following relationship between the radii of the A, B, and O^{2-} ions holds true for a cell axis (a) in the ideal cubic structure,¹

$$a = \sqrt{2}(r_A + r_O) = 2(r_B + r_O) \quad (3)$$

Although few compounds have this ideal cubic structure, many oxides have slightly distorted variants with lower symmetry (e. g., hexagonal or orthorhombic). There are various types of distortions in the perovskite structure that are strongly related to their properties. Tolerance factor (t) can be applied in order to understand the deviations from the ideal cubic structure. *tolerance factor* (t) can be found out from the following equation.¹

$$t = \frac{(r_A+r_O)}{\sqrt{2}(r_B+r_O)} \quad (4)$$

In perovskite-type compounds, the value of t lies between approximately 0.80 and 1.10 and the ideal cubic structure has the value of t close to 1. It has been found that the oxides with the lower t values (0.85) crystallize in the distorted variant of cubic form such as orthorhombic or rhombohedral while greater than 1 gives hexagonal or tetragonal structure including units of face sharing BO₆ octahedra. Thus, the crystal structure can be transformed by substituting A or B cation by another cation of different ionic radius which alters the Tolerance factor.

II. Oxygen deficient perovskites

Oxygen deficient perovskite (ODP) oxides are a class of compounds having less oxygens than in perovskite oxides and it is represented by general formula ABO_{3-x} or A₂B₂O_{6-δ} where x or δ represent oxygen deficiency. Figure 1.2.2 demonstrates a structure of ODP. If A and B have different cations (where A and A' are alkaline earth metal ions and B and B' are transition metal ions) like in CaSrFeMnO₅, the formula can be expressed as AA'BB'O_{6-δ}. In oxygen deficient perovskites, the oxygen vacancy (also called as defect) can transform the coordination geometry around B cation from octahedra to tetrahedra⁴ or

square pyramidal⁴ geometry. There are many ways of vacancy ordering/disordering which make oxygen deficient perovskites possible to have structural flexibility⁵⁻⁶. If tetrahedral geometries are formed, BO₄ tetrahedra can share corners with other BO₄ tetrahedra or BO₆ octahedra. This corner sharing tetrahedra can arrange in a regular pattern forming a long chain. This chain may form layer alternating with the layer of BO₆ octahedra. These alternating layers are demonstrated in figure 1.2.2. A number of different space group symmetries arise due to difference in the ordering of the tetrahedral chains within the unit cell.⁷ The space group is determined by the relative orientation of the tetrahedral chains. There are two possible orientations, which are arbitrarily called right-handed and left-handed. If all tetrahedral chains have the same orientation, the space group *Ibm2* is obtained. If the tetrahedral chains have the same orientation within each layer but are oriented opposite to the chains in the next tetrahedral layer, the resulting space group is *Pnma*. The random orientation of tetrahedral chains leads to the space group *Icmm*. A less common space group is *Pbcm*, where each tetrahedral chain is oriented opposite to all of its nearest neighbors within the same layer and in the neighboring layers. These space groups belong to brownmillerite structures.

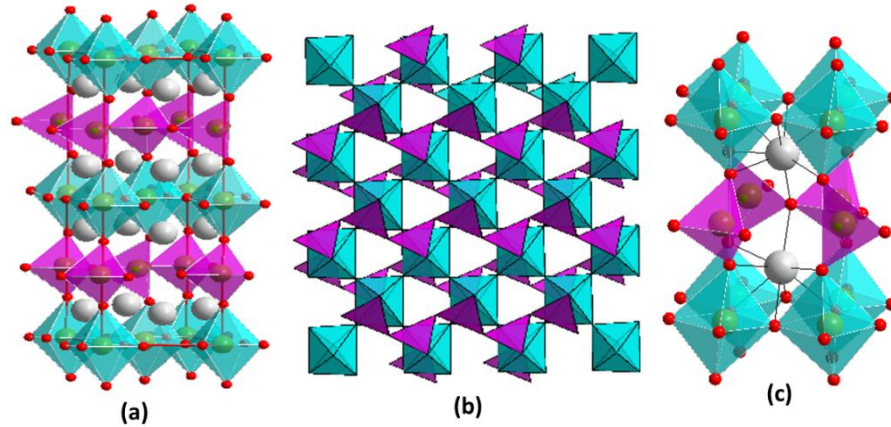


Figure 1.2.2. Crystal structure of $\text{CaSrFeCoO}_{6-\delta}$ (a) crystal structure showing unit cell with alternating $(\text{Fe/Co})\text{O}_6$ octahedra (cyan) and $(\text{Fe/Co})\text{O}_4$ tetra (pink) layers. The large white spheres are Sr atoms, the green spheres inside octahedra and tetrahedra are Fe and Co atoms and small red spheres are oxygen atoms. (b) A view along b axis to show the orientation of tetra next to each other in each layer. All atoms are removed for clarity. (c) shows the coordination geometry around the Sr atoms. Note that the Sr is 8-coordinated.

III. Physical properties and their possible applications.

The oxygen deficient perovskites contain BO_6 octahedra, BO_4 tetrahedra and/or BO_5 square pyramids. In such a case, the B cation can have multiple oxidation states like Fe^{3+} and Fe^{4+} which lead to charge transport.⁴ Sometimes these structures are distorted due to some kind of structural strains leading to the creation of structure induced small polarons.⁸⁻
⁹ This also makes the materials conductive.

B cations in perovskite oxides are transition metals. Transition metal complexes with unpaired d-electrons in transition metal are magnetic. The spin of a single electron is $+(1/2)$ or $-(1/2)$. when two electrons are paired with each other, the magnetic moments are counter balanced due to opposite spins but when the electron is unpaired, it creates a weak magnetic

field. More unpaired electrons increase the paramagnetic effects. When a transition metal is in coordination complex, its electron configuration changes due to the repulsive forces between electrons in the ligands and electrons in the metal. Depending on the strength of the ligand, the compound may be paramagnetic or diamagnetic.

In recent years, oxygen deficient perovskites have been studied for the application in energy production and storage such as oxygen evolution reaction, hydrogen evolution reaction and battery materials.

IV. Roll of A- and B-site cations

When A-site or B-site cation is substituted in a material, it may result in the transformation of crystal structure in the material due to the radii variation. This structural transformation can affect properties of these materials. When B-site cation is substituted, the crystal structure changes due to the change in the B-site ionic radius or the charge on the cation. $\text{Sr}_2\text{Fe}_2\text{O}_5$ has been reported to have a vacancy-ordered structure containing FeO_6 octahedra and FeO_4 tetrahedra¹⁰. when one of the Fe atoms (which is B-site cation) is substituted with Mn, the resulting compound, $\text{Sr}_2\text{FeMnO}_5$, contains vacancies distributed randomly, without any type of ordering.¹¹ Similarly, tetragonal compound, $\text{Sr}_2\text{Fe}_2\text{O}_{6-\delta}$ with magnetic moments in spin-density wave state, transforms to cubic $Pm-3m$ structure of $\text{Sr}_2\text{FeMnO}_{6-\delta}$ when one of the Fe atoms is replaced by Mn. The resulting material, $\text{Sr}_2\text{FeMnO}_{6-\delta}$, has inhomogeneous magnetic ground state, where the majority of the sample contains fluctuating spins.¹¹ Even minor changes to the B-site cations can sometimes lead to major changes, as highlighted by the difference between $\text{Sr}_2\text{Fe}_{1.9}\text{Cr}_{0.1}\text{O}_{6-\delta}$, cubic $Pm-3m$, and $\text{Sr}_2\text{Fe}_{1.9}\text{Co}_{0.1}\text{O}_{6-\delta}$, orthorhombic $Cmmm$.¹² Again this leads to significant variation of magnetic properties in these two materials.¹²

The material properties can also be affected by changes in the A-site cation. An example is the difference between the two compounds $\text{Ca}_2\text{Fe}_2\text{O}_5$ and $\text{Sr}_2\text{Fe}_2\text{O}_5$.¹³⁻¹⁴ While both of these materials have ordered structures, where Fe atoms have both octahedral and tetrahedral geometry, the change in the A-site cation leads to different space groups. $\text{Ca}_2\text{Fe}_2\text{O}_5$ crystallizes in the primitive space group $Pnma$,¹⁵ whereas $\text{Sr}_2\text{Fe}_2\text{O}_5$ has a body-centered space group $Icmm$.¹⁰ A similar effect is observed for $\text{Ca}_2\text{GaMnO}_5$ and $\text{Sr}_2\text{GaMnO}_5$, where the change in the A site cation results in changes in the space group.¹⁶

V. Electrical conductivity of oxygen deficient perovskites

Many ODPs are mixed oxygen ion and electron conducting materials. Electronic transport in ODPs takes place through holes.^{13, 17} It is also called as polaron mechanism. For this mechanism, materials should have elements with multiple oxidation states at B-site.¹⁸⁻¹⁹ For example, $\text{Sr}_2\text{Fe}_2\text{O}_{6-\delta}$, a well-known ODP, has the oxidation states of Fe^{3+} and Fe^{4+} .²⁰ In such materials, the electrons hop through M-O-M bond system. In the case of $\text{Sr}_2\text{Fe}_2\text{O}_{6-\delta}$, the electrons hop through $\text{Fe}^{3+}\text{-O-Fe}^{4+}$ where the Fe^{3+} converts to Fe^{4+} and vice versa after electron hopping. The speed of electron hopping is fast and hence it looks like the positive charge is moving during the electron hopping. So, it is considered as positive charge (also called hole) movement or P-type conductivity and it is called polaron mechanism. The schematic representation of polaron mechanism is shown in figure 1.2.3. The electronic transport in ODPs is governed by various factors. If the hole concentration (polarons) is higher in a material, the electronic transport and electrical conductivity is higher.^{13, 17} It has been shown that changes in the electrical conductivity correlate with changes in the bond lengths and angles.²¹⁻²² The shorter the M-O bond length and the larger the M-O-M bond angle, the better is the orbital overlap and the electronic transport and the conductivity

becomes better. Thus, the electrical conductivity of ODP does not depend on only one factor. The conductivity is p-type in metallic ODPs and the polaron mechanism is temperature activated.²³⁻²⁴

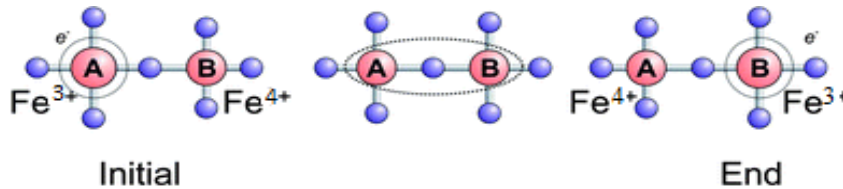


Figure 1.2.3. Representation of electron hopping through $\text{Fe}^{3+}\text{-O-Fe}^{4+}$ bond system

VI. Magnetism in perovskite oxides

Magnetic moment of a system shows the strength and the direction of its magnetism. Magnetism results due to uneven interaction of the magnetic dipole moments. An electron has an electron magnetic dipole moment generated by spinning electric charge. There are many different magnetic behaviors such as paramagnetism, diamagnetism, and ferromagnetism. In perovskite oxides with B cations having unpaired d-electrons such as Fe^{3+} , Mn^{3+} , Co^{3+} , magnetic ordering can take place. However, in most of the cases antiferromagnetism and ferromagnetism take place due to super- and double- exchange, respectively.¹ The energy of the antiferromagnetic system is lower due to the antiparallel alignment of the spins. This system is established by coupling the unpaired d- electrons of two B cations by p-electrons of an intervening oxygen between them as shown in figure

below. The presence of vacancy can affect in the magnetism of perovskite oxides.¹

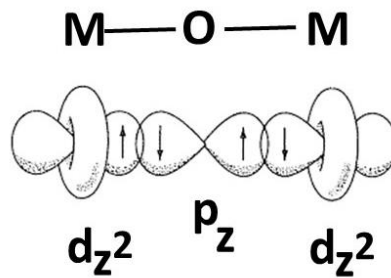


Figure 1.2.4. Super exchange by coupling two metals with unpaired d-electrons with an oxygen anion.

There are different possible anti-ferromagnetic ordering schemes in perovskite oxides such as A-, C- and G-type. A-type AFM has the atoms with opposite moments in adjacent layers. C-type AFM has neighboring atoms in the layers with opposite spins and G-type AFM has all neighboring B ions with opposite spins. The different schemes are shown below in figure 1.2.5.

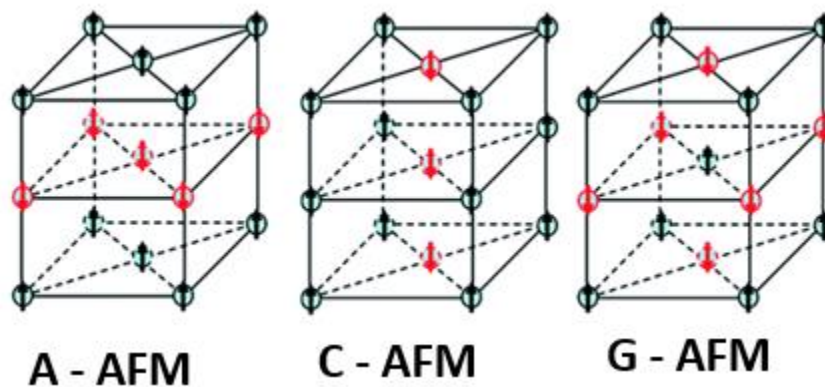


Figure 1.2.5. Three different ordering schemes in antiferromagnetic perovskite oxides

VII. Oxygen evolution reaction

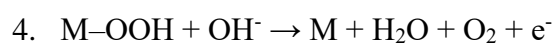
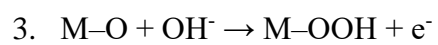
Oxygen evolution reaction deals with electrolysis of water. Water electrolysis is the process of electrically splitting water into oxygen and hydrogen. The reaction can be expressed as

$$2\text{H}_2\text{O} \rightarrow 2\text{H}_2 + \text{O}_2$$

Here, H_2 is evolved at cathode and O_2 is evolved at anode. The reaction is associated with 1.23 V of potential in all media at standard condition.²⁵ The efficiency of electrolyzer system is limited by the kinetic overpotential losses associated with the oxygen evolution reaction (OER) at the anode in both acidic and basic medium.

Overpotential is the potential difference between the potentials achieving a specific current density and 1.23 V. Usually it is measured in mV, as an example if a catalyst achieves $E = 1.53$ V, then it bears an overpotential of 300 mV. Different electrocatalysts have been studied to reduce the overpotential for the oxygen evolution reaction. Recently, ODPs have attracted attention toward this research. Different mechanisms have been proposed for the OER in alkaline media for ODPs.²⁶⁻²⁷ The commonly accepted mechanism in alkaline solution involves four steps, where there is a single electron transfer in each step. In the first step, the reaction initiates by the adsorption of OH^- on the active site of the catalyst, i.e., metal site, M. In the second step, a hydroxide from the electrolyte abstracts a proton from M-OH to form M-O and water. In the third step, M-O combines with a hydroxide to form a peroxide. Finally, in the fourth step, the peroxide intermediate reacts with OH^- to give an oxygen and water and regenerate the catalyst.

1. $\text{M} + \text{OH}^- \rightarrow \text{M-OH} + \text{e}^-$
2. $\text{M-OH} + \text{OH}^- \rightarrow \text{M-O} + \text{H}_2\text{O} + \text{e}^-$



CHAPTER 2
TRANSFORMATION OF STRUCTURE, ELECTRICAL CONDUCTIVITY AND
MAGNETISM IN $AA'Fe_2O_{6-\delta}$, $A=Sr, Ca$ and $A'=Sr$ ¹

INTRODUCTION

The applications of oxygen-deficient perovskites in areas such as solid oxide fuel cells (SOFCs), superconductors, magnetoresistants, and gas diffusion membranes indicate the importance of this family of materials.²⁸⁻³¹ The general formula for oxygen-deficient perovskites can be represented as ABO_{3-x} or $AA'BB'O_{6-\delta}$, where the B/B' cations (which can be the same or different) have octahedral, tetrahedral, or square-pyramidal coordination geometries. The A/A' cations (which again can be the same or different) occupy the free spaces in between the above polyhedra. The vacant sites, that are created due to oxygen deficiency, can have a random distribution in the crystal structure. In such cases, the average structure retains the perovskite-type atomic arrangement, but with partial site-occupancy (as opposed to full occupancy) on oxygen positions.³² An alternative scenario involves an ordered arrangement of vacant sites. There can be different types of vacancy-ordering depending on various parameters, including the degree of oxygen deficiency. For

¹ The work described in this chapter was published in *Inorganic Chemistry* (2017, vol. 56, p. 9716-9724)

example, materials with large concentration of defects, i.e., $\delta \approx 1$, usually form structures where the oxide deficiency appears in alternating layers, where corner-sharing B'O₄ tetrahedra are formed. This leads to a structure that contains layers of BO₆ octahedra separated by B'O₄ tetrahedra. This is called brownmillerite-type structure.^{6, 33-34} Another type of ordering involves the formation of square pyramidal geometry around the B-site cations.³⁵ In materials with smaller degree of oxygen deficiency, other schemes of vacancy-ordering are observed, involving the formation of both square-pyramidal and octahedral coordination geometries.³⁶

Understanding various parameters that determine the crystal structure of oxygen-deficient perovskites is important, as there is a direct correlation between their structure and functional properties. The manipulation of cations on the B-site is known to affect the structure of oxygen-deficient perovskites. For example, despite structural similarities between Ca₂FeAlO₅ and Ca₂FeGaO₅, they have different space groups, *Ibm2* (*Ima2*) for the former and *Pcmn* (*Pnma*) for the latter.³⁷ Both materials feature the brownmillerite-type structure, described above, containing octahedral and tetrahedral layers. The corner-sharing tetrahedra form chains that run parallel to the octahedral layers, and have two possible orientations, called right handed (R) and left handed (L). In Ca₂FeAlO₅, all tetrahedral chains have the same orientation (either R or L), leading to space group *Ibm2* (*Ima2*). In Ca₂FeGaO₅ however, the R and L orientations appear alternately from one tetrahedral layer to the next, resulting in space group *Pcmn* (*Pnma*).³⁷

The effect of the A-site cation on the crystal structure is also important. For example, Sr₂GaMnO₅ has a body-centered structure described by *Ima2* or *Imcm* space group,³⁸ whereas Ca₂GaMnO₅ has a primitive structure with space group *Pnma*.³⁸ However, both of

these materials have a similar structure-type, containing octahedra and tetrahedra, but with different space group symmetries.

In this article, we study materials with formula, $AA'\text{Fe}_2\text{O}_{6-\delta}$, where $A=\text{Sr}, \text{Ca}$ and $A'=\text{Sr}$. The Sr-containing phase, $\text{Sr}_2\text{Fe}_2\text{O}_{6-\delta}$, is known to have various oxygen contents. The fully oxidized material, $\text{Sr}_2\text{Fe}_2\text{O}_6$, can only be obtained if the initial air-synthesis is followed by heating under 30 MPa of pure oxygen.³⁶ Products with different degrees of oxygen deficiencies can be synthesized if samples are heated under different gas atmospheres.³⁶ However, the direct synthesis in air at 1250 C, without any additional gas treatment, leads to a product with formula $\text{Sr}_2\text{Fe}_2\text{O}_{5.75}$, where $\delta \approx 0.25$.³⁶ Regarding the Ca-containing analogue, $\text{CaSrFe}_2\text{O}_{6-\delta}$, little information is known. The formation of an orthorhombic structure with similar composition through liquid nitrogen quenching and vacuum treatment has been reported.³⁹ However, the magnetic structure and electrical transport properties of this material are not known. Here, we show that $\text{CaSrFe}_2\text{O}_{6-\delta}$ can be synthesized under the same conditions as the Sr_2 -analogue. We have performed neutron diffraction experiments to examine the crystal structure and explore the long-range magnetic order in the CaSr-material. We have also conducted extensive charge transport studies on both Sr_2 and CaSr compounds. These studies have revealed the sharp contrast between these two materials and demonstrated the dramatic transformation of magnetism and electrical conductivity in $AA'\text{Fe}_2\text{O}_{6-\delta}$ as a function of A-site cation.

EXPERIMENTAL

Both materials were synthesized under the same synthesis conditions. Stoichiometric proportions of the precursors, SrCO_3 (Sigma Aldrich, 99.9%), CaCO_3 (Alfa Aesar, 99.95%), and Fe_2O_3 (Alfa Aesar, 99.998%) were used for solid-state syntheses. The

mixtures of precursor powders were ground using agate mortar and pestle, pressed into pellets and heated in air at 1000°C for 24 hours. The pellets were then ground and refired in air at 1250 °C for 24 hours. In all cases, the furnace heating and cooling rates were set at 100 °C/h.

The phase purity and structure of polycrystalline samples were examined by powder X-ray diffraction at room temperature using a Bruker D8 Discover diffractometer with $\text{CuK}\alpha$ radiation and a PANalytical Empyrean diffractometer with $\text{CuK}\alpha_1$ radiation ($\lambda = 1.54056 \text{ \AA}$). The Rietveld refinements were carried out using *GSAS* software⁴⁰ and *EXPGUI* interface.⁴¹ The morphological analyses were performed using a high resolution field-emission scanning electron microscope (SEM). The electrical properties of the polycrystalline samples were investigated using electrochemical impedance spectroscopy (EIS). AC impedance measurements were performed in the frequency range 0.1 Hz – 1 MHz using a computer-controlled frequency response analyzer. Similarly, 2-probe DC measurements were carried out by measuring the output current by applying constant voltage of 1 mV. X-ray photoelectron spectroscopy data were obtained using Mg $\text{K}\alpha$ radiation (1253.6 eV) at room temperature. Thermogravimetric analysis was done from 25 to 800 °C in air. Magnetic susceptibility data were obtained by applying magnetic field of 1000 Oe in the temperature range 2 K to 400 K. Neutron diffraction experiments were performed on POWGEN diffractometer at Oak Ridge National Laboratory, with center wavelength of 1.333 Å, covering the d-spacing range 0.4142 – 6.1363 Å.

RESULTS AND DISCUSSION

Crystal structure

The crystal structure is transformed as a result of replacing one of the Sr atoms with Ca on the A-site. The Sr₂-compound is known to have a tetragonal crystal structure³⁶ consisting of corner sharing FeO₆ octahedra and FeO₅ square-pyramids. Figures 2.1 and 2.2 show the Rietveld refinement profile and crystal structure of this material. The refined structural parameters are listed in Table 2.1. The FeO₅ square-pyramids form dimers that are separated by FeO₆ octahedra. There is no connectivity between different dimers in the structure. The octahedral and square-pyramidal Fe sites alternate within each layer. As seen in Figure 2.2c and Table 2.1, there are two distinct crystallographic positions where A-site cations (Sr²⁺) reside. These two sites have coordination numbers 11 and 12.

The substitution of one Ca for Sr leads to a dramatic change in the crystal structure. Our neutron and X-ray diffraction experiments show that the CaSr-compound has an orthorhombic structure, consisting of alternating layers of octahedra and tetrahedra, as shown in Figure 2.3. The FeO₆ octahedra share corners with other octahedra within the same layer, and with the tetrahedra in the layers above and below. The tetrahedral layer actually consists of chains of FeO₄ tetrahedra that run parallel to the octahedral layers. The A-site cations in this material have coordination number 8 (Figure 2.3c). This is the so-called brownmillerite-type structure. Materials with this structure-type usually have orthorhombic *Ibm2*, *Pnma*, *Pbcm* or *Icmm* space groups depending on the relative orientation of tetrahedral chains (Figure 2.3b).³³⁻³⁴ As mentioned before, the tetrahedral

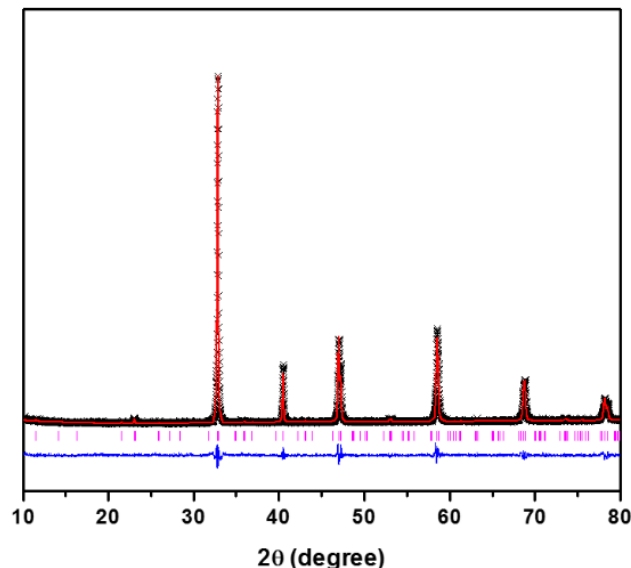


Figure 2.1. Rietveld refinement profile for powder X-ray diffraction data of $\text{Sr}_2\text{Fe}_2\text{O}_{6-\delta}$ in $I4/mmm$ space group. Stars represent experimental data, red solid is the model, vertical tick marks show Bragg peak positions, and the blue line represents the difference plot.

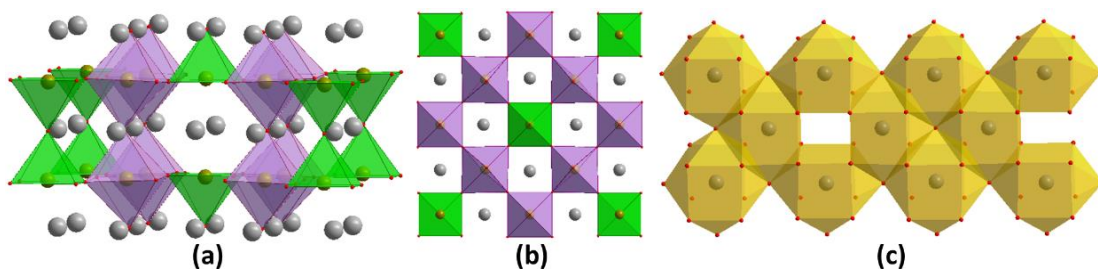


Figure 2.2. Crystal structure of $\text{Sr}_2\text{Fe}_2\text{O}_{6-\delta}$. (a) and (b) show the alternating FeO_6 octahedra (purple) and FeO_5 square pyramids (green), viewed along the a and c axes, respectively. The large grey spheres are Sr atoms. (c) shows the coordination geometry around the Sr atoms. Note the presence of both 11 and 12-coordinated Sr atoms.

chains have two possible orientations, right handed (R) and left handed (L). The space group $Ibm2$ is obtained when all tetrahedral chains have the same orientation. However, if the R and L orientations appear alternately from one tetrahedral layer to the next, the space group $Pnma$ is obtained. The $Pbcm$ space group is less common,^{33-34,42} where the

orientation of each tetrahedral chain is opposite to all nearest neighbors within the same layer and in the neighboring layers above and below. Finally, the space group *Icmm* is a result of random orientation of tetrahedral chains in the structure. For our CaSr-material, the *Pbcm* space group was readily ruled out, because it requires the formation of a large unit cell with distinct supercell peaks.^{33-34,42} These peaks are absent in neutron and X-ray diffraction data. The *Pnma* structure can be identified by the presence of 131 and 151 peaks, which are also absent in our data, ruling out this space group. The *Icmm* and *Ibm2* models were then examined by Rietveld refinements, leading to a poor fit for *Icmm*, but an excellent fit for *Ibm2* space group (Figure 2.4). The refined structural parameters are listed in Table 2.2.

Table 2.1. Refined structural parameters of Sr₂Fe₂O_{6-δ}.

Space group: <i>I4/mmm</i>						
$a = 10.9343(6) \text{ \AA}$ $b = 10.9343 \text{ \AA}$ $c = 7.6988(4) \text{ \AA}$			$R_p = 0.0216$	$wR_p = 0.0312$		
Element	x	y	z	Occupancy	U _{iso}	Multiplicity
Sr1	0.2601(5)	0	0	1	0.015(2)	8
Sr2	0.2478(4)	0	0.5	1	0.014(2)	8
Fe1	0	0	0.25	1	0.024(7)	4
Fe2	0.25	0.25	0.25	1	0.007(4)	8
Fe3	0.5	0	0.25	1	0.033(7)	4
O1	0	0	0.5	1	0.017(1)	2
O2	0.123(2)	0.123(2)	0.225(2)	1	0.017(1)	16
O3	0.253(2)	0.253(2)	0.5	1	0.017(1)	8
O4	0.126(2)	0.626(2)	0.25	1	0.017(1)	16
O5	0.5	0	0	1	0.017(1)	4

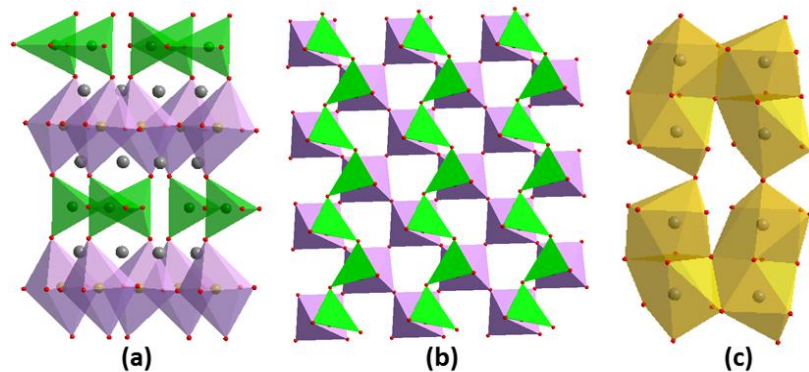


Figure 2.3. Crystal structure of $\text{CaSrFe}_2\text{O}_{6-\delta}$. (a) The octahedral FeO_6 (purple) and tetrahedral FeO_4 (green) layers. Grey spheres represent Sr. (b) View from top to highlight the chain formation in the tetrahedral layer. The Sr atoms are omitted for clarity. (c) Coordination geometry of Sr atoms. Note that Sr is 8-coordinated.

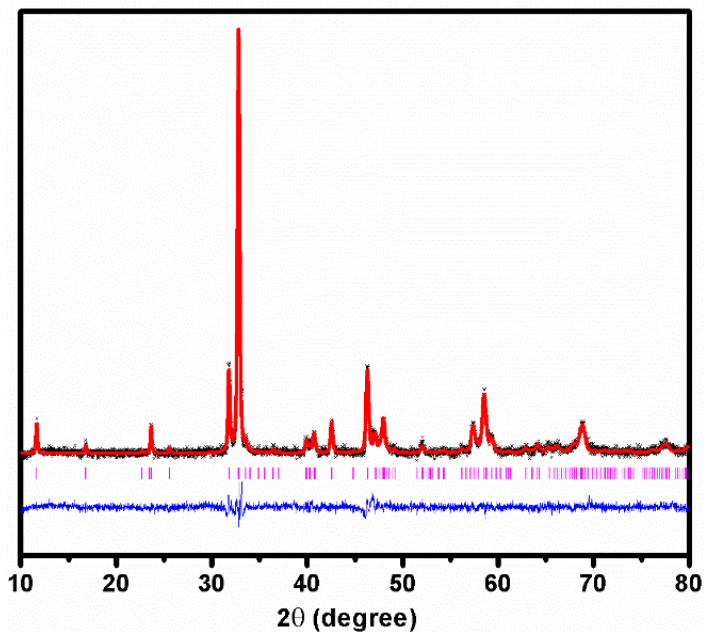


Figure 2.4. Rietveld refinement profile for powder X-ray diffraction data of $\text{CaSrFe}_2\text{O}_{6-\delta}$, space group $Ibm2$. Black stars, red line, vertical tick marks and lower blue line represent the experimental data, structural model, Bragg peak positions and difference plot, respectively.

Table 2.2. Refined structural parameters of $\text{CaSrFe}_2\text{O}_{6-\delta}$.

Space group: <i>Ibm2</i>						
a =	b =		c =	Rp =	wRp =	
5.6314(3) Å	15.1807(8) Å		5.4695(3) Å	0.0174	0.0237	
Elements	x	y	z	Occupancy	U _{iso}	Multiplicity
Ca1	0.5127(4)	0.1108(1)	0.009(4)	0.5	0.013(1)	8
Sr1	0.5127(4)	0.1108(1)	0.009(4)	0.5	0.013(1)	8
Fe1	0.0763(6)	0.25	-0.003(6)	1	0.010(2)	4
Fe2	0	0	0	1	0.020(2)	4
O1	0.227(3)	0.0067(5)	0.295(5)	1	0.015(3)	8
	-					
O2	0.0820(1)	0.1485(4)	0.002(8)	1	0.015(3)	8
O3	0.382(3)	0.25	0.891(6)	1	0.015(3)	4

The morphology and crystallite sizes of both Sr_2 and CaSr materials were also examined using scanning electron microscopy. Figure 2.5 shows the surfaces of sintered pellets for both materials. The crystallite size decreases as a result of replacing one Sr with Ca. In addition, the crystallites seem to be packed more densely and have more contact with each other in the CaSr -material.

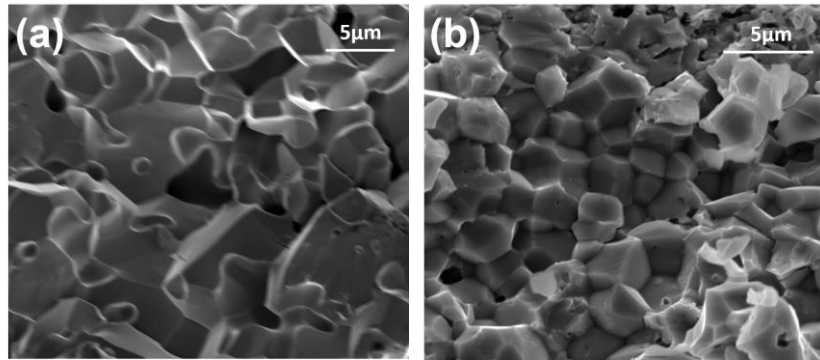


Figure 2.5. Scanning electron microscopy images of (a) $\text{Sr}_2\text{Fe}_2\text{O}_{6-\delta}$ and (b) $\text{CaSrFe}_2\text{O}_{6-\delta}$.

Some comments on the oxygen contents of these compounds are in order. Note that for both compounds, Fe_2O_3 was used as starting material and the synthesis conditions were identical. If iron retains its +3 oxidation state, the oxygen stoichiometry in $\text{AA}'\text{Fe}_2\text{O}_{6-\delta}$ formula should be 5, resulting in $\delta = 1$. We have performed X-ray photoelectron spectroscopy experiments on the CaSr-compound, to determine the oxidation state of Fe. As shown in Figure 2.6, the satellite peak at ~ 8 eV higher than the Fe $2p_{3/2}$ peak is a signature of Fe^{3+} .⁴³⁻⁴⁴ Therefore, the oxygen content of the CaSr-compound should be very close to 5. This is consistent with the crystal structure of the CaSr-compound, and the formation of brownmillerite-type structure, which has oxygen stoichiometry of 5. This behavior, namely the retention of +3 oxidation state in perovskite-based oxides synthesized at high temperature, has been observed before.³² This is in sharp contrast to the Sr_2 -compound, where the tetragonal structure implies the oxygen stoichiometry of 5.75, i.e., $\delta = 0.25$, which has also been confirmed by thermogravimetric analyses.³⁶ This indicates that a considerable amount of iron in the Sr_2 -compound has been oxidized during the synthesis. Note that both Sr_2 and CaSr materials are synthesized under the same condition. Therefore, the difference in the B-site cation oxidation state as a result of variation in the ionic radius of the A-site cation is remarkable.

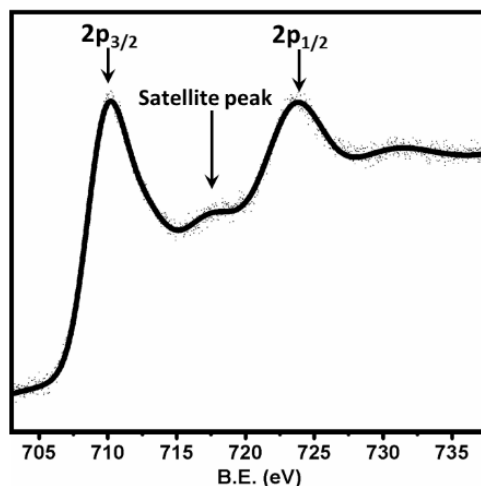


Figure 2.6. X-ray photoelectron spectroscopy data for $\text{CaSrFe}_2\text{O}_{6-\delta}$.

The transformation of the crystal structure upon changing the A-site, from Sr_2 to CaSr , is clearly related to the average cation size. Note that Ca and Sr share the same crystallographic site. This structural change may be explained in terms of the relationship between ionic radii and the coordination geometry of the A-site cations in the two structure types. When only Sr^{2+} cation is present, the tetragonal structure is stabilized, where this large cation is accommodated in 11 and 12-coordinated A-sites. However, when the average ionic radius on the A-site is decreased (due to the presence of Ca^{2+}), the orthorhombic structure, featuring 8-coordinated A-sites, is preferred. At the other extreme, namely in a material with only Ca on A/A' sites, the structure remains ordered, as observed in $\text{Ca}_2\text{Fe}_2\text{O}_5$, which also features the brownmillerite-type structure but a different space group.⁴⁵

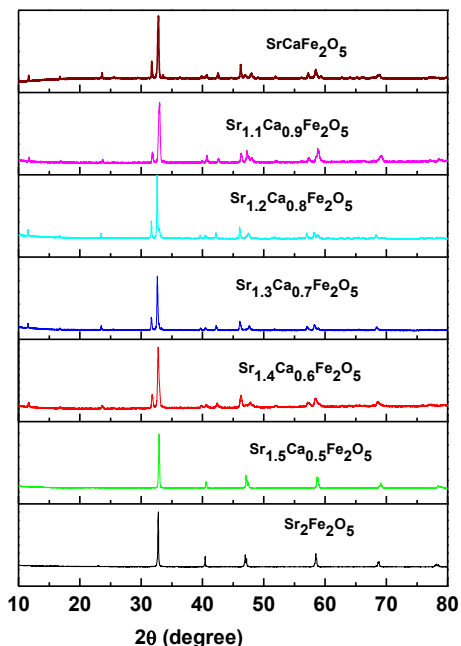


Figure 2.7. Powder X-ray diffraction data for the series of materials with varying Ca/Sr ratios.

To investigate this structural transformation further, we set out to determine the A-site ionic radius that prompts this structural change. We synthesized a series of compounds, listed in Figure 2.7, where the Sr/Ca ratio was varied systematically. These experiments showed that transformation from tetragonal structure (with octahedral and square pyramidal geometry) to orthorhombic structure (with octahedral and tetrahedral geometry) takes place at Sr/Ca ratio of 1.4/0.6. Using this ratio, the average cation size on the A-site can be calculated. As mentioned before, the A-site cations in the tetragonal phase have coordination numbers (CN) 11 and 12. Ionic radii for CN=12 have been tabulated⁴⁶ for Sr^{2+} , 1.44 Å, and Ca^{2+} , 1.34 Å. Using these radii, one can calculate the average ionic radius required for the structural transformation to be ~ 1.41 Å.

Magnetic structure

The change in the A-site cation and subsequent alteration of the crystal structure leads to significant changes in the magnetic order. The Sr₂ compound is known to have an incommensurate magnetic structure with propagation vector $k = (0.687, 0, 0.326)$, where magnetic moments are in “spin-density wave” state.⁴⁷ The magnetic moment value has been found to be $2.54(4) \mu_B$ at 11 K. All magnetic moments are tilted by -35.3 degrees with respect to the c axis. The moments are aligned within planes perpendicular to the body diagonal of the unit cell, i.e., [111] direction. The magnetic transition temperature is 75 K.⁴⁷

We have shown that the magnetic structure is transformed upon replacing CaSr for Sr₂ on the A-site. We studied the magnetic structure of the CaSr-compound using neutron diffraction. Figure 2.8 shows the Rietveld refinement profile for simultaneous refinement of crystal and magnetic structures of CaSr-material. Neutron experiments at 10 K indicated that the CaSr-compound is antiferromagnetically ordered, as evident from strong magnetic reflections. In materials with this type of crystal structure, the relative intensities of the two main magnetic peaks is indicative of the orientation of magnetic moments.⁴² If this ratio is close to 1, the magnetic moments are oriented along the longest unit cell axis. However, if the intensity ratio is close to 3, the magnetic moments are aligned along the shortest axis. In our neutron diffraction data, these peaks appear at $d \approx 4.43 \text{ \AA}$ and 4.51 \AA (Figure 2.8) with relative intensity close to 3, indicating that the magnetic moment orientation should be parallel to the shortest axis. Magnetic structure refinements with neutron diffraction data showed that magnetic moments are indeed parallel to the shortest axis, c. These

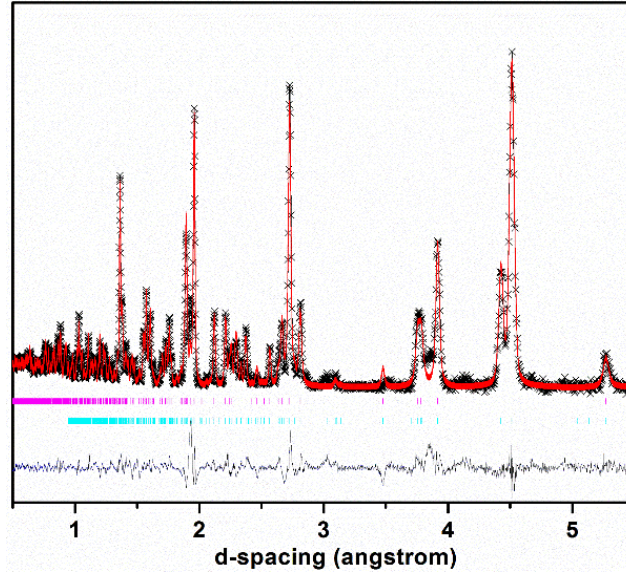


Figure 2.8. Refinement of the crystal and magnetic structures using neutron diffraction data for $\text{CaSrFe}_2\text{O}_{6-\delta}$. The upper and lower tick marks represent the peak positions for crystal and magnetic structures, respectively.

refinements also revealed that each magnetic moment is aligned anti-parallel to all of its nearest neighbors, forming the so-called G-type antiferromagnetic structure, as shown in Figure 2.9. The magnetic unit cell has the same size as the crystallographic unit cell. The magnitude of magnetic moments of the octahedral and tetrahedral Fe atoms were also determined. The magnetic moment values at 10 K are $4.6(2) \mu_B$ and $3.9(2) \mu_B$, for octahedral and tetrahedral sites, respectively. In addition, we performed neutron diffraction experiments at 300 K. These experiments indicated that the G-type antiferromagnetic order in the CaSr-material persists even at room temperature. The magnetic moments are still oriented along the c-axis and the magnitudes of moments at 300 K are $4.0(2) \mu_B$ and $3.5(2) \mu_B$ for the octahedral and tetrahedral sites, respectively.

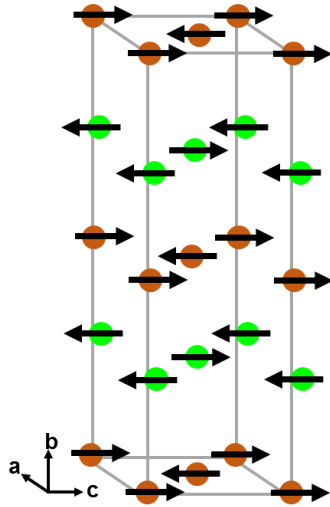


Figure 2.9. The G-type antiferromagnetic order in CaSrFe₂O_{6.8}. Note that magnetic moments on each Fe site are aligned opposite to all nearest neighbors. The moments are oriented along the *c*-axis.

Note the sharp contrast between the CaSr-compound, featuring antiferromagnetic order even at room temperature, and the Sr₂-material, where the spin-density wave state occurs below 75 K. We also performed magnetic susceptibility measurements on the CaSr-material in the temperature range 2 – 400 K, as shown in Figure 2.10. A broad feature and divergence between zero-field-cooled and field-cooled data were observed at about 52 K. This behavior has been observed before for antiferromagnetic materials at temperatures far below their Neel temperature,³³ and corresponds to short-range magnetic domains or possible magnetic side product.³³ However, the absence of any sharp transition combined with the neutron diffraction results that show long-range magnetic order at 300 K, indicate that the Neel temperature for this material should be higher than 400 K.

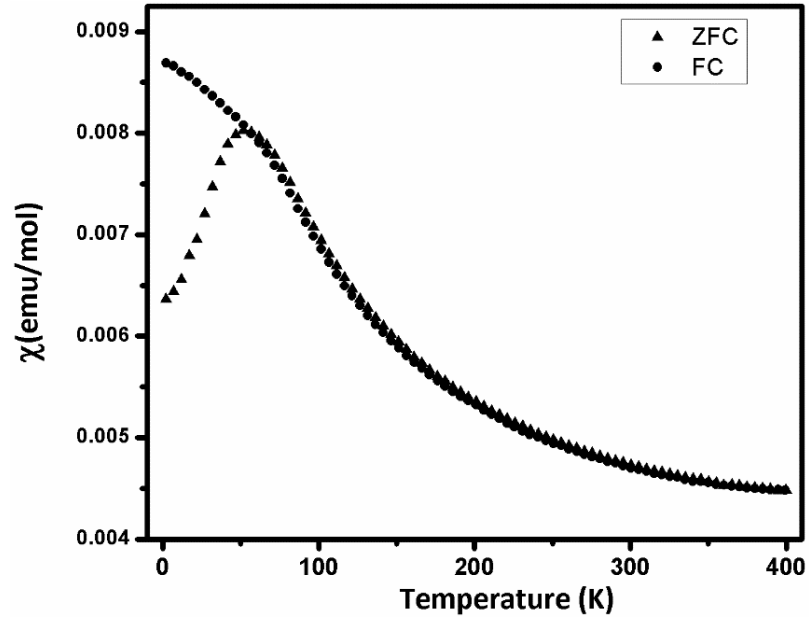


Figure 2.10. Magnetic Susceptibility data for $\text{CaSrFe}_2\text{O}_{6-\delta}$.

Electrical properties

The change in the crystal structure has a pronounced effect on electrical transport properties. The electrical conductivity measurements determine the resistance, R , of each material, and the resistivity, ρ , is calculated from $\rho = RA/L$, where L and A are the length and cross sectional area of cylindrical samples, respectively. Conductivity, σ , is then calculated from the inverse of resistivity. The total conductivities of $\text{Sr}_2\text{Fe}_2\text{O}_{6-\delta}$ and $\text{CaSrFe}_2\text{O}_{6-\delta}$ were obtained using both DC and AC methods. In each case both DC and AC techniques led to very similar total conductivity values, as shown in Table 2.3. Note that various parameters contribute to the total conductivity, including electrode reactions, bulk and grain-boundary resistances, ionic and/or electron transport phenomena. In perovskite-based oxides, heterovalent atoms having more than one stable oxidation state

(e.g., Fe³⁺/Fe⁴⁺) are needed on the B-site for electronic conductivity. The metal (M) 3*d* and oxygen 2*p* orbitals overlap and electron hopping occurs through M–O–M pathways.

Table 2.3. Room temperature conductivity and activation energies.

	Total conductivity, σ (Scm ⁻¹)		Activation energy (E_a) in eV
	AC	DC	
Sr ₂ Fe ₂ O _{6-δ}	7.698 x 10 ⁻¹	8.540 x 10 ⁻¹	0.118
CaSrFe ₂ O _{6-δ}	1.201 x 10 ⁻¹	1.616 x 10 ⁻¹	0.653 for 298 – 673 K (25 – 400 °C) 0.201 for 673 – 1073 K (400 – 800 °C)

The M–O bond distance and M–O–M angle determine the degree of overlap. Shorter bonds and larger angles are associated with greater orbital overlap and higher conductivity.⁴⁸ Due to the presence of corner-sharing octahedra and tetrahedra in the CaSr compound, the average Fe–O–Fe bond angle (138.8°) in this material is smaller than that for the Sr₂-compound (177.2°). Therefore, smaller degree of orbital overlap is expected in the CaSr-compound. The corner-sharing of octahedra and tetrahedra leads to distortions in the coordination geometry of Fe atoms, resulting in a wide range of Fe–O bond lengths in the CaSr-material, from 1.780(7) Å to 2.302(7) Å. However, the Fe–O bond lengths in the Sr₂-compound are close to each other and range from 1.92(3) Å to 1.97(3) Å.

As observed in Table 2.3, at room temperature, there is nearly one order of magnitude difference between the total conductivity of the Sr₂-material and that of the CaSr-compound, indicating the significant effect of crystal structure on the electrical transport properties.

To operate any device that works based on conductive oxides over a wide temperature range, knowledge of the charge transport properties as a function of temperature is required. Therefore, variable-temperature DC conductivity studies were performed for both materials at the temperature range of 298 K– 1073 K (25 °C – 800 °C). From these experiments the activation energies were obtained, as shown in Table 2.3. The conductivity trends during heating and cooling cycles and the Arrhenius plots for both materials are shown in Figure 2.11. The plot in Figure 2.11b was used for fitting with the Arrhenius equation for thermally activated conductivity,⁴⁹⁻⁵¹ which helped to find the activation energy of total conductivity.

$$\sigma T = \sigma^{\circ} e^{\frac{-E_a}{kT}} \quad (5)$$

where σ° is a pre-exponential factor and a characteristic of a material, and E_a , k and T are the activation energy for the conductivity, Boltzmann constant and absolute temperature, respectively. The activation energy for the total conductivity (E_a) can be calculated from slope of the line of best fit in $\log \sigma T$ vs $1000/T$ plot. As shown in Table 2.3, E_a value for the total conductivity of $\text{Sr}_2\text{Fe}_2\text{O}_{6-\delta}$ is 0.118 eV. For $\text{CaSrFe}_2\text{O}_{6-\delta}$ two E_a values are obtained, 0.653 eV for 25 – 400 °C (298 – 673 K) and 0.201 eV for 400 – 800 °C (673 – 1073 K).

There is a sharp contrast between the CaSr and Sr_2 compounds with regards to their conductivity trends as a function of temperature. The Sr_2 compound shows metallic properties,⁵² while the CaSr-material is a semiconductor. As mentioned above, the average Fe–O–Fe bond angle in the Sr_2 -compound is greater than that in the CaSr-material. Several authors have discussed the correlation between increase in bond angles and the broadening

of valence and conduction bands in perovskites, leading to changes in properties from insulator or semiconductor to metallic systems.^{48,53-54} The broadening of bands and overlap between the metal $3d$ and oxygen $2p$ bands closes the band gap completely, leading to the formation of hybrid M–O–M bands, and metallic properties. The charge transfer occurs through these hybrid bands.^{48, 53-54}

As observed in Figure 2.11, $\text{Sr}_2\text{Fe}_2\text{O}_{6-\delta}$ displays a trend where conductivity decreases gradually with respect to temperature in the entire range from 298 K to 1073 K, indicative

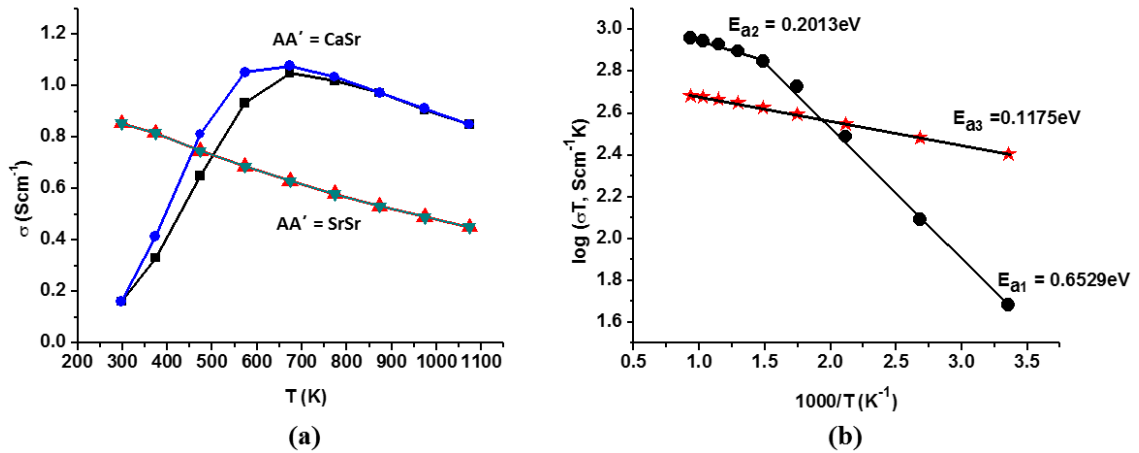
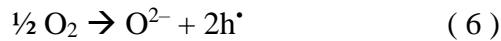


Figure 2.11. (a) Total conductivity of $\text{Sr}_2\text{Fe}_2\text{O}_{6-\delta}$ and $\text{CaSrFe}_2\text{O}_{6-\delta}$ as a function of temperature. For $\text{Sr}_2\text{Fe}_2\text{O}_{6-\delta}$, the heating and cooling data (red and green) overlap. For $\text{CaSrFe}_2\text{O}_{6-\delta}$ hysteresis is observed between heating (black squares) and cooling data (blue circles). (b) Arrhenius plot of the total conductivity for $\text{Sr}_2\text{Fe}_2\text{O}_{6-\delta}$ (red stars) and $\text{CaSrFe}_2\text{O}_{6-\delta}$ (black circles).

of metallic properties. The decrease in conductivity as a function of temperature in a metallic system is a result of increase in the frequency of collisions between charge carriers and phonons.⁵³

On the contrary, the conductivity of $\text{CaSrFe}_2\text{O}_{6-\delta}$ increases gradually with the rise in temperature, a behavior typical of a semiconductor. The conductivity then decreases after ~ 673 K. In materials that feature the same structure type as CaSr-compound, i.e., alternating layers of octahedra and tetrahedra, increase in electrical conductivity as a function of temperature is usually observed.⁵⁵

The conductivity mechanism is through the formation of polarons. The different bond lengths of corner-sharing tetrahedra and octahedra in this structure-type introduce structural distortions, resulting in lattice polarizations which favor polaronic charge transport mechanism⁵⁶⁻⁵⁷. The dependence of conductivity on oxygen partial pressure has been observed in these materials indicating the *p*-type semiconductority.⁵⁵ Also, the dominance of electronic conductivity above room temperature in high oxygen partial pressure, e.g., O_2 partial pressure in air, has been shown for perovskite-type systems. In these cases, the main charge carriers are electron holes, leading to *p*-type semiconductority.⁵⁷⁻⁶¹ The extrinsic holes are formed through the absorption of oxygen molecules on the surface of the sample, facilitated by the presence of oxygen vacancies. The process can be described using the following idealized equations^{57, 59}:



In ferrites, the variable valence of iron is essential for charge compensation and electronic conductivity.



The formation of Fe^{4+} ions allows the polaronic electronic conductivity to occur through $\text{Fe}^{3+}-\text{O}^{2-}-\text{Fe}^{4+}$ pathway.^{57, 61-62}

The increase in conductivity as a function of temperature^{50, 55, 57} is explained in terms of temperature-activated hole formation and increased polaron mobility.⁵⁰ Another feature observed in Figure 2.11 is a change in the electrical conductivity trend for the CaSr-compound above ~ 673 K. This behavior has been observed in similar materials before.^{55, 57, 63-64} Some researchers have observed greater loss of oxygen in thermogravimetric analysis (TGA) above a certain temperature close to the temperature of the conductivity transition.⁶³⁻⁶⁴ They have assigned the decrease in conductivity above a particular temperature to the loss of oxygen and disruption of the $\text{Fe}^{3+}\text{—O}^{2-}\text{—Fe}^{4+}$ conduction pathways.⁶³⁻⁶⁴ Our TGA data (Figure 2.12) show a feature between $370 - 440$ °C ($643 - 713$ K), where the weight loss is interrupted by a plateau and a slight weight-gain, before the descending trend in weight continues above 440 °C. The feature in TGA data matches the temperature where the change in conductivity trend occurs. The weight loss is somewhat accelerated above 440 °C, as seen from the slope of the TGA plot. (Figure 2.12) Overall, the total weight loss for the material is less than 1%.

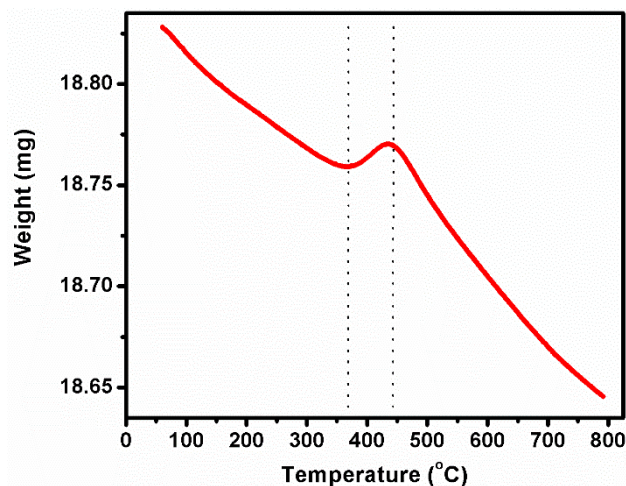


Figure 2.12. Thermogravimetric analysis data for $\text{CaSrFe}_2\text{O}_{6-\delta}$ in air

It is worth noting that the release of oxygen results in more oxygen vacancies, which enhances the oxide ion conductivity. The decrease in total conductivity is observed because the increase in ionic conductivity is less significant than the decrease in electronic conductivity.⁶⁴

We also examined the possibility of any structural phase change at high temperature, which could contribute to the decrease in conductivity above ~ 673 K. We heated a sample of CaSr-compound to 1073 K (800 °C), followed by quenching into liquid nitrogen to trap the potential high temperature phases. The XRD data indicated that the crystal structure had remained intact and no structural changes had occurred.

Some researchers have noted that the discontinuity in conductivity trend sometimes occurs close to the Neel temperature.⁵⁷ Some authors have even used electrical conductivity to determine the Neel temperature.⁶⁵ We note that our CaSr-material is antiferromagnetically ordered at room temperature. A comparison between the refined magnetic moments, 4.6 (2) μ_B and 3.9 (2) μ_B , at 10 K and the corresponding values at 300 K, 4.0 (2) μ_B and 3.5 (2) μ_B , indicates that the magnetic moments magnitude remains considerably high at room temperature. Also, the magnetic susceptibility data indicate that the Neel temperature should be higher than 400 K.

Another interesting feature of the electrical conductivity of CaSr-compound is the pronounced hysteresis in the conductivity data obtained during heating and cooling cycles below ~ 673 K. The conductivity values during cooling are greater than those obtained during heating. The observation of this feature confirms the contribution of oxide ion conductivity to total conductivity of this material, making it a mixed electronic-ionic conductor, as described before for some mixed conductors.^{62, 66} The oxygen

absorption/desorption phenomena, which are slower than electron diffusion, are responsible for the observation of these hystereses.^{62,66} This also indicates that oxygen loss has a positive impact on overall conductivity and cannot be responsible for the change in conductivity trend above 673 K. The temperature-activated mobility of polarons seems to reach a maximum, where no further increase in mobility occurs with increasing temperature. The collisions between charge carriers lead to decrease in conductivity as temperature increases further, similar to the behavior observed in metallic systems.

CONCLUSION

The alteration of electrical properties and magnetism of oxygen-deficient perovskites $AA'\text{Fe}_2\text{O}_{6-\delta}$, $A=\text{Sr}, \text{Ca}$; $A'=\text{Sr}$, as a result of changing the crystal structure, due to the effect of the A-site cation, has been demonstrated. It has been shown that the incommensurate magnetic structure of the Sr_2 compound, featuring magnetic moments in spin-density wave state which are perpendicular to the body diagonal of the unit cell, can be transformed into a long-range G-type antiferromagnetic system upon changing the A-site cations into CaSr. This occurs as a consequence of a structural alteration. The structure with alternating FeO_5 square-pyramidal dimers and FeO_6 octahedra is converted into a structure featuring alternating layers of tetrahedra and octahedra. The electrical properties are also transformed by changes in the A-site cation, where a metallic system is converted into a semiconductor featuring mixed ionic-electronic conductivity, as evident from charge transport studies in the temperature range 298 K– 1073 K.

CHAPTER 3

UNRAVELING THE ROLE OF STRUCTURAL ORDER IN TRANSFORMATION OF ELECTRICAL CONDUCTIVITY IN $\text{Ca}_2\text{FeCoO}_{6-\delta}$, $\text{CaSrFeCoO}_{6-\delta}$ AND $\text{Sr}_2\text{FeCoO}_{6-\delta}$

INTRODUCTION

Oxygen deficient perovskite oxides possess unique properties that make them ideal candidates for application in devices such as gas diffusion membranes¹, ceramic membranes for oxygen separation², sensors³, solid oxide fuel cells (SOFCs)⁴, superconductors and colossal magnetoresistants.⁵

The oxygen deficient perovskite oxides are represented by general formula ABO_{3-x} or $\text{A}_2\text{B}_2\text{O}_{6-\delta}$. The A and B sites can contain more than one type of cation. Oxygen-deficient perovskites can have a variety of structures depending on several factors including the extent of anion deficiency and vacancy order/disorder. While disordered vacancies in oxygen-deficient perovskites are common, there are a number of ways for the vacancies, created due to oxygen deficiency, to order. This leads to great diversity and variation in structure and properties of this family of compounds⁶⁻⁷. The vacancies result in different coordination geometries such as tetrahedral or square pyramidal.⁸⁻¹⁰ One of the structure-

² The work described in this chapter was published in *Inorganic Chemistry* (2017, vol. 56, p. 14494-14505)

types containing tetrahedral geometry comprises corner-sharing tetrahedra which form chains that run almost perpendicular to the longest unit cell axis (Figure 3.1). The tetrahedra in these chains also share apexes with octahedral layers above and below them. Therefore, the overall structure appears as a combination of octahedral and tetrahedral layers as shown in Figure 3.1. This is called the brownmillerite-type structure. In situations like this, where there is more than one unique crystallographic site for the A or B cations, the general formula can be expressed as $AA'BB'O_{6-\delta}$. The variation in the type of cations on A or B sites, affects the structure and properties of these materials. For example, $Sr_2Fe_2O_5$ has a vacancy-ordered structure containing FeO_6 octahedra and FeO_4 tetrahedra.¹¹ Replacing one of the Fe atoms for Mn leads to a change in crystal structure. The resulting material, Sr_2FeMnO_5 , contains vacancies that are distributed randomly, without any type of ordering.¹² Another example is the difference between Ca_2FeAlO_5 and Ca_2FeGaO_5 .¹³ These two materials have the same structure-type, but the change in the B-site cation results in a change in the space group. The Al-containing compound crystallizes in *Ibm2* space group, while the Ga-containing material has space group *Pcmm*.¹³ The material properties can also be affected by changes in the A-site cation. An example is the differences between the two compounds $Ca_2Fe_2O_5$ and $Sr_2Fe_2O_5$.¹⁴⁻¹⁵ While both of these materials have ordered structures, where Fe atoms have both octahedral and tetrahedral geometry, the change in the A-site cation leads to different space groups. $Ca_2Fe_2O_5$ crystallizes in the primitive space group *Pnma*¹⁶, whereas $Sr_2Fe_2O_5$ has a body-center space group *Icmm*¹¹. A similar effect is observed for Ca_2GaMnO_5 and Sr_2GaMnO_5 , where the change in the A-site cation results in changes in the space group.¹⁷

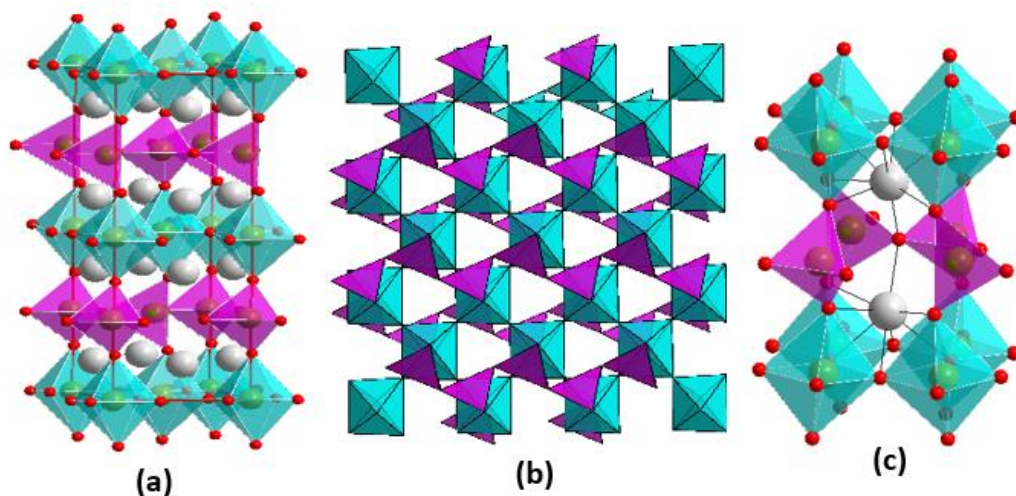


Figure 3.1. Crystal structure of $\text{CaSrFeCoO}_{6-\delta}$. (a) The crystallographic unit cell. The alternating $(\text{Fe/Co})\text{O}_6$ octahedra (cyan) and $(\text{Fe/Co})\text{O}_4$ tetra (pink) are highlighted. The large grey spheres are the A-site cations, $\text{Ca}^{2+}/\text{Sr}^{2+}$. (b) A view along the b axis (longest axis) to show the uniform orientation of tetrahedral chains. The A-site cations are omitted for clarity. (c) The coordination geometry around the A-site cation. There are 8 oxygens that are close enough to the A-site cation to be in its coordination sphere.

In the above examples, the change in the A-site cation only affects the crystal symmetry, and the overall structure-type remains the same. In this article, we show significant changes in structure and electrical properties due to the variation in the A-site cation. We demonstrate that changes to the structural order have major consequences with regard to the electrical charge transport in three oxygen-deficient perovskites, $\text{Ca}_2\text{FeCoO}_{6-\delta}$, $\text{CaSrFeCoO}_{6-\delta}$ and $\text{Sr}_2\text{FeCoO}_{6-\delta}$.

EXPERIMENTAL

All three materials, $\text{Ca}_2\text{FeCoO}_{6-\delta}$, $\text{CaSrFeCoO}_{6-\delta}$ and $\text{Sr}_2\text{FeCoO}_{6-\delta}$, were synthesized under the same condition. The precursor compounds CaCO_3 (Alfa Aesar, 99.95%), Fe_2O_3 (Alfa Aesar, 99.998%), Co_3O_4 (Alfa Aesar, 99.7%) and SrCO_3 (Aldrich, 99.9%) were used in stoichiometric proportions for solid state syntheses. The precursor powders were mixed and ground together using agate mortar and pestle, pressed into a pellet and heated in air

at 1000 °C for 24 hours. Then the sample was reground and refired in air at 1200 °C for 24 hours followed by slow cooling. In all cases, the heating and cooling rates were 100 °C/h. The phase purity and structure of the polycrystalline samples were studied by powder X-ray diffraction at room temperature using CuK α 1 radiation ($\lambda = 1.54056 \text{ \AA}$), and step-size 0.008°. The *GSAS* software¹⁸ and *EXPEGUI* interface¹⁹ were used for Rietveld refinements. The sample morphologies were examined using a high-resolution field-emission scanning electron microscope (SEM). X-ray photoelectron spectroscopy was performed at room temperature using Al K α radiation (1486.7 eV). The electrical properties were investigated by DC and AC conductivity measurements on pressed pellets that had been sintered at 1200 °C. The densities of sintered pellets were ~50%, ~27% and ~76% of the theoretical densities for Ca₂FeCoO_{6- δ} , CaSrFeCoO_{6- δ} and Sr₂FeCoO_{6- δ} , respectively. The relative densities are consistent with SEM results, as described in the next section. Electrochemical impedance spectroscopy (EIS) was performed in the frequency range 0.1 Hz–1 MHz using a computer-controlled frequency response analyzer at room temperature. The 2-probe DC measurements were performed in the temperature range 298 to 1073 K (25 – 800 °C) by applying a constant voltage, 10 mV, and collecting the output current. Variable temperature electrical conductivity measurements were carried out during both heating and cooling cycles. The rate of heating and cooling for conductivity measurements was 3 °C min⁻¹. Iodometric titrations were performed by dissolving about 50 mg of sample and excess KI (~2 g) in 100 mL of 1 M HCl. 5 mL of the solution was then pipetted out, and the iodine that had been generated in the solution was titrated using 0.025 M Na₂S₂O₃. Near the end point of the titration, 10 drops of starch solution were added to act as indicator. All steps were performed under argon atmosphere. Neutron diffraction

experiments with center wavelength of 1.333 Å were performed on powder samples (~4 g) in vanadium sample holders at 300 K on POWGEN diffractometer at Oak Ridge National Laboratory.

RESULTS AND DISCUSSION

Crystal structure

We have determined the crystal structure of $\text{CaSrFCoO}_{6-\delta}$ and demonstrated the sharp contrast between this material and $\text{Ca}_2\text{FeCoO}_{6-\delta}$ ²⁰ and $\text{Sr}_2\text{FeCoO}_{6-\delta}$.²¹

Researchers studying CO_2 absorption²¹ have previously identified a phase with a composition similar to $\text{CaSrFCoO}_{6-\delta}$. However, they could only determine the cell dimensions, and no other structural information is available for this material. We examined the structure of this material through a series of Rietveld refinement analyses using monochromatic X-ray and time-of-flight neutron diffraction. The data indicate that this material has an orthorhombic structure featuring tetrahedral chains that are sandwiched between octahedral layers. As shown in Figure 3.1, the tetrahedral chains run parallel to the octahedral layers. Each tetrahedron in the chain shares corners with the octahedral layers above and below. This material is the brownmillerite-type structure that was described above.

Materials with this structure-type usually crystalize in space groups *Pnma*, *Ibm2*, *Icmm* or *Pbcm*.²²⁻²³ The space group is determined by relative orientation of tetrahedral chains. There are two possible orientations, which are arbitrarily called right-handed and left-handed. If all tetrahedral chains have the same orientation, the space group *Ibm2* is obtained. If the tetrahedral chains have the same orientation within each layer but are oriented opposite to the chains in the next tetrahedral layer, the resulting space group will

be *Pnma*. The random orientation of tetrahedral chains leads to space group *Icmm*. A less common space group is *Pbcm*,²⁰ where each tetrahedral chain is oriented opposite to all of its nearest neighbors within the same layer and in the neighboring layers. Materials that crystallize in space group *Pbcm* have a large unit cell, that has twice the volume of the unit cell for other space groups mentioned above. The large unit cell is represented by supercell reflections in powder diffraction data, making this type of structure easily identifiable. The absence of *Pbcm* supercell reflections in the powder X-ray diffraction data of $\text{CaSrFCoO}_{6-\delta}$ rules out this space group. The other primitive space group, *Pnma*, is identified by the presence of 131 and 151 peaks in the powder diffraction data, which are absent in the body-centered systems. The 131 peak is especially prominent when present. The absence of these peaks in the PXRD data of $\text{CaSrFCoO}_{6-\delta}$ indicates that this material does not have a primitive unit cell and crystallizes in one of the body-centered space groups, *Icmm* or *Ibm2*. Multiple Rietveld refinements with these two space groups were performed using high-resolution $\text{K}\alpha_1$ XRD datasets on different $\text{CaSrFCoO}_{6-\delta}$ samples to ensure the reproducibility of the results. With *Icmm* space group, the atomic parameters could only be refined individually, while simultaneous refinement of all atomic parameters led to the divergence of the Rietveld refinements. This was observed consistently for multiple samples and

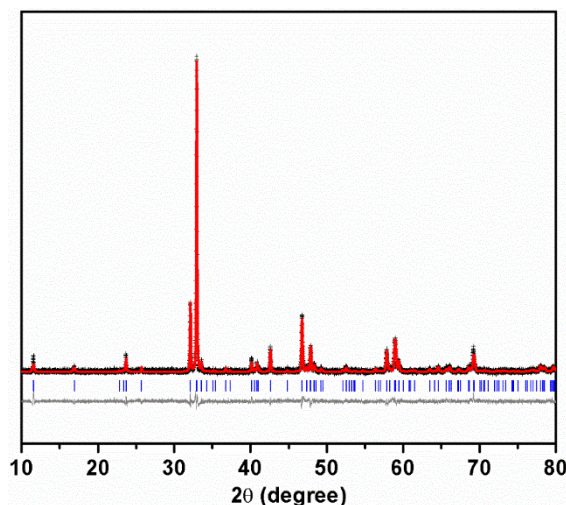


Figure 3.2. Rietveld refinement profile for powder X-ray diffraction data of $\text{CaSrFeCoO}_{6-\delta}$. Crosses represent experimental data, solid red line is the *Ibm2* model, vertical tick marks show Bragg peak positions, and the lower line represents the difference plot.

refinement trials. The *Ibm2* space group, however, always led to an excellent fit. All profile parameters, background, unit cell dimensions, atomic positions, and thermal displacement factors were refined simultaneously, giving an excellent fit to *Ibm2* space group. The Rietveld refinement profile is shown in Figure 3.2 and the refined atomic parameters are listed in Table 3.1. Given the inherent limitation of laboratory X-ray diffraction with regard to differentiating elements with similar atomic numbers, such as Fe and Co, neutron diffraction experiments were undertaken to study the distribution of Fe and Co on different positions in this material. Given the large difference between the neutron scattering lengths of Fe, 9.45, and Co, 2.49, these two nuclei are readily distinguishable by neutrons. The neutron diffraction results and Rietveld refinement profile are shown in Table 3.2 and Figure 3.3, respectively. Initially two models were tested where Fe and Co were placed exclusively on tetrahedral and octahedral sites, and vice versa. However, the refined thermal displacement factors on tetrahedral and octahedral sites became unusually large on

one site and negative on the other. Therefore, the site occupancies on these two sites were refined, leading to an excellent fit and atomic parameters that are shown in Table 3.2. As observed here, Fe and Co are distributed nearly evenly over the octahedral and tetrahedral sites.

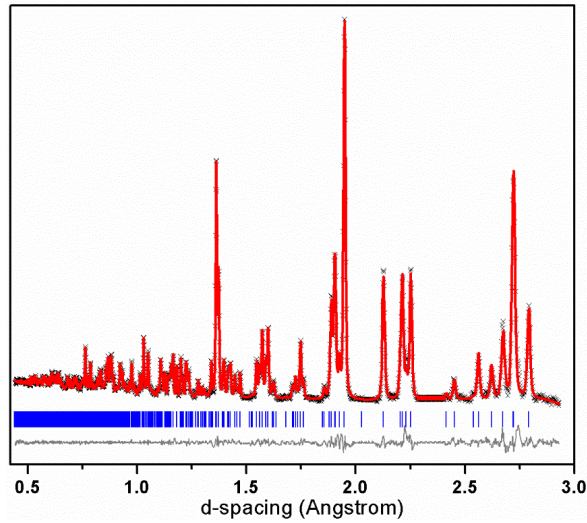


Figure 3.3. Neutron diffraction Rietveld refinement profile for $\text{CaSrFeCoO}_{6-\delta}$. Magnetic reflections have been omitted. Crosses represent experimental data, solid red line is the *Ibm2* model, vertical tick marks show Bragg peak positions, and the lower line represents the difference plot.

Table 3.1. Refined structural parameters of CaSrFeCoO_{6-δ} using powder X-ray diffraction.

Space group: <i>Ibm2</i>						
$a = 5.5576(2) \text{ \AA}, b = 15.1658(5) \text{ \AA}, c = 5.4141(2) \text{ \AA}, R_p = 0.0164, wR_p = 0.0220$						
Elements	x	y	z	Occupancy	U _{ISO}	Multiplicity
Ca1	0.5103(6)	0.1116(2)	-0.004(6)	0.5	0.024(1)	8
Sr1	0.5103(6)	0.1116(2)	-0.004(6)	0.5	0.024(1)	8
Fe1	0.0776(9)	0.25	-0.011(7)	1	0.030(3)	4
Co1	0	0	0	1	0.031(2)	4
O1	0.25(1)	0.0008(8)	0.268(7)	1	0.042(3)	8
O2	-0.075(2)	0.1544(6)	-0.005(1)	1	0.042(3)	8
O3	0.372(4)	0.25	0.85(1)	1	0.042(3)	4

Therefore, both tetrahedral and octahedral layers contain almost equal quantities of Fe and Co. These findings highlight the strength of neutron diffraction in tackling problems that cannot be resolved by X-rays. To study the correlation between crystal structure and electrical conductivity, we also synthesized Ca₂FeCoO_{6-δ} and Sr₂FeCoO_{6-δ} (hereafter referred to as Ca₂ and Sr₂ analogues) under the same conditions as CaSrFeCoO_{6-δ} (hereafter CaSr-compound). Table 3.3 compares the space groups and unit cell parameters for all three compounds. The Sr₂ material crystallizes in the cubic space group *Pm-3m*.^{21, 24} The formation of the cubic structure with space group *Pm-3m* was confirmed by our Rietveld

Table 3.2. Refined atomic parameters of CaSrFeCoO_{6-δ} in *Ibm2* space group using neutron diffraction.

Elements	x	y	z	Occupancy	U _{iso}
Ca1	0.5125(6)	0.1110(2)	0.010(2)	0.48(5)	0.0140(8)
Sr1	0.5125(6)	0.1110(2)	0.010(2)	0.52(5)	0.0140(8)
Fe1	0.0664(9)	0.25	-0.031(2)	0.46(3)	0.022(2)
Co1	0.0664(9)	0.25	-0.031(2)	0.54(3)	0.022(2)
Fe2	0	0	0	0.52(2)	0.009(1)
Co2	0	0	0	0.48(2)	0.009(1)
O1	0.2393(8)	0.0094(2)	0.266(2)	1	0.0106(6)
O2	-0.057(1)	0.1406(2)	0.008(3)	1	0.0204(7)
O3	0.370(1)	0.25	0.889(2)	1	0.027(1)

refinement results. Figures 3.4 and 3.5 show the crystal structure and Rietveld refinement profile of the Sr₂ compound. The refined atomic parameters are listed in Table 3.4. The Ca₂ compound has a brownmillerite-type *Pbcm* structure²⁰ (Figure 3.6) with a large unit cell, which is double the size of that for a typical brownmillerite, and ordered arrangement of tetrahedral chains, where each chain is oriented opposite to all of its nearest-neighbors. Our Rietveld refinements confirm the formation of the *Pbcm* structure²⁰ (Figure 3.7) under the same synthesis conditions as the other two materials. Table 3.5 lists the refined atomic parameters for the Ca₂ compound.

Table 3.3. Comparison of space groups and unit cell parameters for $\text{Ca}_2\text{FeCoO}_{6-\delta}$, $\text{CaSrFeCoO}_{6-\delta}$ and $\text{Sr}_2\text{FeCoO}_{6-\delta}$

	$\text{Sr}_2\text{FeCoO}_5$	CaSrFeCOO_5	$\text{Ca}_2\text{FeCoO}_5$
Space group	$Pm-3m$	$Ibm2$	$Pbcm$
Lattice parameters			
a (Å)	3.86469(3)	5.5576(2)	5.36854(8)
b (Å)	3.86469(3)	15.1658(5)	11.1063(2)
c (Å)	3.86469(3)	5.4141(2)	14.8079(2)
V (Å ³)	57.722(1)	456.33(4)	882.92(3)

The trend in the structural order in progression from Sr_2 -compound to CaSr and Ca_2 materials is remarkable. In the Sr_2 material, the vacant sites, created due to oxygen deficiency, are distributed randomly. In the CaSr compound the vacancies are ordered. The vacant sites only appear in alternating layers, forming tetrahedral chains, instead of octahedral geometry that is commonly observed in perovskites. All tetrahedral chains in this material have the same orientation, as evident from its space group. The Ca_2 material has the same type of vacancy order. However, an additional type of ordering is also present, namely the alternating orientation of tetrahedral chains within and between layers. Therefore, it is evident that as the Ca content increases, the degree of ordering also increases.

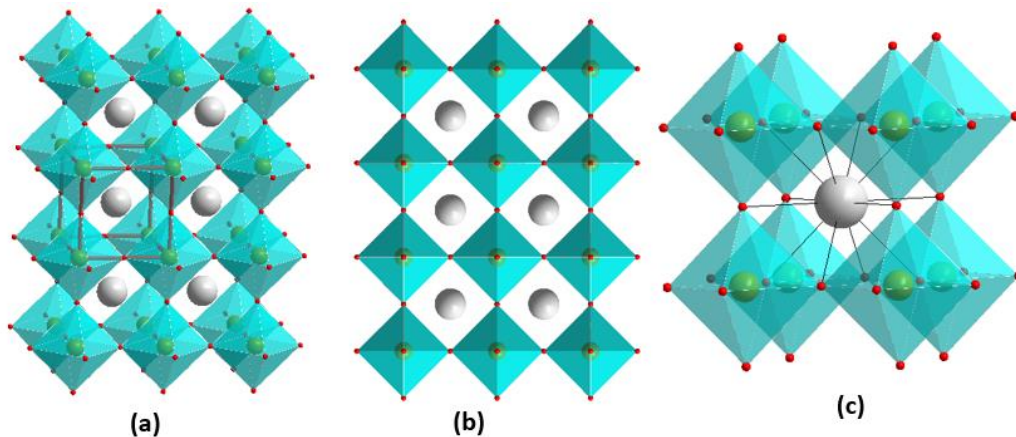


Figure 3.4. Crystal structure of $\text{Sr}_2\text{FeCoO}_{6-\delta}$. (a) The crystallographic unit cell and corner-sharing $(\text{Fe}/\text{Co})\text{O}_6$ octahedra (cyan) are highlighted. The large grey spheres are the Sr atoms. (b) A view along the unit cell axis. Due to cubic symmetry, the three axes are identical. (c) The coordination geometry around the Sr atom, which is 12-coordinated.

We investigated the oxygen contents of all three materials using iodometric titration, which showed that the formulae for the three compounds can be described as $\text{Sr}_2\text{FeCoO}_{6-\delta}$ ($\delta = 0.5$), $\text{CaSrFeCoO}_{6-\delta}$ ($\delta = 0.8$) and $\text{Ca}_2\text{FeCoO}_{6-\delta}$ ($\delta = 0.9$). Note the greater oxygen content of the disordered Sr_2 material. We have also confirmed these results by monitoring the oxygen loss due to the heating of samples in argon at temperatures up to 1200 °C, which usually leads to oxygen stoichiometry of 5, i.e., $\delta = 0$, in oxygen-deficient perovskites.^{10, 23} We also explored the correlation between the A-site cation and the morphology and crystallite size by performing scanning electron microscopy studies on all three materials. Interestingly, the CaSr compound has the smallest crystallite size, as shown in Figure 3.8. The Sr_2 and Ca_2 compounds have comparable crystallite sizes. However, the contact between crystallites is enhanced in the Sr_2 material compared to the other compounds.

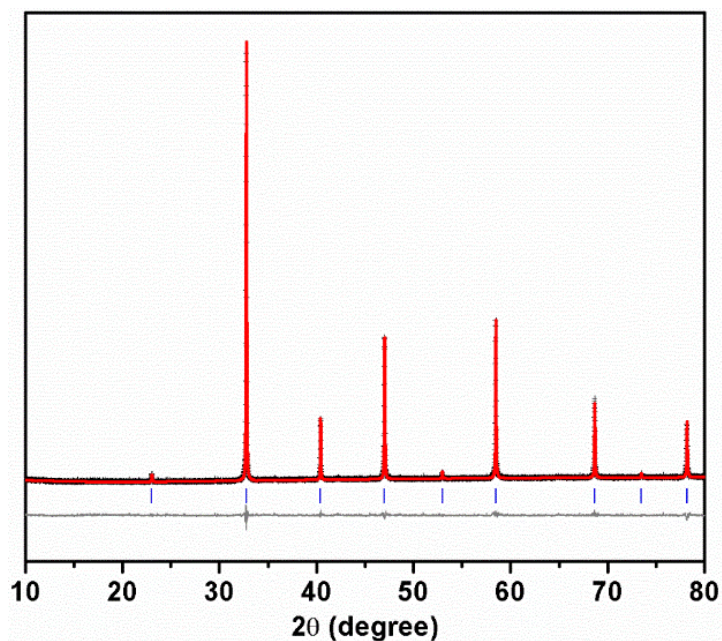


Figure 3.5. Rietveld refinement profile for powder X-ray diffraction data of $\text{Sr}_2\text{FeCoO}_{6-\delta}$ refined in $Pm-3m$ space group. Crosses represent experimental data, solid red line is the model, vertical tick marks show Bragg peak positions, and the lower blue line represents the difference plot.

Table 3.4. Refined structural parameters of $\text{Sr}_2\text{FeCoO}_{6-\delta}$.

Space group: $Pm-3m$						
$a = 3.86469(3) \text{ \AA}$, $R_p = 0.0142$, $wR_p = 0.0192$						
Element	x	y	z	Occupancy	U_{iso}	Multiplicity
Sr1	0.5	0.5	0.5	1	0.0183(3)	1
Fe1	0	0	0	0.5	0.0177(4)	1
Co1	0	0	0	0.5	0.0177(4)	1
O1	0	0	0.5	0.92	0.0220(6)	3

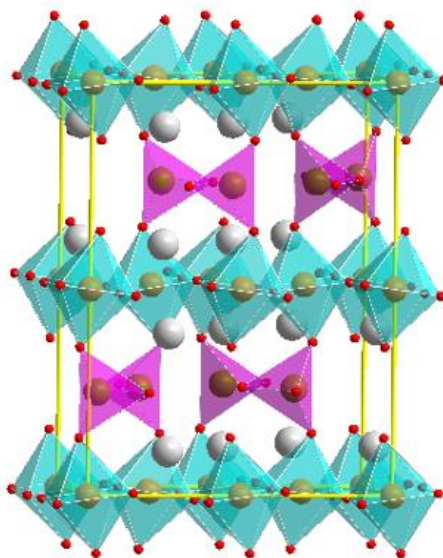


Figure 3.6. Crystal structure of $\text{Ca}_2\text{FeCoO}_{6-\delta}$ featuring alternating $(\text{Fe/Co})\text{O}_6$ octahedra (cyan) and $(\text{Fe/Co})\text{O}_4$ tetrahedra (pink). The large grey spheres are Ca atoms. The crystallographic unit cell is highlighted using yellow lines. Note that the unit cell here is 2-times larger than that for the CaSr analogue.

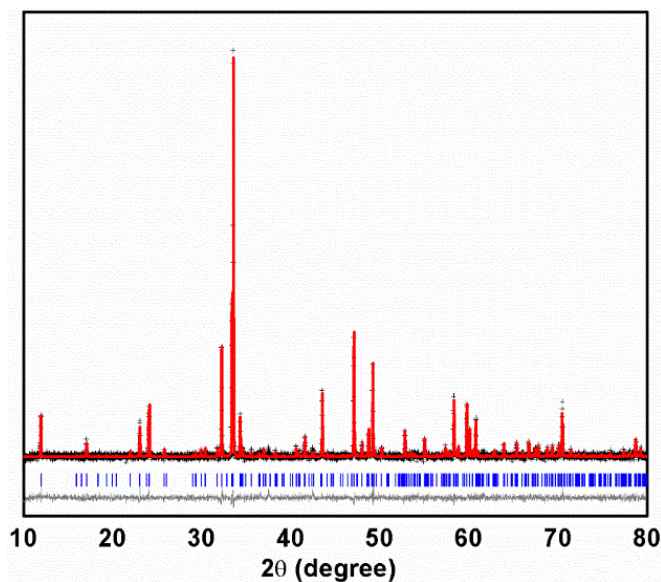


Figure 3.7. Rietveld refinement profile for powder X-ray diffraction data of $\text{Ca}_2\text{FeCoO}_{6-\delta}$ refined in $Pbcm$ space group. Crosses represent experimental data, red solid line is the model, vertical tick marks show Bragg peak positions, and the blue line represents the difference plot.

To investigate these structural transitions further, we carried out a series of experiments and synthesized 21 different materials by systematically varying the Ca/Sr ratio to determine the average ionic radius that is required on the A-site to promote these structural transformations. The ionic radii play an essential role in the formation of different perovskite-type structures.²⁵ For our materials, the transition from disordered structure to the ordered system occurs when the Ca/Sr ratio is greater than 0.3/1.7. (Figure 3.9) We also determined the Ca/Sr ratio that is required for transition from the *Ibm2* structure (where all tetrahedral chains have the same orientation) to the *Pbcm* system (with alternating orientation of tetrahedral chains). This transition was found to occur at Ca/Sr ratio 1.2/0.8, as indicated by the appearance of (120) peak at $2\theta \approx 23^\circ$ in Figure 3.10. Using the ionic radii for 12-coordinated Sr^{2+} , 1.44 Å, and Ca^{2+} , 1.34 Å,²⁶ one can calculate the average ionic radius that prompts each of these phase transitions. The transition from a disordered to ordered system occurs when the average ionic radius on the A-site is greater than ~ 1.42 Å. The transition from the ordered system with uniform orientation of chains to the more-ordered system, with alternating chain orientation, takes place when the average ionic radius is larger than 1.39 Å.

Table 3.5. Refined structural parameters of $\text{Ca}_2\text{FeCoO}_{6-\delta}$.

Space group: <i>Pbcm</i>						
$a = 5.36854(8) \text{ \AA}$, $b = 11.1063(2) \text{ \AA}$, $c = 14.8079(2) \text{ \AA}$, $R_p = 0.0167$, $wR_p = 0.0215$						
Element	x	y	z	Occupancy	U_{iso}	Multiplicity
Ca1	-0.006(2)	0.757(2)	0.393(1)	1	0.038(8)	8
Ca2	-0.491(3)	0.516(2)	0.609(1)	1	0.035(7)	8
Fe1	0.439(3)	0.719(1)	0.25	0.5	0.032(7)	4
Co1	0.439(3)	0.719(1)	0.25	0.5	0.032(7)	4
Fe2	-0.054(3)	0.539(2)	0.25	0.5	0.042(8)	4
Co2	-0.054(3)	0.539(2)	0.25	0.5	0.042(8)	4
Fe3	-0.504(3)	0.75	0.5	0.5	0.026(8)	4
Co3	-0.504(3)	0.75	0.5	0.5	0.026(8)	4
Fe4	0.0	0.0	0.0	0.5	0.043(9)	4
Co4	0.0	0.0	0.0	0.5	0.043(9)	4
O1	0.114(8)	0.662(4)	0.25	1	0.04	4
O2	0.604(9)	0.552(4)	0.25	1	0.04	4
O3	-0.213(7)	0.612(4)	0.489(2)	1	0.04	8
O4	-0.760(9)	0.609(4)	0.490(2)	1	0.04	8
O5	0.042(7)	0.459(4)	0.359(3)	1	0.04	8
O6	0.527(6)	0.781(4)	0.365(4)	1	0.04	8

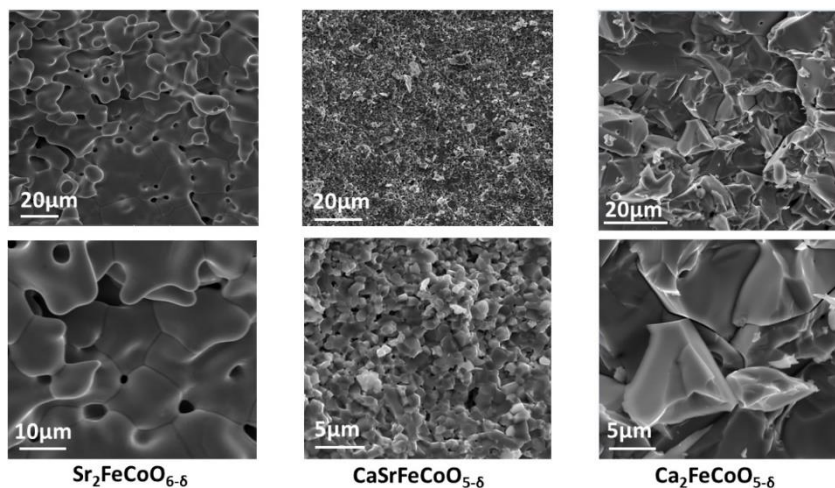


Figure 3.8. Scanning electron microscopy images for $\text{Sr}_2\text{FeCoO}_{6-\delta}$, $\text{CaSrFeCoO}_{6-\delta}$ and $\text{Ca}_2\text{FeCoO}_{6-\delta}$

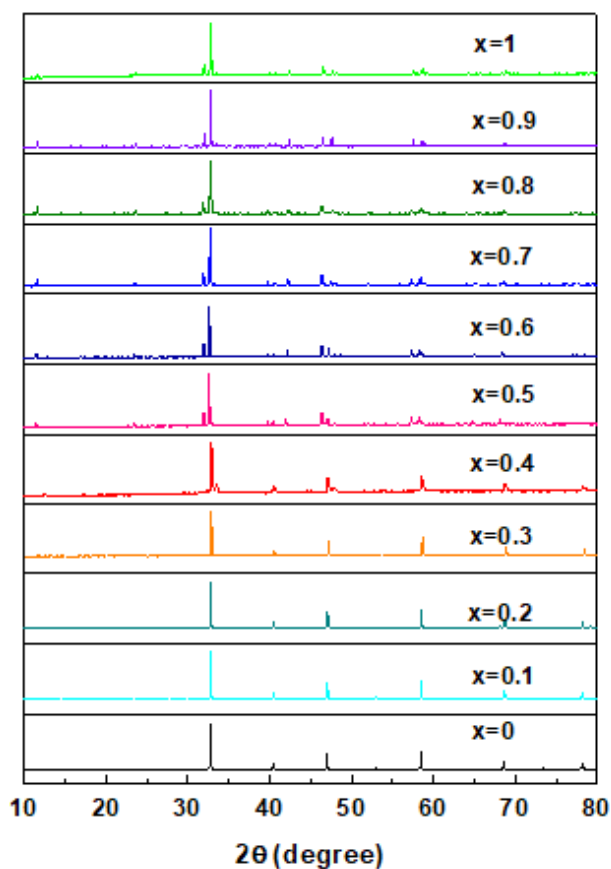


Figure 3.9. Powder XRD data for the series $\text{Sr}_{2-x}\text{Ca}_x\text{FeCoO}_{6-\delta}$, $x = 0 - 1$. The structural transition occurs above $x = 0.3$.

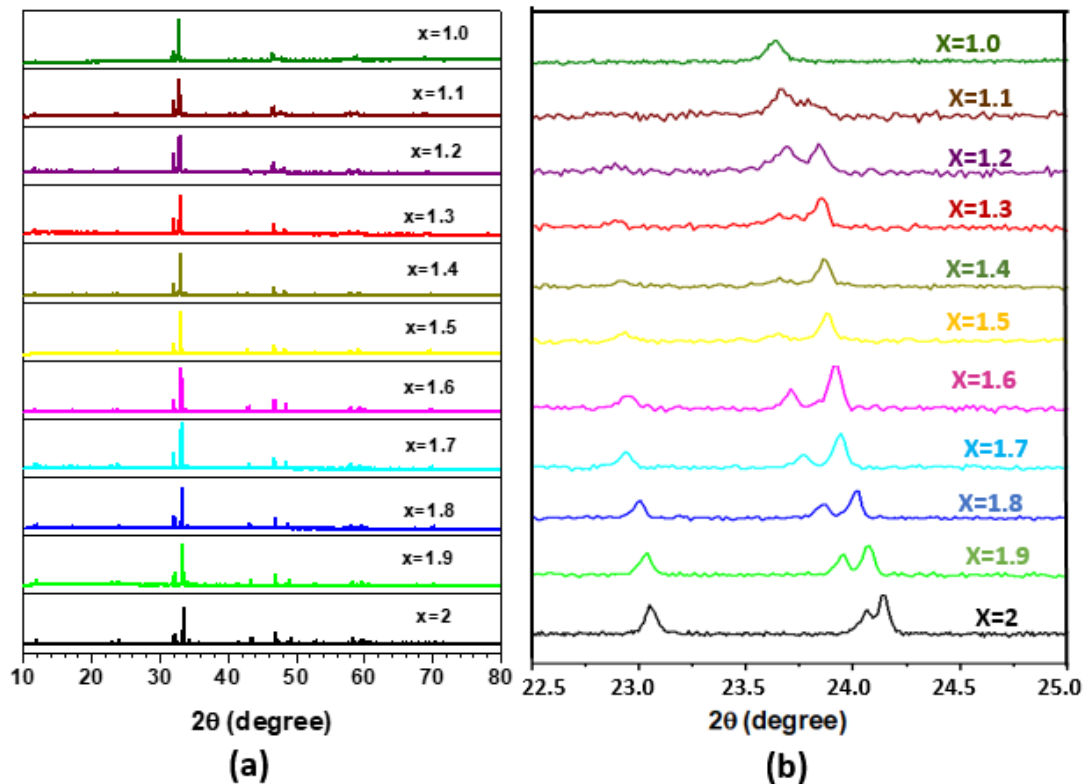


Figure 3.10. Powder XRD data for the series $\text{Sr}_{2-x}\text{Ca}_x\text{FeCoO}_{6-\delta}$, $x = 1 - 2$. The structural transition occurs above $x = 1.2$.

X-ray photoelectron spectroscopy (XPS)

The oxidation states of iron and cobalt in all three materials were explored using XPS analyses, which revealed an interesting trend with regard to the cation oxidation states in these three compounds. We note that the starting materials used in the syntheses, namely Fe_2O_3 and Co_3O_4 , contained Fe^{3+} , Co^{2+} and Co^{3+} . The main XPS peak for Fe^{3+} is the $2p_{3/2}$ peak, which appears at about 710 – 711.5 eV.²⁷⁻²⁹ In our spectra this peak is present. However, additional features are also observed in the spectra indicating that other oxidation states are present as well, as discussed further below. Similar observations are made for

Co, where the dominant Co^{3+} peak, i.e., the $2p_{3/2}$ peak,³⁰⁻³¹ is observed at ~ 780 eV, but additional features signify the presence of other cobalt oxidation states as well.

For Fe, the position and width of the $2p_{3/2}$ peak, as well as the positions of satellite peaks, which appear at higher energy than the $2p_{3/2}$ peak, are indicative of oxidation states.²⁷⁻²⁹ In the XPS spectra of our materials, two satellite peaks are observed for Fe, one at ~ 4 eV higher and another at $\sim 6.5 - 7.5$ eV higher than the center of the $2p_{3/2}$ peak. The first satellite peak, located at ~ 4 eV higher than the $2p_{3/2}$ peak, belongs to Fe^{2+} .²⁸⁻²⁹ The second satellite peak, at $\sim 6.5 - 7.5$ eV higher than the $2p_{3/2}$ peak, is the signature of Fe^{3+} .^{28-29, 32} Therefore, the XPS data show that these materials contain Fe in both divalent and trivalent states. Figure 3.11 shows the Fe XPS spectra for all three materials.

Unlike the Fe spectra that are quite similar for all three compounds, the Co spectra show an interesting variation in oxidation states. The most striking difference is the low energy shoulder on the cobalt $2p_{3/2}$ peak for the Ca_2 and CaSr -compounds, which is absent for the Sr_2 -material, as seen in Figure 3.12. The low energy side of the cobalt $2p_{3/2}$ peak for Ca_2 and CaSr -materials is much wider and is stretched further into the low-energy region, showing a distinct shoulder, which is not present in Sr_2 -material spectrum.

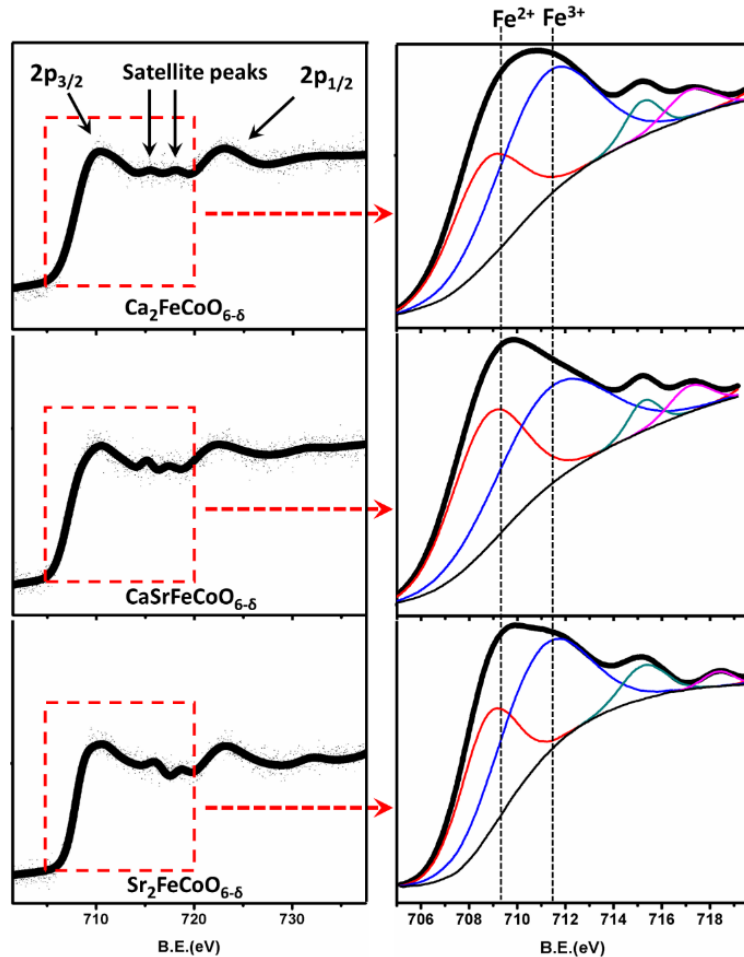


Figure 3.11. The Fe XPS spectra for $\text{Ca}_2\text{FeCoO}_{6-\delta}$, $\text{CaSrFeCoO}_{6-\delta}$ and $\text{Sr}_2\text{FeCoO}_{6-\delta}$

The low energy shoulder is indicative of Co^{2+} .^{30, 33} There is also a shoulder on the high energy side of the $2p_{3/2}$ peak for all three compounds, which represents Co^{4+} .³⁰⁻³¹ Two satellite peaks are present in the cobalt spectra for all three materials, including the Sr_2 -compound that lacks Co^{2+} . The first satellite peak appears at about 785 eV – 787 eV, while the second satellite peak is observed at about 788 eV – 789 eV. The first satellite peak represents tetravalent cobalt,³¹ and is located $\sim 3.5 - 5$ eV higher than the Co^{4+} peak, as expected.³¹

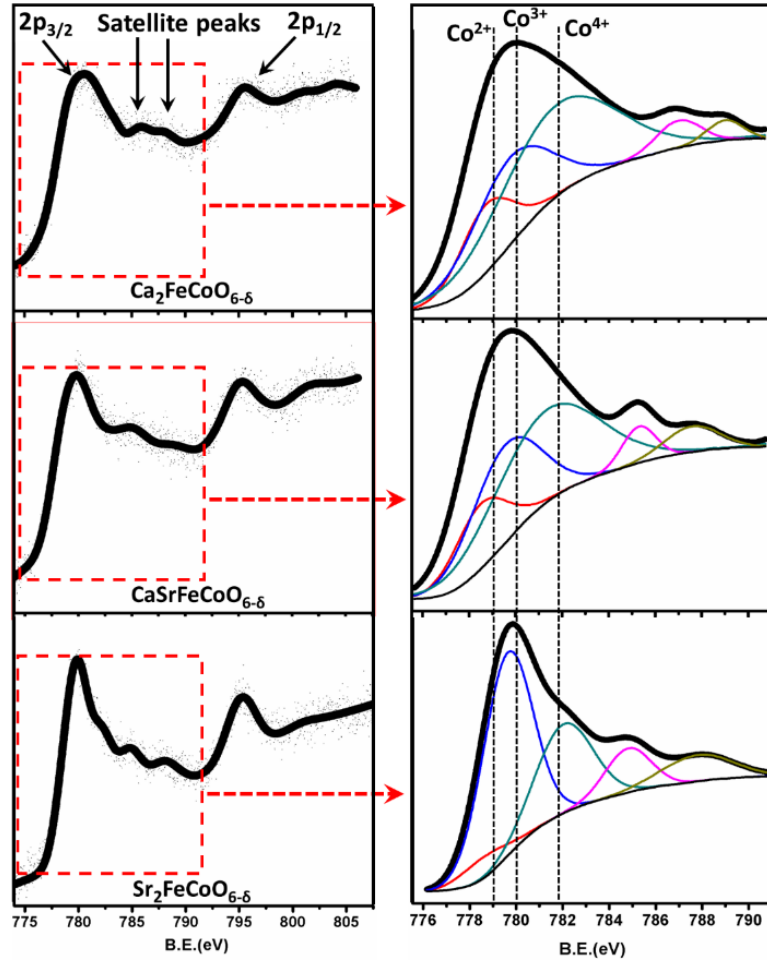


Figure 3.12. The cobalt XPS spectra for $\text{Ca}_2\text{FeCoO}_{6-\delta}$, $\text{CaSrFeCoO}_{6-\delta}$ and $\text{Sr}_2\text{FeCoO}_{6-\delta}$

This satellite peak is especially pronounced in the CaSr and Sr₂-materials. The second satellite peak belongs to Co^{3+} , located at $\sim 8 - 9$ eV higher than the $2p_{3/2}$ peak, as expected for trivalent cobalt.³¹ Note that the relative binding energy of satellite peaks for different oxidation states of cobalt does not follow the same trend as the relative binding energy of the main $2p_{3/2}$ and $2p_{1/2}$ peaks, which have a different origin compared to the satellite peaks. The satellite peak for Co^{4+} appears at lower binding energy than that for Co^{3+} .³¹ In general, some degree of cobalt oxidation is expected at high temperature in air.²⁴ However, the above observations point to an interesting redox phenomenon in these materials, where

further oxidation of cobalt becomes possible through the reduction of iron. In addition, it is remarkable that the disordered Sr₂ compound lacks Co²⁺, while the ordered Ca₂ and CaSr materials contain divalent cobalt. It appears that the disordered structure encourages the oxidation of Co²⁺ to Co³⁺.

Electrical conductivity

The electrical properties of these three materials were studied by DC and AC methods. The total conductivity was found by first obtaining the resistance from the intercept of the data with the real axis (Z') of the Nyquist plot at high frequency in the AC method. Similar values were obtained using DC method by applying constant voltage or current and measuring the output current or voltage. The resistance values obtained using the above methods, can be used to calculate the conductivity (σ) using the following equation:

$$\sigma = L/RA \quad (8)$$

where L and A represent the thickness and cross sectional area of the cylindrical pellet, respectively. The electrical conductivity values for the three compounds, Ca₂FeCoO_{6- δ} , CaSrFeCoO_{6- δ} and Sr₂FeCoO_{6- δ} were obtained by AC method at room temperature and by DC method from 298 to 1073 K. The room temperature conductivity values are listed in Table 3.6. These results show the order of the total conductivity for the three compounds at room temperature:

$$\text{Ca}_2\text{FeCoO}_{6-\delta} < \text{CaSrFeCoO}_{6-\delta} < \text{Sr}_2\text{FeCoO}_{6-\delta}$$

The electrical conductivity increases as the Sr content and structural disorder increase. Note that the Sr₂ compound is the most disordered phase, where oxygen vacancies have random distribution. The Ca₂ material is the most ordered phase featuring vacancy order and also tetrahedral chain order. The bond angles may play a role as well. It has been shown that

changes in electrical conductivity correlate with changes in bond lengths and angles.³⁴⁻³⁵ Some researchers have used density-functional theory calculations to show that when the Co–O–Co bond angles in $\text{La}_{1-x}\text{Sr}_x\text{CoO}_3$ get closer to 180° , the overlap between the unoccupied cobalt 3d conduction band and the occupied oxygen 2p valence band is enhanced, leading to improvement in electrical conductivity.³⁶ Metallic conductivity can be obtained due to the formation of a hybrid band as a result of the enhanced overlap between metal 3d and oxygen 2p bands.³⁶⁻³⁸ A correlation between conductivity and bond angle is also observed when the x-value is varied in $\text{La}_{1-x}\text{Sr}_x\text{CoO}_3$.³⁴⁻³⁵ A change from semiconductivity to metallic conductivity is observed at $x = 0.25$. This change has been explained by the introduction of doped states within the band gap and broadening of these states into a band as x increases, which leads to band overlap and transition from semiconductor to metal. It has been observed that at around $x = 0.25$, where this transition occurs, there is an abrupt increase in the Co–O–Co bond angle.³⁴⁻³⁵ For our materials, the Fe(Co)–O–Fe(Co) bond angles in the Sr_2 compound are 180° , while those angles in the Ca_2 material can be as small as $\sim 123^\circ$.²⁰ The small angles are a consequence of the vacancy-ordered structure, where each tetrahedron shares corners with two tetrahedra as well as two octahedra. In order for the structure to accommodate these simultaneous corner-sharing, the bond angles distort from the ideal perovskite angle (180°). Large bond angles in the Sr_2 compound and smaller angles in the Ca_2 material correlate well with the relative conductivity of these materials at room temperature.

To obtain a more in-depth understanding of the electrical conductivity, variable temperature studies were performed on all three materials. Figure 3.13 shows the conductivity of the three samples during heating and cooling cycles in the temperature

range 298 – 1073 K. The conductivity of $\text{Ca}_2\text{FeCoO}_{6-\delta}$ and $\text{CaSrFeCoO}_{6-\delta}$ increases with temperature indicating the semiconducting nature of these materials. However, the conductivity of $\text{Sr}_2\text{FeCoO}_{6-\delta}$ decreases as the temperature increases, exhibiting metallic behavior.

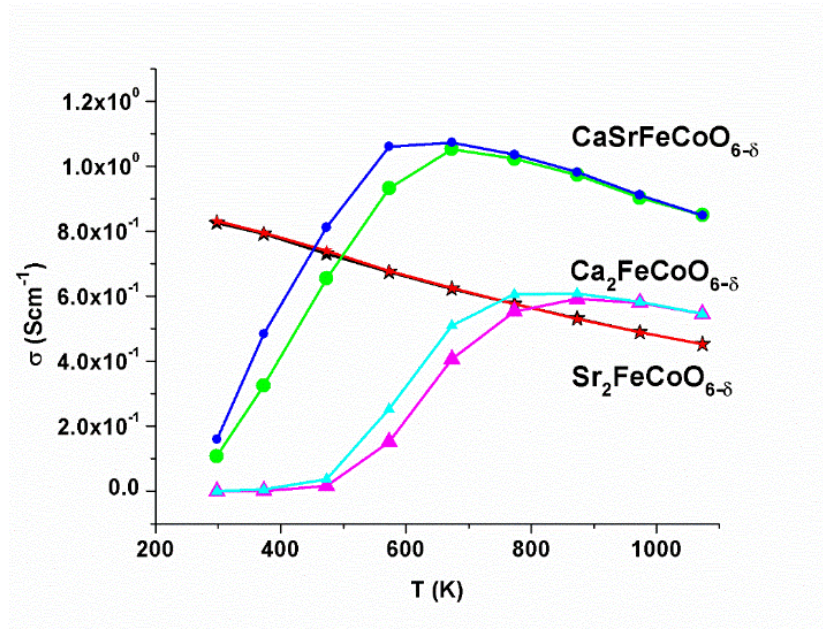


Figure 3.13. Total conductivity of $\text{Sr}_2\text{FeCoO}_{6-\delta}$, $\text{CaSrFeCoO}_{6-\delta}$ and $\text{Ca}_2\text{FeCoO}_{6-\delta}$ as a function of temperature. For $\text{Sr}_2\text{FeCoO}_{6-\delta}$, the heating (red) and cooling (black) data overlap. For $\text{CaSrFeCoO}_{6-\delta}$, the heating data are shown in green and cooling data in blue. For $\text{Ca}_2\text{FeCoO}_{6-\delta}$, the heating and cooling data are shown in pink and cyan, respectively.

The semiconducting properties, observed in the Ca_2 and CaSr compounds, have been observed for other oxygen-deficient perovskites (ODP) before. In general, when oxygen partial pressure is high, e.g., the oxygen partial pressure in air, the electronic conductivity is usually dominant in ODPs.³⁹⁻⁴¹ In semiconducting ODPs, the dependency of conductivity on the oxygen partial pressure indicates the p-type semiconductivity.⁴²⁻⁴⁴ In these p-type semiconductors, the primary charge carriers are electron holes^{39-41, 45-46} The

holes are generated extrinsically due to the absorption of oxygen molecules on the surface, which is aided by the oxide vacancies present in the material. This leads to the following processes:^{40, 45}



The presence of a variable valence metal (M) is essential, as it leads to the formation of small polarons, and electronic transport through the $\text{M}^{3+}\text{-O-M}^{4+}$ network.⁴⁵ The polaronic conductivity in the Ca_2 and CaSr compounds is a result of the structural properties, where structural distortions occur to accommodate the corner-sharing between octahedra and tetrahedra. These distortions lead to lattice polarization that promotes polaronic charge transport.⁴⁵ The polaron mobility is enhanced by rising temperature. This temperature-activated mobility results in an increase in total conductivity,⁴⁷ which can be expressed by the equation

$$\sigma = n e \mu \quad (11)$$

where σ , n , e and μ are conductivity, concentration of electrons/holes, charge of electron and mobility of charge carriers, respectively.

The observed differences in the conductivity of the ordered Ca_2 and CaSr materials compared to the disordered Sr_2 compound are clearly related to the crystal structure, which seem to lead to different conduction mechanisms. The large bond angles (180°) in the Sr_2 compound lead to the enhancement of overlap between metal 3d and oxygen 2p orbitals, leading to metallic conductivity, similar to the situation observed in some other materials, such as $\text{La}_{1-x}\text{Sr}_x\text{CoO}_3$.³⁶ In the ordered Ca_2 and CaSr compounds, the distorted angles do

not allow for good orbital overlap and broadening of bands. The conduction in these materials is through polaronic mechanism, which is activated further at high temperature, leading to enhanced conductivity at elevated temperatures.

For the Sr₂ compound, the decrease in electrical conductivity as a function of temperature occurs due to the increase in collisions between phonons and charge carriers as the temperature increases.³⁷ In addition, for this material, the conductivity as a function of temperature has the same descending trend in the entire temperature range, 298 K – 1073 K.

Unlike the disordered Sr₂ material, the ordered Ca₂ and CaSr compounds exhibit a change in the conductivity trend at high temperature. For the Ca₂ compound, the increase in conductivity continues up to ~ 500 °C (773 K), and then plateaus and even decreases slightly. Similar trend is observed for the CaSr compound, where the increase in conductivity continues up to ~ 300 °C (573 K) and then a plateau and decrease in conductivity is observed. The downturn in conductivity as a function of temperature is indicative of a metal-like conductivity, pointing to a semiconductor to metal transition. There appears to be a limit to the temperature-activated increase in the polaron mobility, beyond which the collisions between phonons and charge-carriers lead to decrease in conductivity and metal-like temperature-dependent behavior. It should be noted that the ionic conductivity is expected to increase at high temperature, due to some oxygen-loss and creation of more vacancies. However, the decrease in electrical conductivity is greater than the increase in ionic conductivity, leading to an overall decrease in total conductivity.

A small degree of oxygen loss at high temperature has been observed through thermogravimetric analysis (TGA) of the CaSr compound in the temperature range, 25 – 800 °C. As shown in Figure 3.14, there is about 1% weight loss as a result of heating up to 800 °C. More interestingly there is an inflection in the TGA data between 300 – 400 °C, matching the temperature where the transition in electrical conductivity occurs.

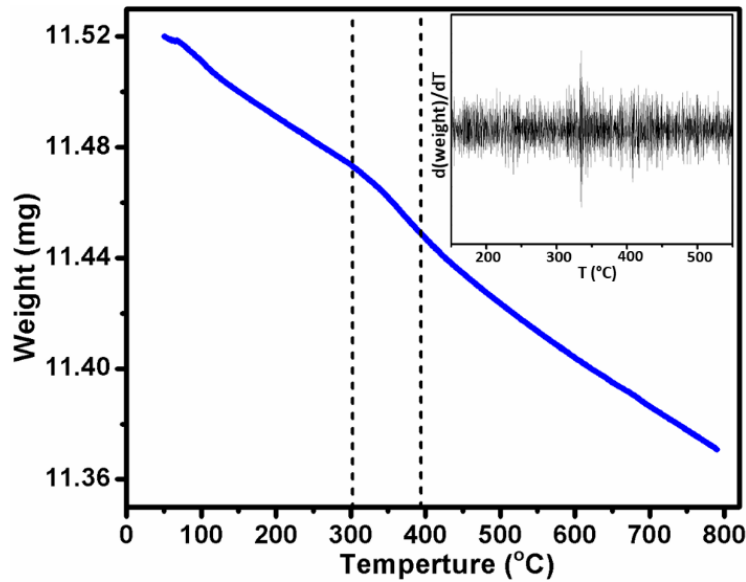


Figure 3.14. Thermogravimetric analysis of $\text{CaSrFeCoO}_{6-\delta}$ in air. An inflection in the data appears in the temperature range between the dashed lines. The inset shows the derivative plot.

In the entire temperature range, the highest conductivity among the three materials is observed for the CaSr-compound at ~ 400 °C. There appears to be an optimum degree of structural order that leads to the highest conductivity at high temperature. Both the disordered Sr_2 -compound and the highly ordered Ca_2 -material have lower conductivities at high temperature compared to the CaSr-compound.

We also tested the possibility of any structural transition at high temperature. This was done by heating the CaSr compound to 800 °C, followed by quenching in liquid nitrogen. However, the XRD data showed no changes in the crystal structure.

Another remarkable property was found when we examined the materials' conductivity during both heating and cooling cycles. For the Sr₂ compound, the conductivity values during both heating and cooling cycles were the same. However, for the Ca₂ and CaSr compounds, the conductivity was greater during the cooling cycle. The observation of these hystereses confirms the contribution of ionic conductivity to the total conductivity as described for other mixed ionic-electronic conductors.⁴⁹⁻⁵⁰ The oxygen absorption/desorption phenomena are relatively slow compared to the electronic transport processes. The oxygen vacancies created at high temperature are not immediately filled when the temperature is lowered. Therefore, the high ionic conductivity persists at lower temperatures, leading to an increase in total conductivity compared to the values obtained during heating. Interestingly, the divergence between the heating and cooling data is only observed below the transition temperature, i.e., in the semiconducting region, for Ca₂ and CaSr compounds. However, above the transition temperature, where the Ca₂ and CaSr materials exhibit metallic behavior, the heating and cooling data overlap. This overlap between heating and cooling data is the same behavior observed for the metallic Sr₂ material in the entire temperature range, 298 – 1073 K.

The Arrhenius equation can be applied to the variation of conductivity with temperature, from which activation energy for conductivity can be obtained.⁴⁵ Figure 3.15 shows the Arrhenius plot for conductivity in the temperature range, 298 – 1073 K.

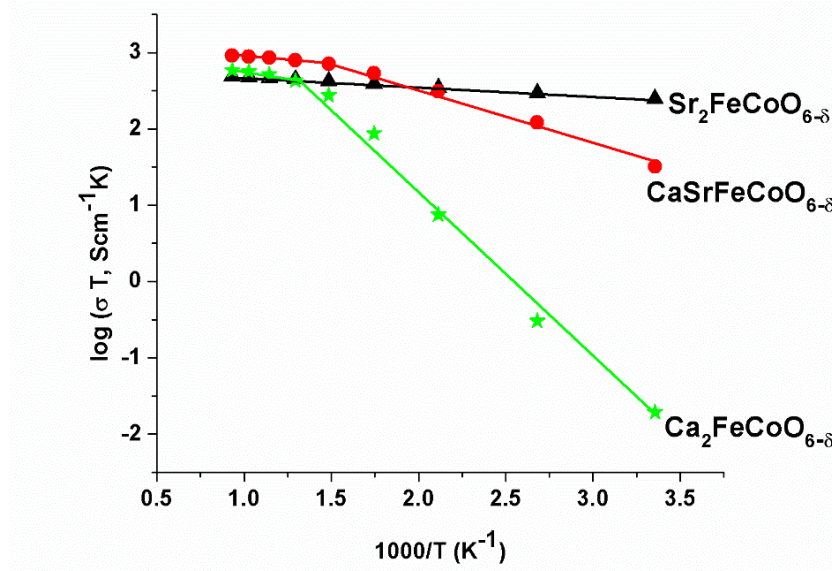


Figure 3.15. Arrhenius plot of the total conductivity for $\text{Sr}_2\text{FeCoO}_{6-\delta}$ (black triangles), $\text{CaSrFeCoO}_{6-\delta}$ (red circles) and $\text{Ca}_2\text{FeCoO}_{6-\delta}$ (green stars).

The straight lines represent the fit using the Arrhenius equation for thermally activated conductivity :^{47 51-52}

$$\sigma T = \sigma^\circ e^{\frac{-E_a}{KT}} \quad (12)$$

where σ° is a pre-exponential factor and a characteristic of a material. E_a , K and T are the activation energy for the electrical conductivity, Boltzmann constant and absolute temperature, respectively. The activation energy (E_a) can be calculated from the slope of the line of best fit in the $\log \sigma T$ vs $1000/T$ plot. These values are listed in Table 3.6. As evident from Figure 3.15 and Table 3.6, the slope of the Arrhenius plot changes at high temperature for the Ca_2 and CaSr compounds, consistent with the change in the conductivity trend. This leads to two different E_a values, where the activation energy at high temperature is smaller than that at low temperature for both Ca_2 and CaSr compounds.

Table 3.6. Room temperature conductivity and activation energies

Sample	Total conductivity at room temperature (Scm^{-1})		Activation energy of total conductivity (E_a) in eV
	AC	DC	
$\text{Ca}_2\text{FeCoO}_{6-\delta}$	6.5×10^{-5}	6.49×10^{-5}	298 K – 800 K: 0.2225 800 K – 1073 K: 0.2587
$\text{CaSrFeCoO}_{6-\delta}$	1.184×10^{-1}	1.077×10^{-1}	298 K – 600 K: 0.72365 600 K – 1073 K: 0.16669
$\text{Sr}_2\text{FeCoO}_{6-\delta}$	8.270×10^{-1}	8.256×10^{-1}	0.12437

CONCLUSION

Considering the importance of solid-state oxides in energy industry, especially for the development of advanced fuel cells, the investigation of methods to tune and control their electrical conductivity is essential. In this article, the correlation between electrical conductivity and structural order has been studied in a series of oxygen-deficient perovskites. Our findings indicate that, transition from disordered to ordered systems can be controlled by controlling the average ionic radius of the A-site cation. The conductivity at room temperature has an inverse correlation with ordering of oxygen vacancies. Furthermore, the least ordered compound exhibits metallic behavior, while the ordered materials are semiconductors. In addition, it appears that high temperature conductivity requires an intermediate level of vacancy-order. At high temperature, the highly ordered and highly disordered systems do not conduct as well as a material with an intermediate degree of ordering. Additionally, structural order leads to a semiconductor-to-metal transition at high temperature, which is absent in the disordered compound. Another effect of ordering is the mixed ionic-electronic conductivity manifested in hysteresis in

conductivity data during heating and cooling cycles. These findings indicate that electrical properties of oxygen-deficient perovskites can be tuned by modifying the structural order in these materials.

CHAPTER 4

MAGNETIC STRUCTURE OF CaSrFeCoO_5 : CORRELATION WITH STRUCTURAL ORDER³

INTRODUCTION

The study of magnetic properties and materials that exhibit various types of magnetism is motivated by scientific curiosity as well as the important applications of magnetic materials in various areas, such as spintronics and magnetic memories.⁶⁷⁻⁶⁹ Among magnetic systems, solid-state oxides are particularly fascinating due to the diversity of properties observed in this series of compounds. Oxygen acts as an effective bridge for magnetic coupling, leading to strong magnetic interactions in many transition-metal oxides. Perovskite-type systems, with general formula ABO_3 , are especially interesting, where A is usually an alkaline-earth metal or lanthanide and B is usually a transition metal. (Figure 4.1) The large A cations are located in spaces between corner-sharing BO_6 octahedra. It is possible to form perovskite materials with some degree of oxygen-deficiency. The vacant sites that are created as a result of oxygen-deficiency can spread in the structure arbitrarily,

³ The work described in this chapter was published in Material Research Bulletin (2018, vol. 106, p. 131-136)

forming a disordered system.^{11, 70} An example is $\text{Sr}_2\text{FeMnO}_5$,¹¹ where oxide vacancies are distributed randomly, forming a disordered cubic structure.¹¹

However, it is also possible to form oxygen-deficient perovskites, in which vacancies have an ordered distribution. The ordering of vacant sites can lead to the formation of new structure-types derived from the perovskite structure. An example is $\text{Ba}_2\text{In}_2\text{O}_5$,⁷¹ in which the vacancies lead to the formation of tetrahedral coordination geometry in alternating layers. The layers, where the tetrahedral geometry appears, contain chains of corner-sharing tetrahedra, that run parallel to the octahedral layers, as shown in Figure 4.1. This arrangement, which is derived from the perovskite system, is called brownmillerite-type structure.^{12, 72-75} The magnetic properties of oxygen-deficient perovskites have a strong correlation with the arrangement of vacant sites and the structure of materials. If the material composition contains magnetic cations, the magnetic order usually occurs when structural order is present.⁷² The lack of structural order usually leads to the absence of magnetic order.⁷² However, there are exceptions, such as $\text{Sr}_2\text{Fe}_{1.5}\text{Cr}_{0.5}\text{O}_5$,⁷⁶ where the vacancies are spread randomly in the structure, forming a disordered system, but the magnetic order is still present, and a long-range antiferromagnetic order is observed.⁷⁶

In this article, we describe the magnetic structure of CaSrFeCoO_5 ,⁷⁷ determined using neutron diffraction experiments. The magnetic order has been discussed in the context of materials with similar compositions, to highlight the magnetic properties that are unique to this compound.

EXPERIMENTAL

CaSrFeCoO_5 was synthesized using CaCO_3 , SrCO_3 , Fe_2O_3 , and Co_3O_4 as starting materials. The powders of the precursors were ground, thoroughly mixed, and then pelletized. The pellets were heated at 1000°C in air for 24 hours, followed by regrinding and refiring at 1200°C and 1250°C , for 24 hours each. The same synthesis procedure was also used to synthesize the Ca_2 analogue, $\text{Ca}_2\text{FeCoO}_5$ using CaCO_3 , Fe_2O_3 , and Co_3O_4 . Similarly, the Sr_2 analogue was also synthesized under the same conditions.

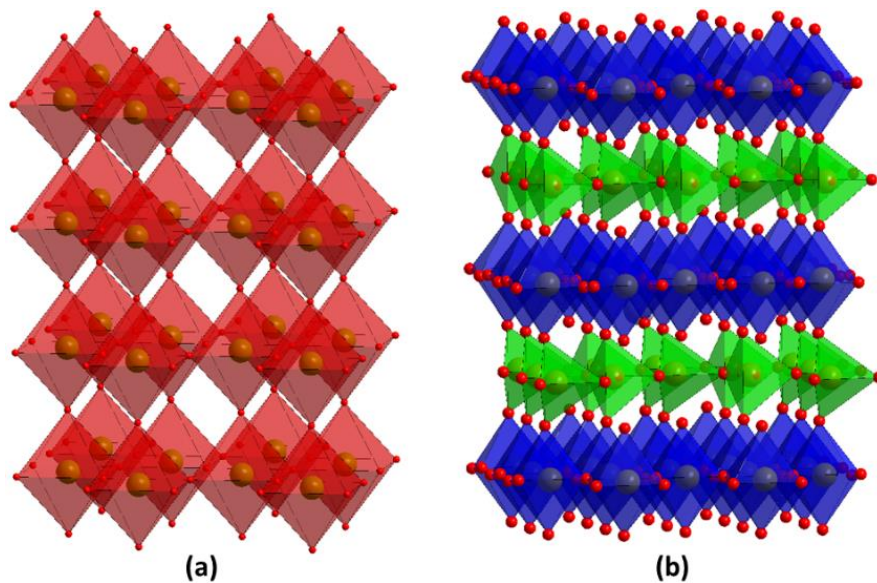


Figure 4.1. Comparison between (a) perovskite and (b) brownmillerite structure. In brownmillerite, the oxygen vacancies are ordered. The difference in transition metal coordination geometry is highlighted. The A-site cations that reside in spaces between polyhedra have been omitted for clarity.

Neutron diffraction experiments at 10 K and 300 K were performed on POWGEN diffractometer at Oak Ridge National Laboratory. The center wavelength of neutrons in

these experiments was 1.333 Å, and the d-spacing range was 0.4142 – 6.1363 Å. Rietveld refinements were performed using GSAS program⁴⁰ and EXPEGUI interface.⁴¹ Magnetic susceptibility data were obtained in the temperature range 2 K – 400 K, using the magnetic field of 0.1 T.

RESULTS AND DISCUSSION

To determine the magnetic structure of CaSrFeCoO₅, neutron diffraction experiments were performed at 10 K. The neutron data showed strong magnetic peaks at $d = 4.42$ Å and 4.50 Å, corresponding to 021 and 120 reflections. The presence of these peaks indicates long-range magnetic order.

The crystal structure at 10 K also features structural order, where the vacant sites, created due to oxygen deficiency, are ordered. The space group is *Ibm2*, and unit cell parameters are $a = 5.5870(2)$ Å, $b = 15.1684(6)$ Å, $c = 5.4370(2)$ Å. This structure belongs to the brownmillerite family, (Figure 4.1) where chains of corner-sharing (Fe/Co)O₄ tetrahedra are sandwiched between layers of corner-sharing (Fe/Co)O₆ octahedra. The crystal structure at 10 K was confirmed by Rietveld refinements with neutron diffraction data as shown in Figure 4.2.

The magnetic structure is G-type antiferromagnetic, where the magnetic moment of each transition metal is aligned antiparallel to all nearest neighbors, as depicted in Figure 4.3. The magnetic and crystal structures are commensurate. In materials with brownmillerite-type structure, if the magnetic order occurs, the ratio of intensities of the main magnetic peaks is indicative of the direction of the magnetic moments.^{72, 74} When the (120)/(021) peak ratio is close to 1, the magnetic moments are aligned along the longest unit cell axis.

However, if that ratio is close to 3, the magnetic moments are oriented along the shortest axis.

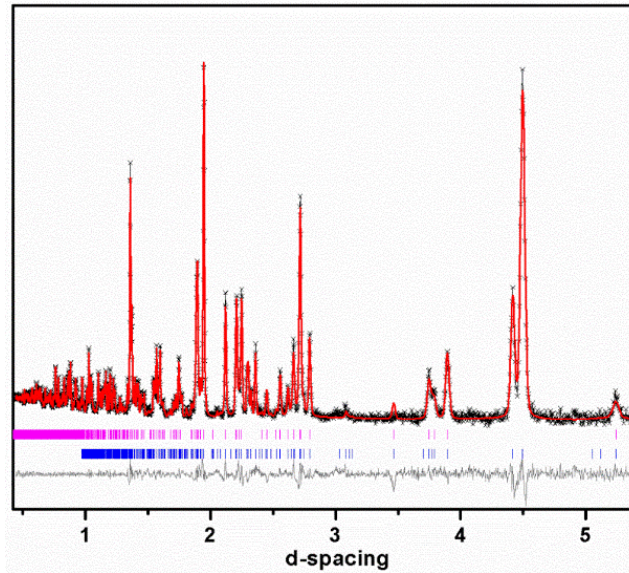


Figure 4.2. Neutron diffraction refinement profile at 10 K for CaSrFeCoO_5 . The crosses are experimental data, the red line is the model and the lower grey line represents the difference plot. The upper and lower vertical tick marks locate the crystal and magnetic structure peak positions.

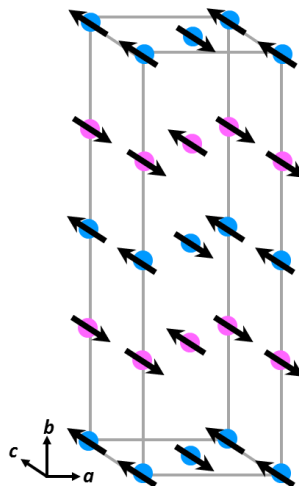


Figure 4.3. G-type antiferromagnetic order in CaSrFeCoO_5

As demonstrated in Figure 4.4, Gaussian fits indicate that the (120)/(021) peaks ratio for CaSrFeCoO_5 is ~ 2.96 , indicating that the magnetic moments should be along the shortest unit cell axis. We then confirmed the orientation of the moments by a series of Rietveld refinements. Initially, we compared three models, by orienting the magnetic moments along the three unit-cell axes and determining their fit to the data. Figure 4.5 shows three different situations where magnetic structure models with moments along the shortest, intermediate and longest unit cell axes were used. As observed here, the model featuring magnetic moments along the longest axis does not match the data, as it requires the two major magnetic peaks, 021 and 120, to have almost the same intensity. The model where magnetic moments are oriented along the intermediate axis is also ruled out, as it requires the magnetic peaks ratio to be $(120)/(021) \approx \frac{1}{3}$. (Figure 4.5) However, the model with magnetic moments along the shortest axis, which requires a 3/1 ratio for (120)/(021) intensities, leads to an excellent fit, as shown in Figure 4.5. The magnetic moments magnitude was also refined giving $3.6(2) \mu_B$ at 10 K. There is a sharp contrast between the magnetic structure of CaSrFeCoO_5 and that of the Ca-analogue, $\text{Ca}_2\text{FeCoO}_5$, which has a magnetic structure with moments oriented along the longest axis at 10 K.⁷⁴ The stark difference between the magnetic structures of the CaSr and Ca_2 compounds is remarkable. The presence of Sr on the A-site appears to direct the magnetic moments along the shortest axis. In addition, the G-type antiferromagnetic order in CaSrFeCoO_5 is retained up to room temperature, as demonstrated by neutron diffraction experiments at 300 K, shown in Figure 4.6. The magnetic structure and orientation of magnetic moments remain unchanged compared to those at 10 K. However, as expected, the magnetic moment magnitude at 300 K, $3.2(1) \mu_B$, is smaller than that at 10 K, $3.6(2) \mu_B$.

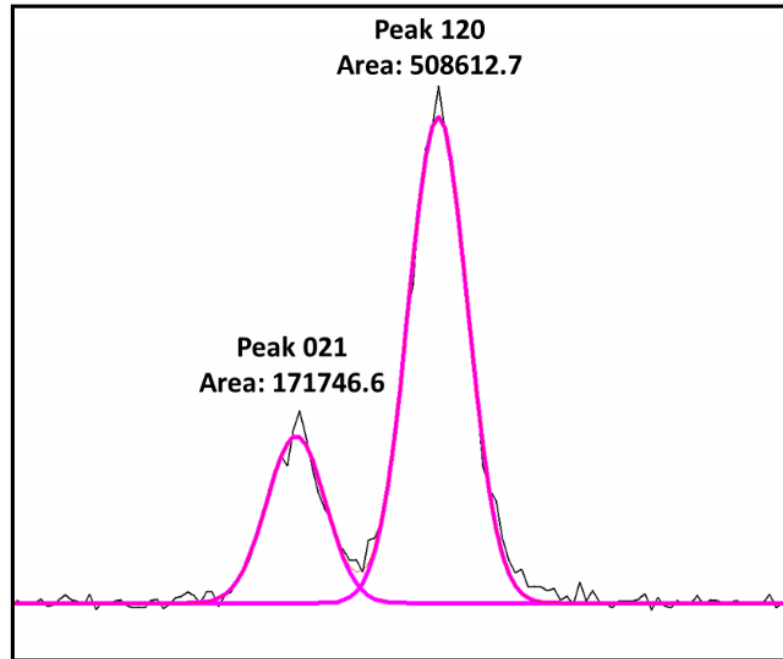


Figure 4.4. Gaussian fit for (021) and (120) magnetic peaks, indicating (120)/(021) ratio of ~2.96.

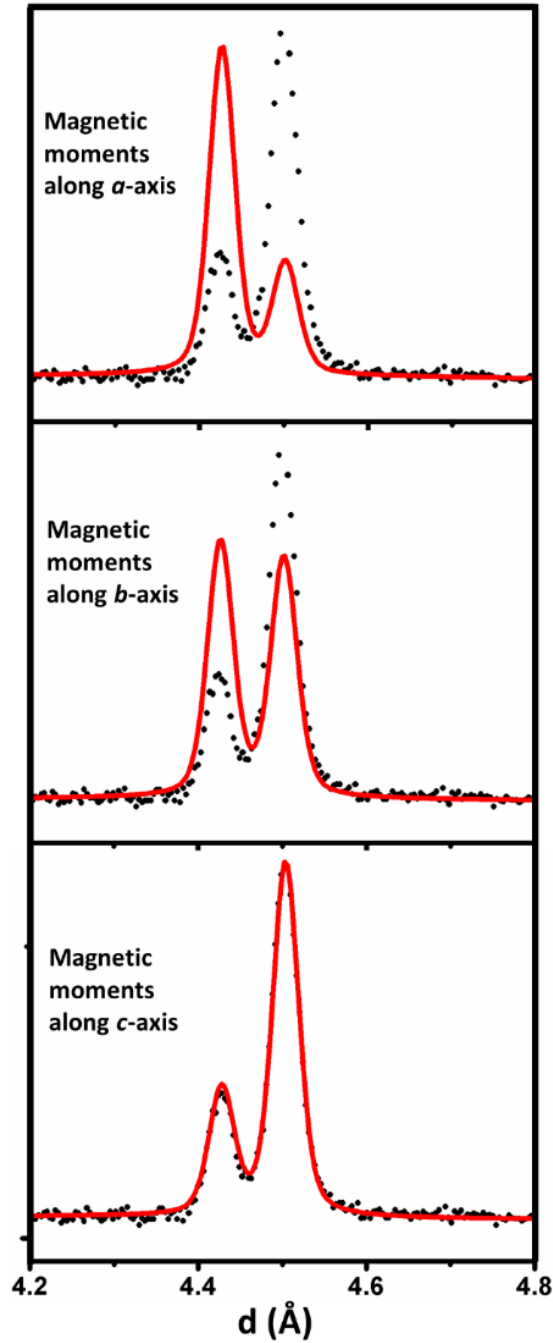


Figure 4.5. Fits for (021) and (120) magnetic peaks in neutron diffraction data using three different models with magnetic moments along a (intermediate), b (longest), or c (shortest) axis. As shown here, the model with moments along the c -axis leads to an excellent fit.

The neutron diffraction data at both 10 K and 300 K highlight the role of Sr in directing the magnetic moments in a particular orientation, i.e. along the shortest unit cell axis, regardless of the temperature. This demonstrates another significant difference compared to the Ca_2 analogue. In $\text{Ca}_2\text{FeCoO}_5$, the direction of magnetic moments changes as temperature increases.⁷⁴ The moments in the Ca_2 compound are oriented along the longest unit axis at 10 K, and along the shortest axis at 300 K.⁷⁴

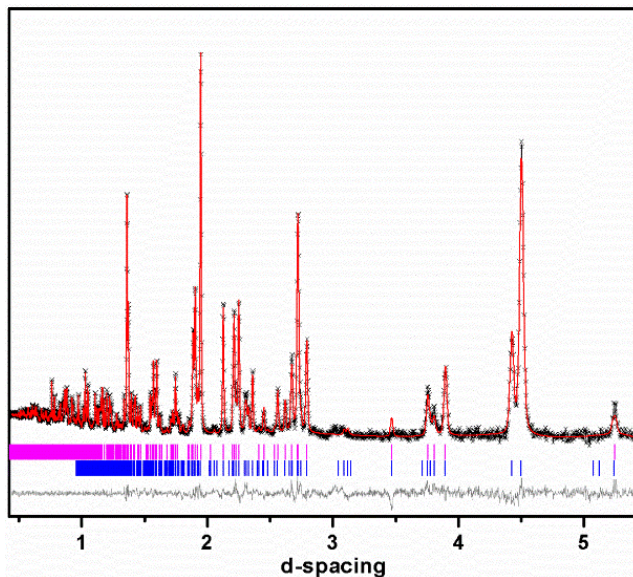


Figure 4.6. Neutron diffraction refinement profile at 300 K for CaSrFeCoO_5 . The crosses are experimental data, the red line is the model and the lower grey line represents the difference plot. The upper and lower vertical tick marks locate the crystal and magnetic structure peak positions.

A comparison to the Mn analogue⁷² further highlights the interesting magnetic properties of CaSrFeCoO_5 . If a composition containing Mn instead of Co is synthesized under the same conditions, i.e., 1250 °C in air, a disordered structure is formed that lacks magnetic order.⁷² This material undergoes a transition to a spin-glass state below ~30 K, and does

not have any long-range magnetic order.⁷² This observation indicates that the presence of cobalt in the material composition encourages the G-type magnetic order along the shortest unit-cell axis in CaSrFeCoO_5 . However, the presence of cobalt is not the only factor governing the formation of this magnetic structure. An optimum A-site cation combination is also required, as evident from comparison to the Ca_2 analogue.⁷⁴ Therefore, CaSrFeCoO_5 appears to be an optimum composition for this type of magnetic order to occur.

The magnetic susceptibility data were also obtained in the temperature range 2 K – 400 K, as demonstrated in Figure 4.7. $\text{Ca}_2\text{FeCoO}_5$ shows a divergence between zero-field-cooled (ZFC) and field-cooled (FC) data below ~ 220 K, as observed in Figure 4.7a. This temperature is where the re-orientation of magnetic moments in the Ca_2 compound is completed, as described previously.⁷⁴

For CaSrFeCoO_5 , there is divergence between the zero-field-cooled and field-cooled data below ~ 100 K, and the magnetic susceptibility trend for ZFC becomes opposite to that of FC data below 100 K, down to 50 K (Figure 4.7b). Below 50 K, the upward magnetic susceptibility trend is the same for both ZFC and FC data, but the separation between them persists. Both features at 50 K and 100 K are only observed in the ZFC data and corresponded to short-range domains. The material has long-range magnetic order at 10 K and 300 K, as observed in neutron diffraction data.

To our knowledge the magnetic properties of the Sr_2 analogue,⁷⁸ synthesized under the same condition as the CaSr-compound, i.e., 1250 °C in air, has not been studied previously. We synthesized the Sr_2 analogue, which has a cubic disordered structure⁷⁸ and obtained magnetic

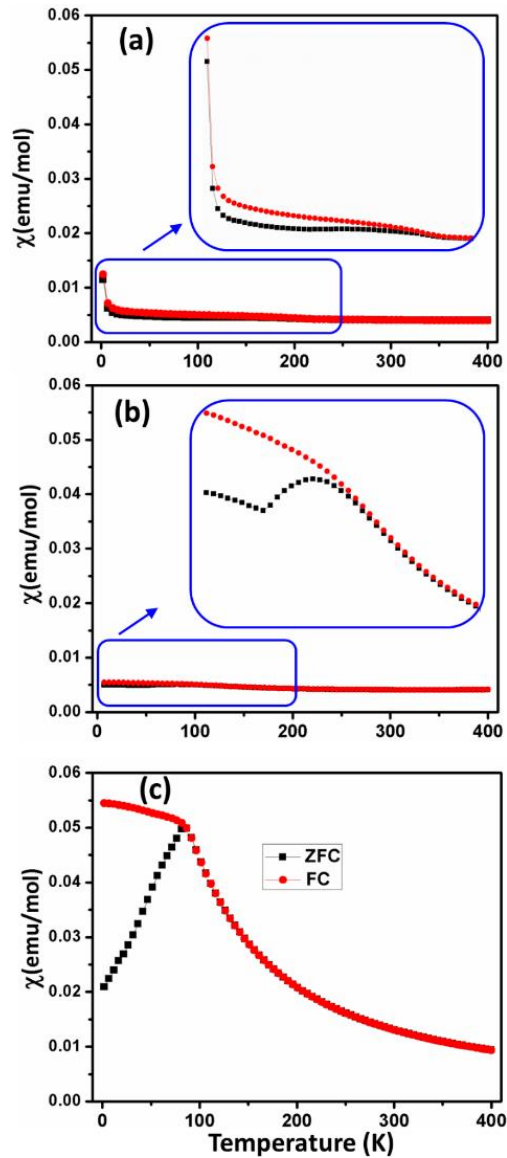


Figure 4.7. Magnetic susceptibility data for CaSrFeCoO_5 , as well as its Ca_2 and Sr_2 analogues. Images in a, b and c show the Ca_2 , CaSr and Sr_2 compounds, respectively. Black squares show zero-field-cooled and red circles represent field-cooled data.

susceptibility data for this material as well. In the zero-field-cooled data, the magnetic susceptibility increases as the temperature decreases down to ~ 80 K, where a sudden downturn in susceptibility begins. The field-cooled data shows a different trend, where the slope of the susceptibility data changes drastically below 87 K, but the upturn trend

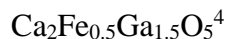
continue. This feature, demonstrated in Figure 4.7c, has been previously observed for some other oxygen-deficient perovskites.^{11, 72} This is usually indicative of spin-glass magnetic behavior, where the disorder in magnetic moments is quenched. This observation further confirms the important effect of the A-site cation on magnetic properties, where changing Ca₂ to CaSr and Sr₂, leads to significant changes in magnetism of these material.

CONCLUSION

The magnetic structure of CaSrFeCoO₅ consists of antiferromagnetically ordered moments that are oriented antiparallel to their nearest neighbors, as determined by neutron diffraction at 10 K and 300 K. This ordering arrangement is the so-called G-type antiferromagnetic structure. The magnetic moment orientation is along the shortest unit cell axis. The G-type antiferromagnetic order persists up to room temperature and the orientation of magnetic moments also remains unchanged. Comparisons have been made between CaSrFeCoO₅ and materials with similar compositions, where CaSr is replaced by Ca₂ and Sr₂, or Co is replaced by Mn. These analogue materials show significantly different magnetic properties, from spin-glass to ordered moments that reorient if heated to room temperature. These observations indicate that CaSrFeCoO₅ is an optimum composition for this G-type antiferromagnetic order, where the arrangement and orientation of magnetic moments remain unchanged up to room temperature.

CHAPTER 5

ELECTRICAL PROPERTIES OF ORDERED OXYGEN-DEFICIENT PEROVSKITE



INTRODUCTION

Many oxygen-deficient perovskite oxides exhibit mixed ionic-electronic conductivity.²³ Mixed conducting materials are important in different areas, such as gas sensing devices,⁷⁹ electrodes for solid-oxide fuel cells⁸⁰, and electrocatalysts.⁸¹

Oxygen deficient perovskites have general formula $\text{ABO}_{3-\delta}$, where δ represents the oxygen deficiency. The B-site cations usually form BO_6 , BO_5 , or BO_4 polyhedra depending on the structure, while the A-site cations reside in spaces between the polyhedra. The crystal structure can vary depending on different parameters including the magnitude of δ . For example, a series of structures have been observed for $\text{SrMnO}_{3-\delta}$ ⁸² and $\text{Sr}_2\text{Fe}_2\text{O}_{3-\delta}$ ⁸³ due to the variation of oxygen stoichiometry. The crystal structure of oxygen-deficient perovskites also depends on the arrangement of defects that are generated due to oxygen-deficiency.^{4, 84-87} The defects can be distributed in a disordered^{76, 88-89} or ordered fashion.⁴

⁴ The work described in this chapter was published in IONICS (2019, vol. 25, p. 1315-1321)

^{12, 73-75, 84-87, 90} One of the common structures, resulting from the ordering of defects, is brownmillerite-type structure.^{4, 12, 73-75, 84-87, 90} In brownmillerite materials, the ordering of defects results in tetrahedral coordination geometry in alternating layers. As shown in Figure 5.1, the BO_4 tetrahedra and BO_6 octahedra alternate in the crystal lattice. The tetrahedra form chains that run parallel to the octahedral layers. The orientation of tetrahedral chains with respect to each other can be different, leading to different space groups in brownmillerite compounds.

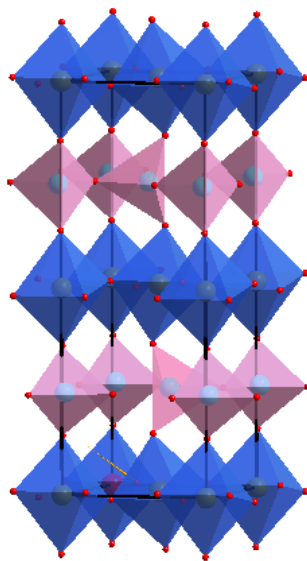


Figure 5.1. Brownmillerite structure of $\text{Ca}_2\text{Fe}_{0.5}\text{Ga}_{1.5}\text{O}_5$

Changes in the A or B-site cations in oxygen-deficient perovskites, $\text{ABO}_{3-\delta}$, can change the crystal structure. One example is the significant difference between $\text{Sr}_2\text{Fe}_2\text{O}_5$, which has a brownmillerite-type structure, and $\text{Ba}_2\text{Fe}_2\text{O}_5$, that features a complex structure containing tetrahedral, square-pyramidal and octahedral geometry.⁸⁶ The change in the crystal structure leads to significant differences in electrical properties of $\text{Sr}_2\text{Fe}_2\text{O}_5$ and $\text{Ba}_2\text{Fe}_2\text{O}_5$.⁸⁶ Another example is the phase transitions in $\text{La}_{1-x}\text{Sr}_x\text{FeO}_{3-\delta}$ as a result of Sr-substitution on the A-site, leading to variation in physical properties.⁹¹ The effect of the B-

site cation is demonstrated by phase transitions in $\text{SrFe}_{1-x}\text{Nb}_x\text{O}_{3-\delta}$ ($x = 0.05, 0.1, 0.2, 0.3,$ and 0.4) where an $I4/mmm$ tetragonal structure transforms into a cubic structure with $Pm-3m$ space group.⁹² The same study also reported a structural transition between cubic and orthorhombic due to the variation of the B-site cation.⁹²

Most oxygen-deficient perovskites contain transition metals on the B-site. However, main group metals, particularly those from group 13, can also be incorporated into these compounds, and occupy some of the B-sites.⁹³⁻⁹⁵ Nevertheless, in most cases, the majority of cations on the B-site are still transition metal cations.⁹³⁻⁹⁵ Brownmillerite materials, where the transition metals are eliminated from the structure, are interesting because they can exhibit predominantly ionic conductivity. Thus, they can be used in applications such as fuel cell electrolytes, where ionic conductivity is needed, but electronic conductivity is undesirable. One prominent example of a brownmillerite compound, which possesses only main group elements on the B-site, is the In-containing material $\text{Ba}_2\text{In}_2\text{O}_5$ ⁷¹ and its doped analogues.⁹⁶⁻⁹⁷ This material can be synthesized by solid-state method at high temperature.⁷¹ However, the situation is different for Ga-only brownmillerite compounds, which seem to require high pressure to form.⁹⁸ For example, $\text{Ca}_2\text{Ga}_2\text{O}_5$ has been made under 2.5 GPa of pressure.⁹⁸ In addition, $\text{Sr}_2\text{Ga}_2\text{O}_5$ has been synthesized under 1.5 GPa of pressure, but this material does not form a brownmillerite structure.⁹⁹

There is one report on the crystal structure of $\text{Ca}_2\text{Fe}_{0.5}\text{Ga}_{1.5}\text{O}_5$, synthesized using standard solid-state synthesis method.⁹⁸ However, that study only reports the crystal structure using X-ray diffraction, and no other information regarding properties of $\text{Ca}_2\text{Fe}_{0.5}\text{Ga}_{1.5}\text{O}_5$ has been reported. In the current study, we have shown that $\text{Ca}_2\text{Fe}_{0.5}\text{Ga}_{1.5}\text{O}_5$ represents the maximum level of Ga-doping in $\text{Ca}_2\text{Fe}_2\text{O}_5$ system, which can be achieved by solid-state

synthesis method. We have examined the possibility of magnetic order in $\text{Ca}_2\text{Fe}_{0.5}\text{Ga}_{1.5}\text{O}_5$ using neutron diffraction and bulk magnetometry, and have also studied electrical properties of this compound in a wide temperature range, 25 – 800 °C.

MATERIALS AND METHODS

Solid-state synthesis method was employed to prepare $\text{Ca}_2\text{Fe}_{0.5}\text{Ga}_{1.5}\text{O}_5$. The powders of the precursors CaCO_3 (Alfa Aesar, 99.95%), Fe_2O_3 (Alfa Aesar, 99.998%), and Ga_2O_3 (Sigma Aldrich, 99.99%) were mixed, pressed into a pellet, and heated at 1000 °C for 24 h in air. The samples were then reground and refired at 1200 °C for 24 h in air, followed by slow cooling. The heating and cooling rates were 100 °C/h. Synthesis of compositions containing higher Ga-content was also attempted. However, single phase products could only be obtained at the maximum Ga-concentration of 1.5 per formula unit. Iodometric titrations were performed under argon atmosphere, as described previously.⁸⁶

High resolution field-emission scanning electron microscopy (SEM) was used to study the micro-structure. X-ray photoelectron spectroscopy (XPS) was carried out at room temperature using Al $K\alpha$ radiation (1486.7 eV). The electrical properties were investigated by direct-current (DC) and alternating-current (AC) on pellets that had been sintered at 1200 °C. The AC electrochemical impedance spectroscopy measurements were performed in the frequency range of 0.1 Hz to 1 MHz using a computer-controlled frequency response analyzer. The DC measurements were done by applying a constant voltage of 10 mV and collecting the output current. Variable-temperature electrical conductivity measurements were carried out during both heating and cooling cycles with 10 °C intervals. At each measurement temperature, enough time was given for conductivity equilibrium to be achieved before moving to the next temperature. Bulk magnetization data were obtained

on a vibrating-sample magnetometer using a quartz sample holder in the temperature range 2 K – 400 K. Powder X-ray diffraction measurements were done at room temperature using Cu K α 1 radiation ($\lambda = 1.54056 \text{ \AA}$). Neutron diffraction experiments were performed on POWGEN diffractometer at Oak Ridge National Laboratory, with center wavelength of 0.7 \AA . Rietveld refinements were done using GSAS software¹⁰⁰ and EXPEGUI interface.¹⁰¹

RESULTS AND DISCUSSION

Crystal structure

As discussed in the experimental section, $\text{Ca}_2\text{Fe}_{0.5}\text{Ga}_{1.5}\text{O}_5$ represents the highest degree of Ga-doping in the brownmillerite compound, $\text{Ca}_2\text{Fe}_2\text{O}_5$, which can be achieved by solid-state synthesis method. Higher degree of Ga-doping is only possible if the synthesis is done in high pressure, 2.5 GPa.⁹⁸ The only report on $\text{Ca}_2\text{Fe}_{0.5}\text{Ga}_{1.5}\text{O}_5$ describes X-ray diffraction data of this material, indicating *Pcmn* space group.¹⁰² Here, we study the structure using a combination of neutron and X-ray diffraction. The common space groups for brownmillerite compounds are *Imma*, *Ima2*, *Pnma* (*Pcmn*) and *Pbcm*.^{4, 74-75, 84, 87}

The *Pbcm* space group is recognized by the presence of superstructure peaks, given that materials crystalizing in this space group have unit cells that are double the size of those for typical brownmillerites.^{4, 74-75, 84, 87} These superstructure peaks do not appear in the diffraction data for $\text{Ca}_2\text{Fe}_{0.5}\text{Ga}_{1.5}\text{O}_5$, ruling out the *Pbcm* space group. The *Pnma* space group is identified by the presence of the 131 peak, which is absent in I-centered space groups.^{4, 74-75, 84, 87} The powder X-ray and neutron diffraction data for $\text{Ca}_2\text{Fe}_{0.5}\text{Ga}_{1.5}\text{O}_5$ show the 131 peak, indicative of space group *Pnma*. This was then confirmed by Rietveld refinements. Table 5.1 lists the refined structural parameters, and Figure 5.2 shows the X-ray and neutron refinement profiles. In these refinements, initially Fe and Ga were mixed

on both octahedral and tetrahedral sites. Refining the site-occupancies on these sites indicates that Fe is exclusively located on the octahedral site, while Ga occupies all of the tetrahedral sites and half of the octahedral positions.

Table 5.1 The refined structural parameters for $\text{Ca}_2\text{Fe}_{0.5}\text{Ga}_{1.5}\text{O}_5$ from neutron diffraction. Space group: $Pnma$, $a = 5.3669(2)$, $b = 14.6214(5)$, $c = 5.5927(2)$, $R_p = 0.0744$, $wR_p = 0.0479$

Elements	x	y	z	Multiplicity	Occupancy	U_{iso}
Ca	0.0076(6)	0.1075(1)	0.5281(3)	8	1	0.0013(2)
Ga1	0.0463(4)	0.25	0.0700(4)	4	1	0.0025(3)
Ga2	0.0	0.0	0.0	4	0.5	0.0004(2)
Fe	0.0	0.0	0.0	4	0.5	0.0004(2)
O1	0.3991(7)	0.25	0.1279(6)	4	1	0.0052(4)
O2	0.0193(5)	0.6412(2)	0.0710(4)	8	1	0.0063(3)
O3	0.2513(6)	0.0140(1)	0.2489(7)	8	1	0.0020(2)

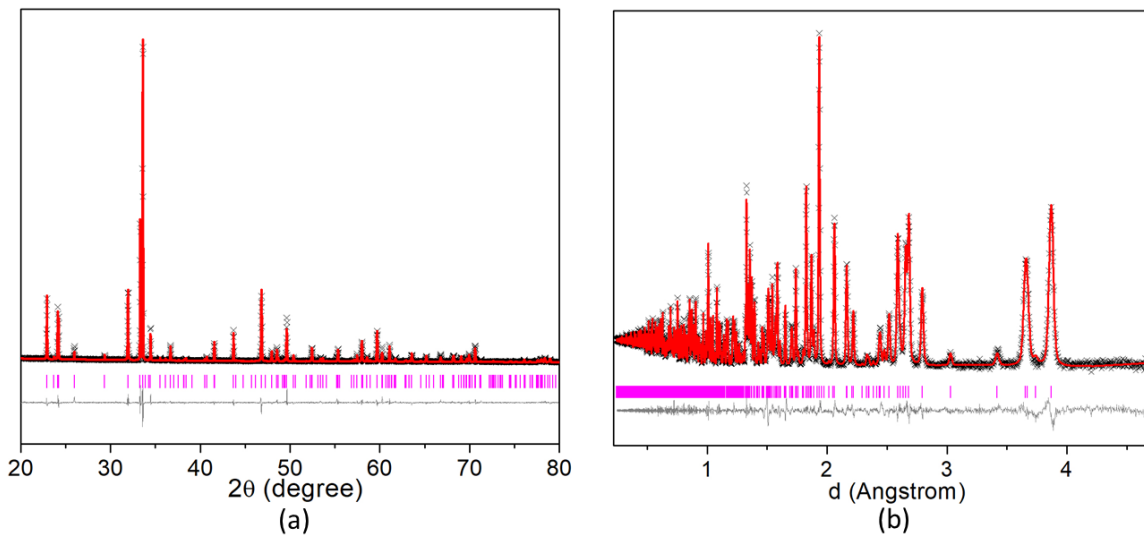


Figure 5.2 Refinement profiles for $\text{Ca}_2\text{Fe}_{0.5}\text{Ga}_{1.5}\text{O}_5$ using (a) X-ray and (b) neutron diffraction

Scanning electron microscopy data show high sinterability and good contact between crystallites of $\text{Ca}_2\text{Fe}_{0.5}\text{Ga}_{1.5}\text{O}_5$, as shown in Figure 5.3. Oxidation state of Fe was investigated by X-ray photoelectron spectroscopy (XPS). The $2\text{P}_{3/2}$ peaks for trivalent and tetravalent Fe are expected to appear at $\sim 710\text{-}711\text{ eV}$ ¹⁰³⁻¹⁰⁴ and $\sim 712\text{-}713\text{ eV}$,^{44, 105} respectively. In addition, a satellite peak appearing at about 7-9 eV higher than the $2\text{P}_{3/2}$ peak is the signature of trivalent Fe.¹⁰³⁻¹⁰⁴ The XPS data for $\text{Ca}_2\text{Fe}_{0.5}\text{Ga}_{1.5}\text{O}_5$ (Figure 5.4) show the $2\text{P}_{3/2}$ peak for Fe at $\sim 710\text{ eV}$ followed by a satellite peak at $\sim 718\text{ eV}$, confirming that Fe is primarily in trivalent state. There is also a slight shoulder on the right side of the Fe $2\text{P}_{2/3}$ peak, which indicates the presence of a small amount of tetravalent Fe. These findings were then confirmed by iodometric titrations, which showed the accurate oxygen stoichiometry to be 5.07 moles per formula unit, i.e., $\text{Ca}_2\text{Fe}_{0.5}\text{Ga}_{1.5}\text{O}_{5.07}$. These results confirm the XPS findings that the oxidation state of Fe is primarily 3+, along with a small amount of tetravalent Fe.

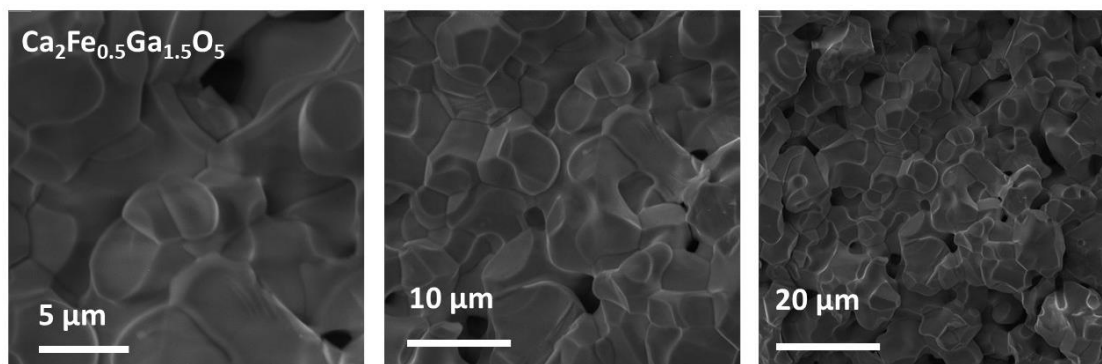


Figure 5.3 SEM images of $\text{Ca}_2\text{Fe}_{0.5}\text{Ga}_{1.5}\text{O}_5$, showing good contact between the crystallites

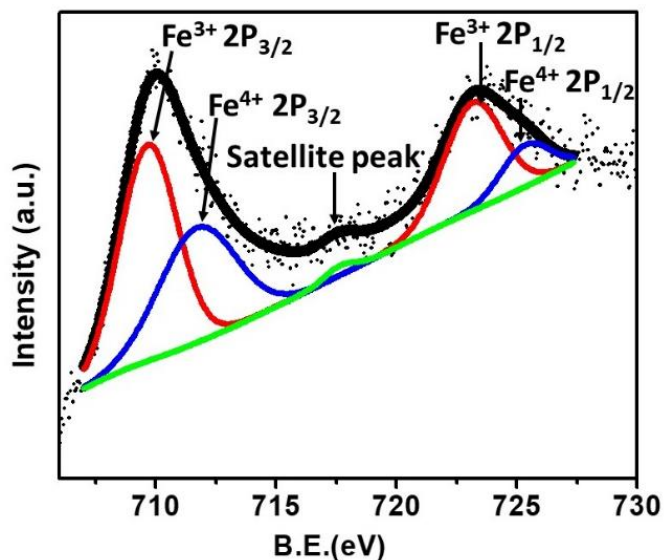


Figure 5.4 X-ray photoelectron spectroscopy data for $\text{Ca}_2\text{Fe}_{0.5}\text{Ga}_{1.5}\text{O}_5$

Electrical properties

The electrical properties of $\text{Ca}_2\text{Fe}_{0.5}\text{Ga}_{1.5}\text{O}_5$ were studied by alternating current (AC) and direct current (DC) methods. In DC method, the output current (I) is measured while applying a constant voltage. This current is then converted into resistance using Ohm's law. In AC impedance spectroscopy, the resistance is determined from the intercept of the data with the real axis (Z') of the Nyquist plot at low frequency. The resistance values (R) are then used to calculate the conductivity (σ) using the following equation:

$$\sigma = L/RA \quad (13)$$

where L and A represent the thickness and cross-sectional area of the sample, respectively.

The electrical conductivity was also obtained at variable temperatures from 25 to 800 °C (Figure 5.5). In brownmillerite compounds, the electronic conductivity is achieved due to the presence of cations that have multiple stable oxidation states such as $\text{Fe}^{2+}/\text{Fe}^{3+}/\text{Fe}^{4+}$.

Variable oxidation states can also be created due to oxygen loss, i.e., partial reduction of

cations,¹⁰⁶ or oxygen absorption, leading to partial oxidation.^{50, 107} These processes result in the formation of small polarons.⁵⁰ The electrons hop through $M^{m+}-O-M^{n+}$ conduction pathways, which are created due the presence

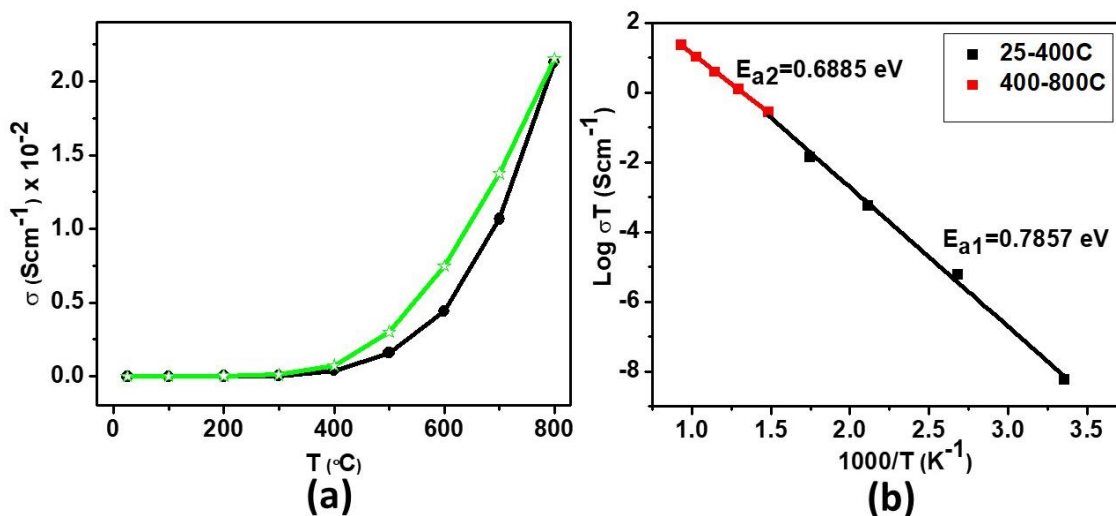


Figure 5.5 (a) Electrical conductivity of $\text{Ca}_2\text{Fe}_{0.5}\text{Ga}_{1.5}\text{O}_5$ as a function of temperature. (b) Arrhenius plot and activation energies for $\text{Ca}_2\text{Fe}_{0.5}\text{Ga}_{1.5}\text{O}_5$

variable oxidation states.¹⁰⁸⁻¹⁰⁹ However, many brownmillerite materials are mixed-conductors, where the total conductivity includes contribution from both electron and oxide-ion conductivity. The latter can become dominant when the transition metals are eliminated from the material composition.⁷¹

In $\text{Ca}_2\text{Fe}_{0.5}\text{Ga}_{1.5}\text{O}_5$, contributions from both ionic and electronic conductivity are expected, considering the oxygen-vacancies and the presence of variable oxidation states of Fe in the material composition. The conductivity of $\text{Ca}_2\text{Fe}_{0.5}\text{Ga}_{1.5}\text{O}_5$, can be compared to a predominantly ionic conductor, $\text{Ba}_2\text{In}_2\text{O}_5$, which shows electrical conductivity values, that are less than $\sim 10^{-3} \text{ Scm}^{-1}$ at 700 $^{\circ}\text{C}$.⁷¹ Whereas the conductivity of $\text{Ca}_2\text{Fe}_{0.5}\text{Ga}_{1.5}\text{O}_5$ at the same temperature is more than one order of magnitude higher, $\sim 10^{-2} \text{ Scm}^{-1}$. The higher

conductivity of $\text{Ca}_2\text{Fe}_{0.5}\text{Ga}_{1.5}\text{O}_5$ may be attributed to the contribution of the electronic conductivity in addition to the ionic conductivity.

In oxide materials, the bulk, grain-boundary and electrode-interface resistance can be determined using AC impedance spectroscopy. The observation of semicircles in the Nyquist plot of impedance spectroscopy indicates significant contribution from ionic conductivity, as described by other researchers.¹¹⁰ The fit to the impedance data for $\text{Ca}_2\text{Fe}_{0.5}\text{Ga}_{1.5}\text{O}_5$ at 200 °C is shown in Figure 5.6. Three resistance-capacitance (RC) units were used for this fit, where the RC unit at highest frequency (left) corresponds to the bulk resistance. The semicircle in the middle shows the grain-boundary resistance and the semicircle at the lowest frequency (right) represents the electrode interface resistance.

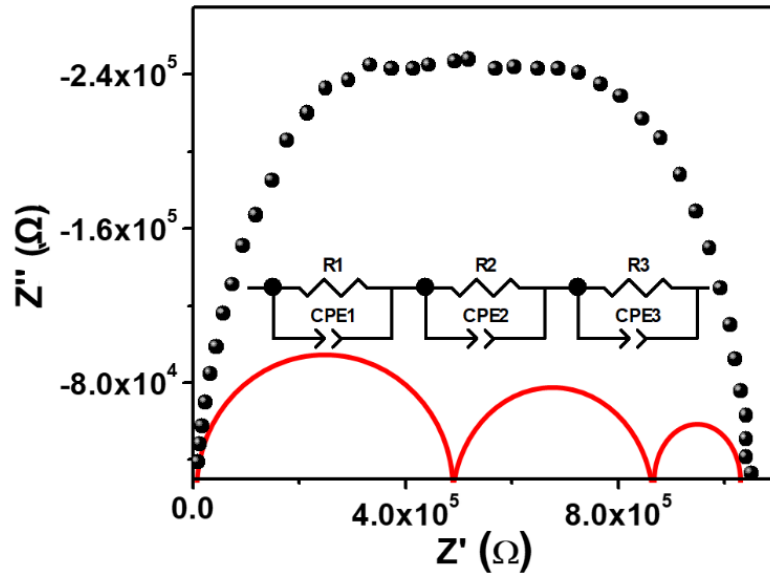


Figure 5.6 AC impedance data for $\text{Ca}_2\text{Fe}_{0.5}\text{Ga}_{1.5}\text{O}_5$ at 200 °C. Three resistance-capacitance units indicate the bulk (left), grain boundary (middle) and electrode interface (right) resistance.

In some oxide materials, an increase in conductivity as a function of temperature is observed. This behavior is seen in $\text{Ca}_2\text{Fe}_{0.5}\text{Ga}_{1.5}\text{O}_5$. The temperature-dependent increase in electrical conductivity is expected, due to an increase in the mobility of charge carriers,⁹ according to the following relation:

$$\sigma = ne\mu \quad (14)$$

where σ , n , e , and μ are the conductivity, concentration of charge carriers, charge of electron, and mobility of the charge carriers, respectively. In addition, the loss of oxygen at higher temperature, as shown by thermogravimetric analysis (Figure 5.7), can enhance the ionic conductivity, due to the increase in concentration of defects. It is known that oxide ion conductivity is enhanced above 500 °C.¹¹¹⁻¹¹² Figure 5.6 shows a sharp increase in conductivity of $\text{Ca}_2\text{Fe}_{0.5}\text{Ga}_{1.5}\text{O}_5$ above 500 °C.

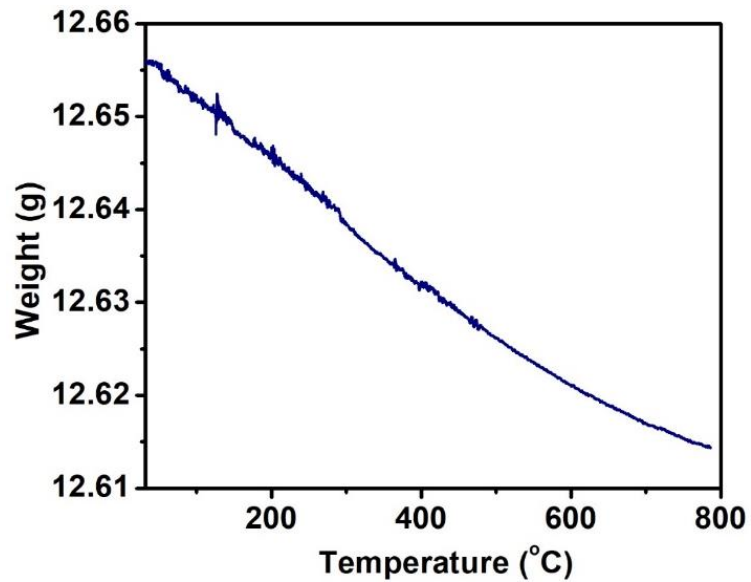


Figure 5.7 Thermogravimetric analysis for $\text{Ca}_2\text{Fe}_{0.5}\text{Ga}_{1.5}\text{O}_5$

We performed the variable-temperature conductivity measurements during both heating and cooling cycles. As noted in the experimental section, at each measurement temperature, enough time was given (~40 minutes) for the conductivity to plateau, i.e., equilibrate, before moving to the next temperature. An interesting observation is the presence of small hysteresis, where the conductivity values obtained during cooling have higher values than those obtained during heating. This behavior has been observed in some other materials before.¹¹³⁻¹¹⁴ Several researchers have reported such hysteresis,¹¹³⁻¹¹⁴ which have been attributed to oxygen-desorption,¹¹³ or defect-mediate ion mobility.¹¹⁴ In $\text{Ca}_2\text{Fe}_{0.5}\text{Ga}_{1.5}\text{O}_5$, the hysteresis is very small, but it indicates the effect of oxide ion conductivity. As shown by TGA (Figure 5.7) this material loses oxygen as temperature increases. The loss of oxygen can lead to enhanced ionic mobility, resulting in a small increase in total conductivity. The re-absorption of the lost oxygen upon cooling is a very slow process compared to the electronic transport phenomena. As a result, the enhanced ionic conductivity is retained after cooling the material, leading to hysteresis. It is noted that the hysteresis is observed at 500 °C and higher, where the contribution of ionic conductivity is expected to be more significant.¹¹¹⁻¹¹²

We have also calculated the activation energies for the increase in electrical conductivity as a function of temperature. For thermally activated conductivity, activation energy can be calculated using the Arrhenius equation:⁴⁹⁻⁵¹

$$\sigma T = \sigma^0 e^{\frac{-E_a}{kT}} \quad (15)$$

where σ^0 is a preexponential factor and a characteristic of the material. E_a , K , and T are the activation energy for the electrical conductivity, Boltzmann constant, and absolute temperature, respectively. The activation energy (E_a) is calculated from the slope of the

line of best fit in the $\log \sigma T$ versus $1000/T$ plot. The Arrhenius plot and activation energies for $\text{Ca}_2\text{Fe}_{0.5}\text{Ga}_{1.5}\text{O}_5$ are presented in Figure 5.6, showing values close to those typically observed in this class of compounds.

CONCLUSIONS

$\text{Ca}_2\text{Fe}_{0.5}\text{Ga}_{1.5}\text{O}_5$ represents the highest degree of Ga-doping in the brownmillerite compound, $\text{Ca}_2\text{Fe}_2\text{O}_5$, which can be reached through solid-state synthesis method. The non-magnetic Ga^{3+} cation leads to the absence of long range magnetic order at temperatures where the parent material shows antiferromagnetic order. The bulk magnetization studies indicate that this material exhibits paramagnetic behavior above 250 K, and short-range magnetic interactions below this temperature. The electrical conductivity of $\text{Ca}_2\text{Fe}_{0.5}\text{Ga}_{1.5}\text{O}_5$ indicates semiconducting behavior, and mixed ionic-electronic conductivity. The properties of $\text{Ca}_2\text{Fe}_{0.5}\text{Ga}_{1.5}\text{O}_5$ are consistent with results from XPS and iodometric titrations, which indicate that Fe is primarily in trivalent state, accompanied by a small amount of tetravalent Fe.

CHAPTER 6

ENHANCED ELECTRICAL PROPERTIES IN $\text{BaSrFe}_2\text{O}_{6-\delta}$ ($\delta=0.5$): A DISORDERED DEFECT- PEROVSKITE ⁵

1. INTRODUCTION

Oxygen deficient perovskites have emerged as an interesting class of functional materials for application in areas such as oxygen separation membranes¹¹⁵⁻¹¹⁶, electrodes in solid oxide fuel cells¹¹⁷, and promoters in Lithium sulfur batteries.¹¹⁸ Oxygen-deficient perovskites have general formula $\text{ABO}_{3-\delta}$ or $\text{A}_2\text{B}_2\text{O}_{6-\delta}$ where A is an alkaline-earth or rare-earth metal and B is usually a transition metal with octahedral coordination. Here, δ represents the degree of oxygen-deficiency, which results in the formation of defects in the crystal structure. These vacant sites can be distributed in a random or ordered manner in the structure.^{72, 84} The defects convert the octahedral BO_6 units into other types of polyhedra, such as square pyramids¹¹⁹⁻¹²⁰ or tetrahedra.⁸⁹ The type of structure in this class of materials depends on several factors, including the concentration of defects, i.e., δ value, as well as the nature of the A- and B-site cations. For example, $\text{Sr}_2\text{Mn}_2\text{O}_{6-\delta}$ can have different space

⁵ The work described in this chapter was published in *Inorganic Chemistry* (2019, vol. 167, p. 69-74)

groups depending on the amount of oxygen-deficiency.¹²¹ Similarly, $\text{Sr}_2\text{Fe}_2\text{O}_{6-\delta}$ shows a series of structures as a function of variation in δ .⁸³

Not surprisingly, the nature of the B-site cation also affects the structure and properties.^{75,}

⁸⁸ For example, both $\text{Ca}_2\text{Mn}_2\text{O}_5$ ¹¹⁹ and $\text{Ca}_2\text{Cr}_2\text{O}_5$ ¹²² have defect-ordered structures, but the type of ordering in these two compounds is different. $\text{Ca}_2\text{Mn}_2\text{O}_5$ contains only one type of B-site coordination, namely square pyramidal MnO_5 units.¹¹⁹ However, $\text{Ca}_2\text{Cr}_2\text{O}_5$ contains alternating layers of CrO_4 tetrahedra and CrO_6 octahedra,¹²² forming the so-called brownmillerite-type structure. These structural differences result in very different magnetic¹²²⁻¹²³ and electrical properties.^{110, 124} In some cases, even small variation, ~5%, of the B-site cation can cause significant changes to the distribution of defects in the structure, as observed for $\text{Sr}_2\text{Fe}_{1.9}\text{Cr}_{0.1}\text{O}_{6-\delta}$ ¹² as compared to its parent compound $\text{Sr}_2\text{Fe}_2\text{O}_{6-\delta}$.⁴

Similar situation applies to the role of A-site cation.^{85, 90} For example, partial substitution of Ca in $\text{Ca}_2\text{FeCoO}_{6-\delta}$ results in $\text{CaSrFeCoO}_{6-\delta}$, which has a different space group, leading to different magnetic and electrical properties.⁸⁴ Note that in this case, the substitution on the A-site leads to the change in the space group, but the overall structural framework in both compounds is the same. Both materials have defect-ordered brownmillerite-type structure.

In this article, we demonstrate drastic changes in the distribution of defects as a result of increase in the average ionic radius of the A-site cations. We report $\text{BaSrFe}_2\text{O}_{6-\delta}$ ($\delta=0.5$) which has a disordered cubic structure, whereas the Ca-analogue, $\text{CaSrFe}_2\text{O}_{6-\delta}$ ($\delta=1$),⁴ is known to be a defect-ordered material with orthorhombic structure. The remarkably higher

electrical conductivity of $\text{BaSrFe}_2\text{O}_{6-\delta}$ ($\delta=0.5$) and the transformation of magnetic properties have been demonstrated.

2. EXPERIMENTAL

Both compounds $\text{CaSrFe}_2\text{O}_{6-\delta}$ ($\delta=1$) and $\text{BaSrFe}_2\text{O}_{6-\delta}$ ($\delta=0.5$) were synthesized under identical conditions by solid state method. The powders of the precursor compounds CaCO_3 (Alfa Aesar, 99.95%), SrCO_3 (Alfa Aesar, 99.95%), BaCO_3 (Alfa Aesar, 99.95%), and Fe_2O_3 (Alfa Aesar, 99.998%) were mixed in stoichiometric proportions and ground together using agate mortar and pestle. The powder was then pressed into a pellet and heated for 24 h at 1000 °C in air. Subsequently, the samples were reground and refired at 1200 °C for 24 h in air. The heating and cooling rates were 100 °C/h. The phase purity and structure of the polycrystalline samples were determined by powder X-ray diffraction at room temperature using Cu $K\alpha_1$ radiation ($\lambda = 1.54056 \text{ \AA}$). Neutron diffraction experiments were performed on POWGEN diffractometer at Oak Ridge National Laboratory. The GSAS software⁴⁰ and EXPEGUI interface¹²⁵ were used for Rietveld refinements. In these refinements, the peak profile parameters, background, sample displacement, unit-cell parameters, atomic coordinates and thermal displacement factors were refined simultaneously. The neutron diffraction data were also used to refine the site occupancy of oxygen and show that it matched the observed results from XPS and iodometric titrations.

The microstructures were studied using high resolution field-emission scanning electron microscopy (SEM). The electrical properties were investigated by direct-current (dc) method on pellets that had been sintered at 1200 °C. Alternating current (ac) measurements of resistance were also performed. As expected from a material with predominantly

electronic conductivity, no semicircle was observed.¹²⁶⁻¹²⁷ The resistance obtained from the intercept with the real axis in the Nyquist plot was the same as that obtained from dc measurements. The 4-probe conductivity measurements were performed in the temperature-range from 25 to 800 °C. The sample was kept at each temperature until a plateau in conductivity was reached, before increasing the temperature. The rate of heating between different measurement temperatures was 3 °C/min. Iodometric titrations were performed by dissolving about 50 mg of sample and excess KI (~2 g) in 100 mL of 1M HCl. A total of 5 mL of the solution was then pipetted out, and iodine that had been generated in the solution was titrated against 0.025 M Na₂S₂O₃. Near the end point of the titration, 0.2mL of a starch solution was added to act as an indicator. All steps were performed under argon atmosphere. X-ray photoelectron spectroscopy (XPS) was done at room temperature using Al K α radiation (1486.7 eV) to study the oxidation states of Fe.

3. RESULT AND DISCUSSIONS

3.1. Crystal structure

The crystal structures are determined by powder X-ray and neutron diffraction. Also, the degree of oxygen-deficiency (δ) and the Fe oxidation states have been studied by iodometric titrations and X-ray photoelectron spectroscopy. A phase change is observed between CaSrFe₂O_{6- δ} ($\delta=1$) and BaSrFe₂O_{6- δ} ($\delta=0.5$), where the arrangement of defects changes from ordered to disordered. This transformation has significant consequences in terms of charge transport properties, as discussed in the next section. Note that both materials were synthesized under identical conditions. For BaSrFe₂O_{6- δ} ($\delta=0.5$) all

diffraction peaks can be indexed on cubic $Pm-3m$ space group, as confirmed by Rietveld refinements using X-ray and neutron diffraction data, shown in Figure 6.1.

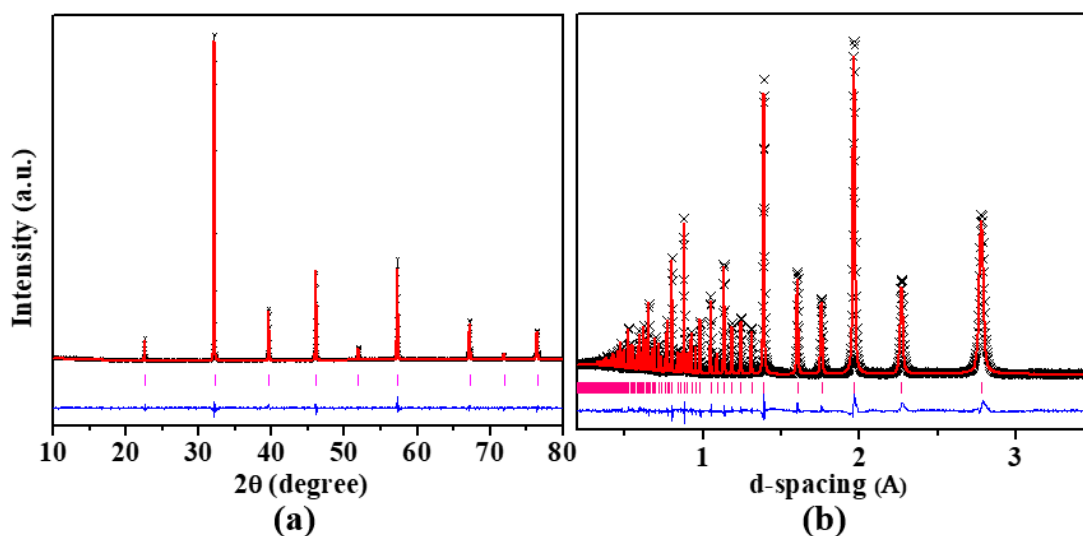


Figure 6.1. Rietveld refinement profiles for $\text{BaSrFe}_2\text{O}_{6-\delta}$ ($\delta=0.5$): (a) X-ray and (b) neutron diffraction data.

In this structure, the defects, created due to oxygen-deficiency, have a random distribution. As a result, the average structure looks similar to that of a typical perovskite^{70, 88} (Figure 6.2), but with partial occupancy on the oxygen positions (Table 6.1). This is in sharp contrast to the structure of $\text{CaSrFe}_2\text{O}_{6-\delta}$ ($\delta=1$),⁴ (Figure 6.2) which is known to contain an ordered array of defects, that appear in alternating layers, converting the octahedral geometry into tetrahedra in those layers. The outcome is a structure with alternating FeO_6 octahedra and FeO_4 tetrahedra,⁴ the so called brownmillerite-type structure.⁷²⁻⁷⁴ Clearly, the average ionic radius on the A-site of the oxygen-deficient perovskites $\text{A}_2\text{Fe}_2\text{O}_{6-\delta}$ is the

driving force behind the structural transformation from defect-ordered to disordered. The average A-site ionic radius for $\text{CaSrFe}_2\text{O}_{6-\delta}$ ($\delta=1$) is 1.39 Å,

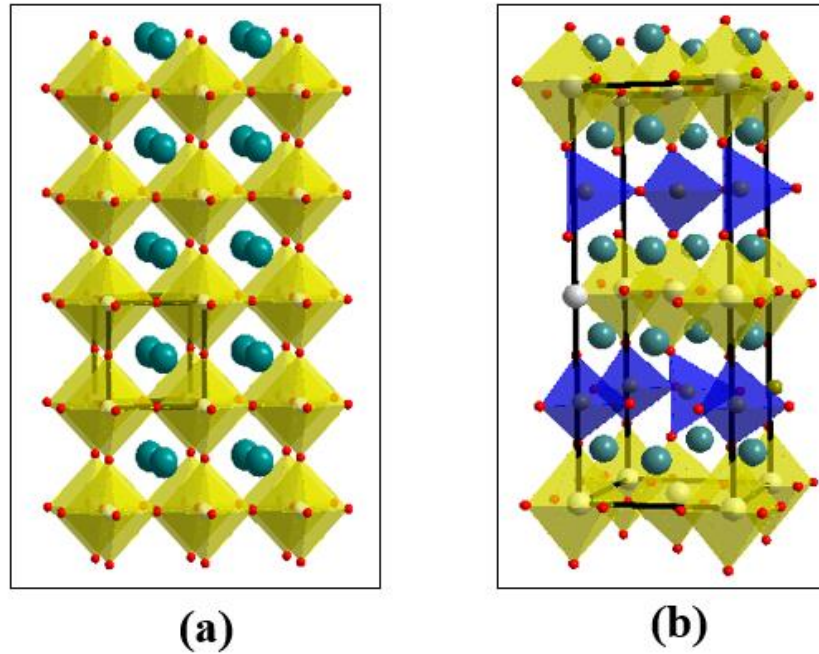


Figure 6.2. Crystal structures of (a) $\text{BaSrFe}_2\text{O}_{6-\delta}$ ($\delta=0.5$) and (b) $\text{CaSrFe}_2\text{O}_{6-\delta}$ ($\delta=1$).

Table 6.1. Refined structural parameters from neutron diffraction data for $\text{BaSrFe}_2\text{O}_{6-\delta}$ ($\delta=0.5$), space group $Pm-3m$, $a = 3.92851(4)$, $R_p = 0.041$, $wR_p = 0.033$

	x	y	z	Uiso	occupancy	multiplicity
Ba1	0	0	0	0.0056(7)	0.5	1
Sr1	0	0	0	0.0056(7)	0.5	1
Fe1	0.5	0.5	0.5	0.0072(6)	1.0	1
O1	0	0.5	0.5	0.0145(1)	0.902(3)	3

while for $\text{BaSrFe}_2\text{O}_{6-\delta}$ ($\delta=0.5$), it is 1.52 Å.¹²⁸ It is noted that the coordination environment of the A-site cation is different in the two materials. In $\text{CaSrFe}_2\text{O}_{6-\delta}$ ($\delta=1$), the $\text{Ca}^{2+}/\text{Sr}^{2+}$ ions are 8-coordinated, whereas $\text{BaSrFe}_2\text{O}_{6-\delta}$ ($\delta=0.5$) contains 12-coordinated $\text{Ba}^{2+}/\text{Sr}^{2+}$ cations.

Given the structural distortions in $\text{CaSrFe}_2\text{O}_{6-\delta}$ ($\delta=1$), which occur in order to accommodate the simultaneous corner-sharing between octahedra and tetrahedra, the Fe–O–Fe bond angles deviate significantly from 180° and can be as small as 146.2(2)°. However, the bond angles in $\text{BaSrFe}_2\text{O}_{6-\delta}$ ($\delta=0.5$) are 180°, as expected from a cubic structure. The Fe–O bond distances are also different, ranging from 1.842(4) Å to 2.150(4) Å for $\text{CaSrFe}_2\text{O}_{6-\delta}$ ($\delta=1$), and 1.964(2) Å for $\text{BaSrFe}_2\text{O}_{6-\delta}$ ($\delta=0.5$).

The morphology and crystallite sizes of both materials were studied using scanning electron microscopy (SEM). Figure 6.3 shows the SEM images of sintered pellets. There is a significant increase in grain size in transition from $\text{CaSrFe}_2\text{O}_{6-\delta}$ ($\delta=1$) to $\text{BaSrFe}_2\text{O}_{6-\delta}$ ($\delta=0.5$).

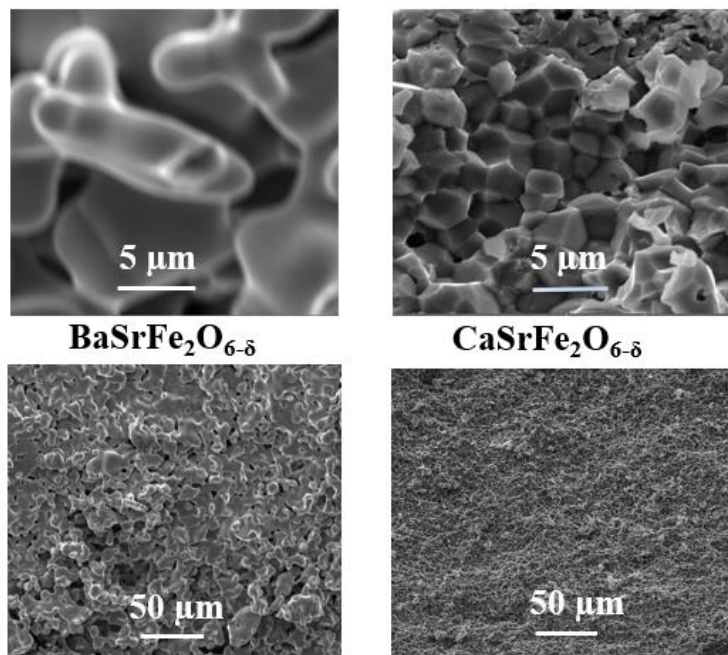


Figure 6.3. Scanning electron microscopy images of sintered pellets of (a) $\text{BaSrFe}_2\text{O}_{6-\delta}$ ($\delta=0.5$) and (b) $\text{CaSrFe}_2\text{O}_{6-\delta}$ ($\delta=1$).

The degree of oxygen-deficiency and oxidation state of Fe cations were also investigated using X-ray photoelectron spectroscopy (XPS) study and iodometric titrations. Note that Fe_2O_3 was used as starting material in the synthesis of both compounds, and the synthesis conditions were identical. If iron preserves its +3 oxidation state, the number of oxygens per formula unit in $\text{AA}'\text{Fe}_2\text{O}_{6-\delta}$ should be 5, resulting in $\delta = 1$. Oxidation state of Fe is determined based on the position of the $2\text{P}_{3/2}$ peak as well as the satellite peak associated with $2\text{P}_{3/2}$. As shown in the XPS data (Figure 6.4), the $2\text{P}_{3/2}$ peak appears at ~ 710 eV, followed by a satellite peak at ~ 718 eV, indicating the presence of Fe^{3+} in $\text{BaSrFe}_2\text{O}_{6-\delta}$ ($\delta=0.5$).^{44, 129-130} The shoulder on the high energy side of the $2\text{P}_{3/2}$ peak indicates that Fe^{4+} is also present in $\text{BaSrFe}_2\text{O}_{6-\delta}$ ($\delta=0.5$).¹³⁰ These results were also confirmed by iodometric titrations, which provided a quantitative understanding of the

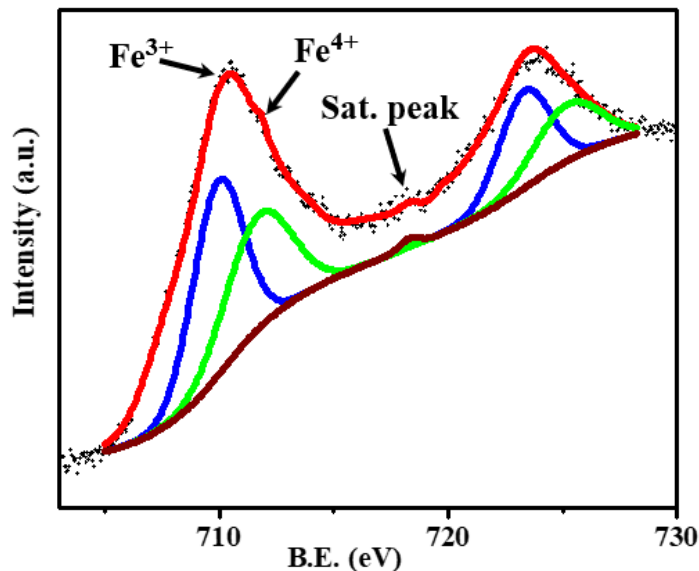


Figure 6.4. X-ray photoelectron spectroscopy data for $\text{BaSrFe}_2\text{O}_{6-\delta}$ ($\delta=0.5$).

concentration of oxygen-defects. Iodometric titration indicated that the oxygen stoichiometry in $\text{BaSrFe}_2\text{O}_{6-\delta}$ ($\delta=0.5$) is 5.5 per formula unit, corresponding to $\delta = 0.5$ and confirming the presence of both Fe^{3+} and Fe^{4+} . This is also consistent with the oxygen site-occupancy obtained from Rietveld refinement using neutron diffraction data (Table 6.1). Similar analyses, using XPS and iodometric titrations, have shown that $\text{CaSrFe}_2\text{O}_{6-\delta}$ ($\delta=1$) contains only Fe^{3+} , with 5 oxygens per formula unit, i.e., $\delta = 1$.⁴ It is interesting that the increase in ionic radius on the A-site facilitates the oxidation of Fe in $\text{BaSrFe}_2\text{O}_{6-\delta}$ ($\delta=0.5$), leading to greater oxygen-content and smaller concentration of defects compared to $\text{CaSrFe}_2\text{O}_{6-\delta}$ ($\delta=1$). These findings are consistent with the crystal structures determined using Rietveld refinements. The structure of $\text{BaSrFe}_2\text{O}_{6-\delta}$ ($\delta=0.5$) can accommodate a greater amount of oxygen on lattice sites, whereas, the brownmillerite-type framework of $\text{CaSrFe}_2\text{O}_{6-\delta}$ ($\delta=1$) can accommodate only up to 5 oxygens per formula unit, and any additional oxygen would need to be located on interstitial sites. Therefore, the structural

differences between the two compounds lead to more facile oxidation of Fe in one material compared to the other.

3.2. Magnetic properties

The change in the distribution of defects and the subsequent changes in the crystal structure have a major impact on the magnetic properties. $\text{CaSrFe}_2\text{O}_{6-\delta}$ ($\delta=1$) is known to feature antiferromagnetic order.⁴ Previous studies using neutron diffraction at 10 K have shown an antiferromagnetic system where the magnetic moment on each Fe site is oriented opposite to all of its nearest neighbors.⁴ We therefore, performed neutron diffraction on $\text{BaSrFe}_2\text{O}_{6-\delta}$ ($\delta=0.5$) at 10 K to be able to make direct comparison between the two materials. In addition, the bulk magnetization data for $\text{BaSrFe}_2\text{O}_{6-\delta}$ ($\delta=0.5$) show a transition at ~ 50 K. Thus, the neutron experiments at 10 K can shed light on the magnetic state below the transition temperature for $\text{BaSrFe}_2\text{O}_{6-\delta}$ ($\delta=0.5$). Given the large magnetic moments associated with Fe atoms, any long-range magnetic order can be readily identified. However, neutron diffraction experiments (Figure 6.1) show no magnetic peaks for $\text{BaSrFe}_2\text{O}_{6-\delta}$ ($\delta=0.5$), indicating the absence of long-range magnetic order, in sharp contrast to the situation in $\text{CaSrFe}_2\text{O}_{6-\delta}$ ($\delta=1$).⁴

As stated above, the bulk magnetization data (Figure 6.5) for $\text{BaSrFe}_2\text{O}_{6-\delta}$ ($\delta=0.5$) feature a transition at ~ 50 K, where the zero-field-cooled and field-cooled data diverge. This type of transition has been observed in other oxygen-deficient perovskites before and has been attributed to transition into a spin-glass state.^{12, 72} The inverse susceptibility plot versus temperature indicates that the Currie-Weiss behavior does not occur below ~ 300 K. The linear paramagnetic trend is observed above this temperature. The fit to this linear region results in the Currie constant of 6.64(4) and Weiss constant of -254(4). The negative value

of the Weiss constant indicates that short-range antiferromagnetic interactions are present. The isothermal magnetization data for $\text{BaSrFe}_2\text{O}_{6-\delta}$ ($\delta=0.5$) at 5 K show small hysteresis implying the presence of a small uncompensated moment. The isothermal data at 300 K is linear without any hysteresis, as expected from a typical

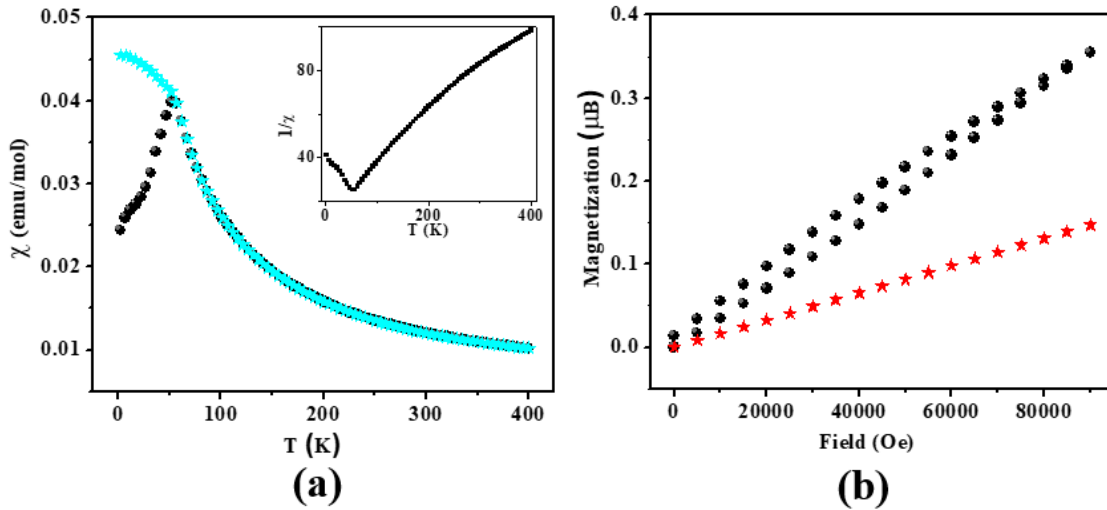


Figure 6.5. Bulk magnetization data of $\text{BaSrFe}_2\text{O}_{6-\delta}$ ($\delta=0.5$) (a) ZFCFC magnetic susceptibility data. The inset shows inverse of susceptibility versus temperature. (b) Isothermal magnetization data at 5 K and 400 K.

paramagnetic system. This is consistent with the observation from inverse susceptibility plot, which shows paramagnetic behavior above 300 K.

Overall, the transformation of magnetic properties as a result of changes in the distribution of defects is remarkable. The transition from defect-order in $\text{CaSrFe}_2\text{O}_{6-\delta}$ ($\delta=1$) to disorder in $\text{BaSrFe}_2\text{O}_{6-\delta}$ ($\delta=0.5$) results in the change from antiferromagnetic order to spin-glass magnetic state.

3.3. Electrical properties

The resistance values (R) obtained from 4-probe measurements were used to calculate the conductivity (σ) using the following equation:

$$\sigma = L/RA \quad (16)$$

where L represents the distance between the voltage probes and A indicates the cross-sectional area of the pellet through which the current is applied. The electrical conductivity was obtained at variable temperatures from 25 to 800 °C. As shown in Figure 6.6, the conductivity of BaSrFe₂O_{6- δ} ($\delta=0.5$) is considerably higher than that of CaSrFe₂O_{6- δ} ($\delta=1$) in the entire temperature range. Therefore, the increase in the average ionic radius of the A-site, and the subsequent transformation of the crystal structure, lead to a significant increase in the electrical conductivity.

Oxygen-deficient perovskites can show mixed electronic and oxide-ion conductivity.^{29, 131-133} In situations where the B-site cations have more than one stable oxidation state, such as Fe³⁺/Fe⁴⁺, the electronic conductivity is usually dominant in ambient condition.¹³⁴ The electron transport occurs through hopping of electrons through Metal-Oxygen-Metal bond system.¹⁰⁸⁻¹⁰⁹ The degree of electrical conductivity in oxygen deficient perovskites depends on a number of factors. Conductivity is higher for shorter M–O bond lengths and for larger M^{m+}–O–Mⁿ⁺ bond angles.¹³⁵ As mentioned in the previous section, the simultaneous corner-sharing between tetrahedra and octahedra leads to distortions in the structure of CaSrFe₂O_{6- δ} ($\delta=1$), which results in a range of Fe–O bond distances, from 1.842(4) Å to 2.150(4) Å. Due to these distortions, the average bond distance in CaSrFe₂O_{6- δ} ($\delta=1$) is similar to that of BaSrFe₂O_{6- δ} ($\delta=0.5$), which has a cubic structure, and Fe–O = 1.964(2) Å. More importantly, the bond angles in CaSrFe₂O_{6- δ} ($\delta=1$) are significantly deviated from

linearity and can be as small as 146° . Whereas, the bond angles in $\text{BaSrFe}_2\text{O}_{6-\delta}$ ($\delta=0.5$) are 180° , which facilitate the electronic conductivity through $\text{M}^{n+}-\text{O}-\text{M}^{n+}$ pathways. In addition, as demonstrated by XPS and iodometric titration, nearly all of the Fe atoms in $\text{CaSrFe}_2\text{O}_{6-\delta}$ ($\delta=1$) are in trivalent state, whereas in $\text{BaSrFe}_2\text{O}_{6-\delta}$ ($\delta=0.5$) both trivalent and tetravalent Fe cations are present. As a result, there is a significant number of $\text{Fe}^{3+}-\text{O}-\text{Fe}^{4+}$ conduction pathways in $\text{BaSrFe}_2\text{O}_{6-\delta}$ ($\delta=0.5$), leading to the enhanced conductivity.

To study the behavior of these materials in a wide temperature-range, the electrical conductivity was examined from 25 to 800 °C. For both compounds, the conductivity initially increases with temperature, indicating semiconducting behavior. Multiple studies have shown p-type semiconductivity in oxygen-deficient perovskites,^{24, 136-137} due to the dependence on oxygen partial pressure,^{58-59, 138} and the formation of holes as charge carriers.^{9, 23, 58-59}

As shown in Figure 6.6, the increase in conductivity of $\text{BaSrFe}_2\text{O}_{6-\delta}$ ($\delta=0.5$) is significantly greater than that of $\text{CaSrFe}_2\text{O}_{6-\delta}$ ($\delta=1$). At 400 °C the difference between the conductivity of the two materials is more than one order of magnitude. The rise in conductivity continues up to 400 °C, where an inflection point is observed for both materials. Above this temperature, the conductivity

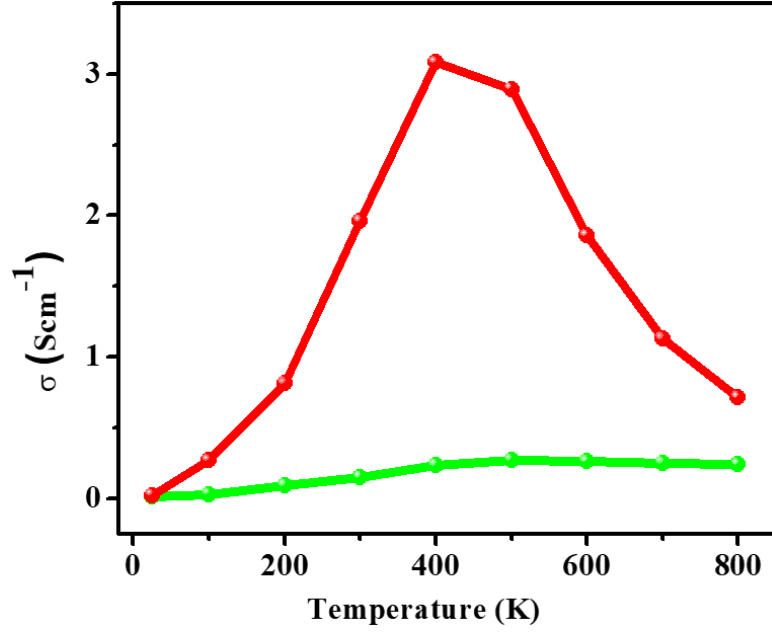
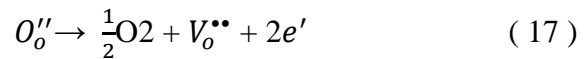


Figure 6.6. Electrical conductivity as a function of temperature for BaSrFe₂O_{6-δ} (δ=0.5) (red) and CaSrFe₂O_{6-δ} (δ=1) (green).

of CaSrFe₂O_{6-δ} (δ=1) nearly plateaus. The change is more drastic for BaSrFe₂O_{6-δ} (δ=0.5), where a sharp decrease in conductivity occurs above 400 °C. The drastic change in conductivity seems to correlate with the degree of oxygen loss, as demonstrated by the thermogravimetric analysis (TGA) data in Figure 6.7. Above 400 °C, there is a sudden decline in the TGA data, indicating the onset of significant oxygen loss, as has been observed before.^{106, 139-140} This can result in a decrease in the concentration of Fe³⁺-O-Fe⁴⁺ conduction pathways, leading to a decrease in conductivity.^{134, 141-142}

The mechanism of oxygen vacancy creation can be expressed by following equations, using Kroger-Vink notation.^{134, 139-140, 143}



Where O_o'' , $V_o^{\bullet\bullet}$ and e' represent lattice oxygen, vacancy and electron respectively.

The change in conductivity as a function of temperature can be described using the Arrhenius equation for thermally activated conductivity:⁴⁹⁻⁵¹

$$\sigma T = \sigma^0 e^{\frac{-E_a}{KT}} \quad (19)$$

where σ^0 is a pre-exponential factor and a characteristic of the material. E_a , K , and T are the activation energy for the electrical conductivity, Boltzmann constant, and absolute temperature, respectively.

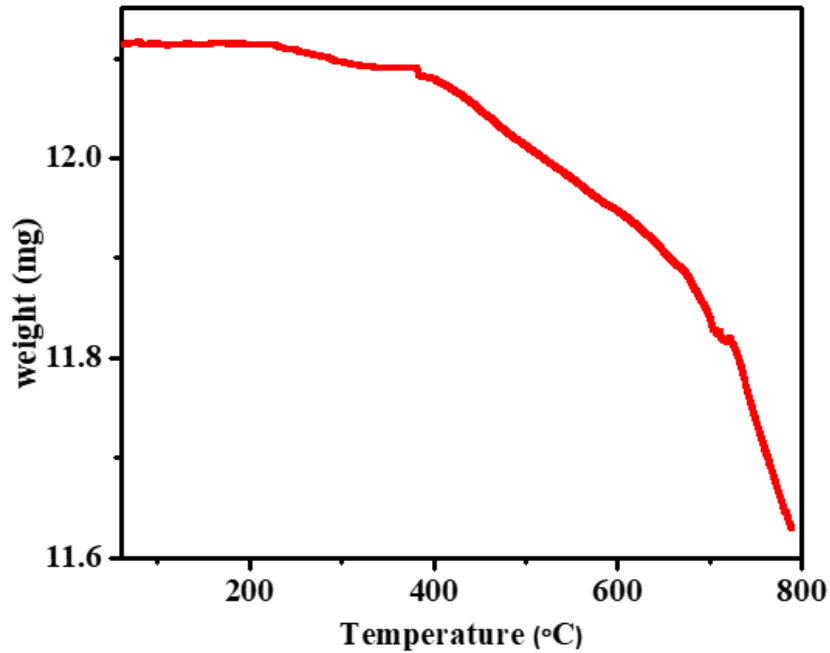


Figure 6.7. Thermogravimetric analysis data for $\text{BaSrFe}_2\text{O}_{6-\delta}$ ($\delta=0.5$).

Table 6.2. Electrical conductivity, σ (S cm^{-1}), and activation energies, E_a (eV), for increase in electrical conductivity up to 400 °C.

	25 °C	400 °C	800 °C	E_a (eV)
$\text{BaSrFe}_2\text{O}_{6-\delta}$ ($\delta=0.5$)	2.22×10^{-2}	3.08	7.13×10^{-1}	0.241
$\text{CaSrFe}_2\text{O}_{6-\delta}$ ($\delta=1$)	1.27×10^{-2}	2.3×10^{-1}	2.4×10^{-1}	0.174

The activation energy (E_a) for the change in conductivity as a function of temperature can be determined from the slope of the line of best fit in the $\log \sigma T$ versus $1000/T$ plot,⁴⁹⁻⁵¹ as shown in Figure 6.8. The activation energies for the increase in conductivity between 25 to 400 °C are 0.174 eV and 0.241 eV, for $\text{CaSrFe}_2\text{O}_{6-\delta}$ ($\delta=1$) and $\text{BaSrFe}_2\text{O}_{6-\delta}$ ($\delta=0.5$), respectively.

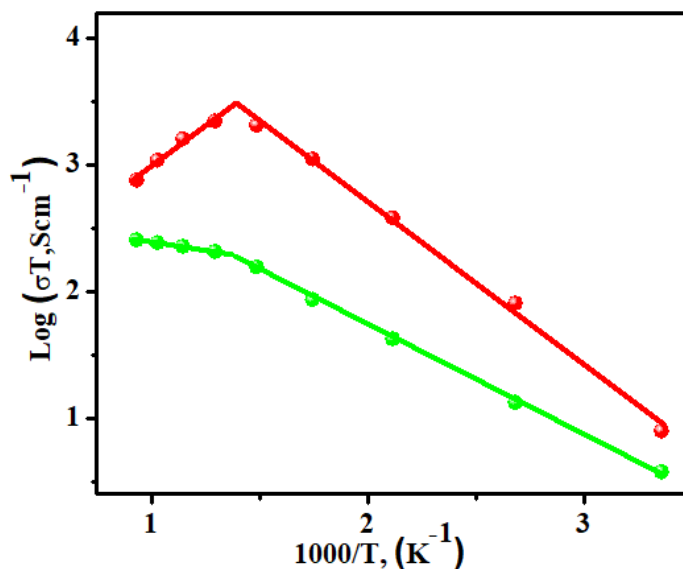


Figure 6.8. Arrhenius plot of the electrical conductivity for $\text{BaSrFe}_2\text{O}_{6-\delta}$ ($\delta=0.5$) (red) and $\text{CaSrFe}_2\text{O}_{6-\delta}$ ($\delta=1$) (green).

CONCLUSIONS

The increase in the average ionic radius of the A-site in $\text{A}_2\text{Fe}_2\text{O}_{6-\delta}$ leads to structural transformation between $\text{CaSrFe}_2\text{O}_{6-\delta}$ ($\delta=1$) and $\text{BaSrFe}_2\text{O}_{6-\delta}$ ($\delta=0.5$). The latter features disordered distribution of defect sites, that are created due to oxygen deficiency, whereas the former is known to contain defect-order. The change in the structure results in the

variation of magnetic properties, where one material is antiferromagnetically ordered, while the other shows spin-glass behavior. The structural changes also lead to the transformation of electrical properties, where the electrical conductivity of $\text{BaSrFe}_2\text{O}_{6-\delta}$ ($\delta=0.5$) is over one order of magnitude greater than that of $\text{CaSrFe}_2\text{O}_{6-\delta}$ ($\delta=1$). These results demonstrate that in oxygen-deficient perovskites, the change in the defect arrangement can be used as an effective tool to manipulate the electrical properties.

CHAPTER 7

CHARGE-TRANSPORT PROPERTIES OF $\text{Ca}_2\text{FeGaO}_{6-\delta}$ and $\text{CaSrFeGaO}_{6-\delta}$: THE EFFECT OF DEFECT-ORDERED⁶

1. INTRODUCTION

Oxygen-deficient perovskites have been studied for their various properties, such as mixed ion and electronic conductivity,²³ which is essential to the operation of solid oxide fuel cells.¹¹⁷ These materials have also been extensively studied as oxygen transport membranes, given that oxide ion diffusion through an ion conductive material produces nearly pure oxygen.¹⁴⁴ Usually, the ion transport in perovskite oxides takes place at high temperature,¹⁴⁵ but some oxygen-deficient perovskites such as SrFeO_{3-x} or SrCoO_{3-x} exhibit oxygen mobility at room temperature.^{132, 146} Given the attractive properties of this class of compounds, it is important to explore the parameters that control those properties. The structure-property relationships are particularly important.

The general formula of oxygen-deficient perovskites is $\text{ABO}_{3-\delta}$. Here, A is usually a lanthanide or alkaline-earth metal and B is a transition metal. A-site or B-site cations can have more than one type of element. In such cases, the general formula can be written as

⁶ The work described in this chapter was published in *Material Chemistry and Physics* (2019, vol. 238, p. 121924)

AA'BB'O_{6-δ}. The degree of oxygen-deficiency can affect the structural order.¹² For example, SrMnO_{3-δ} shows a four-layered (4L) hexagonal structure for $0 \leq \delta \leq 0.12$.¹⁴⁷ This structure transforms into a cubic perovskite structure if the degree of oxygen-deficiency changes to $0.25 \leq \delta \leq 0.38$.^{147-148,82} Another example is Sr₂Fe₂O_{6-δ}, where a series of different phases have been reported, depending on the variation of the δ value.⁸³ The arrangement of oxygen-vacancies in the crystal lattice is also important. The defects, generated due to oxygen deficiency, can be arranged in ordered^{4, 72, 86, 89} or disordered⁸⁸⁻⁸⁹ manner, leading to different structure and properties.^{4, 90} One of the common types of defect-order results in the brownmillerite structure, which contains alternating BO₆ octahedra and B'O₄ tetrahedra. The formation of brownmillerite-type structure can be controlled by altering the A- or B-site cations. For example, the substitution of A-site cations in Sr₂FeMnO₅, which has a disordered cubic structure, leads to Ca₂FeMnO₅, which features brownmillerite-type ordering.⁸⁵ The changes in the arrangement of defects leads to significant changes in electrical properties. The electrical conductivity of the ordered Ca₂ compound is almost unaffected by the change in atmosphere from argon to air, while the conductivity of the disordered Sr₂ compound increases significantly in air compared to the argon atmosphere.⁸⁵ Another example is the differences in electrical properties of Ca₂FeCoO_{6-δ}, which has brownmillerite-type structure,⁷⁴ and Sr₂FeCoO_{6-δ}, which lacks the ordering of defects.⁸⁴ The latter exhibits metallic properties, whereas the former displays semiconducting behavior.⁸⁴

The above examples are related to situations where the properties of an ordered material are compared to those of a disordered system. In this article, we show that the electrical

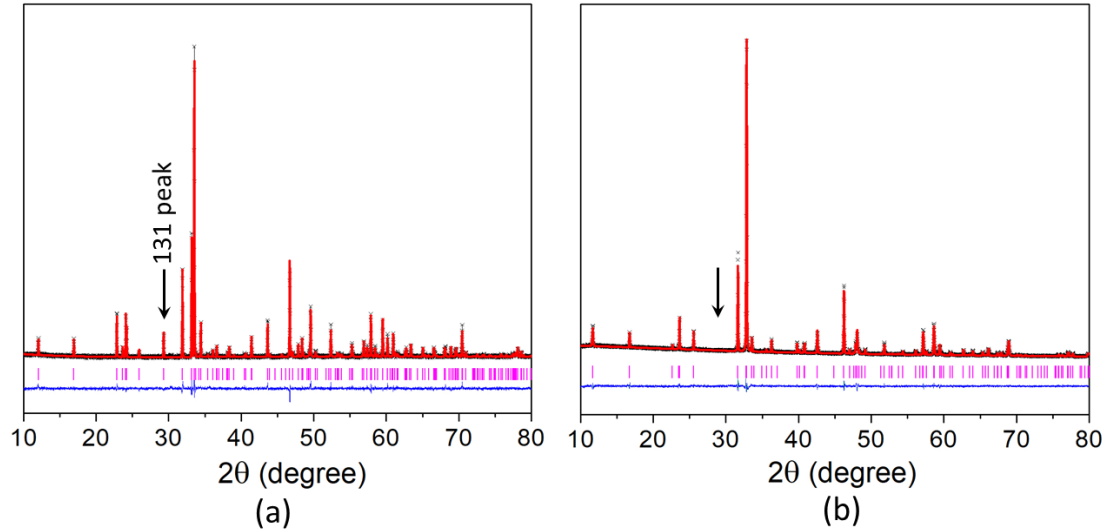


Figure 7.1. Rietveld refinement profiles for powder X-ray diffraction data of (a) $\text{Ca}_2\text{FeGaO}_{6-\delta}$ in $Pnma$, and (b) $\text{CaSrFeGaO}_{6-\delta}$ in $Ibm2$ space group. Black crosses represent experimental data, the solid red line is the model, pink vertical tick marks show Bragg peak positions, and the lower blue line represents the difference plot. The arrows show the position of 131 peak, which is present for $\text{Ca}_2\text{FeGaO}_{6-\delta}$ and absent for $\text{CaSrFeGaO}_{6-\delta}$.

properties can be manipulated by subtle changes to the arrangement of defects, while maintaining the defect-order in the system. We report a new oxygen-deficient perovskite, $\text{CaSrFeGaO}_{6-\delta}$, which unlike its Ca-only analogue, $\text{Ca}_2\text{FeGaO}_{6-\delta}$, has a non-centrosymmetric structure. Little information is known about the Ca-only analogue, with only magnetodielectric properties reported.³⁷ Here, we perform neutron diffraction, X-ray photoelectron spectroscopy, and charge-transport studies on both $\text{Ca}_2\text{FeGaO}_{6-\delta}$ and $\text{CaSrFeGaO}_{6-\delta}$, to demonstrate that the manipulation of defect-order can be used as a tool to control the electrical properties of oxygen-deficient perovskites.

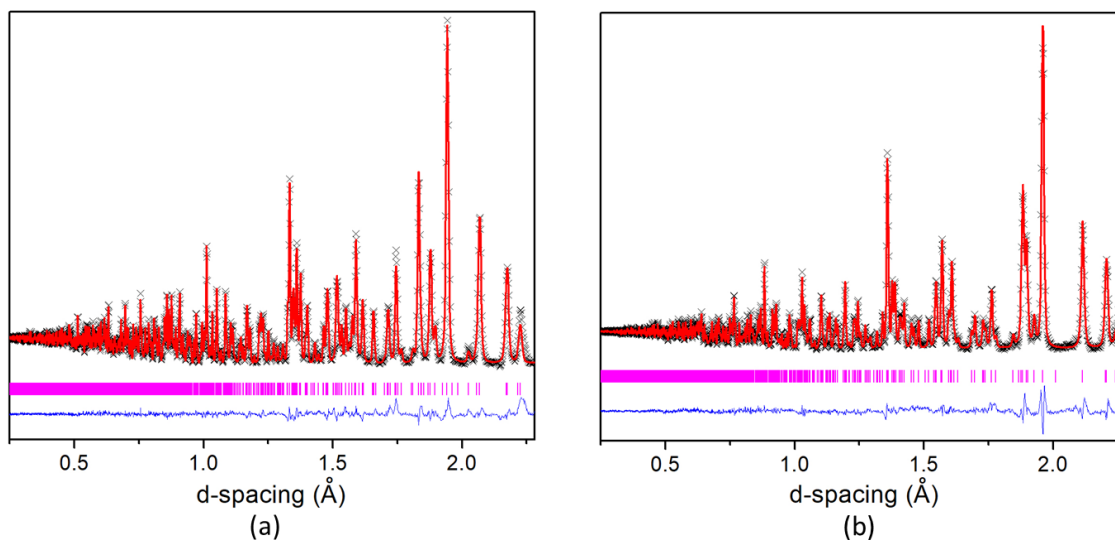


Figure 7.2. Rietveld refinement profiles for powder neutron diffraction data of (a) $\text{Ca}_2\text{FeGaO}_{6-\delta}$ in $Pnma$, and (b) $\text{CaSrFeGaO}_{6-\delta}$ in $Ibm2$ space group. Black crosses represent experimental data, the solid red line is the model, pink vertical tick marks show Bragg peak positions, and the lower blue line represents the difference plot.

2. EXPERIMENTAL

Solid-state synthesis method was used to synthesize the materials $\text{CaSrFeGaO}_{6-\delta}$ and $\text{Ca}_2\text{FeGaO}_{6-\delta}$. The synthesis of the Sr_2 -analogue was also attempted, but it consistently led to multiphase products. The powders of the precursor compounds, CaCO_3 (Alfa Aesar, 99.95%), SrCO_3 (Alfa Aesar, 99.95%), Fe_2O_3 (Alfa Aesar, 99.998%) and Ga_2O_3 (Sigma Aldrich, 99.99%) were mixed in stoichiometric proportions and ground together using an agate mortar and pestle, pressed into a pellet, and calcined in air at 1000 °C for 24 h. The samples were then reground and sintered at 1200 °C for 24 h in the same environment, followed by slow cooling. The heating and cooling rates were 100 °C/h. The phase purity and structure of the polycrystalline samples were determined by powder X-ray diffraction (XRD) at room temperature using $\text{Cu K}\alpha 1$ radiation ($\lambda = 1.54056 \text{ \AA}$). Neutron diffraction experiments were performed on POWGEN beamline at Oak Ridge National Laboratory,

with center wavelength of 0.7 Å. The GSAS software¹⁰⁰ and EXPGUI interface¹⁰¹ were used for Rietveld refinements. The microstructures were studied using high resolution field-emission scanning electron microscopy (SEM). X-ray photoelectron spectroscopy (XPS) was performed at room temperature using Al K α radiation (1486.7 eV) to study the oxidation states of Fe. The electrical properties were investigated by direct-current (DC) and alternating-current (AC) methods, on samples that had been sintered at 1200 °C. The AC electrochemical impedance spectroscopy measurements were done in the frequency range 0.1 Hz to 1 MHz using a computer-controlled frequency response analyzer. The DC measurements were performed at constant voltage of 10 mV, in the temperature range 25 – 800 °C. The conductivity measurements were performed at 100 °C intervals, and equilibrium was reached at each temperature of measurement before moving to the next temperature. The rate of heating between measurement-temperatures was 3 °C/min. Iodometric titrations were performed by dissolving about 50 mg of the sample and excess KI (~2 g) in 100 mL of 1M HCl. A total of 5 mL of the solution was then pipetted out, and the iodine that had been generated in the solution was titrated against 0.025 M Na₂S₂O₃. Near the end point of the titration, 0.2 mL of a starch solution was added to act as an indicator. All steps were performed under argon atmosphere.

3. RESULTS AND DISCUSSION

3.1. Crystal structure

Structural characterizations involved Rietveld refinements with powder X-ray and neutron diffraction data based on different crystallographic models. Both Ca₂FeGaO_{6- δ} and CaSrFeGaO_{6- δ} are defect-ordered oxygen-deficient perovskites with brownmillerite-type

structure. X-ray diffraction data for $\text{Ca}_2\text{FeGaO}_{6-\delta}$ has been reported,¹⁴⁹ showing *Pcmn* (*Pnma*) space group. Here, we study the crystal structures using neutron diffraction, and show the structural transformation upon changing the average ionic-radius on the A-site. Brownmillerite compounds usually crystallize in one of the four space groups *Imma*, *Ibm2*, *Pnma*, or *Pbcm*,^{4, 72, 84} depending on the relative orientation of tetrahedral chains. There are two possible chain-orientations, which are arbitrarily called right-handed and left-handed. If the tetrahedral chains are oriented randomly relative to each other, the space group will be *Imma* (*Icmm*).¹⁵⁰ If all tetrahedral chains have the same orientation in all layers, the space group will be *Ibm2* (*Ima2*).^{4, 72, 84} If the tetrahedral chains have the same orientation within each layer but are oriented opposite to the chains in the next tetrahedral layer, the space group will be *Pnma*.^{4, 72, 84} Finally, if each tetrahedral chain is oriented opposite to its nearest neighbors within the same layer and the next layer, the space group will be *Pbcm*.^{4, 72, 74, 84}

The two primitive space groups are readily identifiable by their characteristic peaks. Space group *Pbcm* can be easily distinguished from others due to the presence of superstructure peaks in its powder diffraction data, considering that its unit cell is double the size of those of the other three space groups.^{4, 72, 74, 84} Space group *Pnma* is recognized by the presence of 131 and 151 peaks, which are absent in the body-centered systems. The 131 peak is

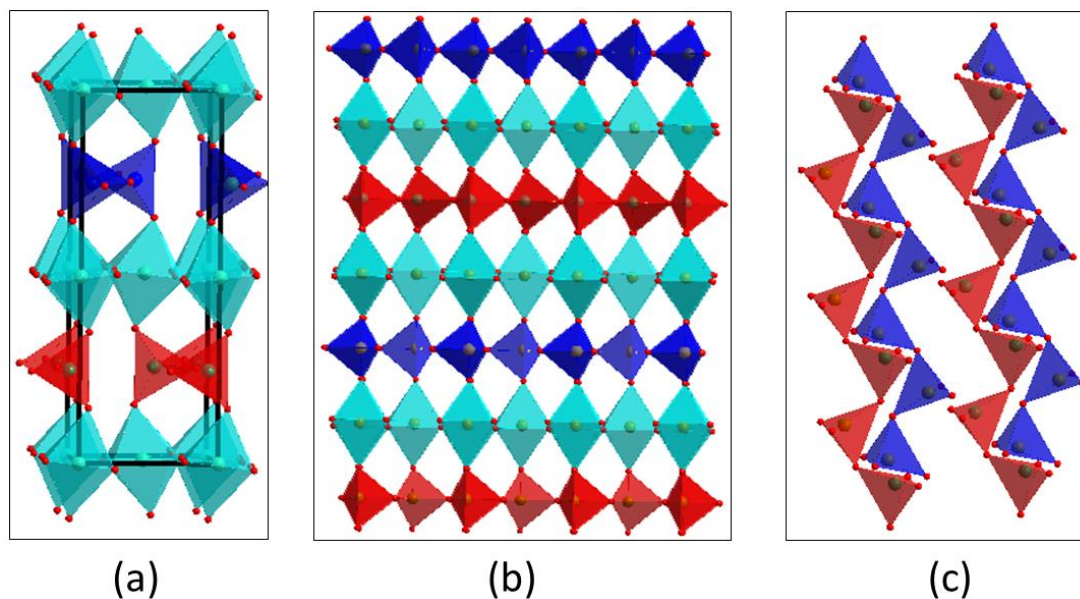


Figure 7.3. (a) Unit cell of $\text{Ca}_2\text{FeGaO}_{6-\delta}$, $Pnma$. (b) Alternating octahedral and tetrahedral coordination geometry in $\text{Ca}_2\text{FeGaO}_{6-\delta}$. The Ca atoms, located in spaces between polyhedra, are omitted for clarity. (c) Orientation of tetrahedral chains in two neighboring layers, which are opposite to each other in $\text{Ca}_2\text{FeGaO}_{6-\delta}$ (top view). The tetrahedral sites are primarily occupied by Ga and octahedral sites by Fe. The red and blue colors represent the two different orientations of tetrahedral chains.

particularly prominent.^{4, 72, 84} We examined all four space groups in our Rietveld refinements. All peaks can be indexed to orthorhombic unit cell for both compounds. The $Pbcm$ space group was readily ruled out for both materials, as the superstructure peaks associated with this space group were absent. For $\text{Ca}_2\text{FeGaO}_{6-\delta}$, the presence of the 131 peak indicated that the space group should be primitive $Pnma$, which was confirmed by Rietveld refinements with both X-ray (Figure 7.1a) and neutron diffraction data (Figure 7.2a). These refinements also showed that the octahedral sites are primarily occupied by

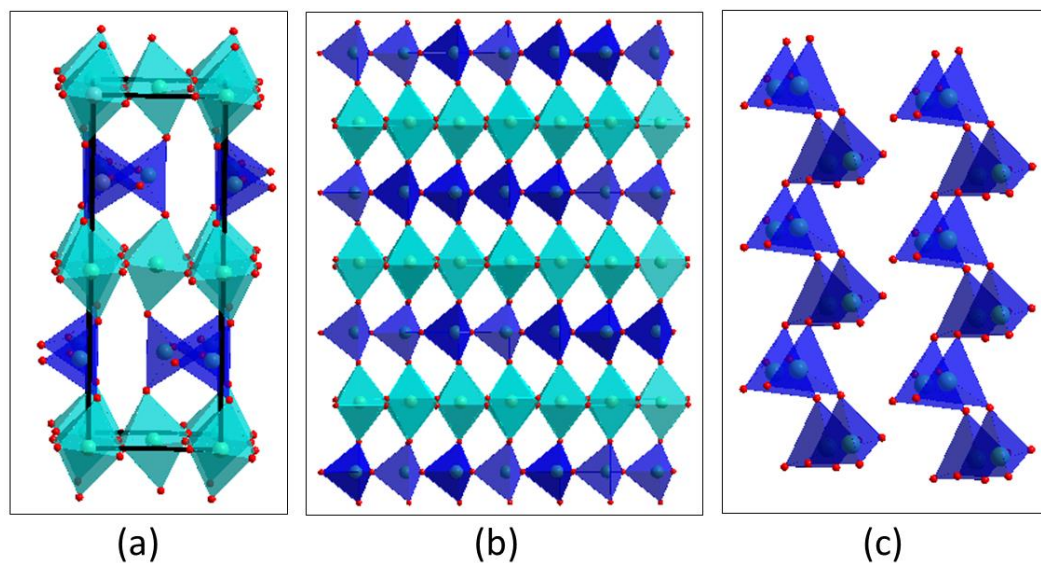


Figure 7.4. (a) Unit cell of $\text{CaSrFeGaO}_{6-\delta}$, *Ibm2*. (b) Alternating octahedral and tetrahedral coordination geometry in $\text{CaSrFeGaO}_{6-\delta}$. The Ca/Sr atoms, located in spaces between polyhedra, are omitted for clarity. (c) Orientation of tetrahedral chains in two neighboring layers (top view). All tetrahedral chains have the same orientation in $\text{CaSrFeGaO}_{6-\delta}$.

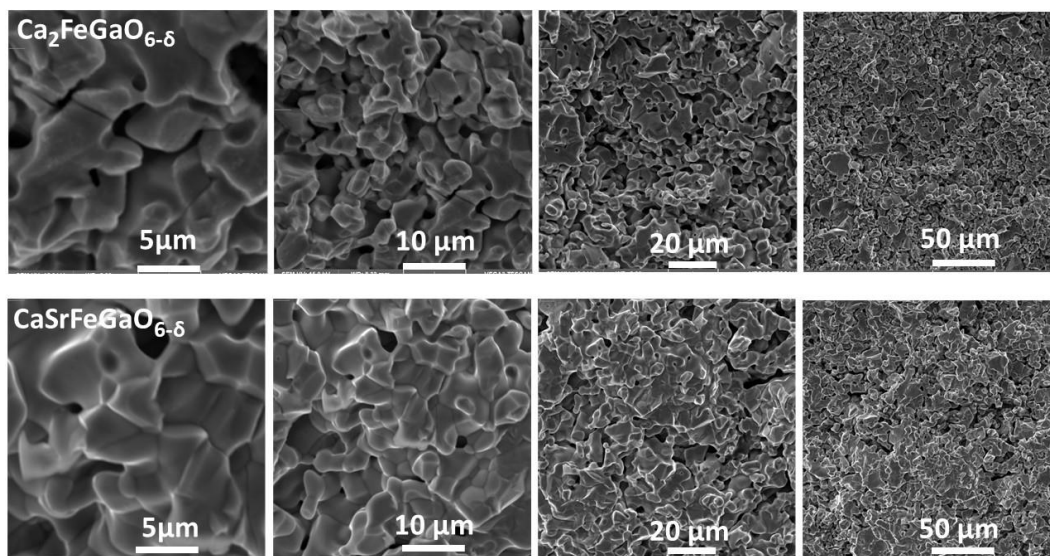


Figure 7.5. Scanning electron microscopy images of $\text{Ca}_2\text{FeGaO}_{6-\delta}$ and $\text{CaSrFeGaO}_{6-\delta}$.

Fe and tetrahedral sites by Ga. Table 7.1 shows the refined structural parameters for $\text{Ca}_2\text{FeGaO}_{6-\delta}$.

Interestingly, $\text{CaSrFeGaO}_{6-\delta}$ has a different structure, where the superstructure peaks of *Pbcm*, and the 131 peak of *Pnma* are absent, indicating the formation of a body-centered structure. Among the body-centered space groups, *Imma* and *Ibm2*, the latter showed the best fit for this material. The Rietveld refinement profiles for X-ray and neutron diffraction data of $\text{CaSrFeGaO}_{6-\delta}$ are shown in Figures 7.1b and 7.2b, respectively. The distribution of Fe and Ga was also determined from neutron diffraction, which indicated that Fe mostly occupies the octahedral positions, while Ga resides mainly on the tetrahedral sites. Table 7.2 shows the refined structural parameters for $\text{CaSrFeGaO}_{6-\delta}$.

These results demonstrate the important effect of the average ionic radius of the A-site cations on the orientation of tetrahedral chains. Smaller ionic radius in $\text{Ca}_2\text{FeGaO}_{6-\delta}$ favors a more ordered arrangement, where tetrahedral chains in each layer are oriented opposite to the neighboring layers (Figure 7.3), leading to a centrosymmetric structure. Whereas, larger ionic radius in $\text{CaSrFeGaO}_{6-\delta}$ leads to a non-centrosymmetric structure, where all tetrahedral chains have the same orientation (Figure 7.4).

3.2. Microstructure and X-ray photoelectron spectroscopy studies

The microstructure and crystallite size for $\text{Ca}_2\text{FeGaO}_{6-\delta}$ and $\text{CaSrFeGaO}_{6-\delta}$ were studied using scanning electron microscopy (SEM). Figure 7.5 shows the images of sintered pellets for both materials. As observed in this figure, the two compounds contain crystallites with similar size and similar degree of contact. The SEM images also show the uniformity and homogeneity of the crystallites in both $\text{Ca}_2\text{FeGaO}_{6-\delta}$ and $\text{CaSrFeGaO}_{6-\delta}$.

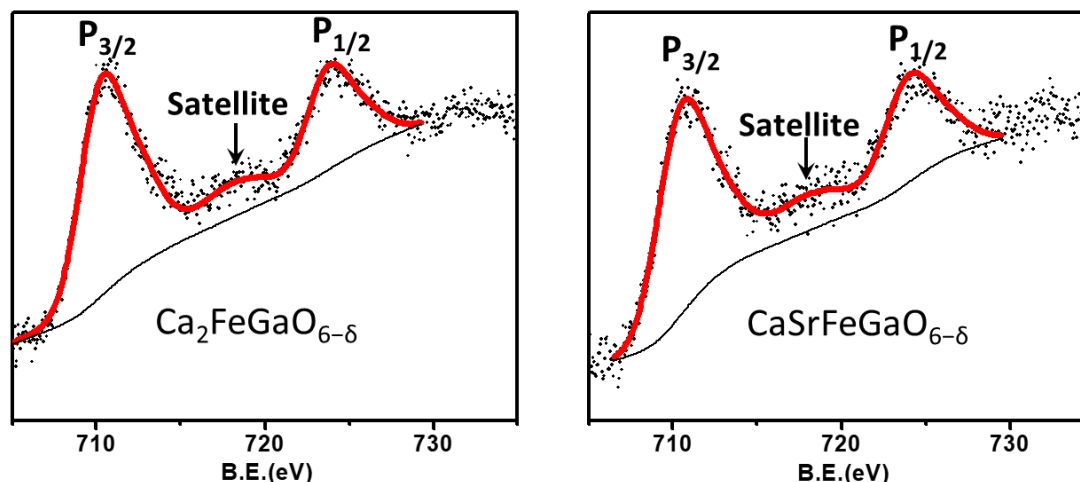


Figure 7.6. X-ray photoelectron spectroscopy data for $\text{Ca}_2\text{FeGaO}_{6-\delta}$ and $\text{CaSrFeGaO}_{6-\delta}$. The data for both materials show the same binding energies for Fe peaks.

We have also performed X-ray photoelectron spectroscopy (XPS) to investigate the oxidation state of iron in both compounds. It should be noted that these materials were synthesized in air using Fe_2O_3 as starting material. Therefore, Fe is expected to be trivalent, but the possibility of its oxidation in air should also be considered. The position of the $2\text{P}_{3/2}$ peaks as well as satellite peaks are indicative of the oxidation states. The $2\text{P}_{3/2}$ peak for trivalent Fe is expected to appear at about 710 – 711.5 eV followed by its satellite peak at about 8 – 9 eV higher in binding energy.^{43-44, 104-105} The satellite peak position is particularly important, as it is the signature of trivalent Fe. The XPS data are shown in Figure 7.6. For both $\text{Ca}_2\text{FeGaO}_{6-\delta}$ and $\text{CaSrFeGaO}_{6-\delta}$, the $2\text{P}_{3/2}$ main peak appears at 710.6 eV followed by a satellite peak at about 8.6 eV higher in energy, namely at 719.2 eV. This indicates that Fe is in trivalent state in both compounds. However, even without the satellite peaks, which can sometimes have low intensity and be hard to detect, it is evident that tetravalent Fe in these compounds can be ruled out, as it should show the $2\text{P}_{3/2}$ peaks at $\sim 712\text{-}713$ eV.^{43-44,}

¹⁰⁴⁻¹⁰⁵ We also performed iodometric titration analysis to confirm the results of XPS measurements. These analyses showed $\delta \approx 1$ for both $\text{CaSrFeGaO}_{6-\delta}$ and $\text{Ca}_2\text{FeGaO}_{6-\delta}$, consistent with primarily trivalent state for Fe, as also demonstrated by XPS. The degree of oxygen deficiency indicates that the oxygen stoichiometry is very close to that expected for ideal brownmillerite, i.e. 5 oxygens per formula unit.

3.3. Electrical properties

The electrical conductivities of these materials were investigated in air by both direct current (DC) and alternating current (AC) methods. In DC technique, the Ohm's law is employed to obtain the resistance (R) using the output current upon applying a certain voltage. For AC impedance spectroscopy,¹⁵¹ the total resistance is measured from the intercept with the real axis (Z') of the Nyquist plot at low frequency. Figure 7.7 shows a representative example of the Nyquist plot and the corresponding fit. The resistance values from both DC and AC methods are similar. The resistance values (R) obtained using the above methods are then used to calculate the conductivity (σ) using the following equation:

$$\sigma = L/RA \quad (20)$$

where L and A represent the thickness and cross-sectional area of the sample, respectively. The room temperature conductivity values, listed in Table 7.3, reveal the interesting effect of the structural order on electrical conductivity. There is an inverse correlation between the degree of order and the magnitude of conductivity. $\text{CaSrFeGaO}_{6-\delta}$, in which all tetrahedral chains have the same orientation, exhibits significantly greater conductivity than $\text{Ca}_2\text{FeGaO}_{6-\delta}$, where the tetrahedral chains have alternating orientations in neighboring layers.

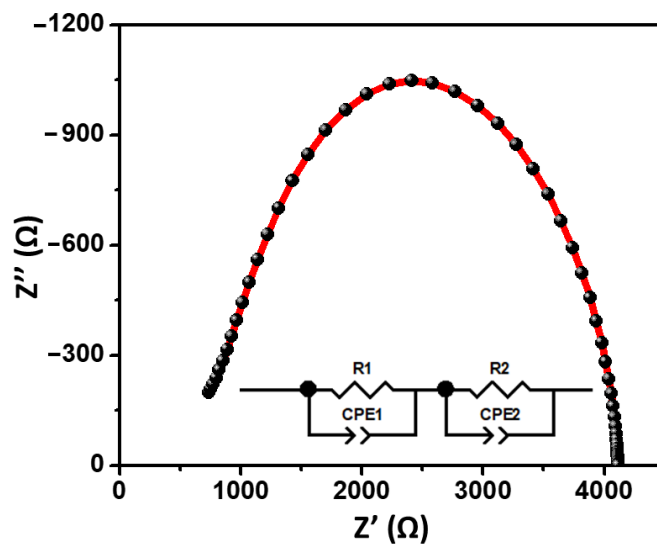


Figure 7.7. Representative example of the Nyquist plot for $\text{CaSrFeGaO}_{6-\delta}$ at 25 °C. The semicircle can be fitted using two resistance–capacitance (RC) units, corresponding to the bulk ($R1 = 766 \Omega$, $CPE1 = 2.6 \times 10^{-8} \text{ F}$) and grain boundary ($R2 = 3397 \Omega$, $CPE2 = 1.3 \times 10^{-7} \text{ F}$).

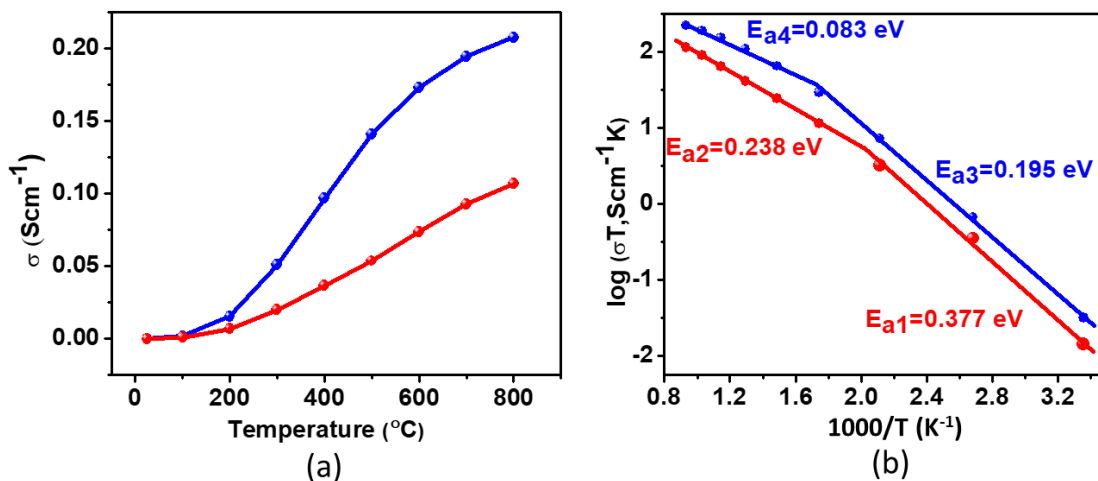


Figure 7.8. (a) Electrical conductivity of $\text{Ca}_2\text{FeGaO}_{6-\delta}$ (red) and $\text{CaSrFeGaO}_{6-\delta}$ (blue) as a function of temperature. (b) Arrhenius plots for electrical conductivity of $\text{Ca}_2\text{FeGaO}_{6-\delta}$ (red) and $\text{CaSrFeGaO}_{6-\delta}$ (blue).

The conductivity mechanism in oxygen-deficient perovskites is based on the hopping of charge carriers through metal-oxygen-metal (M-O-M) pathways.^{108-109, 152-153} Oxygen absorption or desorption leads to the formation of conduction pathways such as $M^{2+}-O-M^{3+}$ and $M^{3+}-O-M^{4+}$, i.e., small polarons, as observed in other oxygen-deficient perovskites.^{9, 109, 154-156} The presence of elements with multiple stable oxidation states are needed for the formation of small polarons.⁹ Both $Ca_2FeGaO_{6-\delta}$ and $CaSrFeGaO_{6-\delta}$ have Fe and Ga on B-site, where only Fe can have flexible oxidation states. During the conduction process through $M^{m+}-O-M^{n+}$ pathway, the charge carriers hop between M^{m+} and M^{n+} , resulting in change of oxidation states of cations.¹⁵²⁻¹⁵³

The degree of electrical conductivity depends strongly on the structural parameters, such as the M-O bond lengths and M-O-M bond angles. Higher conductivity is usually associated with shorter M-O distances or larger M-O-M bond angles. For example, the changes in electrical conductivity of $La_{1-x}Sr_xCoO_3$ correlate with variation in bond angles.^{21, 157} A change from semiconductivity to metallic conductivity in $La_{1-x}Sr_xCoO_3$ has been observed at $x = 0.25$, where there is an abrupt increase in the Co-O-Co bond angle.^{21, 157} For our materials, both $Ca_2FeGaO_{6-\delta}$ and $CaSrFeGaO_{6-\delta}$, have similar oxygen content, as well as similar oxidation state for Fe, as shown by XPS and iodometric titrations. The greater electrical conductivity of $CaSrFeGaO_{6-\delta}$ can be due to larger bond angles in this compound, which enhance the hopping of charge carriers through M-O-M conduction pathways. In $CaSrFeGaO_{6-\delta}$, the M-O-M bond angles are $127.6(2)^\circ$ (between two tetrahedral sites), $143.1(1)^\circ$ (between a tetrahedral and an octahedral site), and $170.68(8)^\circ$

Table 7.1. Refined structural parameters for $\text{Ca}_2\text{FeGaO}_{6-\delta}$ from powder neutron diffraction. Space group $Pnma$, $a = 5.38903(8)$ Å, $b = 14.6517(2)$ Å, $c = 5.60081(8)$ Å, $R_p = 0.0400$, $wR_p = 0.0209$.

Elements	x	y	z	Occupancy	U_{iso}	Multiplicity
Ca	0.0178(2)	0.10796(6)	0.5255(2)	1	0.0018(1)	8
Ga1	0.0496(2)	0.25	0.0682(2)	0.82(1)	0.0011(1)	4
Fe1	0.0496(2)	0.25	0.0682(2)	0.18(1)	0.0011(1)	4
Ga2	0.0	0.0	0.0	0.18(1)	0.00114(7)	4
Fe2	0.0	0.0	0.0	0.82(1)	0.00114(7)	4
O1	0.3979(3)	0.25	0.1275(2)	1	0.0030(2)	4
O2	0.0279(2)	0.64164(6)	0.0733(2)	1	0.0035(1)	8
O3	0.2599(2)	0.01528(6)	0.2401(2)	1	0.00275(9)	8

(between two octahedral sites). The corresponding angles in $\text{Ca}_2\text{FeGaO}_{6-\delta}$ are smaller, $125.65(8)^\circ$, $138.75(5)^\circ$ and $166.11(5)^\circ$, respectively.

The electrical conductivity for $\text{Ca}_2\text{FeGaO}_{6-\delta}$ and $\text{CaSrFeGaO}_{6-\delta}$ were also investigated at variable temperatures from 25 °C to 800 °C. Figure 7.8 shows the conductivity data at different temperatures. For both materials, there is an increase in conductivity as a function of temperature, indicating the semiconducting nature of these compounds. A visible rise in conductivity begins above 100 °C, where a slow increase is observed up to 200 °C, followed by a steep increase above this temperature. The increase in conductivity of

Table 7.2. Refined structural parameters for $\text{CaSrFeGaO}_{6-\delta}$ from powder neutron diffraction. Space group $Ibm2$, $a = 5.6437(1) \text{ \AA}$, $b = 15.0577(4) \text{ \AA}$, $c = 5.4458(1) \text{ \AA}$, $R_p = 0.0450$, $wR_p = 0.0216$.

Elem ents	x	y	z	Occupa ncy	U_{iso}	Multip licity
Ca	0.5202(3)	0.10910(9)	0.0076(5)	0.5	0.0041(2)	8
Sr	0.5202(3)	0.10910(9)	0.0076(5)	0.5	0.0041(2)	8
Ga1	0.0713(3)	0.25	0.0429(4)	0.79(4)	0.0020(3)	4
Fe1	0.0713(3)	0.25	0.0429(4)	0.21(4)	0.0020(3)	4
Ga2	0.0	0.0	0.0	0.20(3)	0.019 (2)	4
Fe2	0.0	0.0	0.0	0.80(3)	0.019 (2)	4
O1	0.7545(4)	-0.01045(9)	0.2526(5)	1	0.0029 (2)	4
O2	-0.0618(3)	0.1416(1)	-0.0237(5)	1	0.0063(3)	8
O3	0.3685(6)	0.25	0.8843(7)	1	0.0077(4)	8

$\text{CaSrFeGaO}_{6-\delta}$ is much sharper compared to that of $\text{Ca}_2\text{FeGaO}_{6-\delta}$. The rise in temperature leads to an increase in the mobility of polarons. This temperature-activated mobility results in enhanced electrical conductivity,⁵⁰ according to the following relation

$$\sigma = ne\mu \quad (21)$$

where σ , n , e , and μ are the conductivity, concentration of electrons/holes, charge of the electron, and mobility of the charge carriers, respectively. An additional contribution can be the rise in ionic conductivity due to the increase in temperature. Some studies¹⁴⁵ indicate that oxide ion transport in perovskites starts at $\sim 500 \text{ }^\circ\text{C}$, although some reports suggest that it can also occur at lower temperatures.^{132, 146} However, it has been shown that at high oxygen partial-pressure, such as in atmospheric air, the electronic conductivity can be dominant over the ionic conductivity in perovskite-based systems.^{9, 23, 58-59, 138, 141}

The activation energy for the increase in conductivity as a function of temperature can be obtained using Arrhenius equation for thermally activated conductivity⁴⁹⁻⁵¹ as follows:

$$\sigma T = \sigma^0 e^{\frac{-E_a}{kT}} \quad (22)$$

where σ^0 is a pre-exponential factor and characteristic of the material. E_a , k , and T are the activation energy for the electrical conductivity, Boltzmann constant, and absolute temperature, respectively. The activation energy (E_a) can be calculated from the slope of the line of best fit in the $\log \sigma T$ versus $1000/T$ plot. Figure 7.8b shows the Arrhenius plot for both materials in the temperature range 25 °C – 800 °C (298 K – 1073 K). The activation energies are lower for $\text{CaSrFeGaO}_{6-\delta}$ compared to $\text{Ca}_2\text{FeGaO}_{6-\delta}$, as shown in Table 7.3. The sharp differences between the electrical properties of these two materials indicate the pronounced impact of structural order on charge-transport in oxygen-deficient perovskites.

Table 7.3. Room Temperature Conductivity and Activation Energies.

compounds	total conductivity, σ (S cm^{-1})		Activation energy, E_a (eV)
	AC	DC	
CaSrFeGaO_5	1.00×10^{-4}	1.07×10^{-4}	0.195 eV for 25 to 300 °C
			0.083 eV for 300 to 800 °C
$\text{Ca}_2\text{FeGaO}_5$	4.80×10^{-5}	4.79×10^{-5}	0.377 eV for 25 to 220 °C
			0.238 eV for 220 to 800 °C

4. CONCLUSIONS

Subtle changes in defect-order can have a significant impact on the electrical conductivity of oxygen-deficient perovskites. Different distribution of defects in $\text{CaSrFeGaO}_{6-\delta}$ leads to different orientation of tetrahedral chains compared to that in $\text{Ca}_2\text{FeGaO}_{6-\delta}$. Importantly, these changes lead to enhanced electrical conductivity in $\text{CaSrFeGaO}_{6-\delta}$, which exhibits significantly greater conductivity than $\text{Ca}_2\text{FeGaO}_{6-\delta}$. Variable-temperature conductivity studies show that the enhanced electrical conductivity of $\text{CaSrFeGaO}_{6-\delta}$ persists at high temperature, up to 800 °C. The XPS and iodometric titration studies show the same degree of oxygen deficiency for both materials. They also indicate similar oxidation states of Fe in both compounds. Therefore, the difference in relative orientation of tetrahedral chains appears to be the main factor that leads to the changes in electrical conductivity between these materials. This indicates that controlling the structural parameters can be used as a tool to control the charge-transport properties of oxygen-deficient perovskites.

CHAPTER 8
DISPARITY IN ELECTRICAL AND MAGNETIC PROPERTIES OF
ISOSTRUCTURAL OXYGEN DEFICIENT PEROVSKITES $\text{BaSrCo}_2\text{O}_{6-\delta}$ AND
 $\text{BaSrCoFeO}_{6-\delta}$ ⁷

INTRODUCTION

We have recently studied^{20, 158} the structure-property relationships in a series of oxygen deficient perovskites (ODPs). These materials have general formula ABO_{3-x} where A is usually an alkaline earth metal or lanthanide, and B is a smaller ion, typically a transition metal, although some main group elements could also reside on the B-site. The ODPs feature interesting properties, from superconductivity¹⁵⁹, to magnetoresistant,¹⁶⁰ and have been considered for different applications including gas sensors¹⁶¹, gas diffusion membranes for gas separation¹⁶², and electrodes in solid oxide fuel cells¹⁶³. In typical perovskites, oxygen atoms form octahedral geometry around the B-site metal, forming BO_6 octahedra. In ODPs, the absence of some oxygen atoms from the structure creates vacancies which may lead to the formation of different coordination geometries, such as

⁷ The work described in this chapter was published in Journal of Materials Science: Materials in Electronics (2018, vol. 29, p. 13464-13473)

tetrahedral (BO_4) or square pyramidal (BO_5).²⁰ Considering the various coordination geometries that can be formed due to the presence of oxygen vacancies, a high degree of structural diversity is observed in ODPs.^{11, 72-76, 164}

Structural changes can sometimes occur through substitution on the A or B-sites. For example, the coordination around the B-site cation can change when the A site cation is substituted in $\text{Sr}_{2-x}\text{Ca}_x\text{Fe}_2\text{O}_{6-\delta}$.²⁰ Here, $\text{Sr}_2\text{Fe}_2\text{O}_{6-\delta}$ has a tetragonal structure and contains alternating octahedral and square pyramidal coordination of the B-site cations. When one Sr is substituted by Ca, i.e., $\text{SrCaFe}_2\text{O}_{6-\delta}$, the structure changes into orthorhombic, and the coordination geometry transforms into alternating tetrahedral and octahedral.²⁰ These structural changes lead to the transformation of electrical properties from metallic to semiconductor. The magnetic structure also changes, where the spin-density wave state in $\text{Sr}_2\text{Fe}_2\text{O}_{6-\delta}$ is converted into long-range G-type antiferromagnetic order in $\text{SrCaFe}_2\text{O}_{6-\delta}$.²⁰ Similar changes in structure and electrical conductivity as a result of substitution on the A-site have been observed for $\text{Sr}_{2-x}\text{Ca}_x\text{FeCoO}_{6-\delta}$.²⁰

Substitution on the B-site can also lead to changes in crystal structure and material properties. For example, the above mentioned tetragonal compound, $\text{Sr}_2\text{Fe}_2\text{O}_{6-\delta}$, which has magnetic moments in spin-density wave state, can be modified by replacing one of the Fe atoms with Mn. The resulting material, $\text{Sr}_2\text{FeMnO}_{6-\delta}$, has a cubic $Pm-3m$ structure and inhomogeneous magnetic ground state, where the majority of the sample contains fluctuating spins at 4K, but a small fraction is magnetically ordered.¹¹ Even minor changes to the B-site cations can sometimes lead to major changes, as highlighted by the difference between $\text{Sr}_2\text{Fe}_{1.9}\text{Cr}_{0.1}\text{O}_{6-\delta}$, cubic $Pm-3m$, and $\text{Sr}_2\text{Fe}_{1.9}\text{Co}_{0.1}\text{O}_{6-\delta}$, orthorhombic $Cmmm$.¹⁶⁴ Again this leads to significant variation of magnetic properties in these two materials.¹⁶⁴

The above examples describe changes in material properties as a consequence of structural modifications due to B-site cation substitution. However, circumstances where cation substitution leads to isostructural materials, which have significantly different electrical and magnetic properties are less common. In the present work, two isostructural oxygen deficient perovskites, $\text{BaSrCo}_2\text{O}_{6-\delta}$ ($\delta = 1.35$) and $\text{BaSrCoFeO}_{6-\delta}$ ($\delta = 0.73$), have been investigated and the significant contrast between their electrical and magnetic properties has been demonstrated. Cubic, $Pm-3m$ structure has been reported for a material with similar composition to $\text{BaSrCo}_2\text{O}_{6-\delta}$ ($\delta = 1.35$), but with greater oxygen content. Also, some information has been reported on bulk magnetization and electrical conductivity in the temperature span of ~ 135 degrees Celsius.¹⁶⁵ $\text{BaSrCo}_2\text{O}_{6-\delta}$ discussed in the current manuscript has about 18% more vacancies, and has been investigated in detail using X-ray photoelectron spectroscopy, SEM, bulk magnetization, and DC and AC electrical conductivity studies in a wide temperature range, 25 °C to 900 °C. Regarding $\text{BaSrCoFeO}_{6-\delta}$, its crystal structure has been reported to be cubic $Pm-3m$,¹⁶⁶ but no information is available on magnetism and electrical conductivity of this material. In this article, an array of characterization methods has been employed to show remarkable differences between the two isostructural materials, $\text{BaSrCo}_2\text{O}_{6-\delta}$ and $\text{BaSrCoFeO}_{6-\delta}$, due to the difference in their oxygen stoichiometry. Most significantly, the disparities between electrical properties and temperature-dependent electrical conductivities are reported here.

EXPERIMENTAL

Syntheses at different temperatures and under argon or air atmosphere were attempted. The powders of precursors BaCO_3 (Alfa Aesar, 99.95%), SrCO_3 (Aldrich, 99.9%), Fe_2O_3 (Alfa Aesar, 99.998%), and Co_3O_4 (Alfa Aesar, 99.7%) were mixed and ground together using

an agate mortar and pestle, pressed into a pellet, and heated at 1100 °C for 24 h. Then the samples were reground and refired at 1100 °C for 24 h, followed by slow cooling. In all cases, the heating and cooling rates were 100 °C/h. BaSrCo₂O_{6-δ} could only be synthesized in argon atmosphere, while BaSrCoFeO_{6-δ} could only be made in air. Syntheses under other conditions led to the formation of multiphase products. The phase purity and structure of the polycrystalline samples were determined by powder X-ray diffraction (XRD) at room temperature using Cu Kα1 radiation ($\lambda = 1.54056 \text{ \AA}$). The GSAS software⁴⁰ and EXPEGUI⁴¹ interface were used for Rietveld refinements. The sample morphologies were studied using high resolution field-emission scanning electron microscopy (SEM). X-ray photoelectron spectroscopy (XPS) was performed at room temperature using Al Kα radiation (1486.7 eV) to study the oxidation states of Fe and Co. The electrical properties were investigated by direct-current (DC) and alternating-current (AC) conductivity measurements on pressed pellets that had been sintered at 1100 °C. Magnetic susceptibility data were obtained by cooling each material to 2 K, then applying magnetic field of 1000 Oe and measuring the magnetization up to 400 K to obtain the zero-field-cooled (ZFC) data. The process was then repeated by cooling the material in the presence of the field and measuring the magnetization to obtain the field-cooled (FC) data. Electrochemical impedance spectroscopy was performed in the frequency range of 0.1 Hz to 1 MHz using a computer-controlled frequency response analyzer at room temperature. Two-probe dc measurements were performed in the temperature range 25 – 900 °C by applying a constant voltage of 10 mV and collecting the output current. Variable-temperature electrical conductivity measurements were carried out during both heating and cooling cycles. The rate of heating and cooling for conductivity measurements was 3 °C/min. Iodometric

titrations were performed by dissolving about 50 mg of the sample and excess KI (~2 g) in 100 mL of 1M HCl. A total of 5 mL of the solution was then pipetted out, and the iodine that had been generated in the solution was titrated against 0.025 M Na₂S₂O₃. Near the end point of the titration, 0.2mL of a starch solution was added to act as an indicator. All steps were performed under argon atmosphere.

RESULTS AND DISCUSSION

Crystal structure and crystallite morphology

As mentioned in the experimental section, single phase cubic structure could only be obtained when syntheses were done in argon for BaSrCo₂O_{6-δ}, and in air for BaSrCoFeO_{6-δ}. This led to the formation of isostructural phases that have different oxygen stoichiometry and presented a great opportunity to study the effect of oxygen content on material properties.

The crystal structures of these materials were characterized by powder X-ray diffraction (PXRD). Figure 8.1 shows the Rietveld refinement profiles for both materials, which have cubic structure with *Pm-3m* space group as previously reported¹⁶⁵⁻¹⁶⁶. The refined unit cell parameters and atomic positions for both materials are listed in Tables 8.1 and 8.2. BaSrCoFeO_{6-δ} has a slightly smaller unit cell, which is also evident from the systematic shift of X-ray diffraction peaks to the right, compared to the data for BaSrCo₂O_{6-δ}. This is consistent with the cation oxidation states in the two materials. As described in the next section, BaSrCoFeO_{6-δ} contains tri- and tetravalent Fe and Co, whereas BaSrCo₂O_{6-δ} contains Co²⁺/Co³⁺. Therefore, the average ionic radius in the latter is greater than that in the former, leading to the difference in the unit cell dimensions.

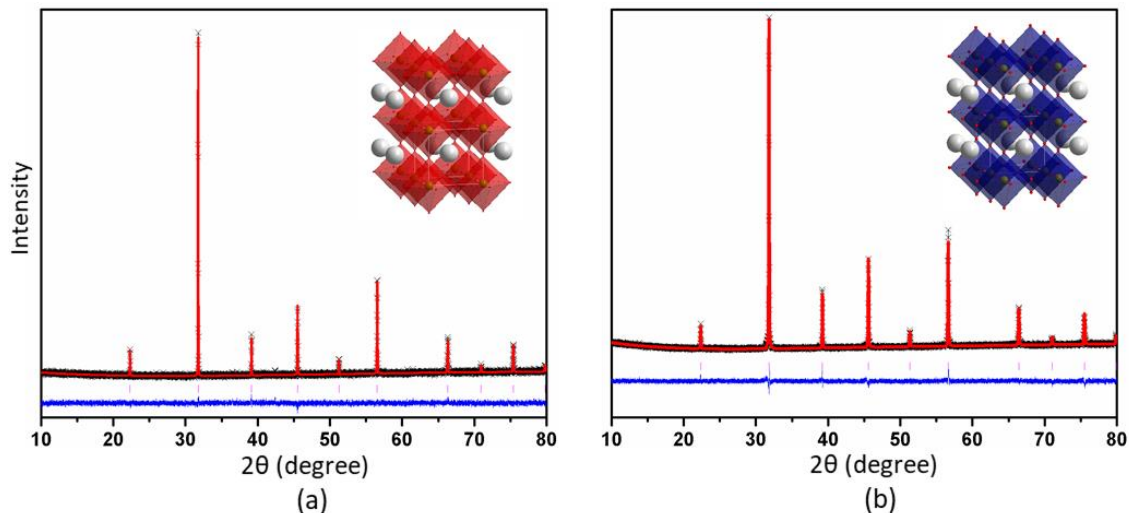


Figure 8.1. Rietveld refinement profile for powder XRD data of a) $\text{BaSrCo}_2\text{O}_{6-\delta}$ and b) $\text{BaSrCoFeO}_{6-\delta}$. Black crosses represent experimental data, the solid red line is the cubic $Pm\text{-}3m$ model, pink vertical tick marks show Bragg peak positions, and the lower blue line represents the difference plot.

Table 8.1. Refined Structural Parameters for $\text{BaSrCoFeO}_{6-\delta}$ using powder X-ray diffraction data.

Space group: $Pm\text{-}3m$, $a = 3.9804(2)\text{\AA}$, $V = 63.066(1)\text{\AA}^3$, $R_p = 0.0323$, $wR_p = 0.0419$						
Elements	x	y	z	Occupancy	Uiso	
Fe	0	0	0	0.5	0.035(1)	
Co	0	0	0	0.5	0.035(1)	
Ba	0.5	0.5	0.5	0.5	0.0202(7)	
Sr	0.5	0.5	0.5	0.5	0.0202(7)	
O	0.5	0	0	0.88	0.056(3)	

Table 8.2. Refined Structural Parameters for BaSrCo₂O_{6-δ} using powder X-ray diffraction data.

Space group: <i>Pm-3m</i> , a = 3.9839(2) Å, V = 63.23(1) Å ³ , Rp = 0.0385, wRp = 0.0492					
Elements	x	y	z	Occupancy	Uiso
Co	0	0	0	1	0.026(2)
Ba	0.5	0.5	0.5	0.5	0.0152(9)
Sr	0.5	0.5	0.5	0.5	0.0152(9)
O	0.5	0	0	0.77	0.084(5)

The morphology and crystallite sizes of both materials were also studied using scanning electron microscopy. Despite having the same crystal structure and same space group, the crystallite morphology for the two materials is significantly different. Figure 8.2 shows the sintered pellets for both materials. As seen in this figure, the crystallite size is larger in BaSrCo₂O_{6-δ}. In addition, the crystallites appear to be more densely packed in BaSrCo₂O_{6-δ}.

δ.

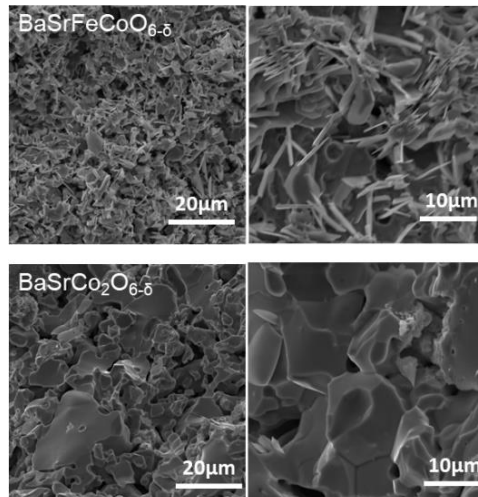


Figure 8.2. Scanning electron microscopy images of BaSrCoFeO_{6-δ} (top) and BaSrCo₂O_{6-δ} (bottom)

X-ray photoelectron spectroscopy (XPS) and iodometric titration

The XPS studies were used to analyze the oxidation states of Fe and Co in both materials. The XPS analyses were guided by the information regarding synthesis conditions, which affect the oxygen content, as well as the iodometric titration results that show the oxygen stoichiometry in each material. Since $\text{BaSrCoFeO}_{6-\delta}$ was synthesized in air, the oxygen content in this compound is expected to be greater than that of $\text{BaSrCo}_2\text{O}_{6-\delta}$, which was made in argon. This is confirmed by iodometric titration results, which indicate the oxygen stoichiometry for the two compounds to be 5.27 and 4.65, corresponding to $\text{BaSrCoFeO}_{6-\delta}$ ($\delta = 0.73$) and $\text{BaSrCo}_2\text{O}_{6-\delta}$ ($\delta = 1.35$), respectively. Note that the starting materials for syntheses were Co_3O_4 and Fe_2O_3 , which contain divalent and trivalent cobalt, as well as trivalent iron. The oxygen stoichiometry of $\text{BaSrCoFeO}_{6-\delta}$ indicates that there should be some tetravalent Fe and/or Co in this material. On the other hand, the low oxygen stoichiometry of $\text{BaSrCo}_2\text{O}_{6-\delta}$ indicates that the oxidation state of cobalt should be a combination of divalent and trivalent.

We discuss the XPS data for $\text{BaSrCo}_2\text{O}_{6-\delta}$ first. The Co $2\text{P}_{3/2}$ peak appears at ~ 780 eV, and two satellite peaks are present at ~ 4.5 eV and 10 eV higher than the $2\text{P}_{3/2}$ peak (Figure 8.3a). Co^{2+} and Co^{4+} are both expected to show satellite peaks at about 5 eV higher than the $2\text{P}_{3/2}$ peak.¹⁶⁷⁻¹⁶⁸ Considering that $\text{BaSrCo}_2\text{O}_{6-\delta}$ was synthesized in argon atmosphere, the oxidation of cobalt to tetravalent state is not expected. In addition, the oxygen stoichiometry determined by iodometric titration indicates $\delta = 1.35$ for $\text{BaSrCo}_2\text{O}_{6-\delta}$, which rules out the possibility of the presence of tetravalent cobalt. Therefore, for this material, the satellite peak at ~ 4.5 eV higher than the $2\text{P}_{3/2}$ peak belongs to Co^{2+} . The satellite peak at ~ 10 eV higher than the $2\text{P}_{3/2}$ peak is signature of Co^{3+} .¹⁶⁷

The XPS spectra for BaSrCoFeO_{6-δ} are shown in Figures 8.3b and c. The Fe³⁺ 2P_{3/2} peak is expected to appear at ~710-711 eV with a satellite peak at ~7-9 eV higher than the 2P_{3/2} peak.^{169, 170-172} Compared to Fe³⁺, the Fe⁴⁺ 2P_{3/2} peak is expected to have higher binding energy, appearing at ~712-713 eV.^{169, 171} In the XPS spectrum for BaSrCoFeO_{6-δ} (Figure 8.3b) the Fe 2P_{3/2} peak appears at ~710 eV with a shoulder at ~713 eV, indicating the presence Fe³⁺ (~710 eV) and Fe⁴⁺ (~713eV) in this material. The satellite peak for Fe³⁺ is present at about 718 eV, as expected.

The XPS spectrum for cobalt in BaSrCoFeO_{6-δ} (Figure 8.3c) is very similar to that of BaSrCo₂O_{6-δ}. The Co 2P_{3/2} peak appears at ~780 eV, along with two satellite peaks at ~5.5 eV and 10 eV higher than the 2P_{3/2} peak. Again, these indicate the presence of Co²⁺ and Co³⁺, as described above. Therefore, iodometric titration and XPS indicate that Fe in BaSrCoFeO_{6-δ} is in tri- and tetravalent states, whereas Co is in di- and trivalent states in both materials.

Magnetic properties.

Magnetic susceptibility as a function of temperature shows another sharp contrast between these two isostructural materials. Both ZFC and FC data were obtained in the temperature range 2 K – 400 K. The magnetic susceptibility data for BaSrCo₂O_{6-δ} (Figure 8.4a) shows ZFC-FC divergence below 300 K. There is no sharp magnetic transition in the temperature range 2 K – 400 K. As shown in the inset of Figure 8.4a, the inverse susceptibility plot

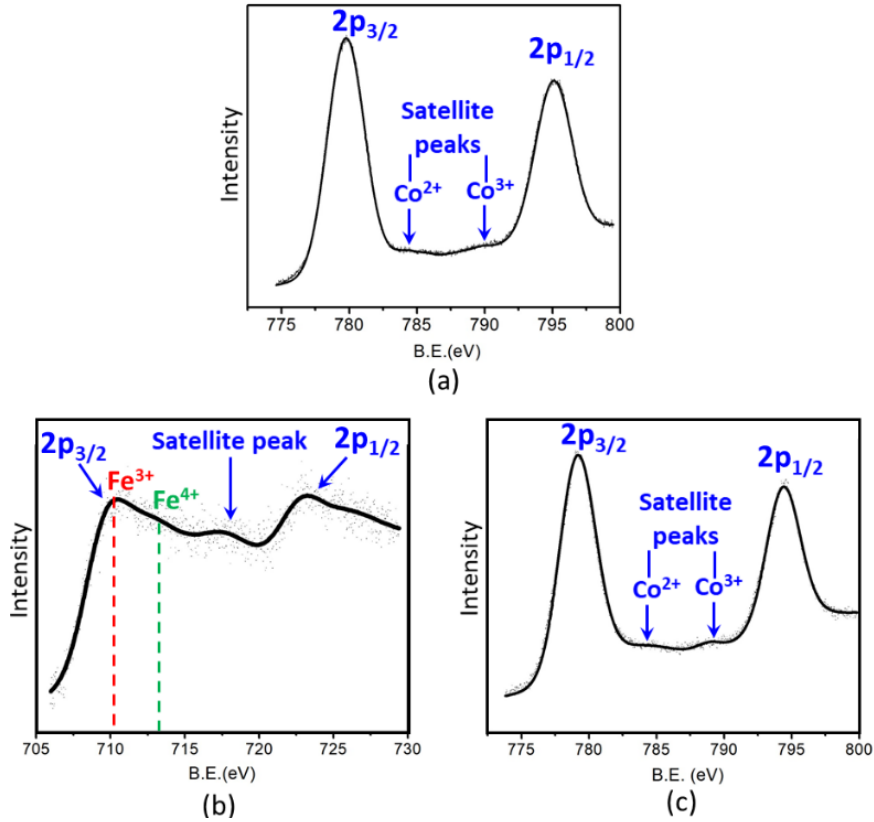


Figure 8.3. X-ray photoelectron spectroscopy data. (a) shows the Co peaks for BaSrCo₂O_{6-δ}. (b) and (c) show the Fe and Co peaks for BaSrCoFeO_{6-δ}, respectively.

shows deviation from linear paramagnetic behavior. The very low magnitude of magnetic susceptibility in the entire temperature range for BaSrCo₂O_{6-δ} indicates that there is little uncompensated moment in this material. This is further confirmed by isothermal magnetization data (Figure 8.4b) that show very low magnetization even at 2 K, where the magnetization value reaches a maximum of 0.16 μ_B at magnetic field of 9 T. As evident from the inverse susceptibility plot, BaSrCo₂O_{6-δ} is not paramagnetic at 2 K. The low magnetization value could be due to antiferromagnetic order, with a transition temperature higher than the measured temperature range. The antiferromagnetic order is consistent with that reported for a similar composition, which has 18% less oxygen-vacancies than our

material and shows $T_N \approx 525$ K.¹⁶⁵ For that composition, only FC data has been reported.¹⁶⁵ The ZFC-FC divergence observed in Figure 8.4a can be indicative of reorientation of magnetic moments while the overall antiferromagnetic order is retained and the low magnetization value persists. This has been observed before for another oxygen-deficient perovskite with formula $\text{Ca}_2\text{FeCoO}_5$,⁷⁴ where neutron diffraction data showed reorientation of magnetic moments from along the a-axis to b-axis while the antiferromagnetic order was retained.⁷⁴ The magnetic susceptibility of $\text{Ca}_2\text{FeCoO}_5$ below the magnetic transition temperature showed ZFC-FC divergence, occurring at the temperature where the magnetic moment reorientation was completed, similar to the situation observed in $\text{BaSrCo}_2\text{O}_{6-\delta}$.⁷⁴

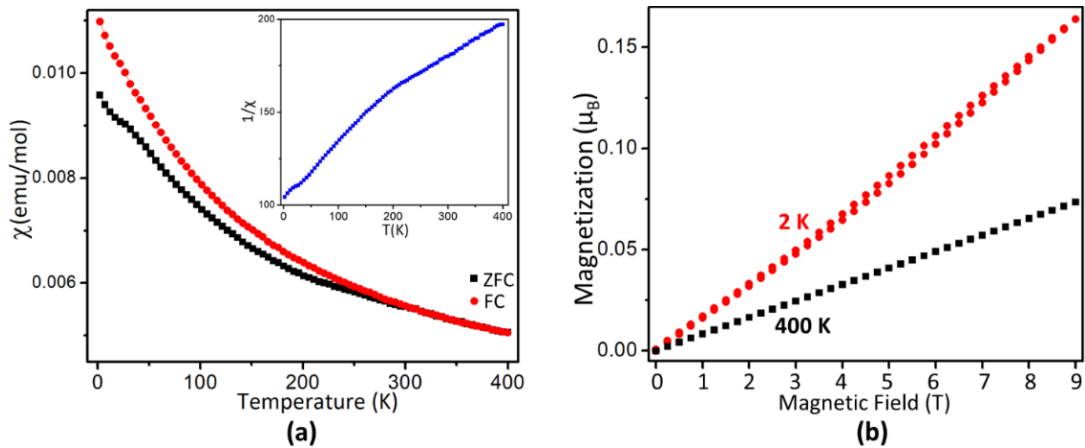


Figure 8.4. Bulk magnetization data for $\text{BaSrCo}_2\text{O}_{6-\delta}$: (a) ZFC and FC magnetic susceptibility data. The inset shows inverse of susceptibility plotted against temperature. (b) Isothermal magnetization versus field, at 2K and 400 K.

For $\text{BaSrCoFeO}_{6-\delta}$, there is no ZFC-FC divergence in the magnetic susceptibility data, as shown in Figure 8.5a. However, the susceptibility deviates significantly from paramagnetic behavior, showing a sharp increase at low temperature, indicative of uncompensated

moments due to ferro- or ferrimagnetic coupling.^{173-174,175-176} This is also evident when inverse susceptibility is plotted as a function of temperature, where the only linear region is in the temperature range 300 K – 400 K. The linear paramagnetic region can be fitted using the inverse Curie-Weiss equation:

$$\frac{1}{\chi} = \frac{T-\theta}{C} \quad (23)$$

The fit values are $C = 4.49(3)$ and $\theta = -110(3)$. The negative θ value confirms the presence of ferrimagnetic interactions. Below 300 K, the inverse susceptibility deviates from that of a paramagnetic system. There is no sharp magnetic transition, and the changes are gradual.

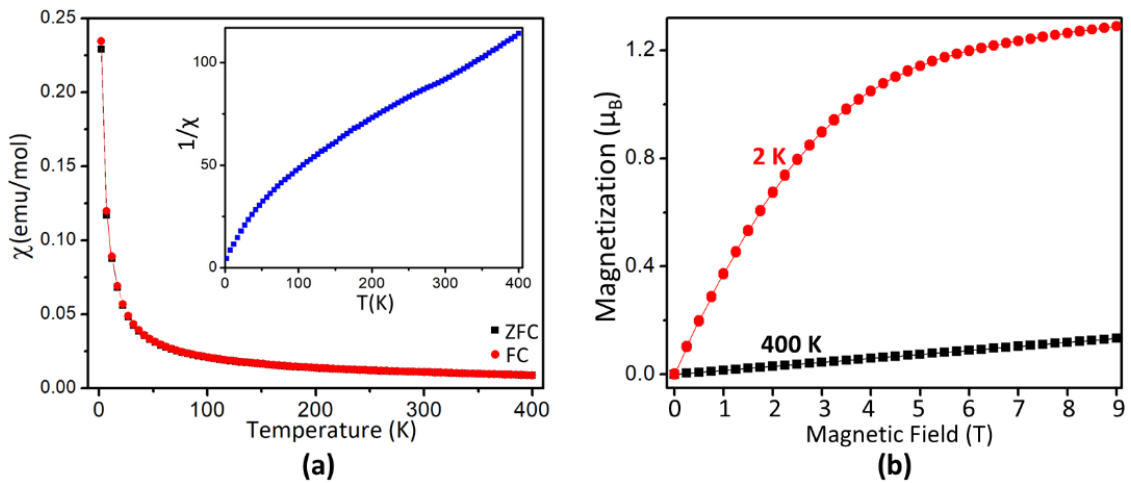


Figure 8.5. Bulk magnetization data for $\text{BaSrCoFeO}_{6-\delta}$: (a) ZFC/FC magnetic susceptibility data. The inset shows inverse of susceptibility versus temperature. (b) Isothermal magnetization data at 2 K and 400 K.

The isothermal magnetization data as a function of field further confirm the ferrimagnetic behavior at low temperature. As shown in Figure 8.5b, isothermal magnetization at 400 K has a typical paramagnetic behavior. However, at 2 K, the isothermal data shows a sharp increase in magnetization followed by a semi-plateau. However, even at high field of ~ 9

T, the magnetization continues to increase gradually and does not reach saturation. In addition, the maximum magnetization at 9 T is $\sim 1.28 \mu_B$, much lower than that anticipated for ferromagnetic coupling of Fe and Co in their trivalent and tetravalent states. This again indicates that the magnetic interactions are ferrimagnetic. Note that as far as electronic configurations are concerned, there are two types of magnetic ions in $\text{BaSrCoFeO}_{6-\delta}$, as suggested by XPS. They are spin 5/2 ions (Fe^{3+} and Co^{4+}) and spin 4/2 ions (Fe^{4+} and Co^{3+}), for high-spin configurations which are common in perovskite-based oxides. If ferrimagnetic coupling occurs between equal concentrations of spin 5/2 and spin 4/2 ions, the expected saturation moment will be $\sim 1 \mu_B$, close to the value obtained experimentally, $\sim 1.28 \mu_B$. The experimental value of $\sim 1.28 \mu_B$ actually matches 52/48% ratio for spin 5/2 to spin 4/2 ions. Another observation is that there is no hysteresis in the isothermal magnetization data at 2 K or 400 K. The data collected while increasing the magnetic field from 0 T – 9 T overlap with the data obtained while decreasing the field from 9 T – 0 T. The absence of hysteresis in the isothermal magnetization at 2 K indicates that the ferrimagnetic interactions are not long-range, and occur in short-range scale, similar to the situation in superparamagnetic systems.¹⁷⁷

The significantly different magnetic properties between the two isostructural materials is interesting. The magnetic susceptibility of $\text{BaSrCo}_2\text{O}_{6-\delta}$ deviates from paramagnetism in the entire temperature range, 2- 400 K. The very low magnetization values even at 2 K and 9 T, indicate antiferromagnetic order in $\text{BaSrCo}_2\text{O}_{6-\delta}$, consistent with a report on a similar material. On the other hand, $\text{BaSrCoFeO}_{6-\delta}$ shows ferrimagnetic properties with large uncompensated moments and isothermal magnetization similar to that observed in superparamagnetic systems, indicating the presence of ferrimagnetic clusters.

Electrical conductivity

The electrical behavior of our samples was studied using DC method, as well as AC electrochemical impedance spectroscopy (EIS). In both methods, the resistance of a material is analyzed to get total conductivity. In AC impedance spectroscopy, the total impedance is generally measured as the low frequency intercept of arc on the real axis (Z') of a Nyquist plot. Whereas DC method requires a constant applied current or voltage to measure the output voltage or current, respectively. Consequently, the total conductivity (σ) is obtained by using the relation $\sigma = L/RA$, where L, R and A represent the thickness, resistance and cross-sectional area of the cylindrical pellet, respectively. The total conductivity values for $\text{BaSrCo}_2\text{O}_{6-\delta}$ and $\text{BaSrCoFeO}_{6-\delta}$ measured using both AC and DC methods at room temperature are listed in Table 8.3. The conductivity values measured by AC and DC methods are the same. Several interesting observations were made with regard to the electrical conductivity of these materials, as follows.

At room temperature, $\text{BaSrCoFeO}_{6-\delta}$ has higher electrical conductivity than $\text{BaSrCo}_2\text{O}_{6-\delta}$. The electrical conductivity in perovskite-based oxides occurs by electron hopping through M–O–M (metal-oxygen-metal) bonds. For this process to happen, metals with multiple oxidation states such as $\text{Fe}^{2+}/\text{Fe}^{3+}/\text{Fe}^{4+}$ or $\text{Co}^{2+}/\text{Co}^{3+}/\text{Co}^{4+}$ are required on the octahedrally coordinated B-site. In our materials, the metal 3d orbitals overlap with oxygen 2p orbitals, and electron hopping occurs through the (Fe/Co)–O–(Fe/Co) or Co–O–Co pathways. The extent of electronic conductivity is affected by the degree of M–O orbital overlap. Shorter M–O bond distance and larger M–O–M bond angles lead to better orbital overlap and higher conductivity.¹⁷⁸

In situations where structural transitions take place, the bond distances and angles are affected leading to changes in electrical conductivity.²⁰ An example is the structural transition between $\text{Sr}_2\text{Fe}_2\text{O}_{6-\delta}$ and $\text{CaSrFe}_2\text{O}_{6-\delta}$, where some bond angles in the latter become significantly small, leading to smaller degree of orbital overlap and lower conductivity at room temperature.²⁰

Table 8.3. Room Temperature Conductivity and Activation Energies.

compounds	total conductivity, σ (S cm^{-1})		Activation energy (E_a)
	AC	DC	
$\text{BaSrFeCoO}_{6-\delta}$	0.07368	0.07365	0.144 eV for 298-473 K (25-200 °C) 0.010 eV for 473-1173 K (200-900 °C)
$\text{BaSrCo}_2\text{O}_{6-\delta}$	0.000134	0.000133	0.218 eV for 298- 673 K (25-400 °C) 0.571 eV for 673-1173 K (400-900 °C)

However, the two materials investigated in the present study, $\text{BaSrCo}_2\text{O}_{6-\delta}$ and $\text{BaSrCoFeO}_{6-\delta}$, have the same crystal structure. The M–O–M bond angles are 180° in both compounds. Nevertheless, the size of the unit cell and bond lengths are slightly different between these two materials. $\text{BaSrCoFeO}_{6-\delta}$ has smaller unit cell and slightly shorter Fe(Co)–O bond distances, 1.9902(1) Å, as compared to those in $\text{BaSrCo}_2\text{O}_{6-\delta}$, 1.9920(1) Å. The improvement in conductivity as a result of decrease in unit cell parameters is expected, as observed in other materials such as $\text{SrFe}_{1-x}\text{Al}_x\text{O}_{3-\delta}$.¹³⁶ In addition, the degree of oxygen deficiency and cation combinations that form the conduction pathways in the two materials are different. Higher degree of oxygen deficiency is expected to decrease the number of conduction pathways. As outlined in the XPS section, $\text{BaSrCoFeO}_{6-\delta}$ has higher oxygen content and contains $\text{Fe}^{3+}/\text{Fe}^{4+}$ and $\text{Co}^{3+}/\text{Co}^{4+}$, while $\text{BaSrCo}_2\text{O}_{6-\delta}$ contains

$\text{Co}^{2+}/\text{Co}^{3+}$. The difference in the room temperature conductivity of these two materials is due to the combination of three factors, namely the subtle difference in bond distances, difference in concentration of oxygen vacancies and the dissimilarity of conduction pathways.

Variable-temperature conductivity studies in the temperature range 25 – 900 °C provide further insight into the properties of these two materials. The measurements were performed under the same conditions used for the synthesis of these materials, namely in air for $\text{BaSrCoFeO}_{6-\delta}$ and in argon for $\text{BaSrCo}_2\text{O}_{6-\delta}$ (Figure 8.6) However, we also performed conductivity measurements in argon atmosphere for $\text{BaSrCoFeO}_{6-\delta}$, which showed the same temperature-dependent trend as the air-measurement, but with lower overall conductivity (Figure 8.7).

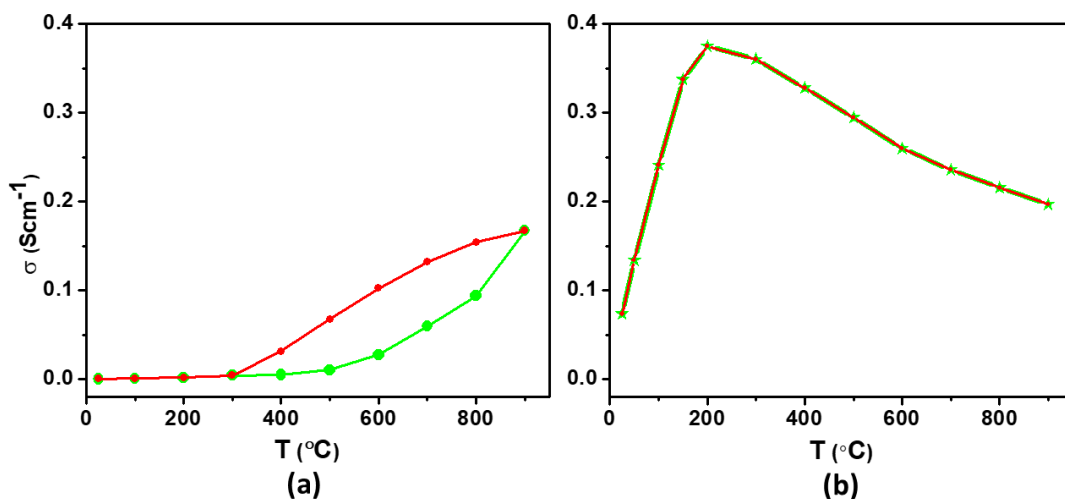


Figure 8.6. Electrical conductivity of (a) $\text{BaSrCo}_2\text{O}_{6-\delta}$ and (b) $\text{BaSrCoFeO}_{6-\delta}$. The measurements were done in the same environment used for synthesis, namely in argon for $\text{BaSrCo}_2\text{O}_{6-\delta}$ and in air $\text{BaSrCoFeO}_{6-\delta}$. Heating data are shown in green and the cooling data in red.

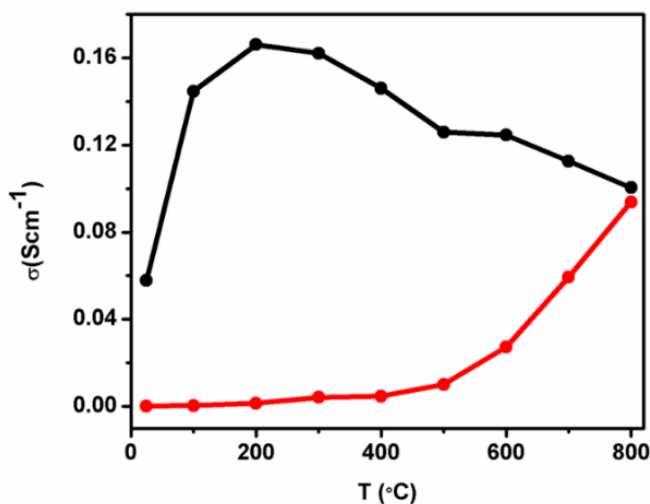


Figure 8.7. comparison of the electrical conductivity for BaSrCo₂O_{6-δ} and BaSrCoFeO_{6-δ} both obtained in argon atmosphere.

There is a sharp contrast between the BaSrCo₂O_{6-δ} and BaSrCoFeO_{6-δ} with regard to their electrical conductivity as a function of temperature. Comparison between the two materials reveals significant increase in conductivity as a function of temperature for BaSrCoFeO_{6-δ} up to 200 °C, whereas BaSrCo₂O_{6-δ} shows electrical conductivity which is nearly independent of temperature up to 400 °C. The retention of the same level of conductivity over a range of nearly 400 degrees can be a very useful property, especially in applications such as sensors where the change in conductivity should only be induced by the analyte and not temperature.

Above 400 °C, BaSrCo₂O_{6-δ} shows increase in conductivity, a typical behavior of semiconductors. However, BaSrCoFeO_{6-δ} exhibits a transition above 200 °C, where a downturn in conductivity begins and continues to 900 °C (Figure 8.6).

Another interesting feature of the electrical conductivity of BaSrCo₂O_{6-δ} is the distinct hysteresis between the conductivity data obtained during heating and cooling cycles.

(Figure 8.6) Whereas, BaSrCoFeO_{6-δ} shows nearly identical conductivity values during heating and cooling cycles. The temperature-activated enhancement of conductivity in BaSrCo₂O_{6-δ} is retained upon cooling the material, leading to the observation of hysteresis. The activation energies for electrical conductivity of both materials were also calculated using Arrhenius plots. The plots in Figure 8.8 were used for fitting with the Arrhenius equation for thermally activated conductivity,^{51, 179-180} as shown below:

$$\sigma T = \sigma^{\circ} e^{-E_a/kT} \quad (24)$$

where σ° is a pre-exponential factor and a characteristic of a material, and E_a , k , and T are the activation energy for the conductivity, Boltzmann constant, and absolute temperature, respectively. The activation energy for the total conductivity (E_a) can be obtained from the slope of the line of best fit in the $\log \sigma T$ vs $1000/T$ plot. As shown in Table 8.3, the E_a values are higher for BaSrCo₂O_{6-δ} compared to BaSrCoFeO_{6-δ}. Note that activation energies are dependent on the change in conductivity as a function of temperature. BaSrCo₂O_{6-δ} has very small conductivity at low temperature (in the order of 10^{-4} Scm⁻¹), and its conductivity increases to 0.167 Scm⁻¹ at high

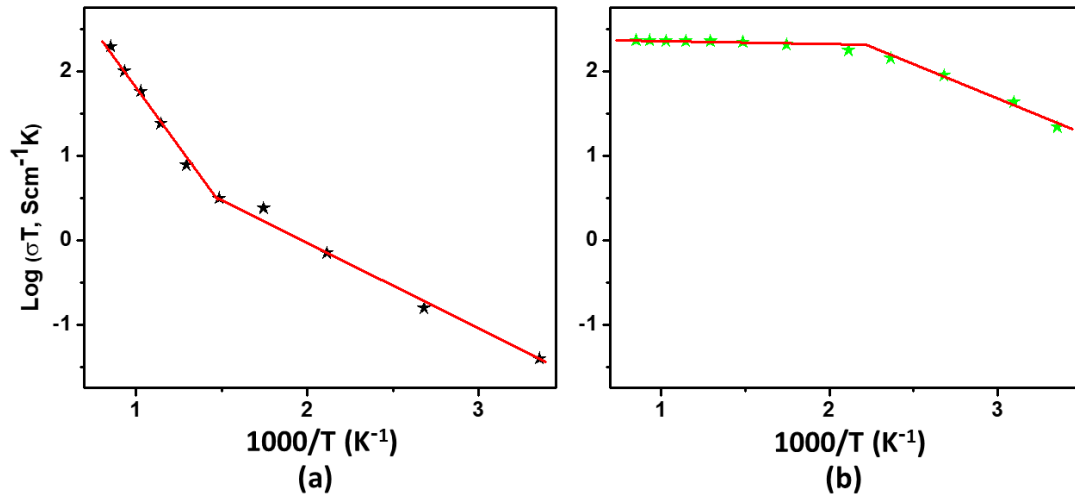


Figure 8.8. Arrhenius plot for electrical conductivity of (a) $\text{BaSrCo}_2\text{O}_{6-\delta}$ and (b) $\text{BaSrCoFeO}_{6-\delta}$.

temperature. Therefore, the change in conductivity as a function of temperature is large for this material. This leads to a large slope in the Arrhenius plot and higher activation energy for $\text{BaSrCo}_2\text{O}_{6-\delta}$. For $\text{BaSrCoFeO}_{6-\delta}$, the conductivity is higher, but the difference between the conductivity values at low and high temperature is not as significant as that of $\text{BaSrCo}_2\text{O}_{6-\delta}$.

CONCLUSIONS

The isostructural oxygen-deficient perovskites $\text{BaSrCo}_2\text{O}_{6-\delta}$ and $\text{BaSrCoFeO}_{6-\delta}$ show significant disparity in magnetic and electrical properties. The magnetic susceptibility of $\text{BaSrCo}_2\text{O}_{6-\delta}$ deviates from paramagnetism in the entire temperature range, 2 - 400 K. The very low magnetization values even at 2 K and 9 T, indicate antiferromagnetic order in $\text{BaSrCo}_2\text{O}_{6-\delta}$, consistent with a report on a similar material. On the other hand, $\text{BaSrCoFeO}_{6-\delta}$ shows ferrimagnetic properties with large uncompensated moments and isothermal magnetization reminiscent of superparamagnetic systems, indicating the

presence of ferrimagnetic clusters. The differences in electrical conductivity are also remarkable. $\text{BaSrCo}_2\text{O}_{6-\delta}$ shows nearly constant conductivity up to 400 C, followed by semiconducting properties above this temperature. Whereas the $\text{BaSrCoFeO}_{6-\delta}$ shows semiconducting properties up to 200 °C, above which a downturn in conductivity is observed, similar to metallic conductors.

CHAPTER 9
STRUCTURE DEPENDENCE OF ELECTRICAL CONDUCTIVITY AND
ELECTROCATALYTIC PROPERTIES OF $\text{Sr}_2\text{Mn}_2\text{O}_6$ AND $\text{CaSrMn}_2\text{O}_6$ ⁸

1. INTRODUCTION

Perovskite oxides exhibit a wide range of structural, electrical and magnetic properties.^{82, 147-148, 181} They have been studied for their potential applications in different technological fields, such as fuel cells, thermoelectric devices and sensors.^{148, 182-183} The structure and properties of perovskites can vary significantly^{4, 84-85, 92, 120, 184-186} upon variation of the A- or B-site cations in the ABO_3 formula, where the A-cations occupy the 12-coordinated sites located between the BO_6 octahedra.

Given the wide range of transition metal or main group cations that can reside on the B-site, the structural transformation upon B-site doping are frequently observed. Various parameters, such as ionic radius, oxidation state and electronic structure lead to these changes. For example, when Mn is substituted by Fe, the orthorhombic structure of CaMnO_3 ¹²⁴ transforms into the orthorhombic structure of a double perovskite, $\text{Ca}_2\text{FeMnO}_6$, with layered ordering.¹⁸⁷⁻¹⁸⁸ Similarly, $\text{Sr}_2\text{FeMoO}_6$ has a tetragonal structure, while the B-

⁸ The work described in this chapter was published in journal of Chemical Sciences (2019, vol 131, p 109)

site substituted Sr_2FeWO_6 is orthorhombic.¹⁸⁹ The structural transformation leads to significant variation in properties as well, where $\text{Sr}_2\text{FeMoO}_6$ behaves as a half metal and a ferromagnetic material, whereas Sr_2FeWO_6 shows insulating and antiferromagnetic properties.¹⁸⁹ Note that there are two B-site cations in these materials. In situations, where there are two crystallographically distinct positions for the A- or B-site cations, the general formula can be represented by $\text{AA}'\text{B}_2\text{O}_6$ and $\text{A}_2\text{BB}'\text{O}_6$, respectively.

There are also oxide materials where the general formula is similar to that of a typical perovskite, but the connectivity in their crystal lattice is different. An example is SrMnO_3 , better described as $\text{Sr}_2\text{Mn}_2\text{O}_6$ since it has two crystallographically distinct positions for Sr and two for Mn.¹⁸¹ Unlike typical perovskites that contain corner-sharing octahedra, this material has dimeric units of face-sharing MnO_6 octahedra.¹⁸¹ This compound has been of interest in recent years, given the potential of the Mn-based oxides for applications in areas such as sensing,¹⁸² spintronics¹⁹⁰ and solid oxide fuel cells.¹⁸³ Several substituted derivatives have been investigated, showing variations in structure and properties. For example, when 50% of Mn in $\text{Sr}_2\text{Mn}_2\text{O}_6$ is substituted by Fe, the crystal structure changes to a perovskite type system with corner-sharing octahedra.¹⁹¹ The structural transformation also leads to changes in magnetic properties, where the antiferromagnetic arrangement of Mn^{4+} magnetic moments¹⁸¹ in $\text{Sr}_2\text{Mn}_2\text{O}_6$ transforms into ferromagnetic arrangement upon partial substitution of Mn by Fe.¹⁹¹

It is also possible to partially or completely replace the A-site cation in $\text{Sr}_2\text{Mn}_2\text{O}_6$. For example, the Ba substitution on the A-site results in orthorhombic and rhombohedral structures for 50 % and 100 % substitutions, respectively.¹⁹² The structural transformation upon Ba-doping is followed by the change in electrical properties.¹⁹² It is also possible to

replace Sr^{2+} by a smaller cation, namely Ca^{2+} , to obtain $\text{CaSrMn}_2\text{O}_6$, which has a perovskite-type structure¹⁹³ unlike the parent Sr_2 compound. To our knowledge, the effect of doping a smaller A-site cation, i.e., Ca^{2+} , on charge transport properties of $\text{Sr}_2\text{Mn}_2\text{O}_6$ has not been investigated. In this paper, we report the remarkable structure-property relationships, where the structural changes prompted by the replacement of the A-site cation lead to significant enhancement of the electrical charge-transport and electrocatalytic activity. Dramatic increase in the electrical conductivity is observed over a wide range of temperature, due to Ca-doping. Furthermore, we have studied the electrocatalytic activity of both $\text{Sr}_2\text{Mn}_2\text{O}_6$ and $\text{CaSrMn}_2\text{O}_6$ for oxygen-evolution reaction, demonstrating the enhancement of catalytic properties in the latter compound.

2. EXPERIMENTAL

The materials $\text{Sr}_2\text{Mn}_2\text{O}_6$ and $\text{CaSrMn}_2\text{O}_6$ were synthesized in air by solid state method. Stoichiometric amounts of the powders of the precursor compounds CaCO_3 (Alfa Aesar, 99.95%), Mn_2O_3 (Alfa Aesar, 99.998%) and SrCO_3 (Sigma Aldrich, 99.99%) were mixed together using an agate mortar and pestle and pressed into a pellet which was calcined in air at 1000 °C for 24 h in order to decompose the carbonates and start the reaction. The samples were then ground and sintered at 1200 °C for 24 h in the same environment to complete the reaction and form pure products. Both heat treatments were followed by slow cooling. The heating and cooling rates were 100 °C/h. The phase purity and structure of the polycrystalline samples were examined by powder X-ray diffraction at room temperature using Cu $\text{K}\alpha_1$ radiation ($\lambda = 1.54056 \text{ \AA}$). The GSAS software¹⁰⁰ and EXPEGUI interface¹²⁵ were used for Rietveld refinements. The sample morphologies were studied using high resolution field-emission scanning electron microscopy (SEM). The

electrical properties were investigated by 4-point probe measurements. Electrical conductivity was measured at 100 °C intervals from 25 to 800 °C during both heating and cooling cycles. At each measurement point, the temperature was maintained constant until a plateau in conductivity was observed, before changing the temperature. The rate of heating and cooling for conductivity measurements was 3 °C/min. Oxygen contents of each material was determined by iodometric titration as explained elsewhere.^{88, 120, 130}

Electrocatalytic performances of the materials were measured in a three-electrode electrochemical workstation using a rotating disc electrode at 1600 rpm. A glassy carbon electrode loaded with catalysts, a commercial platinum electrode and Ag/AgCl (in 3 M NaCl) were used as working, counter and reference electrodes, respectively. For working electrode preparation, 35 mg of the sample and 20 µL of nafion (5% w/w in water/1-propanol) were mixed in 7 mL of THF and sonicated for 5 minutes. The catalyst ink was loaded onto the glassy carbon electrode (diameter 5 mm, area 0.196 cm²) by four subsequent coatings (each coating with 10 µL). OER was performed in 0.1 M KOH electrolyte which was deaerated by bubbling argon gas for at least 30 min before the measurement started. The cyclic voltammetry (CV) measurements were performed at a scan rate of 10 mV s⁻¹ from 0 to 0.8 V vs Ag/AgCl. The potential versus reversible hydrogen electrode (RHE) was calculated according to Nernst equation:

$$E_{\text{RHE}} = E_{\text{Ag/AgCl}} + 0.059 \text{ pH} + E^{\circ}_{\text{Ag/AgCl}} \quad (25)$$

3. RESULT AND DISCUSSION

3.1. Crystal structure

The X-ray diffraction studies demonstrate the structural changes due to the variation of the A-site cation in these $A_2B_2O_6$ compounds ($A_2 = Sr_2, CaSr$; $B = Mn$). The crystal structure of $Sr_2Mn_2O_6$ can be indexed on a hexagonal cell with space group $P6_3/mmc$, consistent with previous reports.¹⁸¹ Rietveld refinement profile and the refined structural parameters from powder X-ray diffraction data are shown in Figure 9.1 and Table 9.1, respectively. As seen in Figure 9.1, the structure of $Sr_2Mn_2O_6$ consists of dimeric units of face-sharing MnO_6 octahedra. Each dimer is connected to other dimers through corner-sharing, leading to a 3-dimensional network. As shown in Table 9.1, there are two crystallographically distinct Sr sites and two distinct Mn positions, hence the formula $Sr_2Mn_2O_6$. The crystal structure is transformed upon changing the A-site cations from Sr_2 to $CaSr$, as demonstrated in Figure 9.2. The Ca-containing compound, $CaSrMn_2O_6$, features a cubic $Pm-3m$ structure, where individual MnO_6 octahedra are all connected to each other through corner-sharing, consistent with a previous report.¹⁹³ There are no dimeric units in $CaSrMn_2O_6$, as shown in Figure 9.2. There is only one Mn position, and one A-site, jointly occupied by both Ca and Sr, as shown in Table 9.2 that lists the refined structural parameters for $CaSrMn_2O_6$.

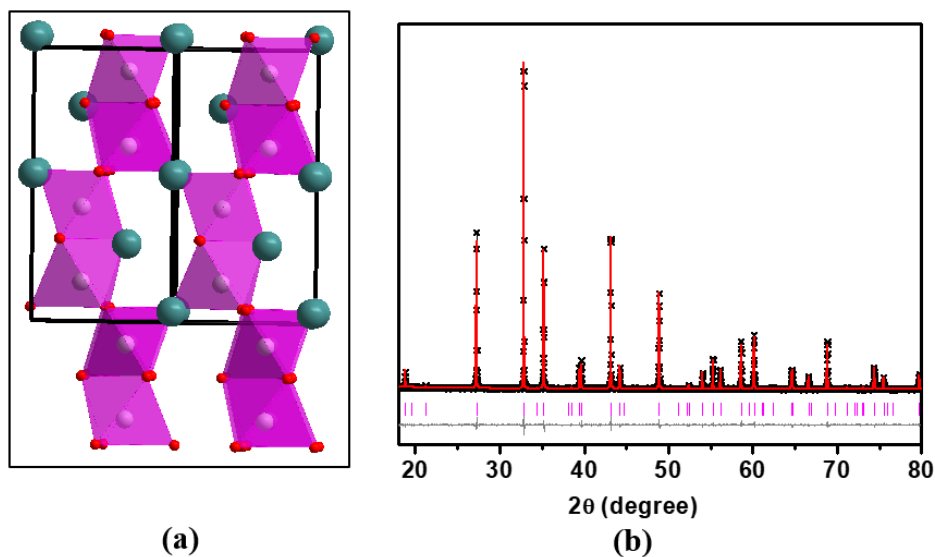


Figure 9.1. (a) Crystal structure and (b) Rietveld refinement profile from X-ray diffraction data for $\text{Sr}_2\text{Mn}_2\text{O}_6$, $P6_3/mmc$. Black crosses represent experimental data, the solid red line is the model, pink vertical tick marks show Bragg peak positions, and the lower grey line represents the difference plot.

Table 9.1. Refined structural parameters for $\text{Sr}_2\text{Mn}_2\text{O}_6$ using powder X-ray diffraction. Space group: $P6_3/mmc$, $a = b = 5.45233(8)\text{\AA}$, $c = 9.0856(1)\text{\AA}$, $R_p=0.030$, $wR_p= 0.038$, $\chi^2 = 1.790$

element	x	y	z	U_{iso}	occupancy	multiplicity
O1	0.191(8)	0.359(1)	0.298(2)	0.020(3)	1	6
O2	-0.021(3)	0.507(5)	0.049(2)	0.021(3)	1	6
Mn1	1/3	2/3	0.4160(8)	0.013(3)	1	2
Mn2	1/3	2/3	0.1412(8)	0.046(4)	1	2
Sr1	1/3	2/3	0.7850(9)	0.0271(7)	1	2
Sr2	0.0	0.0	0.039(1)	0.0298(7)	1	2

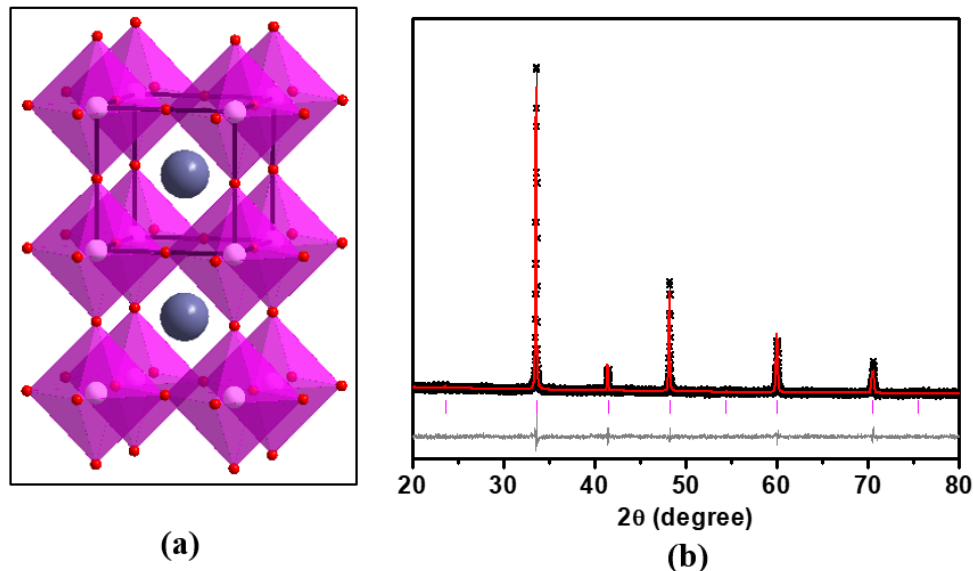


Figure 9.2. (a) Crystal structure and (b) Rietveld refinement profile from X-ray diffraction data for CaSrMn₂O₆, *Pm-3m*. Black crosses represent experimental data, the solid red line is the model, pink vertical tick marks show Bragg peak positions, and the lower grey line represents the difference plot.

Table 9.2. Refined structural parameters for CaSrMn₂O₆ using powder X-ray diffraction data. Space group: *Pm-3m*, $a = 3.7772(1)\text{\AA}$, $R_p = 0.051$, $wR_p = 0.064$, $\chi^2 = 1.406$

	x	y	z	U _{iso}	occupancy	multiplicity
O1	0.5	0.0	0.0	0.043(2)	1	3
Mn1	0.0	0.0	0.0	0.007(1)	1	1
Ca1	0.5	0.5	0.5	0.024(2)	0.5	1
Sr1	0.5	0.5	0.5	0.024(2)	0.5	1

We note that further substitution of Sr by Ca, beyond CaSrMn₂O₆, does not change the polyhedral connectivity. The completely substituted product, that contains only Ca on the A-site, contains the same type of corner-sharing connectivity as CaSrMn₂O₆, although the corner-sharing MnO₆ octahedra are somewhat distorted, leading to orthorhombic symmetry.¹⁹⁴ Nevertheless, the overall picture that emerges is that the transition from

$\text{Sr}_2\text{Mn}_2\text{O}_6$ to $\text{CaSrMn}_2\text{O}_6$ results in significant structural transformation, but further substitution of Sr by Ca does not have a substantial effect on the structure-type.

The Mn-O bond distances in $\text{Sr}_2\text{Mn}_2\text{O}_6$ vary widely, 1.81(2), 1.87(2), 1.91(2), and 2.03(2) Å, due to the existence of two types of polyhedral connectivity, namely face-sharing and corner-sharing. Given the structural differences between the two compounds, direct comparison of the bond distances is not warranted. However, the average Mn-O bond distance in $\text{Sr}_2\text{Mn}_2\text{O}_6$, 1.91 Å, is longer than that of $\text{CaSrMn}_2\text{O}_6$, 1.89 Å. Furthermore, the Mn-O-Mn bond angles in $\text{Sr}_2\text{Mn}_2\text{O}_6$ can be as small as $80.9(3)^\circ$ due to the face-sharing in octahedral dimers. The angle between the corner-sharing octahedra in $\text{Sr}_2\text{Mn}_2\text{O}_6$ is Mn-O-Mn = $166(1)^\circ$. However, $\text{CaSrMn}_2\text{O}_6$ contains only one type of Mn-O-Mn angle, which is 180° , as expected from a cubic perovskite structure.

3.2. Electrical properties

Changes in composition, and the subsequent variation of the crystal structure lead to significant changes in the electrical properties, which were studied by four probe technique. The electrical conductivity (σ) is obtained from the measured resistance (R), using the following equation:¹⁹⁵

$$\sigma = L/RA \quad (26)$$

where L is the voltage probe spacing and A represents the cross-sectional area of the rectangular pellet where the current probes are connected. The remarkable effect of structural transformation is immediately clear from the improvement in the electrical conductivity by five orders of magnitude, $4.5 \times 10^{-1} \text{ S cm}^{-1}$ for $\text{CaSrMn}_2\text{O}_6$, compared to

$1.0 \times 10^{-6} \text{ S cm}^{-1}$ for $\text{Sr}_2\text{Mn}_2\text{O}_6$ at room temperature. The electrical conductivity in oxide materials occurs through M–O–M pathways, where M is the transition metal. It has been demonstrated that larger bond angles lead to enhanced electrical conductivity due to the improved overlap between the metal 3d band and oxygen 2p band.¹³⁵ The change in crystal structure between $\text{Sr}_2\text{Mn}_2\text{O}_6$ and $\text{CaSrMn}_2\text{O}_6$ clearly leads to the enhancement of the Mn–O–Mn bond angles. The face sharing of MnO_6 octahedra in $\text{Sr}_2\text{Mn}_2\text{O}_6$ results in bond angles as small as $80.9(3)^\circ$, as described in the previous section. However, the Mn–O–Mn bond angles in $\text{CaSrMn}_2\text{O}_6$ are 180.0° , due to the cubic structure and corner-sharing between the octahedra.

The superior electrical conductivity of $\text{CaSrMn}_2\text{O}_6$ persists at higher temperature, as evident from the results of conductivity studies in a wide temperature range, 25 – 800 °C, shown in Figure 9.3. Both compounds show increase in conductivity as a function of temperature, a behavior typical of semiconductors. The increase in temperature results in the loss of oxygen and reduction of some of Mn^{4+} ions into Mn^{3+} , leading to facile charge transport through the resultant $\text{Mn}^{4+}\text{--O--Mn}^{3+}$ pathways. In addition, the oxide ion conductivity is enhanced due to the creation of lattice defects upon oxygen loss. Furthermore, the rise in temperature leads to an increase in the mobility of charge carriers, which in turn results in the enhancement of the electrical conductivity as described by the equation: 7

$$\sigma = ne\mu \quad (27)$$

where σ , n , e , and μ are the conductivity, concentration of charge carriers (electrons/holes), charge of the electron, and mobility of the charge carriers, respectively.

The activation energy for the increase in electrical conductivity as a function of temperature can be found using the Arrhenius equation for thermally activated conductivity:⁴⁹⁻⁵¹

$$\sigma T = \sigma^0 e^{\frac{-E_a}{kT}} \quad (28)$$

where σ^0 is a preexponential factor and a characteristic of the material. E_a , k , and T are the activation energy for the increase in conductivity, Boltzmann constant, and absolute temperature, respectively. The activation energy (E_a) is calculated from the slope of the line of best fit in the $\log \sigma T$ versus $1000/T$ plot (Figure 9.3). The E_a values for the sharp rise in conductivity above 500 °C are 0.687 eV for $\text{Sr}_2\text{Mn}_2\text{O}_6$ and 0.449 eV for $\text{CaSrMn}_2\text{O}_6$.

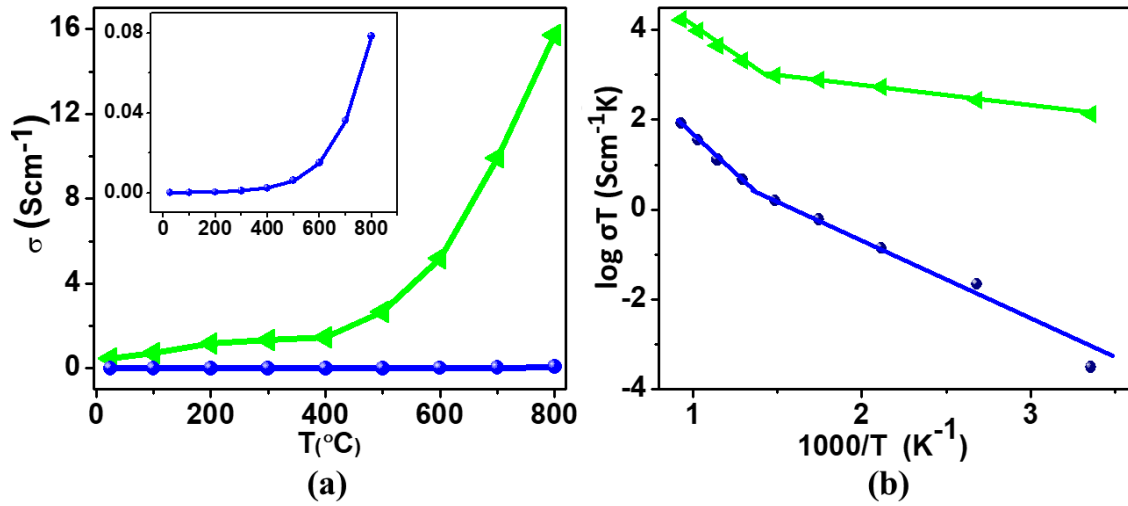


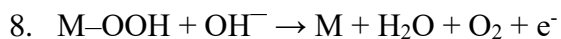
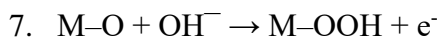
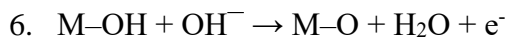
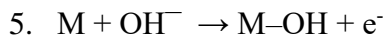
Figure 9.3. (a) Temperature dependent electrical conductivity and (b) Arrhenius plots for $\text{Sr}_2\text{Mn}_2\text{O}_6$ (blue circles) and $\text{CaSrMn}_2\text{O}_6$ (green triangles). The inset in (a) is a zoomed view of the increase in conductivity of $\text{Sr}_2\text{Mn}_2\text{O}_6$.

Table 9.3. Room temperature conductivity and activation energies.

	Conductivity, σ (Scm^{-1})	Activation energy, E_a (eV)
$\text{Sr}_2\text{Mn}_2\text{O}_6$	1.0×10^{-6}	0.382 eV for 25 to 500 °C 0.687 eV for 500 to 800 °C
$\text{CaSrMn}_2\text{O}_6$	4.5×10^{-1}	0.093 eV for 25 to 400 °C 0.449 eV for 400 to 800 °C

3.3. Correlation between electrocatalytic activity and conductivity

The electrocatalytic activity of these materials for oxygen evolution reaction (OER) was studied by cyclic voltammetry in alkaline medium. The OER mechanism in alkaline solution has been examined by several researchers.^{26-27, 196} The commonly accepted mechanism involves four steps, where there is a single electron transfer in each step.^{26-27, 196} In the first step, the reaction initiates by the adsorption of OH^- on the active site of the catalyst, i.e., metal site, M.^{27, 196} In the second step, a hydroxide from the electrolyte abstracts a proton from M-OH to form M-O and water. In the third step, M-O combines with a hydroxide to form a peroxide. Finally, in the fourth step, the peroxide intermediate reacts with OH^- to give an oxygen and water and regenerate the catalyst.



The conventional technique for investigation of OER activity involves the addition of carbon black to the electrode composition in order to enhance the electrical conductivity within the electrode and maximize the utilization of the catalyst.¹⁹⁷⁻¹⁹⁹ However, recent studies have shown that the role of carbon is more complex than a simple enhancement of conductivity.²⁰⁰⁻²⁰¹ For example, it has been shown that cobalt in an OER catalyst is reduced by carbon during the composite preparation process.²⁰² Therefore, OER

experiments without carbon black are preferred,¹³⁵ in order to examine the intrinsic catalytic activity of a material, without interference from carbon.²⁰³ The two materials studied in this work demonstrate the effect of crystal structure and electrical conductivity on OER activity. As observed from Figure 9.4, $\text{CaSrMn}_2\text{O}_6$ shows significantly enhanced onset potential, ~ 1.55 V, compared to $\text{Sr}_2\text{Mn}_2\text{O}_6$, ~ 1.65 V. While these onset potentials are not as good as those of the state of the art catalysts materials, such as RuO_2 , ~ 1.45 V,¹¹⁹ IrO_2 , ~ 1.50 V,¹¹⁹ and BSCF, ~ 1.53 V,²⁰⁴ they are comparable to or better than those of several other reported catalysts, such as CaMnO_3/C (1.6 V),¹¹⁹ Co-based microporous polymers, 1.57 V,²⁰⁵ and Co-phthalocyanine, 1.70 V.²⁰⁵ We have also determined the mass activity of each catalyst, using the catalyst loading mass on the electrode surface (0.2 mg cm^{-2}) and the measured current density for that electrode J (mA cm^{-2}). The inset in Figure 9.4 compares the OER mass activity of the two materials at 1.80 V vs RHE. As observed in this figure, $\text{CaSrMn}_2\text{O}_6$ shows mass activity of 0.42 A/g, compared to 0.28 A/g for $\text{Sr}_2\text{Mn}_2\text{O}_6$.

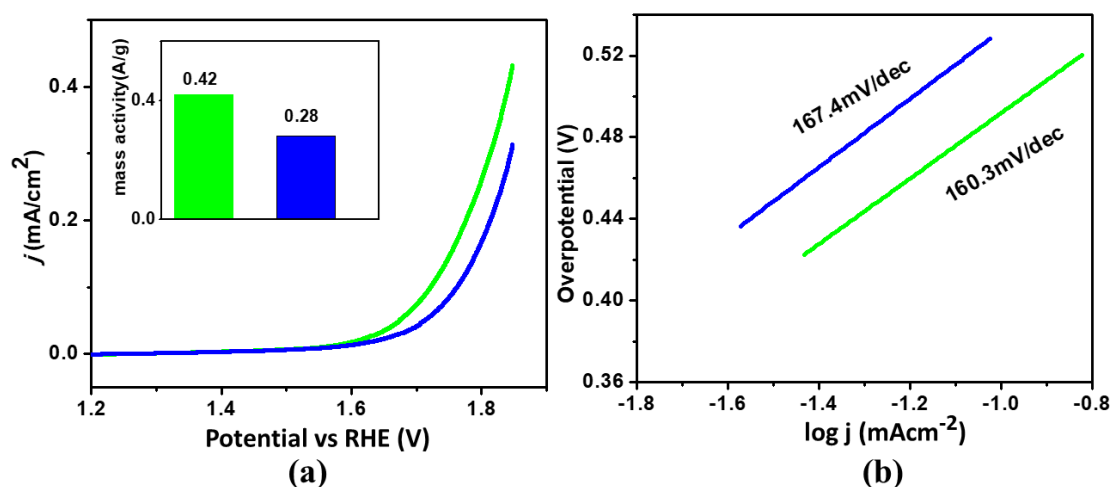


Figure 9.4. (a) Polarization curves for OER with mass activities for $\text{Sr}_2\text{Mn}_2\text{O}_6$ (blue) and $\text{CaSrMn}_2\text{O}_6$ (green). (b) Tafel slopes for $\text{Sr}_2\text{Mn}_2\text{O}_6$ (blue) and $\text{CaSrMn}_2\text{O}_6$ (green).

The kinetics of OER is usually examined using the Tafel equation $\eta = a + b \log j$ where η is the overpotential, and j is the current density.²⁰⁶⁻²⁰⁷ The plot is obtained from the curved portion of the OER cyclic voltammogram, as commonly done in OER analysis.²⁰⁸⁻²⁰⁹ The slope of the Tafel plot, η vs. $\log j$, is used as a measure for the reaction kinetics and is influenced by electron and mass transport ability of the catalyst.²¹⁰⁻²¹¹ Smaller slope is associated with faster reaction, and indicates that once the reaction commences, it proceeds quickly without the need for significant increase in potential.²¹² In other words, small increase in potential leads to the generation of significant current by OER process due to the fast kinetics of the reaction. Small change in potential accompanied by large increase in current results in a small slope in the plot of η vs. $\log j$. The Tafel slopes (Figure 9.4) for $\text{CaSrMn}_2\text{O}_6$ and $\text{Sr}_2\text{Mn}_2\text{O}_6$ are 160.3 mV/dec and 167.4 mV/dec, respectively, consistent with the greater OER activity of $\text{CaSrMn}_2\text{O}_6$ and the improved charge transport in this compound. These Tafel slopes are higher than those observed for highly active catalysts such as BSCF (87 mv/dec).²⁰³ However, they are lower than the Tafel slopes for several other OER catalysts reported in the literature, with values ranging from 220 mV/dec,²¹³ to 184 mV/dec,²¹⁴ and 169 mV/dec.²¹⁵ The relationship between the electrical conductivity and OER activity is remarkable. $\text{CaSrMn}_2\text{O}_6$, which has superior electrical conductivity, also shows higher OER activity compared to $\text{Sr}_2\text{Mn}_2\text{O}_6$. These findings demonstrate an interesting correlation between crystal structure, electrical conductivity and electrocatalytic properties. The modification of the crystal structure can be used as a tool to enhance the electrical conductivity, which in turn can have an impact on the electrocatalytic properties.

4. CONCLUSION

The substitution of 50% of the A-site cations in $\text{Sr}_2\text{Mn}_2\text{O}_6$ results in the formation of $\text{CaSrMn}_2\text{O}_6$, which features a different crystal structure and polyhedral connectivity. The change in the crystal structure leads to a significantly improved electrical conductivity in $\text{CaSrMn}_2\text{O}_6$. Variable-temperature electrical conductivity measurements indicate that the higher conductivity of $\text{CaSrMn}_2\text{O}_6$ persists up to 800 °C. The enhanced conductivity in turn results in superior catalytic activity of $\text{CaSrMn}_2\text{O}_6$ for oxygen evolution reaction. These findings indicate the dependence of the electrical conductivity on crystal structure, and the correlation between structure, charge-transport and electrocatalytic activity.

CHAPTER 10

VARIATION IN ELECTRICAL CONDUCTIVITY OF $A_2Fe_2O_5$ (A=Sr, Ba)⁹

INTRODUCTION

Oxygen deficient perovskites (ODPs) are an important component of solid oxide fuel cells.¹⁶³ They have also been studied for application as gas sensors,¹⁶¹ gas diffusion membranes,¹⁶² and photocatalysts.²¹⁶ Given the structure-property relationship in ODPs, it is important to study the variation in structural order and its impact on the properties of this class of materials. ODPs have the general formula ABO_{3-x} ($A_2B_2O_{6-y}$) where A is usually an alkaline earth metal or lanthanide, and B is a transition metal. As a result of oxygen deficiency, some vacancies are created and some of the BO_6 octahedra are converted into other coordination geometries such as BO_4 tetrahedra or BO_5 square pyramids.⁴ In some cases, the vacant sites appear in random locations within the crystal lattice, and no structural order is present.^{12, 76, 87, 89}

However, the ordered arrangement of the vacant sites is also common.^{4, 72-75, 84} The structural order can be manipulated by substitution on the B-site. For example, $Sr_2Fe_2O_{6-\delta}$ ^{4, 83} and $Sr_2FeMnO_{6-\delta}$ ⁸⁹ synthesized under the same condition, i.e., 1250 °C in air, have

⁹ The work described in this chapter was published in Material Research Express (2018, vol. 5, p. 9076307)

remarkably different structure and properties. $\text{Sr}_2\text{Fe}_2\text{O}_{6-\delta}$ has a tetragonal $I4/mmm$ structure, where vacancy-order leads to the formation of alternating FeO_6 octahedra and FeO_5 square pyramids.^{4, 83} In $\text{Sr}_2\text{FeMnO}_{6-\delta}$, on the other hand, the vacancy order is eliminated and a cubic $Pm-3m$ structure is formed.⁸⁹ These structural changes affect the magnetic properties, where the spin-density wave state in $\text{Sr}_2\text{Fe}_2\text{O}_{5.75}$ ²¹⁷ changes into an inhomogeneous magnetic ground state.⁸⁹

Changes in structural order can also occur due to substitution on the A-site. For example, $\text{Sr}_2\text{FeCoO}_5$, CaSrFeCoO_5 , and $\text{Ca}_2\text{FeCoO}_5$ have significantly different crystal structures.⁸⁴ $\text{Sr}_2\text{FeCoO}_5$ lacks any long-range order and has a cubic $Pm-3m$ structure, whereas CaSrFeCoO_5 exhibits structural order with orthorhombic $Ibm2$ space group.⁸⁴ $\text{Ca}_2\text{FeCoO}_5$ has an even greater degree of ordering and crystallizes in $Pbcm$ space group.^{73-74, 84} These variations in crystal structure lead to differences in electrical conductivity, highlighting the strong structure-property correlations in these compounds.⁸⁴

In this paper, we have studied the electrical properties of $\text{Sr}_2\text{Fe}_2\text{O}_5$ and $\text{Ba}_2\text{Fe}_2\text{O}_5$, that feature drastic differences in structural order and electrical charge transport, as a result of variation in A-site cation.

EXPERIMENTAL

The materials $\text{Ba}_2\text{Fe}_2\text{O}_5$ and $\text{Sr}_2\text{Fe}_2\text{O}_5$ were synthesized under identical conditions through solid state method. The powders of the precursor compounds BaCO_3 (Alfa Aesar, 99.95%), SrCO_3 (Aldrich, 99.9%), and Fe_2O_3 (Alfa Aesar, 99.998%) were mixed and ground together using agate mortar and pestle, pressed into a pellet, and heated in argon at 1200 °C for 24 h. The samples were then reground and refired at 1200 °C for 24 h under the same condition, followed by slow cooling. The heating and cooling rates were 100 °C/h. The

phase purity and structure of the polycrystalline samples were determined by powder X-ray diffraction (XRD) using Cu K α 1 radiation ($\lambda = 1.54056 \text{ \AA}$). The GSAS software¹⁰⁰ EXPEGUI interface¹⁰¹ were used for Rietveld refinements. The sample morphologies were studied using high resolution field-emission scanning electron microscopy (SEM). X-ray photoelectron spectroscopy (XPS) was performed at room temperature using Al K α radiation (1486.7 eV) to study the oxidation states of Fe. The electrical properties were investigated by direct-current (dc) and alternating-current (ac) conductivity measurements on as-prepared pellets that had been sintered at 1100 °C. Electrochemical impedance spectroscopy was performed in the frequency range of 0.1Hz to 1.0 MHz using a computer-controlled frequency response analyzer at room temperature. The two-probe dc measurements were performed in the temperature range of 25 – 900 °C by applying a constant voltage of 10 mV and collecting the output current. Variable-temperature electrical conductivity measurements were carried out during both heating and cooling cycles. The rate of heating and cooling for conductivity measurements was 3 °C/min. Iodometric titrations were performed by dissolving about 50 mg of the sample and excess KI (~2 g) in 100 mL of 1M HCl. A total of 5 mL of the solution was then pipetted out, and the iodine that had been generated in the solution was titrated against 0.025 M Na₂S₂O₃. Near the end point of the titration, 0.2mL of a starch solution was added to act as an indicator. All steps were performed under argon atmosphere. Magnetic susceptibility data were obtained using vibrating sample magnetometry by applying magnetic field of 0.1 T in the temperature range 2 – 400 K. Isothermal magnetization data were obtained at 5 K and 300 K using the magnetic field of 0 – 9 T.

RESULTS AND DISCUSSION

Crystal structure

The crystal structure of the two compounds were confirmed using X-ray diffraction and were consistent with reported structures of these materials.^{218-219,14} Despite being synthesized under identical conditions, $\text{Sr}_2\text{Fe}_2\text{O}_5$ and $\text{Ba}_2\text{Fe}_2\text{O}_5$ have remarkably different crystal structures. Figures 10.1 and 10.2 show Rietveld refinement profiles and crystal structures of the two compounds. $\text{Sr}_2\text{Fe}_2\text{O}_5$ features alternating layers of FeO_6 octahedra and FeO_4 tetrahedra, as shown in Figure 10.1. This is the brownmillerite-type structure, which is one of the common variations of oxygen-deficient perovskites. The refined structural parameters for $\text{Sr}_2\text{Fe}_2\text{O}_5$ are listed in Table 10.1.

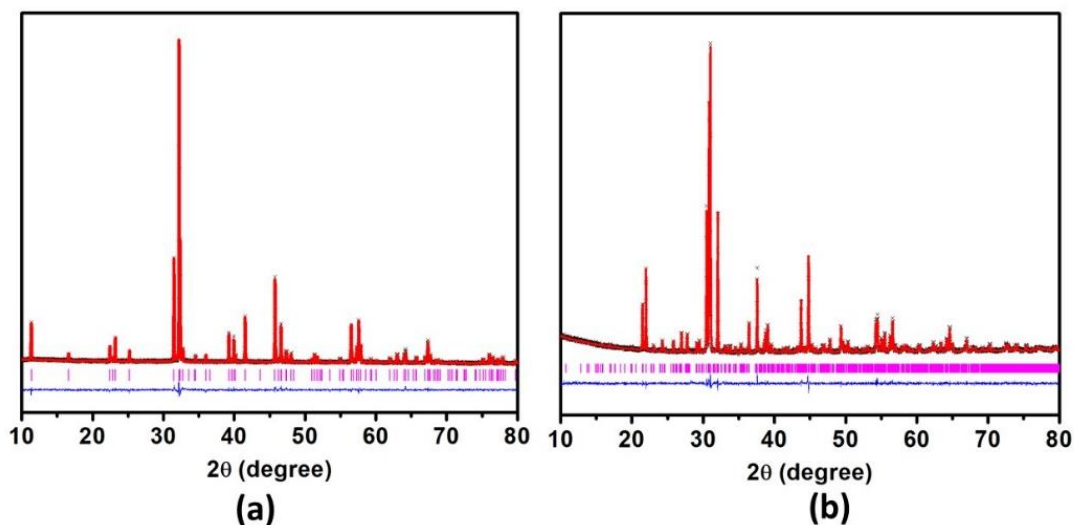


Figure 10.1. Rietveld refinement profile for powder XRD data of (a) $\text{Sr}_2\text{Fe}_2\text{O}_5$, with *Ibm2* space group and (b) $\text{Ba}_2\text{Fe}_2\text{O}_5$ with monoclinic *P2₁/c* space group. The solid red line shows the refinement model, black crosses represent experimental data, pink vertical tick marks show Bragg peak positions, and the lower blue line represents the difference plot.

Table 10.1. Refined structural parameters for $\text{Sr}_2\text{Fe}_2\text{O}_5$ using powder X-ray powder diffraction. Space group is $Ibm2$, and unit cell parameters are $a = 5.68023(6)$, $b = 15.5862(2)$, $c = 5.53425(6)$ Å.

Element	x	y	z	U_{iso}	Occupancy	Multiplicity
Sr1	0.0159(5)	0.1094(1)	0.498(3)	0.0130(9)	1	8
Fe1	0.0	0.0	0.0	0.0128(2)	1	4
Fe2	0.9356(9)	0.25	0.962(3)	0.021(3)	1	4
O1	0.268(4)	0.9904(6)	0.260(9)	0.03	1	8
O2	0.051(2)	0.1396(4)	0.028(4)	0.03	1	8
O3	0.855(3)	0.25	0.622(4)	0.03	1	4

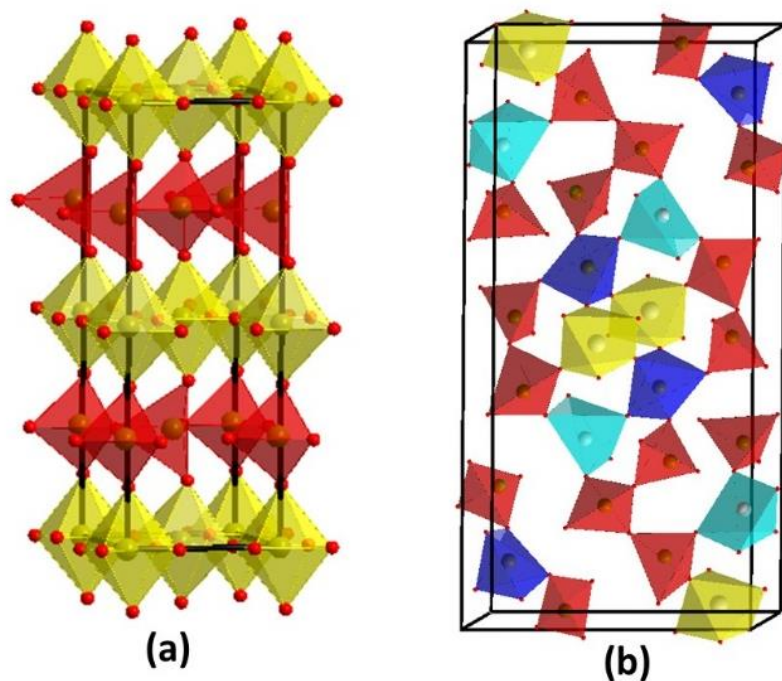


Figure 10.2. Crystal structures of (a) $\text{Sr}_2\text{Fe}_2\text{O}_5$ and (b) $\text{Ba}_2\text{Fe}_2\text{O}_5$.

The crystal structure of $\text{Ba}_2\text{Fe}_2\text{O}_5$ is entirely different and contains a complex array of tetrahedral, square-pyramidal and octahedral coordination geometries around Fe atoms.²¹⁸⁻²¹⁹ Our Rietveld refinement results confirm this complex structure. Tables 10.2 and 10.3 list the refined atomic positions, coordination geometries and bond distances for Fe atoms. There are seven crystallographically distinct Fe sites in $\text{Ba}_2\text{Fe}_2\text{O}_5$. They include four tetrahedral, two square-pyramidal and one octahedral Fe position.

Each FeO_n polyhedron ($n = 4, 5, 6$) shares corners with other types of polyhedra, as well as polyhedra of the same type, as shown in Figures 10.2 and 10.3. For example, each FeO_6 octahedron shares corners with one FeO_6 octahedron, two FeO_4 tetrahedra and three FeO_5 square-pyramids. In the crystal lattice, the FeO_6 octahedra and FeO_5 square-pyramids share all of their apexes with other polyhedra, whereas some of the FeO_4 tetrahedra have one unshared corner. Table 10.4 lists the connectivity between different polyhedra.

Table 10.2. Refined structural parameters for Ba₂Fe₂O₅ using powder X-ray powder diffraction. Space group is *P2*₁/*c* and unit cell parameters are *a* = 6.9772(1), *b* = 11.7376(2), *c* = 23.4575(4) Å, and β = 98.7540(8)°.

Element	x	y	z	U _{iso}	Occupancy	Multiplicity
Ba1	0.054(2)	0.354(1)	0.1148(5)	0.008(4)	1	4
Ba2	0.250(2)	0.614(1)	0.3290(6)	0.027(5)	1	4
Ba3	0.133(2)	0.131(1)	0.3219(5)	0.018(5)	1	4
Ba4	0.322(2)	0.633(1)	0.0391(7)	0.034(5)	1	4
Ba5	0.052(2)	0.615(1)	0.6014(7)	0.012(4)	1	4
Ba6	0.555(2)	0.351(1)	0.2575(6)	0.025(5)	1	4
Ba7	0.351(2)	0.110(1)	0.0357(8)	0.017(4)	1	4
Fe1	0.532(4)	0.364(3)	0.100(2)	0.024(8)	1	4
Fe2	0.385(4)	0.580(3)	0.188(2)	0.024(8)	1	4
Fe3	0.074(4)	0.395(3)	0.258(2)	0.014(7)	1	4
Fe4	0.179(5)	0.155(3)	0.472(2)	0.03(1)	1	4
Fe5	0.427(5)	0.384(3)	0.399(2)	0.014(7)	1	4
Fe6	0.269(5)	0.102(3)	0.176(2)	0.030(7)	1	4
Fe7	0.135(6)	0.624(3)	0.466(2)	0.030(7)	1	4
O1	0	0	0	0.03	1	2
O2	0.28(2)	0.721(9)	0.152(5)	0.03	1	4
O3	-0.04(1)	0.272(9)	0.236(5)	0.03	1	4
O4	0.04(1)	0.046(7)	0.419(4)	0.03	1	4
O5	-0.00(2)	0.25(1)	-0.006(5)	0.03	1	4
O6	0.28(2)	0.51(1)	0.426(6)	0.03	1	4
O7	0.72(2)	0.273(9)	0.069(5)	0.03	1	4
O8	0.05(2)	0.12(1)	0.109(7)	0.03	1	4
O9	0.40(2)	-0.022(9)	0.136(5)	0.03	1	4
O10	0.40(2)	0.261(8)	0.150(5)	0.03	1	4
O11	0.13(2)	-0.001(9)	0.207(5)	0.03	1	4
O12	0.48(1)	0.13(1)	0.253(5)	0.03	1	4
O13	0.17(1)	0.490(9)	0.207(5)	0.03	1	4
O14	0.55(1)	0.491(9)	0.146(4)	0.03	1	4
O15	0.28(2)	0.26(1)	0.418(6)	0.03	1	4
O16	0.37(2)	0.390(8)	0.034(7)	0.03	1	4
O17	0.26(1)	0.372(9)	0.311(5)	0.03	1	4
O18	0.67(2)	0.353(8)	0.465(7)	0.03	1	4

Table 10.3. Different coordination geometry and bond distances of Fe in Ba₂Fe₂O₅.

Central atom	Coordination number	Coordination geometry	Fe-O distance in Å			
Fe1	4	Tetrahedral	O7	O10	O14	
			O16	1.9 (1)	2.0 (1)	1.8 (1)
Fe2	4	Tetrahedral	O2	O12	O13	
			O14	2.0 (1)	1.7 (1)	2.0 (1)
Fe3	4	Tetrahedral	O3	O11	O13	
			O17	1.7(1)	2.1(1)	1.8(1)
Fe4	4	Tetrahedral	O4	O5	O15	
			O16	2.0(9)	1.8(1)	2.0(1)
Fe5	5	Pseudo square pyramidal	O6	O9	O15	O17
			O18	2.0(1)	1.9(1)	1.9(1)
Fe6	5	Square pyramidal	O8	O9	O10	O11
			O12	2.0(2)	2.0(1)	2.2(1)
Fe7	6	Distorted octahedral	O1	O5	O6	O7
			O8	O18	2.0(1)	2.0(1)
			2.0(2)	2.0(1)		

Table 10.4. The connectivity of polyhedra in $\text{Ba}_2\text{Fe}_2\text{O}_5$.

Polyhedron	Corner shared to polyhedra of:
Fe1 (tetrahedron)	Fe2, Fe4, Fe6, Fe7
Fe2 (tetrahedron)	Fe1, Fe3, Fe6
Fe3 (tetrahedron)	Fe2, Fe5, Fe6
Fe4 (tetrahedron)	Fe1, Fe5, Fe7
Fe5 (pseudo square pyramid)	Fe6, Fe7, Fe7, Fe4, Fe3
Fe6 (square pyramid)	Fe1, Fe2, Fe3, Fe5, Fe7
Fe7 (distorted octahedron)	Fe1, Fe4, Fe5, Fe5, Fe6, Fe7

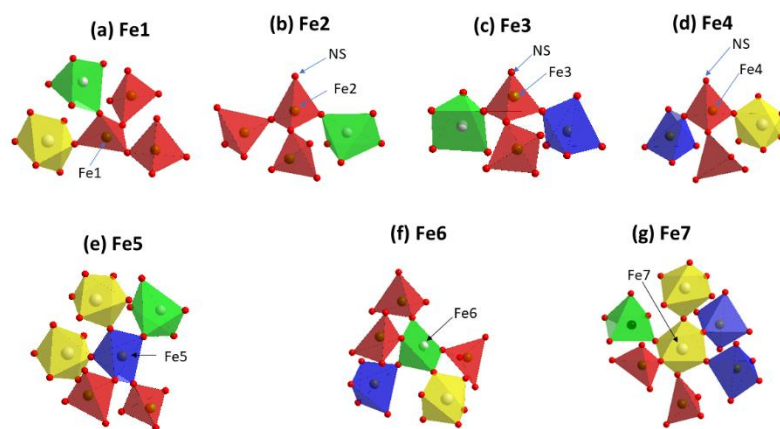


Figure 10.3. The coordination geometry of 7 crystallographically distinct Fe atoms and the connectivity of polyhedra in $\text{Ba}_2\text{Fe}_2\text{O}_5$. Red, green, blue and yellow polyhedra represent tetrahedral, square pyramidal, pseudo square pyramidal and octahedral geometry, respectively (NS = not shared with other polyhedra).

The morphologies of sintered pellets of the two materials were studied by scanning electron microscope (SEM). Figure 10.4 compares the SEM images of $\text{Ba}_2\text{Fe}_2\text{O}_5$ and $\text{Sr}_2\text{Fe}_2\text{O}_5$. As seen here, $\text{Ba}_2\text{Fe}_2\text{O}_5$ is more porous and has smaller crystallite size compared to $\text{Sr}_2\text{Fe}_2\text{O}_5$. The crystallites are more densely packed in $\text{Sr}_2\text{Fe}_2\text{O}_5$.

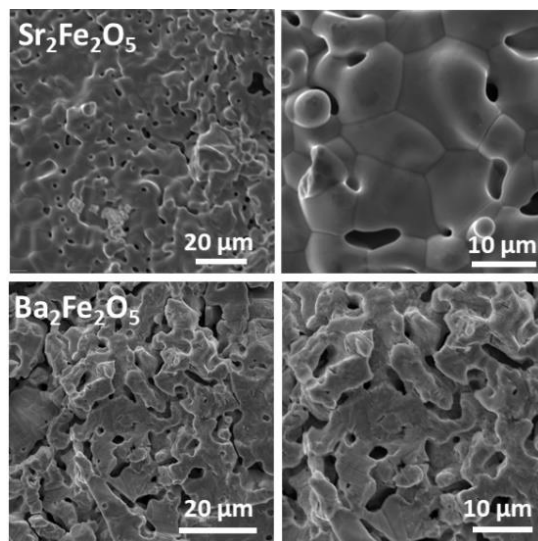


Figure 10.4. Scanning electron microscopy images of $\text{Sr}_2\text{Fe}_2\text{O}_5$ (top) and $\text{Ba}_2\text{Fe}_2\text{O}_5$ (bottom)

Oxidation state of Fe

The oxidation state of Fe in both compounds was analyzed by X-ray Photoelectron Spectroscopy (XPS). The $2\text{P}_{3/2}$ peak for Fe^{3+} usually appears at $\sim 710 - 711$ eV, and a satellite peak is usually present at about $7 - 9$ eV higher than the $2\text{P}_{3/2}$ peak.^{43-44, 103-104, 220}

Both $\text{Ba}_2\text{Fe}_2\text{O}_5$ and $\text{Sr}_2\text{Fe}_2\text{O}_5$ show the $2\text{P}_{3/2}$ peak at ~ 710 eV and the signature satellite peak at about ~ 718 eV, indicative of Fe^{3+} (Figure 10.5). This is expected, as both compounds were synthesized in argon atmosphere with Fe_2O_3 as starting material. Given the inert synthesis condition, the retention of the trivalent state for iron was anticipated.

We also confirmed these findings by performing iodometric titrations, which showed oxygen stoichiometry of 5.06 and 5.02 per formula unit of $\text{Sr}_2\text{Fe}_2\text{O}_5$ and $\text{Ba}_2\text{Fe}_2\text{O}_5$, respectively, consistent with Fe in trivalent oxidation state.

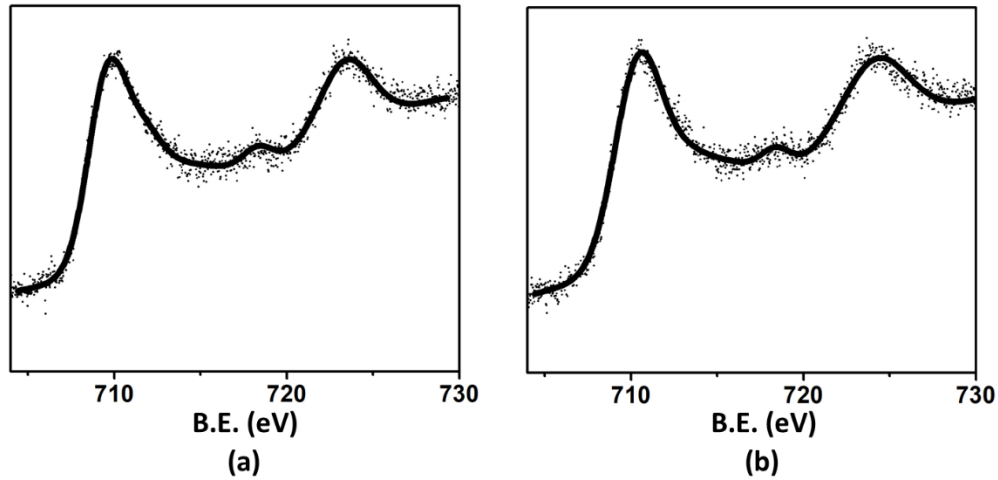


Figure 10.5. X-ray photoelectron spectroscopy data for (a) $\text{Sr}_2\text{Fe}_2\text{O}_5$ and (b) $\text{Ba}_2\text{Fe}_2\text{O}_5$.

Magnetic properties

Previous reports^{219, 221} have shown that both of these materials have antiferromagnetic order with Neel temperature of ~ 693 K and 720 K for $\text{Sr}_2\text{Fe}_2\text{O}_5$ ²²¹ and $\text{Ba}_2\text{Fe}_2\text{O}_5$,²¹⁹ respectively. We performed isothermal magnetization measurements using magnetic field of up to 9 T on both materials. As shown in Figure 10.6, the magnetization of both materials shows linear field-dependent behavior. However, the difference in structural order has an impact on the magnitude of magnetization. At the highest field, 9 T, the magnetization of $\text{Sr}_2\text{Fe}_2\text{O}_5$ reaches a maximum of $0.045 \mu_B$ at 5 K, whereas the magnetization of $\text{Ba}_2\text{Fe}_2\text{O}_5$ is more than 30% higher, and reaches $\sim 0.06 \mu_B$ at 9 T and 5 K. In addition, the isothermal

magnetization of $\text{Sr}_2\text{Fe}_2\text{O}_5$ at 5 K and 300 K overlap, whereas $\text{Ba}_2\text{Fe}_2\text{O}_5$ shows a clear decrease in magnetization values at 300 K compared to 5 K. The effect of structural order on magnetism is also demonstrated by the magnetic susceptibility data shown in Figure 10.6. As seen here, the molar magnetic susceptibility for $\text{Ba}_2\text{Fe}_2\text{O}_5$ is two times greater than that of $\text{Sr}_2\text{Fe}_2\text{O}_5$. However, the overall magnitude of susceptibility is small for both materials as the temperature range of study, 2 – 400 K, falls in the antiferromagnetic region for both compounds. As stated above, the Neel temperature of $\text{Sr}_2\text{Fe}_2\text{O}_5$ has been previously determined by neutron diffraction to be 693 K.²²¹ Also, the Neel temperature of $\text{Ba}_2\text{Fe}_2\text{O}_5$ has been found using Mossbauer spectroscopy to be 720 K.^{219, 222} Another difference between the two materials is the ZFC/FC splitting, which occurs below ~240 K for $\text{Sr}_2\text{Fe}_2\text{O}_5$, but at a much higher temperature, ~355 K, for $\text{Ba}_2\text{Fe}_2\text{O}_5$.

While both materials have small magnetic moments in the range 2 – 400 K, the effect of variation in structural order on magnetic properties is clear.

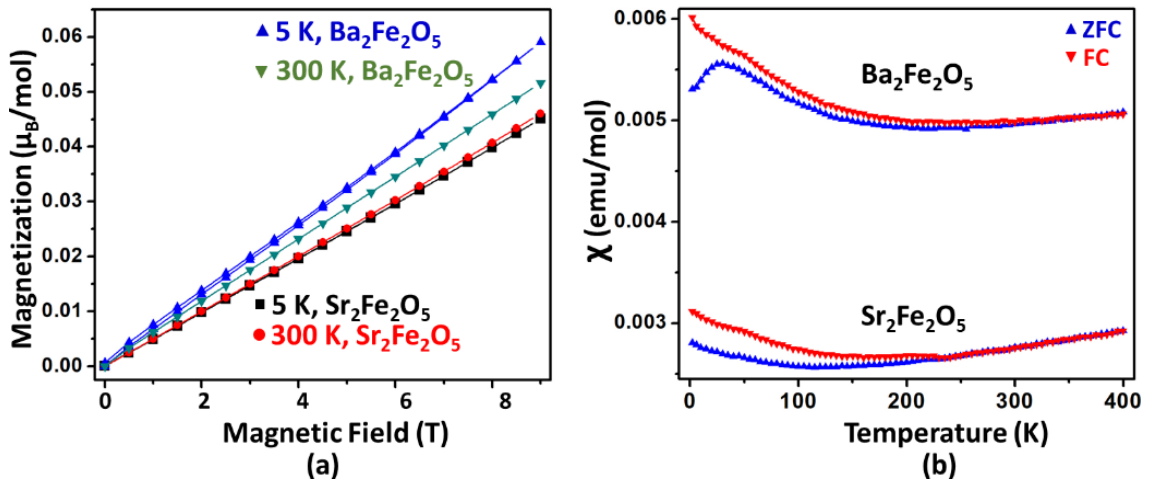


Figure 10.6. (a) Isothermal magnetization data, where black and red show $\text{Sr}_2\text{Fe}_2\text{O}_5$ magnetization at 5 K and 300 K, and blue and green represent the corresponding data for $\text{Ba}_2\text{Fe}_2\text{O}_5$. (b) Magnetic susceptibility data.

Electrical conductivity

The difference in structural order leads to a sharp difference in electrical conductivity of $\text{Ba}_2\text{Fe}_2\text{O}_5$ and $\text{Sr}_2\text{Fe}_2\text{O}_5$. Their electrical conductivities were measured by both direct current (DC) and alternating current (AC) methods using impedance spectroscopy. In impedance spectroscopy, total resistance is obtained from the intercept of the data with the real axis (Z') of the Nyquist plot at low frequency. In DC method, the output current is measured while applying constant voltage, which is then converted into resistance. The resistance (R) is used to determine the conductivity (σ) of a material using the following equation

$$\sigma = L/RA \quad (29)$$

where L and A represent the thickness and cross-sectional area of the cylindrical pellet, respectively. The AC and DC values were similar throughout the whole range of conductivity measurement for both materials. The room temperature conductivity values are listed in Table 10.5, indicating that the room temperature conductivity of $\text{Sr}_2\text{Fe}_2\text{O}_5$ is two orders of magnitude greater than that of $\text{Ba}_2\text{Fe}_2\text{O}_5$. Variable temperature conductivity measurements from 25 °C to 900 °C were also performed to study the temperature-dependent behavior of electrical conductivity (Figure 10.7).

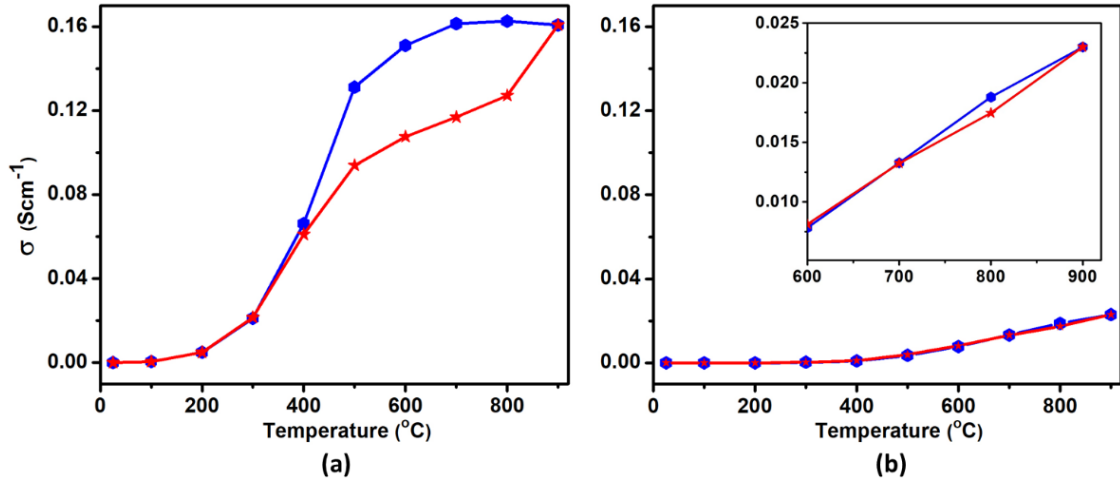


Figure 10.7. Electrical conductivity of (a) $\text{Sr}_2\text{Fe}_2\text{O}_5$ and (b) $\text{Ba}_2\text{Fe}_2\text{O}_5$ in inert atmosphere. Blue circles and red stars represent the data obtained while heating and cooling, respectively. The inset in (b) magnifies the data in the temperature range 600 – 900 $^{\circ}\text{C}$ for $\text{Ba}_2\text{Fe}_2\text{O}_5$.

It is immediately clear that $\text{Sr}_2\text{Fe}_2\text{O}_5$ has greater conductivity than $\text{Ba}_2\text{Fe}_2\text{O}_5$ in the entire temperature range. The temperature-dependent behavior is also drastically different for the two materials. For $\text{Sr}_2\text{Fe}_2\text{O}_5$, there is little change in electrical conductivity up to ~ 200 $^{\circ}\text{C}$, whereas for $\text{Ba}_2\text{Fe}_2\text{O}_5$, the conductivity remains nearly unchanged up to ~ 400 $^{\circ}\text{C}$. For $\text{Sr}_2\text{Fe}_2\text{O}_5$, there is a sharp increase in conductivity in the range 200 – 500 $^{\circ}\text{C}$, a behavior typical of semiconductors. Above 500 $^{\circ}\text{C}$, the increase in conductivity for $\text{Sr}_2\text{Fe}_2\text{O}_5$ slows down, finally reaching a maximum at 700 $^{\circ}\text{C}$, above which the electrical conductivity plateaus.

The temperature-dependent behavior of $\text{Ba}_2\text{Fe}_2\text{O}_5$ is different, where the electrical conductivity remains the same up to 400 $^{\circ}\text{C}$ followed by a mild linear increase between 400 - 900 $^{\circ}\text{C}$. The semiconducting behavior persists up to 900 $^{\circ}\text{C}$ and there are no peaks or plateau regions at high temperature.

Another interesting feature is the observation of hysteresis, where the conductivity values obtained while cooling are lower than the values obtained during heating. For $\text{Sr}_2\text{Fe}_2\text{O}_5$, the hysteresis is large and readily detectable. Whereas, $\text{Ba}_2\text{Fe}_2\text{O}_5$ shows a small hysteresis at 800 °C, but the heating and cooling data overlap at lower temperatures.

The electrical conductivity in oxides occurs by electron hopping through M–O–M' (metal-oxygen-metal) bond system where M and M' have different oxidation states. Thus, metals with variable oxidation states such as $\text{Fe}^{2+}/\text{Fe}^{3+}/\text{Fe}^{4+}$ are required for this process. The increase in temperature leads to enhanced mobility of charge carriers, resulting in increase in electrical conductivity in semiconductors. However, as observed in the TGA data (Figure 10.8), the increase in temperature also leads to the loss of oxygen, which can have a negative impact on electronic conductivity by disrupting some of the M–O–M' conduction pathways. However, it can also have an impact on the ionic conductivity,²²³ as more defects are created due to the loss of oxygen. Therefore, the increase in temperature has multiple consequences that can have positive or negative effects on total conductivity.

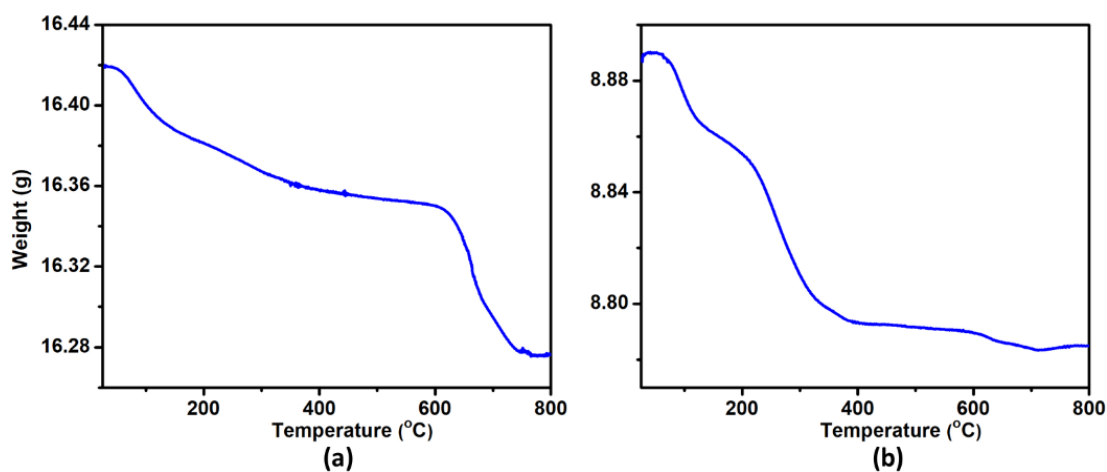


Figure 10.8. Thermogravimetric analysis data for (a) $\text{Sr}_2\text{Fe}_2\text{O}_5$ and (b) $\text{Ba}_2\text{Fe}_2\text{O}_5$.

During the heating-cooling cycle, the temperature-dependent increase in mobility of charge carriers is usually the dominant effect in semiconductors, leading to the commonly observed upturn in conductivity as temperature increases. During cooling, the charge carrier mobility decreases, leading to downturn in conductivity. In our experiments, since the conductivity measurements are done in inert atmosphere, the defects created during heating remain in the crystal lattice, even after the sample is cooled to lower temperatures. While the concentration of these defects is small, they can still have a negative impact on conductivity, as some of the M–O–M' conduction pathways are disrupted. Eventually, as the temperature is lowered further, the conductivity value becomes too small for any parameter other than charge carrier mobility to have a visible impact on conductivity. That is why the hysteresis is only observed at high temperature. Note that the high temperature conductivity of Sr₂Fe₂O₅ is almost one order of magnitude greater than that of Ba₂Fe₂O₅. The hystereses for both materials are present at similar conductivity values. For Sr₂Fe₂O₅ the hysteresis disappears when the material is cooled to 300 °C, where electrical conductivity becomes less than 0.021 Scm⁻¹, and for Ba₂Fe₂O₅ the hysteresis disappears when the material is cooled to 700 °C, where electrical conductivity goes below 0.013 Scm⁻¹.

The activation energies for electrical conductivity (Table 10.5) can be obtained using Arrhenius plot (Figure 10.9) where the Arrhenius equation for thermally activated conductivity^{50-51, 179} is used for fitting:

$$\sigma T = \sigma^{\circ} e^{-E_a/kT} \quad (30)$$

where σ° is a pre-exponential factor and a characteristic of the material, and E_a , k , and T are the activation energy for conductivity, Boltzmann constant, and absolute temperature, respectively. The activation energy for the total conductivity (E_a) is obtained from slope of the line of best fit in the $\log \sigma T$ vs $1000/T$ plot. The activation energies are listed in Table 10.5.

Table 10.5. Room temperature conductivity and activation energies

compounds	total conductivity, σ (S cm ⁻¹)		Activation energy, E_a (eV)
	AC	DC	
Ba ₂ Fe ₂ O ₅	1.15×10^{-7}	1.15×10^{-7}	0.462 eV for 273 to 1173K (25 - 300 °C) 0.448 eV for 273 to 1173K (300 - 900 °C)
Sr ₂ Fe ₂ O ₅	3.65×10^{-5}	3.65×10^{-5}	0.375 eV for 298 to 773K (25 - 300 °C) 0.280 eV for 298 to 773K (300 - 600 °C) 0.089 eV for 773 to 1173K (600 - 900 °C)

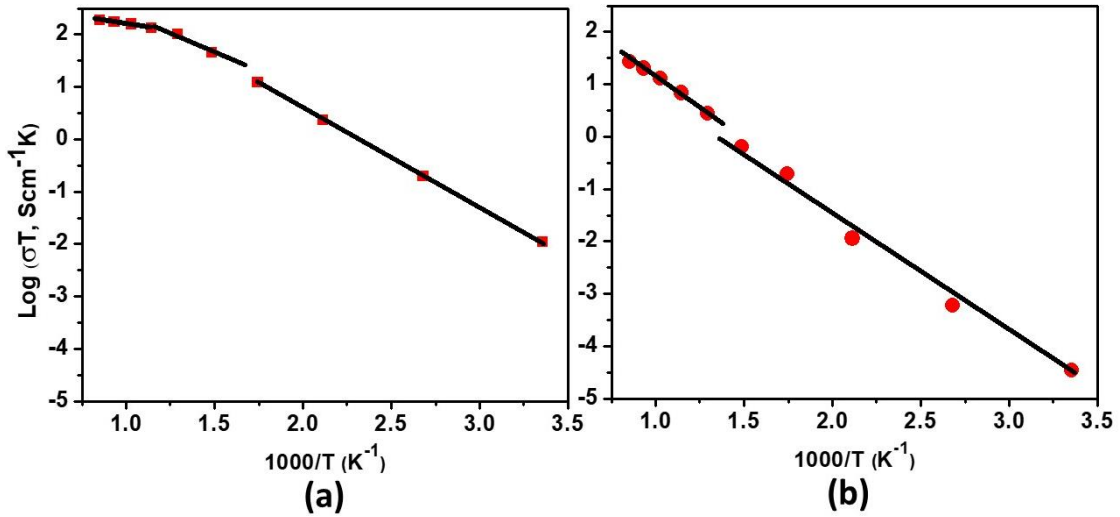


Figure 10.9. Arrhenius plots for electrical conductivity of (a) Sr₂Fe₂O₅ and (b) Ba₂Fe₂O₅.

Overall, the correlation between structural order and electrical conductivity is demonstrated by these two materials, where electrical conductivity varies drastically due to the difference in type of ordering

CONCLUSION

The variation in the type of ordering in oxygen-deficient perovskites can lead to significant differences in magnetic and electrical properties. This has been demonstrated through investigation of $\text{Sr}_2\text{Fe}_2\text{O}_5$ and $\text{Ba}_2\text{Fe}_2\text{O}_5$, which feature two different types of ordering. $\text{Sr}_2\text{Fe}_2\text{O}_5$ contains alternating FeO_4 tetrahedra and FeO_6 octahedra, whereas $\text{Ba}_2\text{Fe}_2\text{O}_5$ has a complex structure, where Fe atoms have tetrahedral, square-pyramidal and octahedral geometry. The effect of these differences on magnetic properties is evident from the considerably higher magnetization of $\text{Ba}_2\text{Fe}_2\text{O}_5$ compared to $\text{Sr}_2\text{Fe}_2\text{O}_5$. In addition, the electrical conductivity of the two compounds are drastically different, with $\text{Sr}_2\text{Fe}_2\text{O}_5$ showing nearly two-orders of magnitude higher conductivity at room temperature. Furthermore, the temperature-dependence of electrical conductivity varies significantly between the two materials, where the conductivity of $\text{Sr}_2\text{Fe}_2\text{O}_5$ reaches saturation at high temperature. This saturation is absent for $\text{Ba}_2\text{Fe}_2\text{O}_5$, where electrical conductivity shows a gradual increase all the way to 900 °C. These findings show the direct correlations between structure and physical properties of oxygen-deficient perovskites.

CHAPTER 11

STUDY OF $\text{Sr}_2\text{Fe}_2\text{O}_{6-\delta}$ AS ANODE ELECTRODE IN Li-ION BATTERY

INTRODUCTION

Lithium ion batteries (LIB) are extensively used in cell phones and laptops. The performance of the LIB is basically rooted on the efficiency of its electrodes and electrolyte. Since LIB has been used in devices like cell phones and laptops, which have become a part of our daily life activities, researchers have been committed to improving the durability and performance of the electrodes and electrolyte of LIB.²²⁴⁻²²⁵ Anode is one of the electrodes that researchers have been showing deep interest in improving the efficiency and durability.²²⁶⁻²²⁹

There are certain criteria that need to be fulfilled by a material to be a good and efficient anode in LIB such as a low atomic weight, low cost, and low standard potential as well as high ionic and electrical conductivities.²³⁰ Graphite is one of the primarily commercially used anode material in LIB.²³¹ Lithium may intercalate between the graphene layers of graphite until a composition of LiC_6 is reached resulting in a theoretical specific capacity of 372 mAh g^{-1} ^{224, 228, 230, 232} but practically the capacity is $\sim 300 - 320 \text{ mAh g}^{-1}$.²³⁰ Graphite has a low potential of around 0.1 V vs. Li/Li+ for most lithium concentrations.^{230, 233} However, it has some defects such as it reacts with organic electrolyte to form an SEI on its surface in the initial few charge and discharge cycles.^{230, 233-234} Many researchers

have been committed to improving the quality and efficiency of the anode and to develop new material to overcome the shortcomings of the graphite anode.^{230, 235} Tin based materials (Sn-oxides, mixed oxides and alloys) and pure and mixed transition metal oxides^{227-228, 236-238} were studied as alternative materials for anode to substitute the graphite. The tin based materials have been reported to be high capacity anode materials where the capacity arises from the reversible Li-Sn alloy formation/decomposition during the charge/discharge cycles.^{228, 230, 234, 236-237} The transition metal oxides are non-intercalating and non-alloying oxides.²³⁰ The reversible capacity in transition metal oxides is believed to develop from reversible oxidation of metal and lithia decomposition/formation.^{230, 239-241}

Later on, materials with different structures and phases such as spinel phase have been studied for the alternative materials for the anode.^{230, 242-243} The reversible capacity in spinel type materials such as ZnCo_2O_4 is believed to arise from Li intercalation into spinel lattice, crystal structure destruction followed by metal particle formation and alloy formation with Zn.^{230, 244-245} Recently, $\text{Ca}_2\text{Fe}_2\text{O}_5$ and $\text{Ca}_2\text{Co}_2\text{O}_5$ have been studied for their possibility of a potential candidate for a better and efficient anode material in LIB by Sharma and Chowdari et.al.²²⁶ $\text{Ca}_2\text{Fe}_2\text{O}_5$ and $\text{Ca}_2\text{Co}_2\text{O}_5$ have the brownmillerite type structures which belong to oxygen deficient perovskite (ODP).²²⁶ Here, the mechanism or the operation of the electrodes is believed to involve the destruction of the crystal lattice to form the nanoparticles of Fe and Co embedded in an amorphous matrix of Li_2O and CaO .²²⁶ The nanoparticles react reversibly with Li_2O contributing to the capacity and Ca is presumed to act as a beneficial spectator ion helping in the stabilization of the amorphous nanometal oxide matrix.²²⁶ We have studied similar type of oxygen deficient perovskite material, $\text{Sr}_2\text{Fe}_2\text{O}_{6-\delta}$ but with different structure and phase, for its potential application as anode in

LIB. In this paper, we report the synthesis and electrochemical property of $\text{Sr}_2\text{Fe}_2\text{O}_{6-\delta}$ that is applicable for LIB anode.

EXPERIMENTAL

Conventional solid-state synthesis method was applied to synthesize the material. Stoichiometric proportions of the precursors, SrCO_3 (Sigma Aldrich, 99.9%), and Fe_2O_3 (Alfa Aesar, 99.998%) were used for the synthesis. The mixtures of precursor powders were ground using agate mortar and pestle, pressed into pellets and calcined at 1000°C for 24 hours. The pellets were then ground and refired in air at 1200°C for 24 hours. In all cases, the furnace heating and cooling rates were set at 100°C/h .

The phase purity and structure of polycrystalline samples were tested by Rietveld refinements of powder X-ray diffraction data taken at room temperature using a PAN analytical Empyrean diffractometer with $\text{CuK}_{\alpha 1}$ radiation ($\lambda = 1.54056 \text{ \AA}$). The Rietveld refinements were carried out using *GSAS* software¹⁰⁰ and EXPEGUI interface.¹²⁵ The micro-structure of the compound was investigated using a high resolution field-emission scanning electron microscope (SEM). X-ray photoelectron spectroscopy (XPS) study and iodometric titration were performed to investigate the oxidation states of Fe. The $\text{Sr}_2\text{Fe}_2\text{O}_{6-\delta}$ powder of accurately weighed (5 mg) was mixed with 3 mg of teflonized acetylene black binder on an agate mortar with pestle to make an anode electrode. The $\text{Sr}_2\text{Fe}_2\text{O}_{6-\delta}$ electrode was used as a working electrode and Li foil as counter electrode separated by piece of glass fiber filter (ADVANTEC, GB-100R, Japan) using 2032 coin-type cell. The electrolyte used was 1M LiPF_6 -EC (ethylene carbonate): DMC (dimethyl carbonate) (1:2 by volume). The

galvanostatic charge-discharge measurements were carried out using Arbin instrument. Charge-discharge measurement were carried out in the voltage range between 3.0 – 0.005 V with a current density of 25 mA g⁻¹. The rate capability test was carried out at different currents of 25, 50, 100, 200, and 500 mA g⁻¹, respectively. The cyclic voltammetry measurement was carried out in the voltage range of 3.0 – 0.005 V with a scan speed of 1 mV s⁻¹ using SP200 Biologic Instrument.

RESULT AND DISCUSSION

The crystal structure of the compound was determined by the analysis of Powder X-ray diffraction (XRD). Sr₂Fe₂O_{6-δ} was found to be tetragonal with space group *I4/mmm*.⁴ Figure 11.1 shows the crystallographic structure of Sr₂Fe₂O_{6-δ}. Figure 11.2 shows the Rietveld refinement profile and crystal structure of the material. The inset picture shows the bifurcation of the peak at higher 2θ angle which helps to distinguish the tetragonal structure (model) from cubic structure. The refined structural parameters are listed in Table 11.1. Sr₂Fe₂O_{6-δ} is an oxygen deficient perovskite (ODP) with a general formula, ABO_{3-δ} (or A₂B₂O_{6-δ}) where Sr occupies A site and Fe occupies B site. Oxygen deficiency in ODPs can form tetrahedral or square pyramidal coordination geometry around B site cations.⁴ The crystal structure of Sr₂Fe₂O_{6-δ} contains square pyramidal and octahedral geometries Sr is 11 or 12 coordinated.⁴ The micro-structure of Sr₂Fe₂O_{6-δ} is investigated by high resolution scanning electron microscopy (SEM). The SEM images are shown in figure 11.3. It seems that the grain shapes are irregular, and the grains show well contact though some pores appear in the sample.

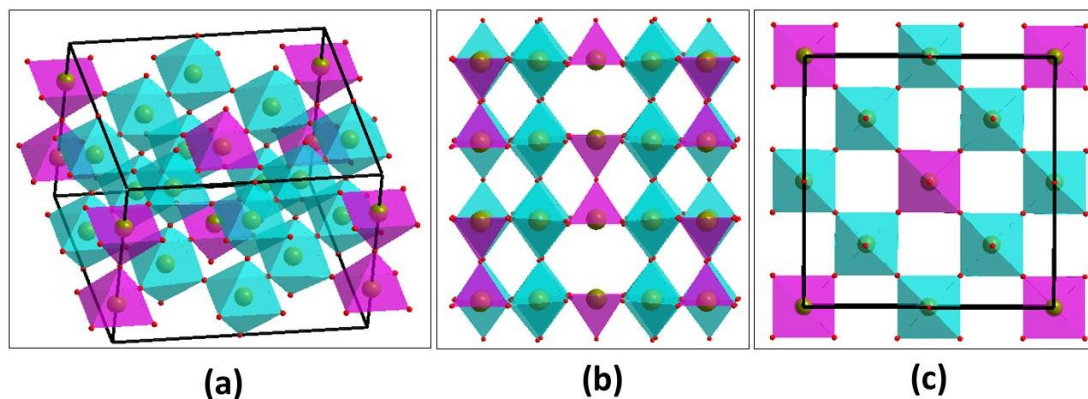


Figure 11.1. Crystal structure of $\text{Sr}_2\text{Fe}_2\text{O}_{6-\delta}$. (a) unit cell (b) side view and (c) Top view of the crystallographic structure which show the alternating FeO_6 octahedra (cyan) and FeO_5 square pyramids (purple). Sr atoms are removed for clarity.

Table 11.1. Refined structural parameters for $\text{Sr}_2\text{Fe}_2\text{O}_{6-\delta}$ from powder X-ray diffraction. Space group $I4/mmm$, $a = 10.9301(2) \text{ \AA}$, $b = 10.9301(2) \text{ \AA}$, $c = 7.6958(2) \text{ \AA}$, $R_p = 0.0211$, $wR_p = 0.0299$.

Elements	x	y	z	Occupancy	U_{iso}	Multiplicity
Sr1	0.2587(6)	0	0	1	0.031(2)	8
Sr2	0.2493(6)	0	0.5	1	0.035(2)	8
Fe1	0.0	0.0	0.25	1	0.042(7)	4
Fe2	0.25	0.25	0.25	1	0.019(3)	8
Fe3	0.5	0	0.25	1	0.060(7)	4
O1	0	0	0.5	1	0.02(1)	2
O2	0.124(2)	0.124(2)	0.216(2)	1	0.02(1)	16
O3	0.251(2)	0.251(2)	0.5	1	0.02(1)	8
O4	0.125 (2)	0.625	0.25	1	0.04(1)	16
O5	0.5	0 (2)	0	1	0.04(3)	4

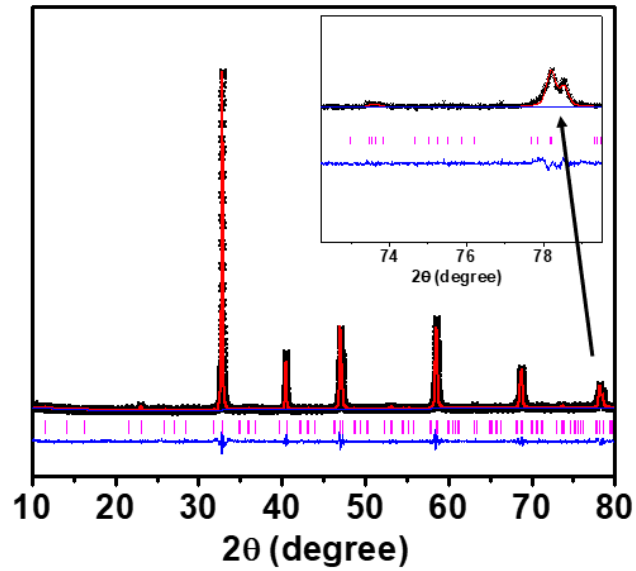


Figure 11.2. Rietveld refinement profile for powder X-ray diffraction data of $\text{Sr}_2\text{Fe}_2\text{O}_{6-\delta}$ in $I4/mmm$ space group. Cross symbols represent experimental data, red solid is the model, vertical tick marks show Bragg peak positions, and the blue line represents the difference plot. Inset shows the peak bifurcation at higher 2θ angle.

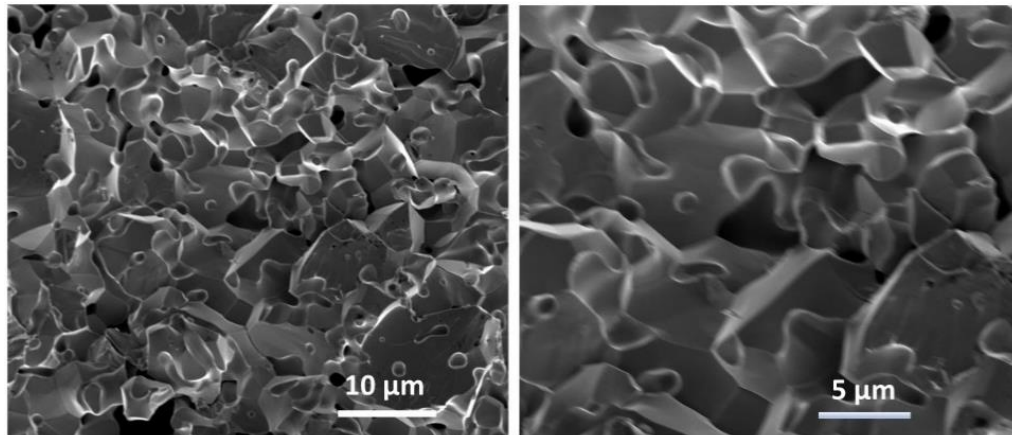


Figure 11.3. SEM images of $\text{Sr}_2\text{Fe}_2\text{O}_{6-\delta}$.

Past studies of Fe based ODPs showed the different oxidation states of +3 and +4 for Fe.^{4, 246-247} So, we performed the X-ray photoelectron spectroscopy (XPS) study and iodometric titration to investigate the oxidation states of Fe in $\text{Sr}_2\text{Fe}_2\text{O}_{6-\delta}$. If the compound contains only +3-oxidation state for Fe, the oxygen stoichiometry in $\text{Sr}_2\text{Fe}_2\text{O}_{6-\delta}$ formula should be 5, or $\delta = 1$. Oxidation state of Fe in a compound is characterized by its $2\text{P}_{3/2}$ peak position. For Fe^{3+} , $2\text{P}_{3/2}$ peak is followed by a satellite peak at around ~ 8 eV. As shown in Figure 11.4 for our material, the $2\text{P}_{3/2}$ peak observed at ~ 710 eV followed by a satellite peak at ~ 8 eV higher than the Fe $2\text{P}_{3/2}$ peak confirmed the presence of Fe^{3+} .⁴³⁻⁴⁴ The XPS data for early transition metals with high-spin unpaired electrons show multiplet structure for the 2p spectra due to spin-orbital and electrostatic interactions.²⁴⁸⁻²⁴⁹ It has been reported that the high-spin Fe^{3+} species can be fitted to multiple peaks.^{43, 248, 250-252} We have followed the same procedure and the Fe 2p spectra obtained could be successfully fitted into four multiplets, indicating the presence of Fe in 3+ oxidation state in the compound. For +4 oxidation state, a peak (fitted) appears at binding energy higher than that of +3 oxidation state⁴⁴. We can see a small bump raised at around 713 eV as indicated by blue arrow in the figure. The fitting also shows a peak associated with the bump at around 713 eV. It indicates the presence of +4 oxidation state. The blue arrows show the peaks in the raw data. It has also been confirmed by iodometric titration, i.e., $\delta = 0.25$ ($\text{Sr}_2\text{Fe}_2\text{O}_{6-\delta}$). Thus, the formula becomes $\text{Sr}_2\text{Fe}_2\text{O}_{5.75}$. To become the oxygen stoichiometry 5.75 (or $\text{Sr}_2\text{Fe}_2\text{O}_{5.75}$), Fe must have mixed oxidation states (+3 and +4). Thus, iodometric titration also indicates that a considerable amount of iron has been oxidized during the synthesis. Note that the starting material was Fe_2O_3 .

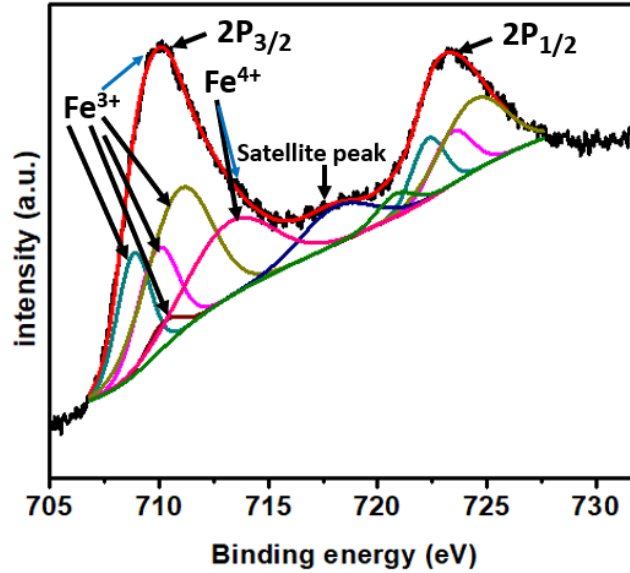


Figure 11.4. X-ray photoelectron spectroscopy data for Sr₂Fe₂O_{6-δ}.

Figure 11.5 depicts the first, second, tenth, twentieth, thirtieth, fortieth and fiftieth cycles of galvanostatic charge/discharge curves of Sr₂Fe₂O_{6-δ} tested at a current density of 25 mA g⁻¹ with voltage range from 3.0 to 0.005 V. It has an initial discharge capacity of 2400 mAh g⁻¹ during the first initial cycle. Higher capacity could result from higher amount of lithium incorporation at defects within crystal surfaces.²²⁹ The first cycle discharging has a plateau similar as seen in other material at the region between 0.9– 0.75 V.^{226, 253} The electrode exhibits a discharge capacity of 840, 570, 500, 490, 460 and 410 mAh g⁻¹ at the 2nd, 10th, 20th, 30th, 40th and 50th cycles, respectively. The first discharge and charge capacities of the as-prepared anode is 2400 mAh g⁻¹ and 680 mAh g⁻¹, respectively; indicating an initial coulombic efficiency of 28.3%. The irreversible capacity is due to the solid/electrolyte interphase (SEI) formation.²⁵⁴⁻²⁵⁵ Therefore, the first discharge irreversible capacity loss of ~1720 mAh g⁻¹ could mainly originate from the reduction of

electrode and the formation of a SEI on the surface of an electrode.²⁵⁵ The voltage profiles for the first discharge shows qualitatively similar to reported data of $\text{Ca}_2\text{Fe}_2\text{O}_5$ and $\text{Ca}_2\text{Co}_2\text{O}_5$ ²²⁶ and quantitatively to that of Fe_2O_3 ²⁵³ with a plateau at around 0.9 V for $\text{Sr}_2\text{Fe}_2\text{O}_{6-\delta}$ until a capacity of around 1000 mAh g^{-1} is reached and thereafter the voltage decreases gradually to 0.005 V, suggesting an electrochemical process similar to $\text{Ca}_2\text{Fe}_2\text{O}_5$ and $\text{Ca}_2\text{Co}_2\text{O}_5$ ²²⁶. The comparative plateau voltage position observed for the compound was found to be sensitive to the crystal structure and nature of metal ion involved in electrochemical reaction.^{226, 253} Similar observations have also been reported for other compounds with 3-d metal oxides.^{226, 253} After the first cycle, the charge and discharge profile shows the analogous curves indicating a reversible insertion/extraction of Li. At the 50th cycle, the average of both the charge and discharge potential is around ~ 1.5 V, suggesting a low average potential, which means $\text{Sr}_2\text{Fe}_2\text{O}_{6-\delta}$ anode is a good electrode with almost no charge/discharge hysteresis.²²⁹ The observed 2nd discharge capacity is around 840 mAh g^{-1} and the 50th cycle is 410 mAh g^{-1} . The corresponding first, second, third and 50th charge capacities are 660, 630, 510 and 350 mAh g^{-1} , respectively. The observed values of the first discharge and charge capacity are higher than the values reported for similar compounds, $\text{Ca}_2\text{Co}_2\text{O}_5$ and $\text{Ca}_2\text{Fe}_2\text{O}_5$.²²⁶

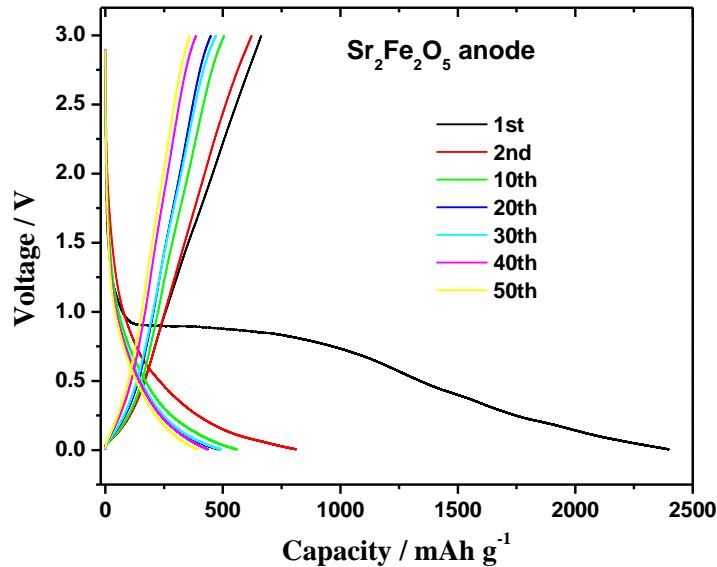


Figure 11.5. Galvanostatic charge-discharge profiles of $\text{Sr}_2\text{Fe}_2\text{O}_{6-\delta}$ anode electrode at the voltage range of 3.0 -0.005 V with a current density of 25 mA/g for 1st, 2nd, 10th, 20th, 30th, 40th and 50th cycles.

Figure 11.6 shows the cycle performance of as prepared $\text{Sr}_2\text{Fe}_2\text{O}_{6-\delta}$ at the current density of 25 mA g⁻¹. The electrode keeps a steady capacity of about 400 mAh g⁻¹ until 50 cycles, which is slightly higher than that of theoretical capacity of graphite anode 372 mAh·g⁻¹.²³⁰ The capacity has been found to be 300 – 320 mAh g⁻¹ in practice for graphite anode.²³⁰ Due to the various irreversible processes such as the formation of solid/electrolyte interphase (SEI) film and electrode decomposition, the capacity of $\text{Sr}_2\text{Fe}_2\text{O}_{6-\delta}$ has a reasonable loss in the first cycle.²⁵⁴⁻²⁵⁶ As shown in the figure, its capacity was maintained up to 50 cycles with an average coulombic efficiency of over 90% but still we need to increase the coulombic efficiency for practical application.

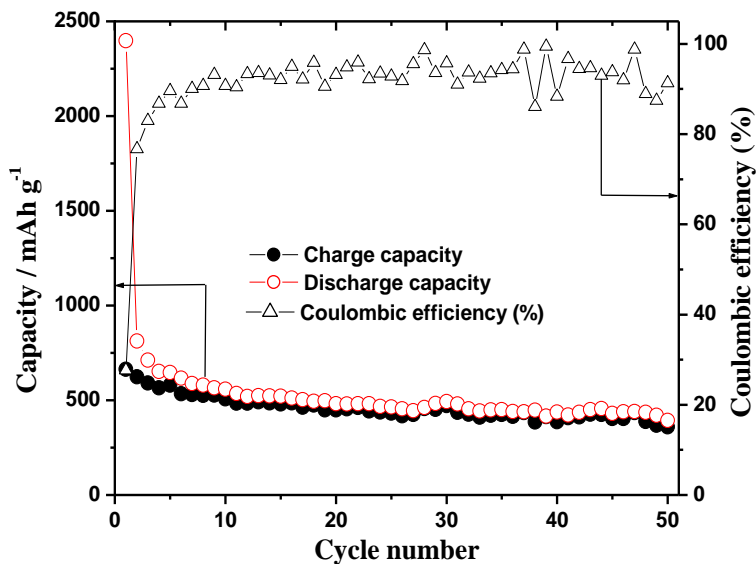


Figure 11.6. Capacities versus cycle numbers of $\text{Sr}_2\text{Fe}_2\text{O}_{6-\delta}$ anode electrode at the voltage range of 3.0 -0.005 V with a current density of 25 mA/g.

Figure 11.7 shows the rate capability test of the $\text{Sr}_2\text{Fe}_2\text{O}_{6-\delta}$ electrode in the voltage range of 3.0-0.005 V under different current densities from 25, 50, 100, 200, and 500 mA g⁻¹. With the increase in current densities from 25, 50, 100, 200, and 500 mA g⁻¹, the $\text{Sr}_2\text{Fe}_2\text{O}_{6-\delta}$ electrode delivers discharge capacities of 1885, 416, 325, 261 and 187 mAh g⁻¹, respectively. On reducing the current rate to the lower value of 50, and 25 mA g⁻¹ after rate performance test, $\text{Sr}_2\text{Fe}_2\text{O}_{6-\delta}$ electrode still retains the discharge capacities of 340, and 390 mAh g⁻¹, indicating good reversibility and high rate capability.

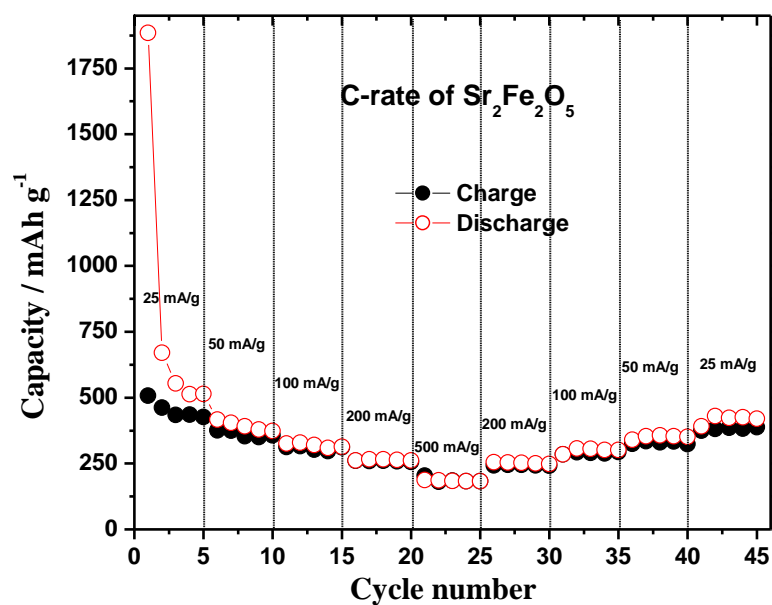


Figure 11.7. C-rate test of $\text{Sr}_2\text{Fe}_2\text{O}_{6-\delta}$ anode electrode at the voltage range of 3.0 – 0.005 V and different current densities of 25, 50, 100, 200, and 500 mA g^{-1} , respectively.

Figure 11.8 shows the cyclic voltammetry of $\text{Sr}_2\text{Fe}_2\text{O}_{6-\delta}$ anode electrode scanned at the voltage range of 0.005- 3.0 V (vs Li/Li^+) with a scan speed of 1 mV s^{-1} for study of the electrochemical mechanism. For the CV testing, the anodic scan (oxidation process) is first performed and then followed by cathodic scan (reduction process). Two peaks are observed in the reduction process of the first cycle, but remaining cycles exhibited only one peak. The voltage profile observed was similar to previous report of Fe_2O_3 ²⁵³ with a long flat plateau at around 0.9 V during discharging. A peak observed between 0.8 V to 1.2 V in CV is indication for nonreversible formation of solid/electrolyte interphase (SEI) on the surface of the electrode²⁵⁷⁻²⁵⁸ which led to irreversible capacity loss.²⁵⁴⁻²⁵⁵ A cathodic peaks in the first cycle is observed in CV at around 0.95 V. This peak is masked by the lines of other CVs. we can see small cathodic peak at around 1.0 V for cycles 2,3,4 and 5. The

2nd, 3rd, 4th and 5th CV curves of have higher extent of overlapping. Such overlapping is suggested to be the result of good reversibility and structural stability.²⁵⁴ The cathodic and anodic peaks can shift left or right for different cycles.^{254, 258-261} The peak at around 0.3 V for the first cycle can be a peak shifted left from those of the other cycles. Thus, the peak at around 0.95 V for the first cycle may be attributed to the crystal structure destruction.^{226, 258, 262} The other reduction peak at around 0.3V for the first cycle and at around 1 V for other remaining cycles could be attributed to electrochemical reaction.^{261, 263} In the oxidation process, the CV curves reveal the shifting of the anodic peak from right to left as the cycle number increases. The chemical process for Fe⁴⁺ is unknown. The chemical process of Fe³⁺ can be described as in the previous report.²²⁶

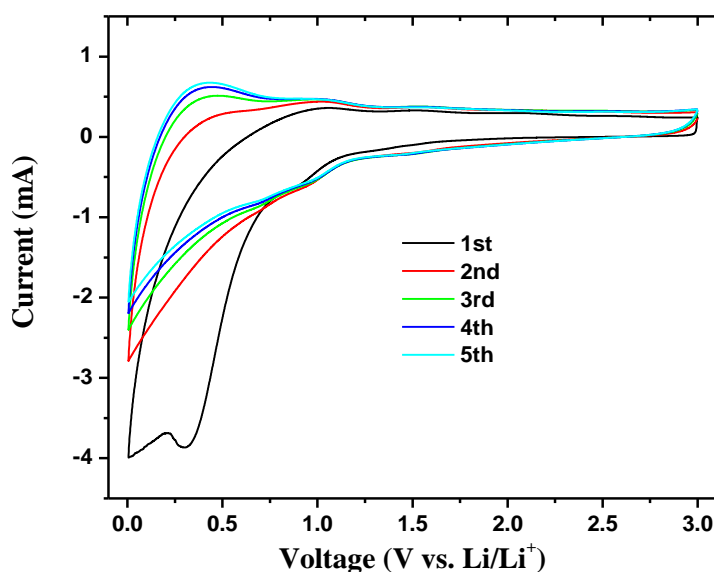
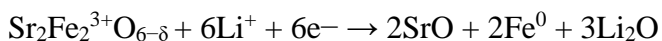
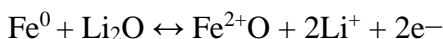


Figure 11.8. Cyclic voltammetry of Sr₂Fe₂O_{6- δ} anode electrode scanned at the voltage range of 3.0 – 0.005 V with a scan speed of 1 mV s⁻¹.

The first discharge reaction for the compounds involves the irreversible crystal structure destruction leading to the formation of metal nanoparticles embedded in an amorphous matrix of SrO and Li₂O.²²⁶



On subsequent charging, these metal particles are converted to their oxides together with the decomposition of Li₂O which can be written as:²²⁶



This reversible displacement reaction, viz. the formation and decomposition of Li₂O accompanied by the reduction and oxidation of metal nanoparticles gives rise to reversible capacity in the subsequent charge–discharge cycles.²²⁶ This is a three-phase reaction between metal oxide, the reduced metal and Li₂O.²²⁶ From the second cycle to the fifth cycle, the CV curves have higher extent overlapping suggesting the good reversibility and structural stability of Sr₂Fe₂O_{6-δ}.²⁵⁴ The way how Fe⁴⁺ undergoes in reaction has not been discussed before and is yet to be researched.

CONCLUSION

Oxygen deficient perovskite, Sr₂Fe₂O_{6-δ} has been synthesized by solid state method to study its anodic property for Li ion battery. Sr₂Fe₂O_{6-δ} electrode showed an initial discharge capacity of 2400 mAh g⁻¹ with large irreversible capacity and low coulombic efficiency of 28.3%. Further charge–discharge measurement of Sr₂Fe₂O_{6-δ} electrode shows the increase

in coulombic efficiency of over 90 %. $\text{Sr}_2\text{Fe}_2\text{O}_{6.8}$ electrode shows the stable capacity of over 393 mAh g^{-1} up to 50 cycles with high reversible capacity at current density of 25 mA g^{-1} and superior reversible capacity throughout the whole studied number of cycles. The rate capability test of $\text{Sr}_2\text{Fe}_2\text{O}_{6.8}$ electrode shows good performance in terms of capacity and can be comparable to the present graphitic carbon anode electrode in Li-ion battery.

CHAPTER 12

REMARKABLE OXYGEN EVOLUTION ACTIVITY OF $\text{Ca}_{2-x}\text{Sr}_x\text{Fe}_2\text{O}_{6-\delta}$ ¹⁰

The rise in global energy consumption has intensified the demand for clean and sustainable energy conversion and storage.²⁶⁴ The oxygen evolution reaction (OER) during water oxidation is an important electrochemical process for renewable-energy technologies, such as water splitting, rechargeable metal-air batteries, and regenerative fuel cells.²⁶⁵⁻²⁷⁰ However, the intrinsically sluggish kinetics of OER hinders the performance of these advanced energy devices, and results in a considerable overpotential for OER.²⁷¹⁻²⁷² The overpotential can be lowered by electrocatalysts, such as IrO_2 and RuO_2 , which show high activity, but their scarcity, high cost and limitations in long-term stability in alkaline solutions hamper their practical use.^{204, 273-275} Designing inexpensive, earth-abundant and efficient electrocatalysts with low overpotential, which are stable upon prolonged exposure to oxidizing conditions in alkaline solutions, has been a major challenge.^{81, 204, 275-276}

Oxygen-deficient perovskites ($\text{ABO}_{3-\delta}$) with alkaline or rare-earth cations on the A-site and 3d-metal cations on the B-site have demonstrated great potential for electrocatalytic

¹⁰ The work described in this chapter was published in *Angewandte Chemie International Edition* (2019, vol. 58, p. 2060-2063)

activity in alkaline solutions.^{119, 135, 199, 201, 209, 266, 275, 277} Much research has been dedicated to understanding the parameters that can improve the OER activity of oxygen-deficient perovskites.^{119, 135, 199, 201, 209, 266, 275, 277} One study reported that a near-unity occupancy of the e_g orbital of the first-row transition metal in perovskite oxides can enhance the intrinsic activity for OER in alkaline solution.²⁶⁶ Based on this descriptor, the oxygen-deficient perovskite $\text{Ba}_{0.5}\text{Sr}_{0.5}\text{Co}_{0.8}\text{Fe}_{0.2}\text{O}_{3-\delta}$ (BSCF) was developed as a highly active catalyst.^{198, 266} Since then, various other oxygen-deficient perovskites have been studied,^{119, 135, 199, 201, 209, 266, 275, 277} but BSCF remains the most highly regarded catalyst for OER. However, cobalt criticality has emerged as a major concern in recent years, and development of cobalt-free catalysts for electrochemical processes such as OER is a priority. Recently, the qualitative pH-dependence of OER catalysis was reported for some Fe-based perovskites, without any quantitative investigation of the OER activity, overpotential, Tafel kinetics, or electrochemically active surface areas.²⁷⁸ In line with efforts to develop inexpensive and earth-abundant electrocatalysts, we report the electrocatalytic activity of a Fe-based oxygen-deficient perovskite, $\text{Sr}_2\text{Fe}_2\text{O}_{6-\delta}$,⁴ which shows greater intrinsic OER activity than BSCF. We also demonstrate the correlations between the electrocatalytic activity, composition and defect-order as well as electrical conductivity in the series $\text{Ca}_2\text{Fe}_2\text{O}_{6-\delta}$, $\text{CaSrFe}_2\text{O}_{6-\delta}$ and $\text{Sr}_2\text{Fe}_2\text{O}_{6-\delta}$.^{4, 279}

All compounds were synthesized under identical conditions, and characterized by Rietveld refinements¹⁰⁰⁻¹⁰¹ using powder X-ray diffraction. The material synthesis methods, Rietveld refinement profiles and the refined structural parameters are provided in the supplementary information. In this series of oxygen-deficient perovskites, the defects created due to oxygen-deficiency are distributed in an ordered fashion, rather than being

spread randomly in the structure. In $\text{Ca}_2\text{Fe}_2\text{O}_{6-\delta}$, the defects only appear in alternating layers, where the coordination number of Fe decreases from 6 to 4. This leads to the formation of alternating tetrahedral and octahedral layers,²⁷⁹ as shown in Figure 12.1a. The tetrahedral layers actually consist of one-dimensional chains, which can have either right-handed or left-handed orientation. In $\text{Ca}_2\text{Fe}_2\text{O}_{6-\delta}$, the tetrahedral chains in each layer are oriented opposite to those in the neighboring layer. $\text{CaSrFe}_2\text{O}_{6-\delta}$ has the same type of defect-order, resulting in alternating tetrahedral and octahedral geometry, but the tetrahedral chains in this compound have the same orientation throughout the crystal lattice (Figure 12.1b).⁴ Finally, $\text{Sr}_2\text{Fe}_2\text{O}_{6-\delta}$ exhibits a different type of defect order, leading to the formation of alternating square pyramidal and octahedral coordination, as shown in Figure 12.1c.⁴

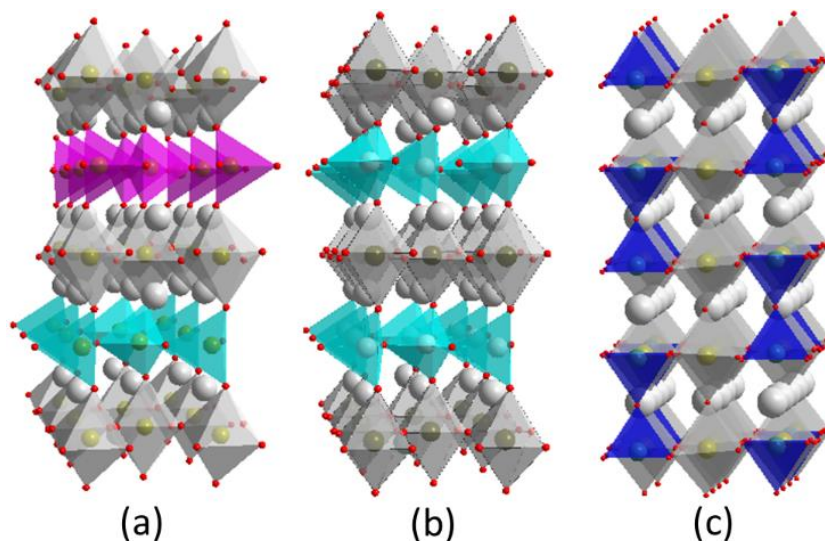


Figure 12.1. Crystal structures of (a) $\text{Ca}_2\text{Fe}_2\text{O}_{6-\delta}$, (b) $\text{CaSrFe}_2\text{O}_{6-\delta}$, and (c) $\text{Sr}_2\text{Fe}_2\text{O}_{6-\delta}$. In (a) and (b), different colors represent different orientations of tetrahedral chains.

The OER activities were studied for all three compounds, $\text{Ca}_2\text{Fe}_2\text{O}_{6-\delta}$, $\text{CaSrFe}_2\text{O}_{6-\delta}$ and $\text{Sr}_2\text{Fe}_2\text{O}_{6-\delta}$, as well as the state of the art materials $\text{Ba}_{0.5}\text{Sr}_{0.5}\text{Co}_{0.8}\text{Fe}_{0.2}\text{O}_{3-\delta}$ ^{26, 204} and RuO_2 .²⁷³ The details of electrode preparation and experimental setup are described in the supplementary information. For OER measurements, carbon black is often added to the electrode composition in order to enhance the conductivity within the electrode and maximize the utilization of the catalyst.¹⁹⁷⁻¹⁹⁹ However, recent studies have shown that carbon plays a more complex role than just a simple conductive support.²⁰⁰⁻²⁰¹ For example, X-ray absorption near-edge spectroscopy study of $\text{Ba}_{0.5}\text{Sr}_{0.5}\text{Co}_{0.8}\text{Fe}_{0.2}\text{O}_{3-\delta}$ /carbon composite electrode demonstrated the reduction of Co during the composite preparation process.²⁰² As a result, some researchers have conducted OER experiments without carbon black.¹³⁵ For the series of materials studied in this work, we performed the OER experiments both with and without carbon black. Both experiments led to similar results, particularly for compounds with higher OER activity, indicating that in these materials carbon black is not essential to the catalytic performance. The experiments without carbon black are preferred, as they demonstrate the intrinsic catalytic activity of each material. The conventional electrode preparation method usually involves drop casting the catalyst on the surface of a glassy carbon (GC) electrode. The GC electrode helps to improve the electrical charge transport. In the present study, the conventional method was initially employed. One of the parameters in the OER activity of a catalyst is the onset potential in polarization curve.^{275, 280-281} As shown in Figure 12.2, the onset potential decreases systematically in progression from $\text{Ca}_2\text{Fe}_2\text{O}_{6-\delta}$ to $\text{CaSrFe}_2\text{O}_{6-\delta}$ and $\text{Sr}_2\text{Fe}_2\text{O}_{6-\delta}$. The latter shows onset potential of 1.5 V, which is similar to those reported for highly active OER

catalysts, such as $\text{Ba}_{0.5}\text{Sr}_{0.5}\text{Fe}_{0.2}\text{Co}_{0.8}\text{O}_{3-\delta}$,^{81, 275} IrO_2 ,^{119, 282} $\text{SrNb}_{0.1}\text{Co}_{0.7}\text{Fe}_{0.2}\text{O}_{3-\delta}$,²⁰⁴ $\text{Ca}_2\text{Mn}_2\text{O}_5$ ¹¹⁹, and Co_3O_4 /carbon nanotubes.²⁸¹

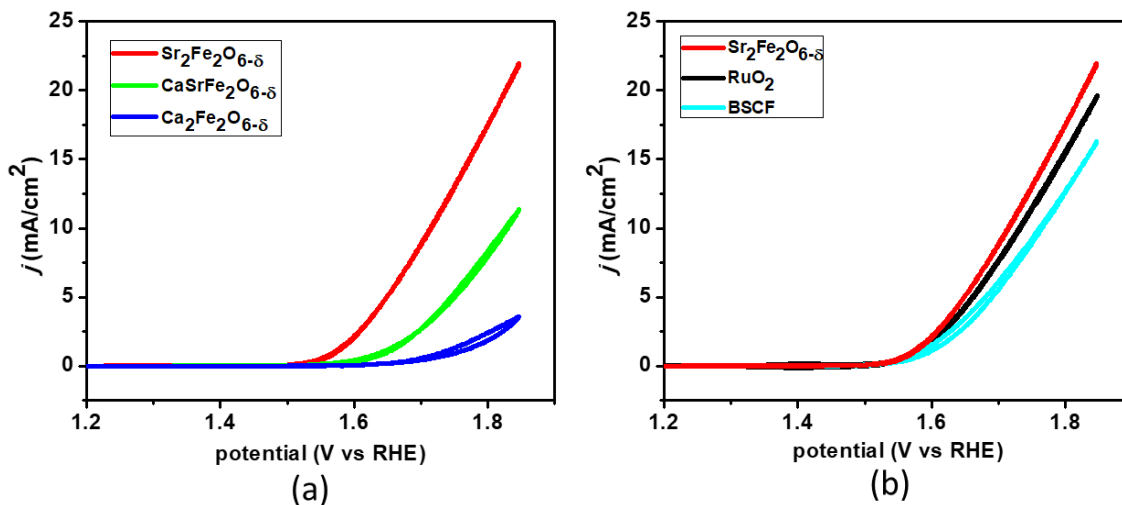


Figure 12.2. (a) Polarization curves showing the OER activities, obtained using the conventional glassy carbon electrode setup. (b) Comparison of the activity of $\text{Sr}_2\text{Fe}_2\text{O}_{6-\delta}$ with state of the art materials RuO_2 and $\text{Ba}_{0.5}\text{Sr}_{0.5}\text{Co}_{0.8}\text{Fe}_{0.2}\text{O}_{3-\delta}$ (BSCF).

The overpotential, beyond the ideal thermodynamic potential of 1.23 V, at 10 mA/cm² is an important parameter in describing the OER activity. The current density of 10 mA/cm² is related to solar fuel synthesis^{204, 283} and the potential at this current density has been adopted as a metric for comparison of different OER catalysts. Among the three compounds, $\text{Ca}_2\text{Fe}_2\text{O}_{6-\delta}$ shows low current density that does not reach 10 mA/cm² in the potentials up to 1.8 V vs RHE. $\text{CaSrFe}_2\text{O}_{6-\delta}$ shows overpotential of 0.60 V, making it a reasonable catalyst. However, the most remarkable OER activity belongs to $\text{Sr}_2\text{Fe}_2\text{O}_{6-\delta}$, that shows overpotential of 0.48 V (Figure 12.2a), which is superior to the state of the art

compound, $\text{Ba}_{0.5}\text{Sr}_{0.5}\text{Co}_{0.8}\text{Fe}_{0.2}\text{O}_{3-\delta}$.^{26, 204} For direct comparison, we examined two of the best OER catalysts, $\text{Ba}_{0.5}\text{Sr}_{0.5}\text{Co}_{0.8}\text{Fe}_{0.2}\text{O}_{3-\delta}$ (BSCF)^{26, 204} and RuO_2 ²⁷³ under the same conditions. As shown in Figure 12.2b, the OER activity of $\text{Sr}_2\text{Fe}_2\text{O}_{6-\delta}$ is superior to both of these catalysts.

The OER kinetics is usually evaluated using Tafel equation $\eta = a + b \log j$ ²⁰⁶⁻²⁰⁷ where η is the overpotential, and j is the current density. Tafel plot, η vs. $\log j$, is influenced by electron and mass transport.²¹⁰⁻²¹¹ Thus, it can provide information about electronic and geometric enhancement in the activity of electrocatalysts.²¹¹ In general, a decrease in the slope of the Tafel plot indicates better kinetics of OER, and smaller slopes represent faster reactions. The Tafel slopes for $\text{Ca}_2\text{Fe}_2\text{O}_{6-\delta}$, $\text{CaSrFe}_2\text{O}_{6-\delta}$ and $\text{Sr}_2\text{Fe}_2\text{O}_{6-\delta}$ are 185mV/dec, 101 mV/dec and 60 mV/dec, respectively, as shown in Figure 12.3. $\text{Sr}_2\text{Fe}_2\text{O}_{6-\delta}$ shows the lowest Tafel slope among the three materials, which is consistent with the highest OER activity, and indicates facile charge transport in this compound.^{210-211, 284}

The electrochemically active surface area (ECSA) of each catalyst was estimated from double layer capacitance, C_{dl} , in non-faradic region,²⁸⁵ where electrode reactions are considered to be negligible and the current is primarily from electrical double layer charge and discharge.²⁸⁵⁻²⁸⁶ The relationship between ECSA and C_{dl} is described by $\text{ECSA} = C_{dl}/C_s$, where C_s is specific capacitance.^{207, 285, 287} Some researchers have treated C_s as a constant, 40 $\mu\text{F}/\text{cm}^2$, when dealing with metal electrodes.^{207, 285} Regardless of the value of C_s , the double layer capacitance, C_{dl} , is clearly proportional to electrochemically active surface area of the electrode (ECSA).^{206, 288-290} Therefore C_{dl} is commonly taken as representative of the magnitude of ECSA.^{206, 289-290} The value of C_{dl} can be obtained using the relationship $C_{dl} = \Delta j/v$,^{206, 289-290} where Δj is the absolute value of the difference between j_{anodic} and j_{cathodic}

from cyclic voltammetry, and ν is the scan rate.^{206, 289-290} The plot of Δj versus ν is frequently utilized, where the magnitude of C_{dl} is equivalent to half of the slope of this plot.^{206, 289-290} Some researchers have plotted $j_{average}$, the average of the absolute values of j_{anodic} and $j_{cathodic}$, versus ν .^{26, 288} In that case, the slope is directly equivalent to C_{dl} and does not need to be divided by 2.²⁸⁸ In Figure 12.4, the values of Δj at the middle potential,²⁰⁶ 0.977 V, are plotted against their corresponding scan rates from cyclic voltammetry experiments (Figure S3), and C_{dl} is obtained as half of the slope of this plot.^{206, 289-290} The C_{dl} for $Sr_2Fe_2O_{6-\delta}$ is significantly greater than that for $CaSrFe_2O_{6-\delta}$ and $Ca_2Fe_2O_{6-\delta}$. This indicates larger ECSA for $Sr_2Fe_2O_{6-\delta}$, consistent with its high OER catalytic activity.

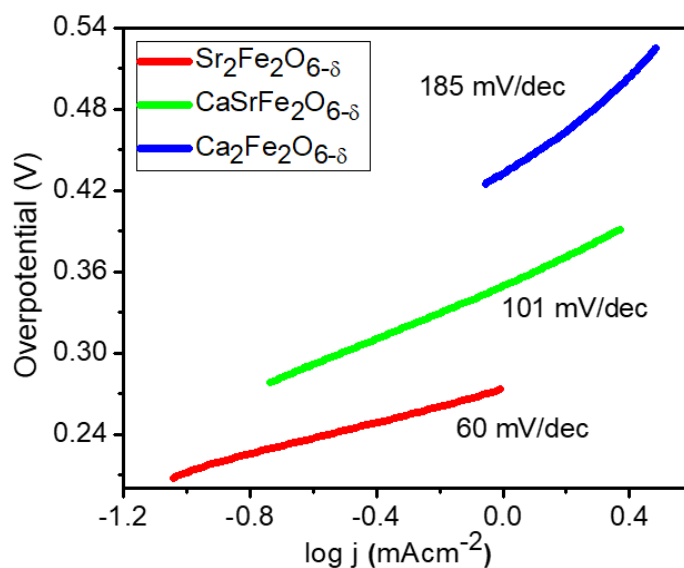


Figure 12.3. Tafel slopes indicating the OER kinetics.

In recent years, in addition to the conventional glassy carbon experiments, some researchers have used pure disks of catalytic oxides, without glassy carbon disk, to examine hydrogen or oxygen evolution activities.²⁹¹⁻²⁹² The advantage of this method is that it

provides information about the intrinsic properties of the catalyst without any interference from the glassy carbon disk, which usually helps with the electrical conductivity. In this method, the material itself is responsible for both electrical conductivity and OER activity, and the contribution from glassy carbon disk is eliminated.²⁹¹⁻²⁹² Considering that this method represents the intrinsic catalytic activity of a material, we performed additional experiments using this technique to further examine the three compounds $\text{Ca}_2\text{Fe}_2\text{O}_{6-\delta}$, $\text{CaSrFe}_2\text{O}_{6-\delta}$, and $\text{Sr}_2\text{Fe}_2\text{O}_{6-\delta}$, as well as the state-of-the-art compound, $\text{Ba}_{0.5}\text{Sr}_{0.5}\text{Co}_{0.8}\text{Fe}_{0.2}\text{O}_{3-\delta}$, which to our knowledge has not been examined using this method.

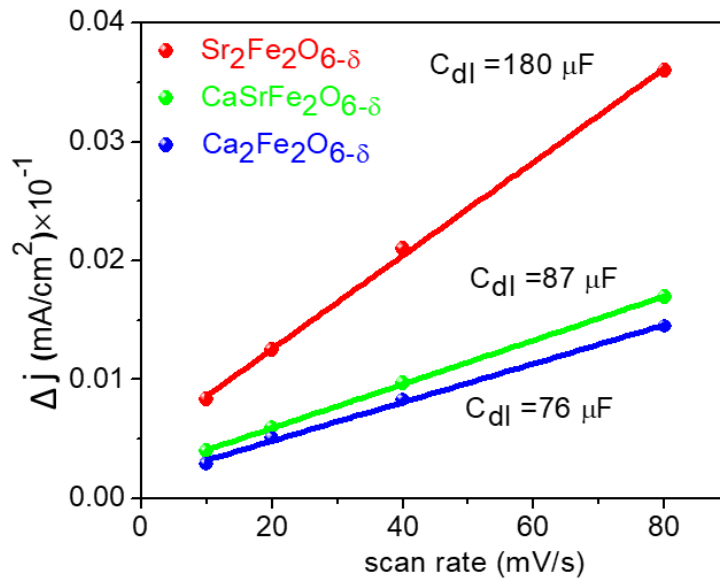


Figure 12.4. Plot of $\Delta j = j_{\text{anodic}} - j_{\text{cathodic}}$ as a function of scan rate. The C_{dl} for each material is equivalent to half of the slope.

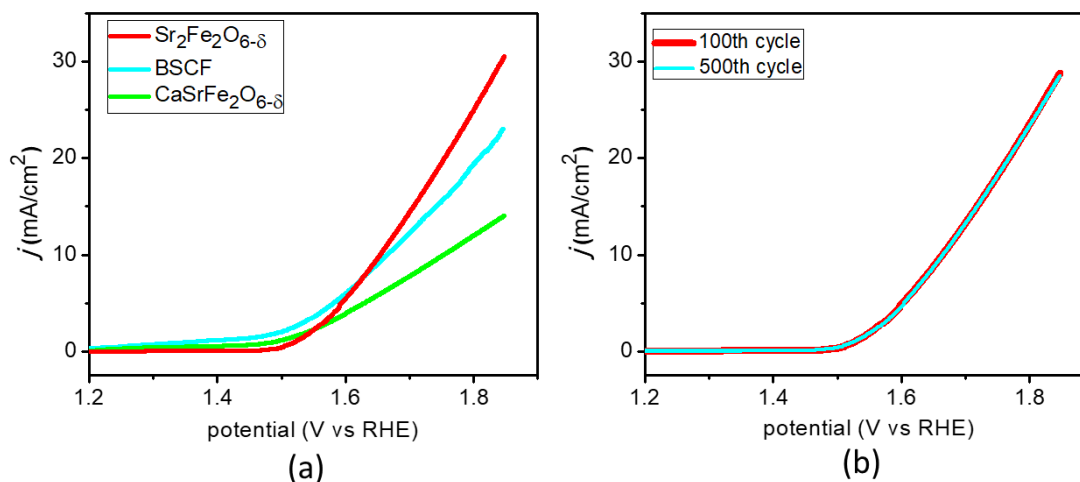


Figure 12.5. (a) Polarization curves showing the OER activities of pure disks of catalysts. (b) Stability test for Sr₂Fe₂O_{6-δ} by performing 500 cycles.

The polarization curves obtained from pure disks indicated almost no OER activity for Ca₂Fe₂O_{6-δ}, which is expected, given the low electrical conductivity of this compound. Our 4-probe measurements show the room temperature conductivity of $1.13 \times 10^{-9} \text{ Scm}^{-1}$ for Ca₂Fe₂O_{6-δ}, $7.78 \times 10^{-3} \text{ Scm}^{-1}$ for CaSrFe₂O_{6-δ}, 7.30 Scm^{-1} for Sr₂Fe₂O_{6-δ}, and $8.17 \times 10^{-3} \text{ Scm}^{-1}$ for Ba_{0.5}Sr_{0.5}Co_{0.8}Fe_{0.2}O_{3-δ}. The enhanced electrical conductivity in Sr₂Fe₂O_{6-δ} can be attributed to two different parameters. The first is the larger average bond angle in Sr₂Fe₂O_{6-δ} ($\sim 170^\circ$) compared to that of Ca₂Fe₂O_{6-δ} and CaSrFe₂O_{6-δ} ($\sim 139^\circ$), which enhances the electron transfer through Mⁿ⁺-O-M^{m+} pathways, where M is a metal (such as Fe) with variable oxidation states n+ and m+. Previous reports on perovskite-based compounds have demonstrated the improvement of the electrical conductivity as a function of bond angle.^[27] The second parameter is the presence of a greater number of Fe³⁺-O-Fe⁴⁺ conduction pathways in Sr₂Fe₂O_{6-δ}. As shown before,^[9] the oxygen stoichiometry in this material is 5.75 (i.e., $\delta = 0.25$), indicating that Fe has both tri- and tetravalent oxidation states. However, Ca₂Fe₂O_{6-δ} and CaSrFe₂O_{6-δ} have oxygen stoichiometry of 5.0 (i.e., $\delta =$

1.0),^[9,10] which indicates that Fe is primarily in +3 oxidation state. We have confirmed the oxygen stoichiometry using iodometric titrations. Note that metals with multiple stable oxidation states are needed for enhanced electronic conductivity. While perovskite-based materials are known to conduct both electrons and ions,^[28] the dominance of electronic conductivity has been demonstrated in this class of materials.^[28] Therefore, the enhancement of the electrical conductivity in $\text{Sr}_2\text{Fe}_2\text{O}_{6-\delta}$ is primarily due to the superior electronic charge transport.

The polarization curves for pure disks of $\text{CaSrFe}_2\text{O}_{6-\delta}$ and $\text{Sr}_2\text{Fe}_2\text{O}_{6-\delta}$ (Figure 12.5) show overpotential values of 0.52 V and 0.42 V, respectively. Considering that the disk is made of pure catalyst, the entire disk surface participates in OER activity, leading to the enhanced overpotential compared to the glassy carbon electrode method. The remarkable overpotential of $\text{Sr}_2\text{Fe}_2\text{O}_{6-\delta}$ disk is due to a combination of good OER catalytic activity and sufficient intrinsic electrical conductivity. As shown in Figure 12.5, the $\text{Sr}_2\text{Fe}_2\text{O}_{6-\delta}$ disk shows better OER activity than the disk of the state-of-the-art catalyst, $\text{Ba}_{0.5}\text{Sr}_{0.5}\text{Co}_{0.8}\text{Fe}_{0.2}\text{O}_{3-\delta}$, consistent with the lower electrical conductivity of $\text{Ba}_{0.5}\text{Sr}_{0.5}\text{Co}_{0.8}\text{Fe}_{0.2}\text{O}_{3-\delta}$ compared to $\text{Sr}_2\text{Fe}_2\text{O}_{6-\delta}$. Also, note the well-defined non-faradaic region and sharp onset for $\text{Sr}_2\text{Fe}_2\text{O}_{6-\delta}$ disk.

Given the outstanding OER activity of $\text{Sr}_2\text{Fe}_2\text{O}_{6-\delta}$ disk, we also examined its stability by repeating the polarization curves over 500 cycles. As shown in Figure 12.5b, this material shows remarkable stability and there is little change to its OER activity after 500 cycles.

The findings described in this communication indicate that the OER activity is enhanced as electrical conductivity increases, leading to the outstanding catalytic activity of an iron-based catalyst, $\text{Sr}_2\text{Fe}_2\text{O}_{6-\delta}$. It has been found for other series of compounds as well.²⁹³

SUPPORTING INFORMATION

Material synthesis and characterization

All materials used for each type of analysis were synthesized under identical conditions. The catalysts used for standard oxygen evolution reaction (OER) on glassy carbon electrode were prepared by sol-gel method. Stoichiometric amounts of metal nitrates were dissolved in water and equimolar concentration of citric acid was also added to the mixture. The solution was heated to 80 °C to form a gel. The sample was then heated for 6 hours at 600 °C, followed by 12 hours at 1200 °C. Similar method was used for the preparation of BSCF. RuO₂ was purchased from Alfa Aesar. The phase purity and structure of polycrystalline samples were examined by powder X-ray diffraction at room temperature using Cu K α 1 radiation ($\lambda = 1.54056 \text{ \AA}$). The Rietveld refinements were carried out using GSAS software and EXPGUI interface.^[11] The refinement profiles are shown in Figure S1.

Electrode preparation

35 mg of the sample was added to 40 μ L of Nafion® D-521 solution and stirred using magnetic stirrer. 7 mL of THF was then added and stirred for a few more minutes and then sonicated for 10 minutes. This mixture was made both with and without carbon powder to test the effect of carbon on OER activity. For experiments with carbon, 7 mg of carbon powder was added prior to adding THF. The catalyst ink was drop casted on the surface of a glassy electrode with a diameter of 5 mm and was left to dry in air overnight.

The OER experiments were also performed on disks of pure samples, without the use of glassy carbon electrode or other additives. A pellet of the material with 5.56 mm diameter and 2.02 mm thickness was prepared by sintering at 1200 °C. One side of the pellet was painted with gold and dried at 800 °C. The pellet was then fixed inside a plastic tube with

the gold paint facing the inside of the tube, as shown in Figure S2. The exposed surface of the pellet faced the outside and was aligned with the opening of the tube. The pellet fitted inside the tube tightly, such that there was no leakage of the solvent to the inside of the tube as confirmed by many repeated experiments. The tube was then attached to a PINE Research rotating disk electrode, where the gold-painted side of the pellet was connected to a copper wire, as shown in Figure S2.

Measurements of OER activity

Electrocatalytic activity measurements were carried out on an electrochemical workstation in a three-electrode glass cell system. A glassy carbon electrode coated with the catalyst or the pure disk of the catalytic material were used as the working electrode. A commercial platinum electrode was used as the counter electrode. Ag/AgCl (in 3 M NaCl) was used as reference electrode and was calibrated against standard hydrogen electrode prior to use. The potential obtained versus Ag/AgCl electrode ($E_{\text{Ag/AgCl}}$) was converted to potential versus reversible hydrogen electrode (E_{RHE}) according to the Nernst equation:

$$E_{\text{RHE}} = E_{\text{Ag/AgCl}} + 0.059 \text{ pH} + E^0_{\text{Ag/AgCl}}$$

where $E^0_{\text{Ag/AgCl}}$ is the potential of the Ag/AgCl electrode versus RHE.

Before starting each measurement, 0.1 M KOH electrolyte was bubbled with oxygen for at least 30 min. The cyclic voltammetry (CV) profiles were recorded at a scan rate of 10 mV s⁻¹ from 0 to 1.85 V vs RHE using a rotating disk electrode, which was continuously rotated at 1600 rpm.

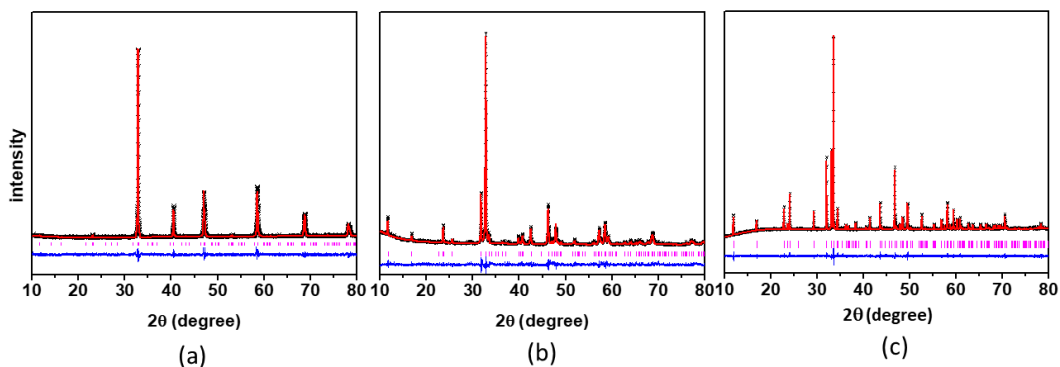


Figure S1. Rietveld refinement profiles using powder X-ray diffraction for (a) $\text{Ca}_2\text{Fe}_2\text{O}_{6-\delta}$, space group $Pnma$, (b) $\text{CaSrFe}_2\text{O}_{6-\delta}$, space group $Ibm2$, and (c) $\text{Sr}_2\text{Fe}_2\text{O}_{6-\delta}$, space group $I4/mmm$. Black symbols are the experimental data, red line represents the model, vertical tick marks show Bragg peak positions, and the lower blue line represents the difference plot.

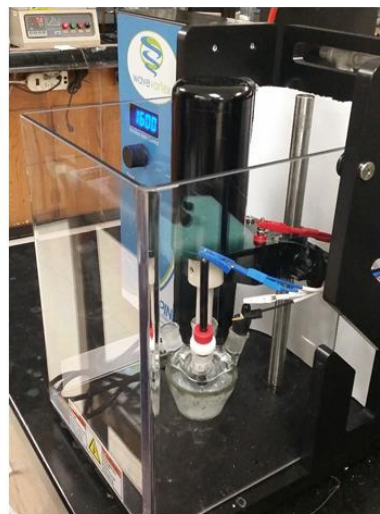
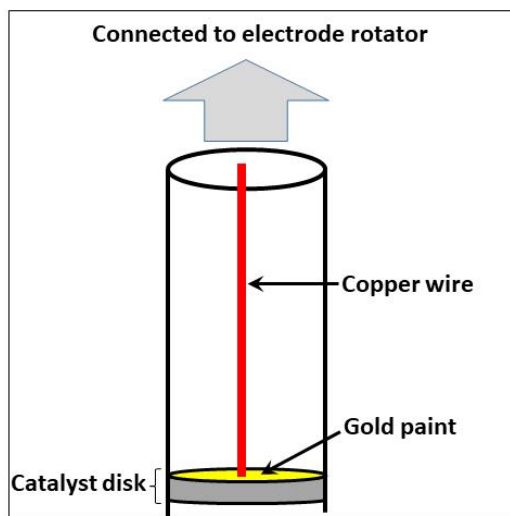


Figure S2. (a) The setup for testing the OER activity of catalysts disks, without glassy carbon electrode. (b) The entire measurement setup.

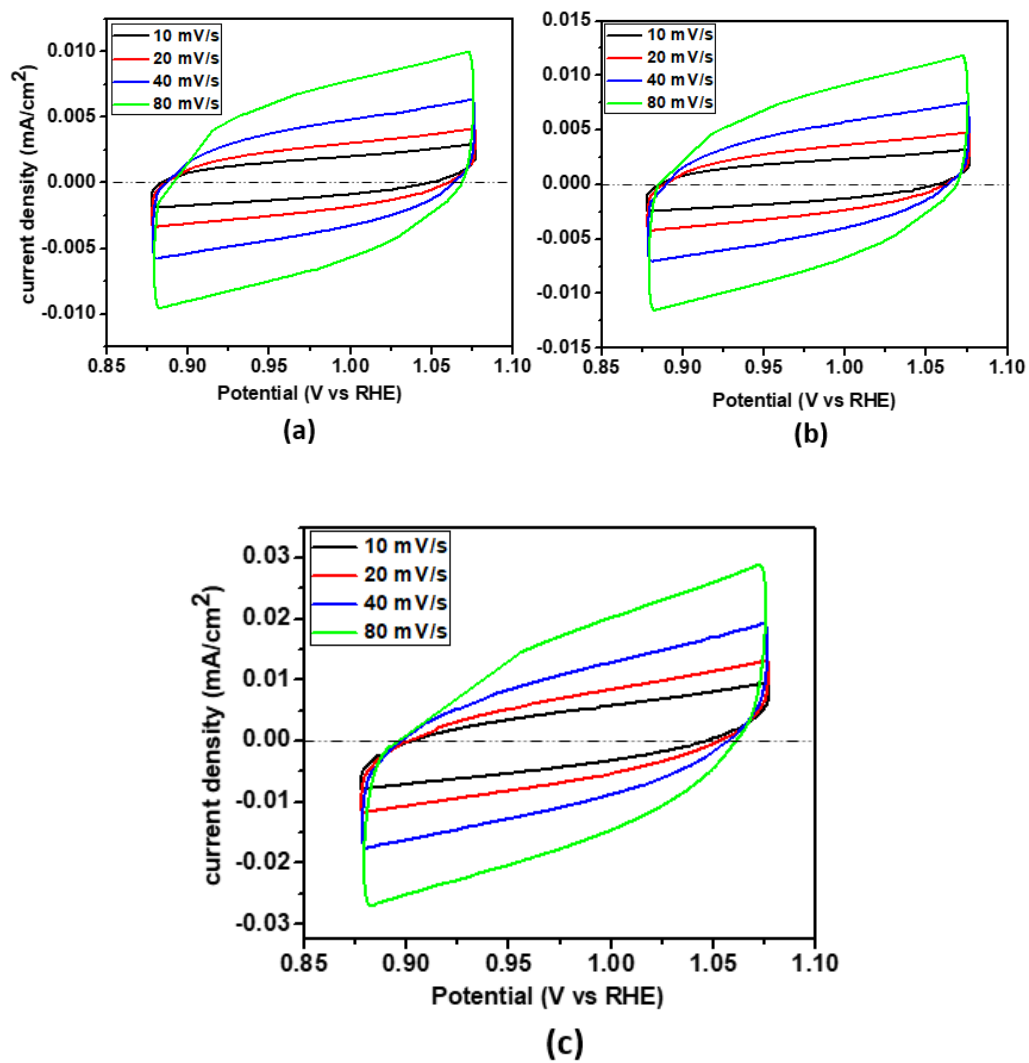


Figure S3. Cyclic voltammetry in non-faradic region to obtain double layer capacitance (Figure 12.4) for the three compounds (a) Ca₂Fe₂O_{6-δ}, (b) CaSrFe₂O_{6-δ}, and (c) Sr₂Fe₂O_{6-δ}.

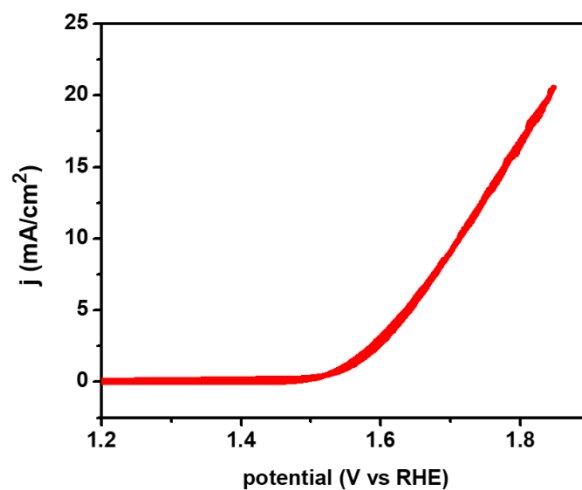


Figure S4. Polarization curve for Sr₂Fe₂O_{6-δ}, obtained using the conventional glassy carbon setup, and with the addition of carbon black to the catalyst. Comparison to Figure 12.2 indicates that carbon black does not improve the OER activity.

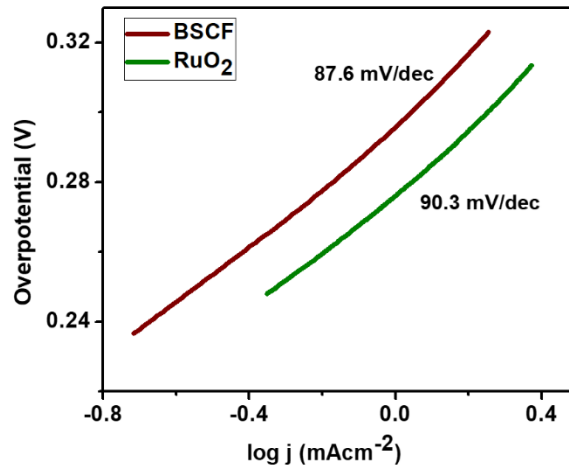


Figure S5. Tafel slopes for BSCF and RuO₂.

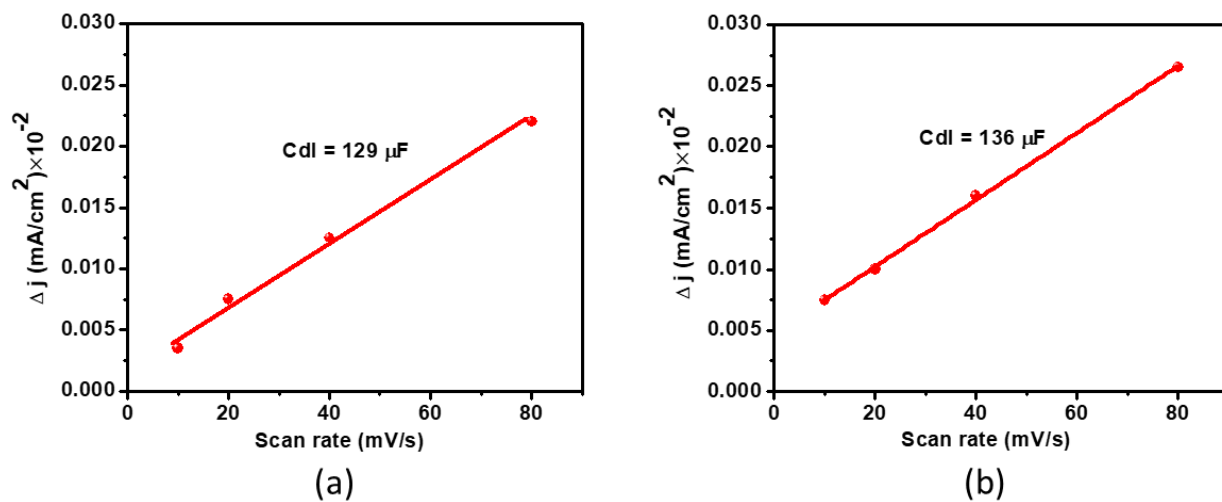


Figure S6. Plot of $\Delta j = j_{\text{anodic}} - j_{\text{cathodic}}$ as a function of scan rate for (a) BSCF and (b) RuO₂. The C_{dl} for each material is equivalent to half of the slope.

Table S1. The refined structural parameters for Ca₂Fe₂O_{6- δ} from powder X-ray diffraction. Space group: *Pnma*, $a = 5.40238(5)$, $b = 14.7018(1)$, $c = 5.57261(5)$, $R_p = 0.013$, $wR_p = 0.018$, $\chi^2 = 1.941$

Elements	x	y	z	occupancy	U_{iso}
Ca	0.4807(5)	0.1080(1)	0.0248(4)	1	0.0281(9)
Fe1	0.0	0.0	0.0	1	0.027(1)
Fe2	-0.0551(6)	0.25	-0.0670(4)	1	0.030(1)
O1	0.261(3)	-0.0154(3)	0.234(1)	1	0.021(1)
O2	0.0297(1)	0.1423(3)	0.0773(8)	1	0.021(1)
O3	0.6084(2)	0.25	-0.124(2)	1	0.021(1)

Table S2. The refined structural parameters for $\text{CaSrFe}_2\text{O}_{6-\delta}$ from powder X-ray diffraction. Space group: $IBM2$, $a = 5.6313(4)$, $b = 15.181(1)$, $c = 5.4695(4)$, $R_p = 0.018$, $wR_p = 0.026$, $\chi^2 = 1.604$

Elements	x	y	z	occupancy	U_{iso}
Ca	0.5127(5)	0.1109(1)	0.008(4)	0.5	0.015(1)
Sr	0.5127(5)	0.1109(1)	0.008(4)	0.5	0.015(1)
Fe1	0.0	0.0	0.0	1	0.022(2)
Fe2	0.0760(7)	0.25	-0.004(7)	1	0.013(2)
O1	0.229(4)	0.0069(6)	0.292(5)	1	0.014(3)
O2	-0.082(1)	0.149(5)	0.001(8)	1	0.014(3)
O3	0.382(3)	0.25	0.887(7)	1	0.014(3)

Table S3. The refined structural parameters for $\text{Sr}_2\text{Fe}_2\text{O}_{6-\delta}$ from powder X-ray diffraction. Space group: $I4/mmm$, $a = 10.9345(7)$, $b = 10.9345(7)$, $c = 7.6988(5)$, $R_p = 0.022$, $wR_p = 0.031$, $\chi^2 = 1.505$

Elements	x	y	z	occupancy	U_{iso}
Sr1	0.2561(7)	0.0	0.0	1	0.026(2)
Sr2	0.2488(7)	0.0	0.5	1	0.041(3)
Fe1	0.0	0.0	0.25	1	0.061(9)
Fe2	0.25	0.25	0.25	1	0.023(3)
Fe3	0.5	0.0	0.25	1	0.042(8)
O1	0.0	0.0	0.25	1	0.024(2)
O2	0.124(2)	0.124(2)	0.208(2)	1	0.024(2)
O3	0.250(2)	0.250(2)	0.5	1	0.024(2)
O4	0.131(2)	0.631(2)	0.25	1	0.024(2)
O5	0.5	0.0	0.0	1	0.024(2)

REFERENCES

1. Tilley, R. J. D., *Perovskites: Structure-Property Relationships*. John Wiley & Sons, Ltd: 2016.
2. Bombik, A.; Leśniewska, B.; Mayer, J.; Pacyna, A. W., Crystal structure of solid solutions $\text{REFe}_{1-x}(\text{Al or Ga})_x\text{O}_3$ (RE=Tb, Er, Tm) and the correlation between superexchange interaction $\text{Fe}^{+3}-\text{O}^{2-}-\text{Fe}^{+3}$ linkage angles and Néel temperature. *J. Magn. Magn. Mater.* **2003**, *257*, 206-219.
3. Karki, S. B.; Ramezanipour, F., Magnetic and electrical properties of BaSrMMoO_6 (M = Mn, Fe, Co, and Ni). *Mater. Today Chem.* **2019**, *13*, 25-33.
4. Hona, R. K.; Huq, A.; Mulmi, S.; Ramezanipour, F., Transformation of structure, electrical conductivity, and magnetism in $\text{AA}'\text{Fe}_2\text{O}_{6-\delta}$, A = Sr, Ca and A' = Sr. *Inorg. Chem.* **2017**, *56*, 9716-9724.
5. Berastegui, P.; Eriksson, S. G.; Hull, S., A neutron diffraction study of the temperature dependence of $\text{Ca}_2\text{Fe}_2\text{O}_5$. *Mater. Res. Bull.* **1999**, *34*, 303-314.
6. Stolen, S.; Bakken, E.; Mohn, C. E., Oxygen-deficient perovskites: linking structure, energetics and ion transport. *Phys. Chem. Chem. Phys.* **2006**, *8* (4), 429-447.
7. Ramezanipour, F.; Greedan, J. E.; Grosvenor, A. P.; Britten, J. F.; Cranswick, L. M. D.; Garlea, V. O., Intralayer Cation Ordering in a Brownmillerite Superstructure: Synthesis, Crystal, and Magnetic Structures of $\text{Ca}_2\text{FeCoO}_5$. *Chem. Mater.* **2010**, *22* (21), 6008-6020.
8. Tilley, R. J. D., defects in solids. *John Wiley & Sons, Inc.* **2008**.
9. Asenath-Smith, E.; Misture, S. T.; Edwards, D. D., Structural behavior and thermoelectric properties of the brownmillerite system $\text{Ca}_2(\text{ZnxFe}_{2-x})\text{O}_5$. *J. Solid State Chem.* **2011**, *184*, 2167-2177.
10. Auckett, J. E.; Studer, A. J.; Sharma, N.; Ling, C. D., Floating-zone growth of brownmillerite $\text{Sr}_2\text{Fe}_2\text{O}_5$ and the observation of a chain-ordered superstructure by single-crystal neutron diffraction. *Solid State Ionics* **2012**, *225*, 432-436.
11. Ramezanipour, F.; Greedan, J. E.; Siewenie, J.; Proffen, T.; Ryan, D. H.; Grosvenor, A. P.; Donaberger, R. L., Local and Average Structures and Magnetic Properties of $\text{Sr}_2\text{FeMnO}_{5+\gamma}$, $\gamma=0.0, 0.5$. Comparisons with $\text{Ca}_2\text{FeMnO}_5$ and the Effect of the A-Site Cation. *Inorg. Chem.* **2011**, *50* (16), 7779-7791.
12. Ramezanipour, F.; Greedan, J. E.; Cranswick, L. M. D.; Garlea, V. O.; Siewenie, J.; King, G.; Llobet, A.; Donaberger, R. L., The effect of the B-site cation and oxygen stoichiometry on the local and average crystal and magnetic structures of $\text{Sr}_2\text{Fe}_{1.9}\text{M}_{0.1}\text{O}_{5+\gamma}$ (M = Mn, Cr, Co; $\gamma = 0, 0.5$). *J. Mater. Chem.* **2012**, *22*, 9522-9538.
13. Shaula, A. L.; Kolotygin, V. A.; Naumovich, E. N.; Pivak, Y. V.; Kharton, V. V., Oxygen Ionic Transport in Brownmillerite-Type and Calcium Ferrite-Based Composite Membranes. *Solid State Phenom.* **2013**, *200*, 286-292.
14. Greaves, C.; Jacobson, A. J.; Tofield, B. C.; Fender, B. E. F., A powder neutron diffraction investigation of the nuclear and magnetic structure of $\text{Sr}_2\text{Fe}_2\text{O}_5$. *Acta Crystallogr., Sect. B* **1975**, *31*, 641-646.
15. Dhankhar, S.; Bhalerao, G.; Ganesamoorthy, S.; Baskar, K.; Singh, S., Growth and comparison of single crystals and polycrystalline brownmillerite $\text{Ca}_2\text{Fe}_2\text{O}_5$. *J. Cryst. Growth* **2017**, *468*, 311.

16. Pomjakushin, V. Y.; Balagurov, A. M.; Elzhov, T. V.; Sheptyakov, D. V.; Fischer, P.; Khomskii, D. I.; Yushankhai, V. Y.; Abakumov, A. M.; Rozova, M. G.; Antipov, E. V.; Lobanov, M. V.; Billinge, S. J. L., Atomic and magnetic structures, disorder effects, and unconventional superexchange interactions in A_2MnGaO_{5+d} ($A=Sr,Ca$) oxides of layered brownmillerite-type structure. *Phys. Rev. B* **2002**, *66*, 184412.
17. Patrakeevev, M. V.; Kharton, V. V.; Bakhteeva, Y. A.; Shaula, A. L.; Leonidov, I. A.; Kozhevnikov, V. L.; Naumovich, E. N.; Yaremchenko, A. A.; Marques, F. M. B., Oxygen nonstoichiometry and mixed conductivity of $SrFe_{1-x}M_xO_{3-\delta}$ ($M=Al, Ga$): Effects of B-site doping. *Solid State Sci.* **2006**, *8* (5), 476-487.
18. Hona, R. K.; Ramezanipour, F., Enhanced electrical properties in $BaSrFe_2O_{6-\delta}$ ($\delta = 0.5$): A disordered defect-perovskite. *Polyhedron* **2019**, *167*, 69-74.
19. Hona, R. K.; Huq, A.; Ramezanipour, F., Charge transport properties of $Ca_2FeGaO_{6-\delta}$ and $CaSrFeGaO_{6-\delta}$: The effect of defect-order. *Mater. Chem. Phys.* **2019**, *238*, 121924.
20. Hona, R. K.; Huq, A.; Mulmi, S.; Ramezanipour, F., Transformation of Structure, Electrical Conductivity, and Magnetism in $AA'Fe_2O_{6-\delta}$, $A = Sr, Ca$ and $A' = Sr$. *Inorganic Chemistry* **2017**, *56* (16), 9716-9724.
21. Mineshige, A.; Kobune, M.; Fujii, S.; Ogumi, Z.; Inaba, M.; Yao, T.; Kikuchi, K., Metal-Insulator Transition and Crystal Structure of $La_{1-x}Sr_xCoO_3$ as Functions of Sr-Content, Temperature, and Oxygen Partial Pressure. *J. Solid State Chem.* **1999**, *142*, 374-381.
22. Mineshige, A.; Inaba, M.; Yao, T.; Ogumi, Z.; Kikuchi, K.; Kawase, M., Crystal Structure and Metal-Insulator Transition of $La_{1-x}Sr_xCoO_3$. *J. Solid State Chem.* **1996**, *121*, 423-429.
23. Patrakeevev, M. V.; Kharton, V. V.; Bakhteeva, Y. A.; Shaula, A. L.; Leonidov, I. A.; Kozhevnikov, V. L.; Naumovich, E. N.; Yaremchenko, A. A.; Marques, F. M. B., Oxygen nonstoichiometry and mixed conductivity of $SrFe_{1-x}M_xO_{3-\delta}$ ($M=Al, Ga$): Effects of B-site doping. *Solid State Sci.* **2006**, *8*, 476-487.
24. Kozhevnikov, V. L.; Leonidov, I. A.; Patrakeevev, M. V.; Mitberg, E. B.; Poepelmeier, K. R., Electrical Properties of the Ferrite $SrFeO_y$ at High Temperatures. *J. Solid State Chem.* **2001**, *158*, 320-326.
25. Cheng, Y.; Jiang, S. P., Advances in electrocatalysts for oxygen evolution reaction of water electrolysis-from metal oxides to carbon nanotubes. *Progress in Natural Science: Materials International* **2015**, *25*, 545-553.
26. Zhu, Y.; Zhou, W.; Sunarso, J.; Zhong, Y.; Shao, Z., Phosphorus-doped perovskite oxide as highly efficient water oxidation electrocatalyst in alkaline solution. *Adv. funct. mater.* **2016**, *26*, 5862-5872.
27. Rong, X.; Parolin, J.; Kolpak, A. M., A Fundamental Relationship between Reaction Mechanism and Stability in Metal Oxide Catalysts for Oxygen Evolution. *ACS Catal.* **2016**, *6*, 1153-1158.
28. Sammells, A. F.; Schwartz, M.; Mackay, R. A.; Barton, T. F.; Peterson, D. R., Catalytic membrane reactors for spontaneous synthesis gas production. *Catal. Today* **2000**, *56* (1-3), 325-328.
29. Li, Q.; Sun, L.; Zeng, X.; Zhao, H.; Huo, L.; Grenier, J.-C.; Bassat, J.-M.; Mauvy, F., Evaluation of a brownmillerite oxide as cathode for solid oxide fuel cells. *J. Power Sources* **2013**, *238*, 11-16.
30. Kobayashi, K. I.; Kimura, T.; Sawada, H.; Terakura, K.; Tokura, Y., Room-temperature magnetoresistance in an oxide material with an ordered double-perovskite structure. *Nature* **1998**, *395* (6703), 677-680.
31. Shunji, T.; Hiroshi, N.; Yoshio, I.; Nobuo, I., The Oxygen-Deficient Perovskite Solid Solution $Nd_{1+x}Ba_{2-x}Cu_3O_y$ and Its Superconductivity. *Jpn. J. Appl. Phys.* **1987**, *26* (12A), L2076.

32. Ramezanipour, F.; Greedan, J. E.; Siewenie, J.; Proffen, T.; Ryan, D. H.; Grosvenor, A. P.; Donaberger, R. L., Local and Average Structures and Magnetic Properties of $\text{Sr}_2\text{FeMnO}_{5+y}$, $y = 0.0, 0.5$. Comparisons with $\text{Ca}_2\text{FeMnO}_5$ and the Effect of the A-Site Cation. *Inorg Chem.* **2011**, *50* (16), 7779-7791.
33. Ramezanipour, F.; Cowie, B.; Derakhshan, S.; Greedan, J. E.; M.D., L.; c, C., Crystal and magnetic structures of the brownmillerite compound $\text{Ca}_2\text{Fe}_{1.039(8)}\text{Mn}_{0.962(8)}\text{O}_5$. *J. Solid State Chem.* **2009**, *182* (153–159), 153–159.
34. Ramezanipour, F.; Greedan, J. E.; Cranswick, L. M. D.; Garlea, V. O.; Donaberger, R. L.; Siewenie, J., Systematic Study of Compositional and Synthetic Control of Vacancy and Magnetic Ordering in Oxygen-Deficient Perovskites $\text{Ca}_2\text{Fe}_{2-x}\text{Mn}_x\text{O}_{5+y}$ and $\text{CaSrFe}_{2-x}\text{Mn}_x\text{O}_{5+y}$ ($x = 1/2, 2/3$, and 1 ; $y = 0-1/2$). *J. Am. Chem. Soc.* **2012**, *134* (6), 3215-3227.
35. Kim, J.; Yin, X.; Tsao, K.-C.; Fang, S.; Yang, H., $\text{Ca}_2\text{Mn}_2\text{O}_5$ as Oxygen-Deficient Perovskite Electrocatalyst for Oxygen Evolution Reaction. *J. Am. Chem. Soc.* **2014**, *136* (42), 14646-14649.
36. Hodges, J. P.; Short, S.; Jorgensen, J. D.; Xiong, X.; Dabrowski, B.; Mini, S. M.; Kimball, C. W., Evolution of Oxygen-Vacancy Ordered Crystal Structures in the Perovskite Series $\text{Sr}_n\text{Fe}_n\text{O}_{3n-1}$ ($n=2, 4, 8$, and ∞), and the Relationship to Electronic and Magnetic Properties. *J. Solid State Chem.* **2000**, *151* (2), 190-209.
37. Wu, J. W.; Wang, J.; Liu, G.; Wu, Y. J.; Liu, X. Q.; Chen, X. M., Giant room-temperature magnetodielectric coupling in spark plasma sintered brownmillerite ceramics. *Appl. Phys. Lett.* **2014**, *105* (22), 222906.
38. Pomjakushin, V. Y.; Balagurov, A. M.; Elzhov, T. V.; Sheptyakov, D. V.; Fischer, P.; Khomskii, D. I.; Yushankhai, V. Y.; Abakumov, A. M.; Rozova, M. G.; Antipov, E. V.; Lobanov, M. V.; Billinge, S. J. L., Atomic and magnetic structures, disorder effects, and unconventional superexchange interactions in $\text{A}_2\text{MnGaO}_{5+d}$ ($\text{A}=\text{Sr}, \text{Ca}$) oxides of layered brownmillerite-type structure. *Phys. Rev. B* **2002**, *66* (18), 184412.
39. Nemudry, A.; Rogatchev, A.; Gainutdinov, I.; Schöllhorn, R., Reactivity of the perovskite system $\text{Ca}_{1-x}\text{Sr}_x\text{FeO}_{2.5}$ in topotactic electrochemical oxidation at ambient temperature. *J Solid State Electrochem.* **2001**, *5* (7), 450-458.
40. Larson, A. C.; Von Dreele, R. B., General Structure Analysis System (GSAS), Los Alamos National Laboratory Report LAUR. **1994**, 86–748.
41. Toby, B. H., *J. Appl. Crystallogr.* **2001**, *34* 210-213.
42. Ramezanipour, F.; Greedan, J. E.; Grosvenor, A. P.; Britten, J. F.; Cranswick, L. M. D.; Garlea, V. O., Intralayer Cation Ordering in a Brownmillerite Superstructure: Synthesis, Crystal, and Magnetic Structures of $\text{Ca}_2\text{FeCoO}_5$. *Chemistry of Materials* **2010**, *22* (21), 6008-6020.
43. Jijil, C. P.; Lokanathan, M.; Chithiravel, S.; Nayak, C.; Bhattacharyya, D.; Jha, S. N.; Babu, P. D.; Kakade, B.; Devi, R. N., Nitrogen doping in oxygen-deficient $\text{Ca}_2\text{Fe}_2\text{O}_5$: A strategy for efficient oxygen reduction oxide catalysts. *ACS Appl. Mater. Interfaces* **2016**, *8*, 34387-34395.
44. Ghaffari, M.; Liu, T.; Huang, H.; Tan, O. K.; Shannon, M., Investigation of local structure effect and X-ray absorption characteristics (EXAFS) of Fe (Ti) K-edge on photocatalyst properties of $\text{SrTi}_{(1-x)}\text{Fe}_x\text{O}_{(3-\delta)}$. *Mater. Chem. Phys.* **2012**, *136*, 347-357.
45. Berastegui, P.; Eriksson, S. G.; Hull, S., A neutron diffraction study of the temperature dependence of $\text{Ca}_2\text{Fe}_2\text{O}_5$. *Materials Research Bulletin* **1999**, *34* (2), 303-314.
46. Shannon, R. D., Revised Effective Ionic Radii and Systematic Studies of Interatomic Distances in Halides and Chalcogenides. *Acta Cryst.* **1976**, *A32*, 751.
47. Reehuis, M.; Ulrich, C.; Maljuk, A.; Niedermayer, C.; Ouladdiaf, B.; Hoser, A.; Hofmann, T.; Keimer, B., Neutron diffraction study of spin and charge ordering in $\text{SrFeO}_{3-\delta}$. *Phys. Rev. B* **2012**, *85* (18), 184109.

48. Cheng, X.; Fabbri, E.; Nachtegaal, M.; Castelli, I. E.; El Kazzi, M.; Haumont, R.; Marzari, N.; Schmidt, T. J., Oxygen Evolution Reaction on $\text{La}_{1-x}\text{Sr}_x\text{CoO}_3$ Perovskites: A Combined Experimental and Theoretical Study of Their Structural, Electronic, and Electrochemical Properties. *Chem. Mater.* **2015**, *27* (22), 7662-7672.
49. Pizzini, S., Physical chemistry of semiconductor materials and processes *John Wiley & Sons Ltd, West Sussex, United Kingdom* **2015**.
50. Asenath-Smith, E.; Lokuhewa, I. N.; Misture, S. T.; Edwards, D. D., p-Type thermoelectric properties of the oxygen-deficient perovskite $\text{Ca}_2\text{Fe}_2\text{O}_5$ in the brownmillerite structure. *J. Solid State Chem.* **2010**, *183*, 1670-1677.
51. Andoulsi, R.; Horchani-Naifer, K.; Férid, M., Electrical conductivity of $\text{La}_{1-x}\text{Ca}_x\text{FeO}_{3-\delta}$ solid solutions. *Ceram. Int.* **2013**, *39*, 6527-6531.
52. Patrakeevev, M. V.; Leonidov, I. A.; Kozhevnikov, V. L.; Kharton, V. V., Ion–electron transport in strontium ferrites: relationships with structural features and stability. *SOLID STATE SCI* **2004**, *6* (9), 907-913.
53. Yu, H.-C.; Fung, K.-Z., Role of Sr Addition on the Structure Stability and Electrical Conductivity of Sr-Doped Lanthanum Copper Oxide Perovskites. *J. Mater.* **2004**, *19* (3), 943-949.
54. Torrance, J. B.; Lacorre, P.; Nazzari, A. I.; Ansaldo, E. J.; Niedermayer, C., Systematic study of insulator-metal transitions in perovskites RNiO_3 (R=Pr,Nd,Sm,Eu) due to closing of charge-transfer gap. *Phys. Rev. B* **1992**, *45* (14), 8209-8212.
55. Shaula, A. L.; Kharton, V. V.; Patrakeevev, M. V.; Waerenborgh, J. C.; Rojas, D. P.; Marques, F. M. B., Defect formation and transport in $\text{SrFe}_{1-x}\text{Al}_x\text{O}_{3-\delta}$. *Ionics* **2004**, *10* (5), 378-384.
56. Tilley, R. J. D., Defects in Solids. *John Wiley & Sons, Hoboken, NJ* **(2008)**.
57. Asenath-Smith, E.; Misture, S. T.; Edwards, D. D., Structural behavior and thermoelectric properties of the brownmillerite system $\text{Ca}_2(\text{Zn}_x\text{Fe}_{2-x})\text{O}_5$. *J. Solid State Chem.* **2011**, *184* (8), 2167-2177.
58. Ren, P.; Maso, N.; Liu, Y.; Ma, L.; Fan, H.; West, A. R., Mixed oxide ion and proton conduction and p-type semiconduction in $\text{BaTi}_{0.98}\text{Ca}_{0.02}\text{O}_{2.98}$ ceramics. *J. Mater. Chem. C* **2013**, *1*, 2426-2432.
59. Ren, P.; Maso, N.; West, A. R., Hole conductivity in oxygen-excess $\text{BaTi}_{1-x}\text{Ca}_x\text{O}_{3-x+\delta}$. *Phys. Chem. Chem. Phys.* **2013**, *15*, 20943-20950.
60. Patrakeevev, M. V.; Kharton, V. V.; Bakhteeva, Y. A.; Shaula, A. L.; Leonidov, I. A.; Kozhevnikov, V. L.; Naumovich, E. N.; Yaremchenko, A. A.; Marques, F. M. B., Oxygen nonstoichiometry and mixed conductivity of $\text{SrFe}_{1-x}\text{M}_x\text{O}_{3-\delta}$ (M=Al, Ga): Effects of B-site doping. *SOLID STATE SCI* **2006**, *8* (5), 476-487.
61. Patrakeevev, M. V.; Leonidov, I. A.; Kozhevnikov, V. L.; Poeppelmeier, K. R., p-Type electron transport in $\text{La}_{1-x}\text{Sr}_x\text{FeO}_{3-\delta}$ at high temperatures. *J. Solid State Chem.* **2005**, *178* (3), 921-927.
62. A. A. Fargali, M. K. Z., M. H. Khedr and A. F. Moustafa, Phase and conductivity dynamics of strontium hexaferrite nanocrystals in a hydrogen gas flow. *Int. J. Phys. Sci.* **2008**, *3* (5), 131.
63. Armstrong, T.; Prado, F.; Manthiram, A., Synthesis, crystal chemistry, and oxygen permeation properties of $\text{LaSr}_3\text{Fe}_{3-x}\text{Co}_x\text{O}_{10}$ ($0 \leq x \leq 1.5$). *Solid State Ion.* **2001**, *140* (1–2), 89-96.
64. Chen, Z.; Ran, R.; Zhou, W.; Shao, Z.; Liu, S., Assessment of $\text{Ba}_{0.5}\text{Sr}_{0.5}\text{Co}_{1-y}\text{Fe}_y\text{O}_{3-\delta}$ ($y = 0.0-1.0$) for prospective application as cathode for IT-SOFCs or oxygen permeating membrane. *Electrochim. Acta* **2007**, *52* (25), 7343-7351.
65. Picard, C.; Gerdanian, P., Determination of the Néel temperature in $\text{YBa}_2\text{Cu}_3\text{O}_z$ by electrical conductivity measurements. *Solid State Commun.* **1993**, *87* (9), 775-778.
66. Richardson, G.; O'Kane, S. E. J.; Niemann, R. G.; Peltola, T. A.; Foster, J. M.; Cameron, P. J.; Walker, A. B., Can slow-moving ions explain hysteresis in the current-voltage curves of perovskite solar cells? *Energy Environ. Sci.* **2016**, *9* (4), 1476-1485.

67. Guite, C.; Kerk, I. S.; Sekhar, M. C.; Ramu, M.; Goolaup, S.; Lew, W. S., All-electrical deterministic single domain wall generation for on-chip applications. *Sci. Rep.* **2014**, *4*, 7459.
68. Tomasello, R.; Martinez, E.; Zivieri, R.; Torres, L.; Carpentieri, M.; Finocchio, G., A strategy for the design of skyrmion racetrack memories. *Sci. Rep.* **2014**, *4*, 6784.
69. Elilarassi, R.; Chandrasekaran, G., Optical, electrical and ferromagnetic studies of ZnO:Fe diluted magnetic semiconductor nanoparticles for spintronic applications. *Spectrochim. Acta Mol. Biomol. Spectrosc.* **2017**, *186*, 120-131.
70. Ramezanipour, F.; Greedan, J. E.; Siewenie, J.; Donaberger, R. L.; Turner, S.; Botton, G. A., A vacancy-disordered, oxygen-deficient perovskite with long-range magnetic ordering: Local and average structures and magnetic properties of Sr₂Fe_{1.5}Cr_{0.5}O₅. *Inorg. Chem.* **2012**, *51*, 2638-2644.
71. Zhang, G. B.; Smyth, D. M., Defects and transport of the brownmillerite oxides with high oxygen ion conductivity — Ba₂In₂O₅. *Solid State Ionics* **1995**, *82* (3), 161-172.
72. Ramezanipour, F.; Greedan, J. E.; Cranswick, L. M. D.; Garlea, V. O.; Donaberger, R. L.; Siewenie, J., Systematic study of compositional and synthetic control of vacancy and magnetic ordering in oxygen-deficient perovskites Ca₂Fe_{2-x}Mn_xO_{5+y} and CaSrFe_{2-x}Mn_xO_{5+y} (x = 1/2, 2/3, and 1; y = 0–1/2). *J. Am. Chem. Soc.* **2012**, *134*, 3215-3227.
73. Turner, S.; Verbeeck, J.; Ramezanipour, F.; Greedan, J. E.; Van Tendeloo, G.; Botton, G. A., Atomic resolution coordination mapping in Ca₂FeCoO₅ brownmillerite by spatially resolved electron energy-loss spectroscopy. *Chem. Mater.* **2012**, *24*, 1904-1909.
74. Ramezanipour, F.; Greedan, J. E.; Grosvenor, A. P.; Britten, J. F.; Cranswick, L. M. D.; Garlea, V. O., Intralayer cation ordering in a brownmillerite superstructure: synthesis, crystal, and magnetic structures of Ca₂FeCoO₅. *Chem. Mater.* **2010**, *22*, 6008-6020.
75. Ramezanipour, F.; Cowie, B.; Derakhshan, S.; Greedan, J. E.; Cranswick, L. M. D., Crystal and magnetic structures of the brownmillerite compound Ca₂Fe_{1.039(8)}Mn_{0.962(8)}O₅. *J. Solid State Chem.* **2009**, *182*, 153-159.
76. Ramezanipour, F.; Greedan, J. E.; Siewenie, J.; Donaberger, R. L.; Turner, S.; Botton, G. A., A Vacancy-Disordered, Oxygen-Deficient Perovskite with Long-Range Magnetic Ordering: Local and Average Structures and Magnetic Properties of Sr₂Fe_{1.5}Cr_{0.5}O₅. *Inorg. Chem.* **2012**, *51* (4), 2638-2644.
77. Homonnay, Z.; Nomura, K.; Juhász, G.; Kuzmann, E.; Hamakawa, S.; Hayakawa, T.; Vértés, A., Microstructure and CO₂-absorption in Sr_{0.95}Ca_{0.05}Co_{0.5}Fe_{0.5}O_{3-δ};#948; and Sr_{0.5}Ca_{0.5}Co_{0.5}Fe_{0.5}O_{3-δ};#948; as studied by Emission Mössbauer Spectroscopy. *J. Radioanal. Nucl. Chem.* **2003**, *255* (3), 425-429.
78. Aksenova, T. V. G.; L. Ya; Cherepanov, V. A., Phase equilibria and crystal structure of the complex oxides in the Sr–Fe–Co–O system. *J. Solid State Chem.* **2008**, *181* (6), 1480-1484.
79. Gómez, L.; Galeano, V.; Parra, R.; Michel, C. R.; Paucar, C.; Morán, O., Carbon dioxide gas sensing properties of ordered oxygen deficient perovskite LnBaCo₂O_{5+δ} (Ln=La, Eu). *Sensors and Actuators B: Chem.* **2015**, *221*, 1455-1460.
80. Liu, P.; Luo, Z.; Kong, J.; Yang, X.; Liu, Q.; Xu, H., Ba_{0.5}Sr_{0.5}Co_{0.8}Fe_{0.2}O_{3-δ}-based dual-gradient cathodes for solid oxide fuel cells. *Ceram. Int.* **2018**, *44* (4), 4516-4519.
81. Chen, G.; Zhou, W.; Guan, D.; Sunarso, J.; Zhu, Y.; Hu, X.; Zhang, W.; Shao, Z., Two orders of magnitude enhancement in oxygen evolution reactivity on amorphous Ba_(0.5)Sr_(0.5)Co_(0.8)Fe_(0.2)O_(3-δ) nanofilms with tunable oxidation state. *Sci. Adv.* **2017**, *3*, e1603206.
82. Suescun, L.; Chmaissem, O.; Mais, J.; Dabrowski, B.; Jorgensen, J. D., Crystal structures, charge and oxygen-vacancy ordering in oxygen deficient perovskites SrMnO_x (x<2.7). *J. Solid State Chem.* **2007**, *180*, 1698-1707.
83. Hodges, J. P.; Jorgensen, J. D.; Xiong, X.; Dabrowski, B.; Mini, S. M.; Kimball, C. W.; Materials Science, D.; Northern Illinois, U., Evolution of oxygen-vacancy ordered crystal structures

- in the perovskite series $\text{Sr}_n\text{Fe}_n\text{O}_{3n-1}$ ($n=2, 4, 8,$ and $\{\infty\}$), and the relationship to electronic and magnetic properties. *J. Solid State Chem.* **2000**, *151*, 209.
84. Hona, R. K.; Huq, A.; Ramezanipour, F., Unraveling the role of structural order in the transformation of electrical conductivity in $\text{Ca}_2\text{FeCoO}_{6-\delta}$, $\text{CaSrFeCoO}_{6-\delta}$, and $\text{Sr}_2\text{FeCoO}_{6-\delta}$. *Inorg. Chem.* **2017**, *56*, 14494-14505.
85. Mulmi, S.; Hona, R. K.; Jasinski, J. B.; Ramezanipour, F., Electrical conductivity of $\text{Sr}_{2-x}\text{Ca}_x\text{FeMnO}_5$ ($x = 0, 1, 2$). *J. Solid State Electrochem.* **2018**, *22*, 2329-2338.
86. Hona, R. K.; Ramezanipour, F., Variation in electrical conductivity of $\text{A}_2\text{Fe}_2\text{O}_5$ ($\text{A} = \text{Sr}, \text{Ba}$): the role of structural order. *Mater. Res. Express* **2018**, *5* (7), 076307.
87. Ramezanipour, F.; Greedan, J. E.; Cranswick, L. M. D.; Garlea, V. O.; Donaberger, R. L.; Siewenie, J., Systematic Study of Compositional and Synthetic Control of Vacancy and Magnetic Ordering in Oxygen-Deficient Perovskites $\text{Ca}_2\text{Fe}_{2-x}\text{Mn}_x\text{O}_{5+y}$ and $\text{CaSrFe}_{2-x}\text{Mn}_x\text{O}_{5+y}$ ($x = 1/2, 2/3,$ and $1; y = 0-1/2$). *J. Am. Chem. Soc.* **2012**, *134* (6), 3215-3227.
88. Hona, R. K.; Ramezanipour, F., Disparity in electrical and magnetic properties of isostructural oxygen-deficient perovskites $\text{BaSrCo}_2\text{O}_{6-\delta}$ and $\text{BaSrCoFeO}_{6-\delta}$. *J. Mater. Sci. Mater. Electron.* **2018**.
89. Ramezanipour, F.; Greedan, J. E.; Siewenie, J.; Proffen, T.; Ryan, D. H.; Grosvenor, A. P.; Donaberger, R. L., Local and average structures and magnetic properties of $\text{Sr}_2\text{FeMnO}_{5+y}$, $y = 0.0, 0.5$. Comparisons with $\text{Ca}_2\text{FeMnO}_5$ and the effect of the A-site cation. *Inorg. Chem.* **2011**, *50*, 7779-7791.
90. Hona, R. K.; Huq, A.; Ramezanipour, F., Magnetic structure of $\text{CaSrFeCoO}_{6-\delta}$: Correlations with structural order. *Mater. Res. Bull.* **2018**, *106*, 131-136.
91. Fossdal, A.; Menon, M.; Wærnhus, I.; Wiik, K.; Einarsrud, M. A.; Grande, T., Crystal Structure and Thermal Expansion of $\text{La}_{1-x}\text{Sr}_x\text{FeO}_{3-\delta}$ Materials. *J. Am. Ceram. Soc.* **2005**, *87* (10), 1952-1958.
92. Anikina, P. V.; Markov, A. A.; Patrakeev, M. V.; Leonidov, I. A.; Kozhevnikov, V. L., The structure, nonstoichiometry, and thermodynamic characteristics of oxygen in strontium ferrite doped with niobium, $\text{SrFe}_{1-x}\text{Nb}_x\text{O}_{3-\delta}$. *Russian J. Phys. Chem. A* **2009**, *83*, 699-704.
93. Colville, A. A.; Geller, S., The Crystal Structure of Brownmillerite, $\text{Ca}_2\text{FeAlO}_5$. *Acta Cryst.* **1971**, (B27), 2311.
94. Hans D'Hondt; JokeHadermann; ArtemM.Abakumov; AnnaS.Kalyuzhnaya; Marina G.Rozova; AlexanderA.Tsirlin; RameshNath; HaiyanTan; JoVerbeeck; EvgenyV.Antipov; GustaafVanTendeloo, Synthesis, crystal structure and magnetic properties of the $\text{Sr}_2\text{Al}_{0.78}\text{Mn}_{1.22}\text{O}_{5.2}$ anion-deficient layered perovskite. *J. Solid State Chem.* **2009**, *182*, 356-363.
95. Lindberg, F.; Istomin, S. Y.; Berastegui, P.; Svensson, G.; Kazakov, S. M.; Antipov, E. V., Synthesis and structural studies of $\text{Sr}_2\text{Co}_{2-x}\text{Ga}_x\text{O}_5$, $0.3 \leq x \leq 0.8$. *J. Solid State Chem.* **2003**, *173* (2), 395-406.
96. Didier, C.; Claridge, J.; Rosseinsky, M., Crystal structure of brownmillerite $\text{Ba}_2\text{InGaO}_5$. *J. Solid State Chem.* **2014**, *218*, 38-43.
97. Mohn, C. E.; Allan, N. L.; Stølen, S., Sr and Ga substituted $\text{Ba}_2\text{In}_2\text{O}_5$: Linking ionic conductivity and the potential energy surface. *Solid State Ionics* **2006**, *177* (3), 223-228.
98. Kahlenberg, V.; Shaw, C. S. J., $\text{Ca}_2\text{Ga}_2\text{O}_5$: a new high pressure oxogallate. In *Z. Kristallogr. - New Cryst. Struct.*, 2001; Vol. 216, p 206.
99. Kahlenberg, V.; Goettgens, V.; Mair, P.; Schmidmair, D., High-pressure synthesis and crystal structures of the strontium oxogallates $\text{Sr}_2\text{Ga}_2\text{O}_5$ and $\text{Sr}_5\text{Ga}_6\text{O}_{14}$. *J. Solid State Chem.* **2015**, *228*, 27-35.
100. Larson, A. C.; Von Dreele, A. C., General structure analysis system (GSAS). *Los Alamos National Laboratory Report LAUR* **1994**, 86 - 748.

101. Toby, B. H., A graphical user interface for GSAS. *J. Appl. Crystallogr.* **2001**, *34*, 210–213.
102. Luo, K.; Amano Patino, M.; Hayward, M. A., $\text{Ca}_2\text{Cr}_{0.5}\text{Ga}_{1.5}\text{O}_5$ —An extremely redox-stable brownmillerite phase. *J. Solid State Chem.* **2015**, *222*, 71–75.
103. Julián Morales, L. S., Francisco Martín, Frank Berry, and Xiaolin Renc, Synthesis and characterization of nanometric iron and iron-titanium oxides by mechanical milling: Electrochemical properties as anodic materials in lithium cells. *J. Electrochem. Soc.* **2005**, *152*, A1748–A1754.
104. Doi, A.; Nomura, M.; Obukuro, Y.; Maeda, R.; Obata, K.; Matsushima, S.; Kobayashi, K., Characterization of Ti-doped CaFe_2O_4 prepared from a malic acid complex. *J. Ceram. Soc. Jpn.* **2014**, *122* (2), 175–178.
105. Ruttanapun, C.; Maensiri, S., *Effects of spin entropy and lattice strain from mixed-trivalent $\text{Fe}^{3+}/\text{Cr}^{3+}$ on the electronic, thermoelectric and optical properties of delafossite $\text{CuFe}_{1-x}\text{Cr}_x\text{O}_2$ ($x = 0.25, 0.5, 0.75$)*, *J. Phys. D: Appl. Phys.* **2015**, *48*, 495103. 2015.
106. Mueller, D. N.; De Souza, R. A.; Yoo, H.-I.; Martin, M., Phase stability and oxygen nonstoichiometry of highly oxygen-deficient perovskite-type oxides: A case study of $(\text{Ba,Sr})(\text{Co,Fe})\text{O}_{3-\delta}$. *Chem. Mater.* **2012**, *24*, 269–274.
107. Shaula, A.; Pivak, Y.; Waerenborgh, J.; Gaczynski, P.; Yaremchenko, A.; Kharton, V., Ionic conductivity of brownmillerite-type calcium ferrite under oxidizing conditions. *Solid State Ionics* **2006**, *177* (33–34), 2923–2930.
108. Zhang, Q.; Xu, Z. F.; Wang, L. F.; Gao, S. H.; Yuan, S. J., Structural and electromagnetic properties driven by oxygen vacancy in $\text{Sr}_2\text{FeMoO}_{6-\delta}$ double perovskite. *J. Alloys Compd.* **2015**, *649*, 1151–1155.
109. Kozhevnikov, V. L.; Leonidov, I. A.; Mitberg, E. B.; Patrakeev, M. V.; Petrov, A. N.; Poeppelmeier, K. R., Conductivity and carrier traps in $\text{La}_{1-x}\text{Sr}_x\text{Co}_{1-z}\text{Mn}_z\text{O}_{3-\delta}$ ($x=0.3$; $z=0$ and 0.25). *J. Solid State Chem.* **2003**, *172*, 296–304.
110. Kontoulis, I.; Steele, B. C. H., Fabrication and conductivity of a new compound $\text{Ca}_2\text{Cr}_2\text{O}_5$. *J. Eur. Ceram. Soc.* **1992**, *9*, 459–462.
111. Bhosale, D. R.; Yusuf, S. M.; Kumar, A.; Mukadam, M. D.; Patil, S. I., High oxide ion conductivity below 500 °C in garnets $\text{La}_x\text{Y}_{3-x}\text{Fe}_5\text{O}_{12+\delta}$. *Phys. Rev. Mater.* **2017**, *1* (1), 015001.
112. Corallini, S.; Ceretti, M.; Cousson, A.; Ritter, C.; Longhin, M.; Papet, P.; Paulus, W., Cubic $\text{Sr}_2\text{ScGaO}_5$ perovskite: structural stability, oxygen defect structure, and ion conductivity explored on single crystals. *Inorg. Chem.* **2017**, *56*, 2977–2984.
113. Fargali, A. A.; Zayed, M. K.; Khedr, M. H.; Moustafa, A. F., Phase and conductivity dynamics of strontium hexaferrite nanocrystals in a hydrogen gas flow. *Intl. J. Phys. Sci.* **2008**, *3*, 131–139.
114. Richardson, G.; O’Kane, S. E. J.; Niemann, R. G.; Peltola, T. A.; Foster, J. M.; Cameron, P. J.; Walker, A. B., Can slow-moving ions explain hysteresis in the current–voltage curves of perovskite solar cells? *Energy & Environ. Sci.* **2016**, *9* (4), 1476–1485.
115. Fabbri, E.; Mohamed, R.; Levecque, P.; Conrad, O.; Kötz, R.; Schmidt, T. J., Composite electrode boosts the activity of $\text{Ba}_{0.5}\text{Sr}_{0.5}\text{Co}_{0.8}\text{Fe}_{0.2}\text{O}_{3-\delta}$ perovskite and carbon toward oxygen reduction in alkaline media. *ACS Catal.* **2014**, *4*, 1061–1070.
116. Zeng, P.; Chen, Z.; Zhou, W.; Gu, H.; Shao, Z.; Liu, S., Re-evaluation of $\text{Ba}_{0.5}\text{Sr}_{0.5}\text{Co}_{0.8}\text{Fe}_{0.2}\text{O}_{3-\delta}$ perovskite as oxygen semi-permeable membrane. *J. Membr. Sci.* **2007**, *291*, 148–156.
117. Liu, P.; Luo, Z.; Kong, J.; Yang, X.; Liu, Q.; Xu, H., $\text{Ba}_{0.5}\text{Sr}_{0.5}\text{Co}_{0.8}\text{Fe}_{0.2}\text{O}_{3-\delta}$ -based dual-gradient cathodes for solid oxide fuel cells. *Ceram. Int.* **2018**, *44*, 4516–4519.
118. Kong, L.; Chen, X.; Li, B. Q.; Peng, H. J.; Huang, J. Q.; Xie, J.; Zhang, Q., A bifunctional perovskite promoter for polysulfide regulation toward stable lithium-sulfur batteries. *Adv. Mater.* **2018**, *30*, 1705219.

119. Kim, J.; Yin, X.; Tsao, K. C.; Fang, S.; Yang, H., Ca₂Mn₂O₅ as oxygen-deficient perovskite electrocatalyst for oxygen evolution reaction. *J. Am. Chem. Soc.* **2014**, *136*, 14646-14649.
120. Hona, R. K.; Ramezanipour, F., Variation in electrical conductivity of A₂Fe₂O₅ (A = Sr, Ba): the role of structural order. *Mater. Res. Express* **2018**, *5*, 076307.
121. Suescun, L.; Chmaissem, O.; Mais, J.; Dabrowski, B.; Jorgensen, J. D., Crystal structures, charge and oxygen-vacancy ordering in oxygen deficient perovskites SrMnO_x (x<2.7). *J. Solid State Chem.* **2007**, *180* (5), 1698-1707.
122. Arevalo-Lopez, A. M.; Attfield, J. P., Crystal and magnetic structures of the brownmillerite Ca₂Cr₂O₅. *Dalton Trans.* **2015**, *44*, 10661-4.
123. Pan, L.; Wei-Hua, W.; Wei-Chao, W.; Ya-Hui, C.; Feng, L.; Hui, L., D-type anti-ferromagnetic ground state in Ca₂Mn₂O₅. *Chin. Phys. Lett.* **2017**, *34*, 027101.
124. Molinari, M.; Tompsett, D. A.; Parker, S. C.; Azough, F.; Freer, R., Structural, electronic and thermoelectric behaviour of CaMnO₃ and CaMnO_(3-δ). *J. Mater. Chem. A* **2014**, *2*, 14109-14117.
125. Toby, B. H., EXPGUI, a graphical user interface for GSAS. *J. Appl. Crystallogr.* **2001**, *34*, 210-213.
126. Mohd Zaid, N. A.; Idris, N. H., Enhanced Capacitance of Hybrid Layered Graphene/Nickel Nanocomposite for Supercapacitors. *Sci. Rep.* **2016**, *6*, 32082.
127. PGR, A.; B, M.; S, S. D.; KS, P., Study of Electrical Properties of Nickel Doped Polyurethane Nanocomposites. *Polym. Sci.* **2018**, *4*, No.1:7.
128. Shannon, R. D., Revised effective ionic radii and systematic studies of interatomic distances in halides and chalcogenides. *Acta Cryst.* **1976**, *32*, 751-767.
129. Jijil, C. P.; Lokanathan, M.; Chithiravel, S.; Nayak, C.; Bhattacharyya, D.; Jha, S. N.; Babu, P. D.; Kakade, B.; Devi, R. N., Nitrogen Doping in Oxygen-Deficient Ca₂Fe₂O₅: A Strategy for Efficient Oxygen Reduction Oxide Catalysts. *ACS Appl. Mater. Interfaces* **2016**, *8* (50), 34387-34395.
130. Hona, R. K.; Huq, A.; Ramezanipour, F., Electrical properties of the ordered oxygen-deficient perovskite Ca₂Fe_{0.5}Ga_{1.5}O₅. *Ionics* **2018**.
131. Iguchi, E.; Hashimoto, T.; Yokoyama, S., Electrical transports and stability of small polarons of O 2p holes in Li_xCo_{1-x}O. *J. Phys. Soc. Jpn.* **1996**, *65*, 221-229.
132. Inoue, S.; Kawai, M.; Ichikawa, N.; Kageyama, H.; Paulus, W.; Shimakawa, Y., Anisotropic oxygen diffusion at low temperature in perovskite-structure iron oxides. *Nat. Chem.* **2010**, *2*, 213.
133. Thangadurai, V.; Schmid Beurmann, P.; Weppner, W., Mixed oxide ion and electronic conductivity in perovskite-type SrSnO₃ by Fe substitution. *Mater. Sci. Eng., B* **2003**, *100*, 18-22.
134. Shaula, A. L.; Kharton, V. V.; Vyshatko, N. P.; Tsipis, E. V.; Patrakeev, M. V.; Marques, F. M. B.; Frade, J. R., Oxygen ionic transport in SrFe_{1-y}Al_yO_{3-δ} and Sr_{1-x}Ca_xFe_{0.5}Al_{0.5}O_{3-δ} ceramics. *J. Eur. Ceram. Soc.* **2005**, *25*, 489-499.
135. Cheng, X.; Fabbri, E.; Nachtegaal, M.; Castelli, I. E.; El Kazzi, M.; Haumont, R.; Marzari, N.; Schmidt, T. J., Oxygen evolution reaction on La_{1-x}Sr_xCoO₃ perovskites: a combined experimental and theoretical study of their structural, electronic, and electrochemical properties. *Chem. Mater.* **2015**, *27*, 7662-7672.
136. Shaula, A. L.; Kharton, V. V.; Patrakeev, M. V.; Waerenborgh, J. C.; Rojas, D. P.; Marques, F. M. B., Defect formation and transport in SrFe_{1-x}Al_xO_{3-δ}. *Ionics* **2004**, *10*, 378-384.
137. Leonidov, I. A.; Patrakeev, M. V.; Bahteeva, J. A.; Mitberg, E. B.; Kozhevnikov, V. L.; Colomban, P.; Poepelmeier, K. R., High-temperature phase equilibria in the oxide systems SrFe_{1-x}Ga_xO_{2.5}-SrFe_{1-x}Ga_xO₃ (x=0, 0.1, 0.2). *J. Solid State Chem.* **2006**, *179*, 1093-1099.
138. Waerenborgh, J. C.; Rojas, D. P.; Shaula, A. L.; Mather, G. C.; Patrakeev, M. V.; Kharton, V. V.; Frade, J. R., Phase formation and iron oxidation states in SrFe(Al)O_{3-δ} perovskites. *Mater. Lett.* **2005**, *59* (13), 1644-1648.

139. Mizusaki, J.; Yoshihiro, M.; Yamauchi, S.; Fueki, K., Nonstoichiometry and defect structure of the perovskite-type oxides $\text{La}_{1-x}\text{Sr}_x\text{FeO}_{3-\delta}$. *J. Solid State Chem.* **1985**, *58*, 257-266.
140. Garces, D.; Setevich, C. F.; Caneiro, A.; Cuello, G. J.; Moggi, L., Effect of cationic order-disorder on the transport properties of $\text{LaBaCo}_2\text{O}_{6-\delta}$ and $\text{La}_{0.5}\text{Ba}_{0.5}\text{CoO}_{3-\delta}$ perovskites. *J. Appl. Cryst.* **2014**, *47*, 325-334.
141. Patrakeeve, M. V.; Leonidov, I. A.; Kozhevnikov, V. L.; Poeppelmeier, K. R., p-Type electron transport in $\text{La}_{1-x}\text{Sr}_x\text{FeO}_{3-\delta}$ at high temperatures. *J. Solid State Chem.* **2005**, *178*, 921-927.
142. Das, V. D.; Bhat, K. S., Electrical conductivity of air-exposed and unexposed lead telluride thin films-temperature and size effects. *J. Phys. D: Appl. Phys.* **1989**, *22*, 162.
143. Bernuy-Lopez, C.; Høydalsvik, K.; Einarsrud, M.-A.; Grande, T., Effect of A-Site Cation Ordering on Chemical Stability, Oxygen Stoichiometry and Electrical Conductivity in Layered $\text{LaBaCo}_2\text{O}_{(5+\delta)}$ Double Perovskite. *Materials* **2016**, *9*, 154.
144. Balachandran, U.; Dusek, J. T.; Maiya, P. S.; Ma, B.; Mievil, R. L.; Kleefisch, M. S.; Udovich, C. A., Ceramic membrane reactor for converting methane to syngas. *Catal. Today* **1997**, *36* (3), 265-272.
145. Skinner, S. J.; Kilner, J. A., Oxygen ion conductors. *Mater. Today* **2003**, *6* (3), 30-37.
146. Nemudry, A.; Weiss, M.; Gainutdinov, I.; Boldyrev, V.; Schöllhorn, R., Room Temperature Electrochemical Redox Reactions of the Defect Perovskite $\text{SrFeO}_{2.5+x}$. *Chem. Mater.* **1998**, *10* (9), 2403-2411.
147. Lee, K. J.; Iguchi, E., Electronic properties of SrMnO_{3x} . *J. Solid State Chem.* **1995**, *114*, 242-248.
148. Kim, C. M.; Seo, J. W.; Choi, S. M.; Seo, W. S.; Lee, S.; Lim, Y. S.; Park, K., Structural and thermoelectric properties of n-type $\text{Sr}_{1-x}\text{Ti}_x\text{MnO}_{3-\delta}$ perovskite system. *Electron. Mater. Lett.* **2015**, *11*, 276-281.
149. Arpe, R.; Müller-Buschbaum, H.; Schenck, R. V., Über Erdalkalimetallloxogallate. VI. Zur Kenntnis von $\text{Ca}_2\text{FeGaO}_5$, ein Beitrag zur Kristallchemie von MMeO₅-Verbindungen. *Z. Anorg. Allg. Chem.* **1974**, *410* (2), 97-103.
150. Ceretti, M.; Corallini, S.; Paulus, W., Influence of phase transformations on crystal growth of stoichiometric brownmillerite oxides: $\text{Sr}_2\text{ScGaO}_5$ and $\text{Ca}_2\text{Fe}_2\text{O}_5$. *Crystals* **2016**, *6*, 146.
151. Chandra, A.; Roberts, A. J.; Slade, R. C. T., Studies of nanostructures and conductivity in the system $\text{V}_x\text{Mo}_{1-x}\text{O}_y$. *Solid State Commun.* **2008**, *147* (3), 83-87.
152. Papaioannou, J. C.; Patermarakis, G. S.; Karayianni, H. S., Electron hopping mechanism in hematite ($\alpha\text{-Fe}_2\text{O}_3$). *J. Phys. Chem. Solids* **2005**, *66*, 839-844.
153. Rosso, K. M.; Smith, D. M. A.; Dupuis, M., An ab initio model of electron transport in hematite ($\alpha\text{-Fe}_2\text{O}_3$) basal planes. *J. Chem. Phys.* **2003**, *118*, 6455-6466.
154. Ellis, B.; Perry, L. K.; Ryan, D. H.; Nazar, L. F., Small Polaron Hopping in Li_xFePO_4 Solid Solutions: Coupled Lithium-Ion and Electron Mobility. *J. Am. Chem. Soc.* **2006**, *128* (35), 11416-11422.
155. Yoshino, T.; Ito, E.; Katsura, T.; Yamazaki, D.; Shan, S.; Guo, X.; Nishi, M.; Higo, Y.; Funakoshi, K. i., Effect of iron content on electrical conductivity of ferropericlae with implications for the spin transition pressure. *J. Geophys. Res. Solid Earth* **2011**, *116* (B4).
156. Sanson, A.; Zaltron, A.; Argiolas, N.; Sada, C.; Bazzan, M.; Schmidt, W. G.; Sanna, S., Polaronic deformation at the $\text{Fe}^{2+/3+}$ impurity site in Fe:LiNbO_3 crystals. *Phys. Rev. B* **2015**, *91* (9), 094109.
157. Mineshige, A.; Inaba, M.; Yao, T.; Ogumi, Z.; Kikuchi, K.; Kawase, M., Crystal Structure and Metal-Insulator Transition of $\text{La}_{1-x}\text{Sr}_x\text{CoO}_3$. *J. Solid State Chem.* **1996**, *121*, 423-429.

158. Hona, R. K.; Huq, A.; Ramezanipour, F., Unraveling the Role of Structural Order in the Transformation of Electrical Conductivity in $\text{Ca}_2\text{FeCoO}_{6-\delta}$, $\text{CaSrFeCoO}_{6-\delta}$, and $\text{Sr}_2\text{FeCoO}_{6-\delta}$. *Inorganic Chemistry* **2017**, *56* (23), 14494-14505.
159. Shunji, T.; Hiroshi, N.; Yoshio, I.; Nobuo, I., The Oxygen-Deficient Perovskite Solid Solution $\text{Nd}_{1+x}\text{Ba}_{2-x}\text{Cu}_3\text{O}_y$ and Its Superconductivity. *Jpn. J. Appl. Phys.* **1987**, *26* (12A), L2076.
160. Maignan, A.; Michel, C.; Hervieu, M.; Raveau, B., A monoclinic manganite, $\text{La}_{0.9}\text{MnO}_{3-\delta}$, with colossal magnetoresistance properties near room temperature. *Solid State Commun.* **1997**, *101*, 277-281.
161. Gómez, L.; Galeano, V.; Parra, R.; Michel, C. R.; Paucar, C.; Morán, O., Carbon dioxide gas sensing properties of ordered oxygen deficient perovskite $\text{LnBaCo}_2\text{O}_{5+\delta}$ (Ln = La, Eu). *Sens. Actuators, B: Chemical* **2015**, *221*, 1455-1460.
162. Leo, A.; Liu, S.; Diniz da Costa, J. C.; Shao, Z., Oxygen permeation through perovskite membranes and the improvement of oxygen flux by surface modification. *Sci. Tech. Adv. Mater.* **2006**, *7*, 819-825.
163. Skinner, S. J., Recent advances in Perovskite-type materials for solid oxide fuel cell cathodes. *Int. J. Inorg. Mater.* **2001**, *3*, 113-121.
164. Ramezanipour, F.; Greedan, J. E.; Cranswick, L. M. D.; Garlea, V. O.; Siewenie, J.; King, G.; Llobet, A.; Donaberger, R. L., The effect of the B-site cation and oxygen stoichiometry on the local and average crystal and magnetic structures of $\text{Sr}_2\text{Fe}_{1.9}\text{M}_{0.1}\text{O}_{5+y}$ (M = Mn, Cr, Co; y = 0, 0.5). *J. Mater. Chem.* **2012**, *22* (19), 9522-9538.
165. Boulahya, K.; Ruiz-Morales, J. C.; Hernando, M.; González-Calbet, J. M.; Parras, M., Synthesis, Structural, Magnetic, and Electrical Study of $\text{BaSrCo}_2\text{O}_5$, a Highly Disordered Cubic Perovskite. *Chem. Mater.* **2009**, *21* (10), 2045-2054.
166. Tomkiewicz, A. C.; Tamimi, M. A.; Huq, A.; McIntosh, S., Evidence for the low oxygen stoichiometry of cubic $\text{Ba}_{0.5}\text{Sr}_{0.5}\text{Co}_{0.5}\text{Fe}_{0.5}\text{O}_{3-\delta}$ from in-situ neutron diffraction. *Solid State Ionics* **2013**, *253*, 27-31.
167. Dupin, J. C.; Gonbeau, D.; Benlilou-Moudden, H.; Vinatier, P.; Levasseur, A., XPS analysis of new lithium cobalt oxide thin-films before and after lithium deintercalation. *Thin Solid Films* **2001**, *384*, 23-32.
168. Davison, N.; McWhinnie, W. R.; Hooper, A., X-ray photoelectron spectroscopic study of cobalt(II) and nickel(II) sorbed on hectorite and montmorillonite. *Clays Clay Miner.* **1991**, *39* (1), 22-27.
169. Ghaffari; M. Liu, T.; Huang, H.; Tan, O. K.; Shannon, M., Investigation of local structure effect and X-ray absorption characteristics (EXAFS) of Fe (Ti) K-edge on photocatalyst properties of $\text{SrTi}_{(1-x)}\text{Fe}_x\text{O}_{(3-\delta)}$. *Mater. Chem. Phys.* **2012**, *136*, 347-357.
170. Morales, J., Sánchez, L., Martín, F., Berry, F., Renc, X., Synthesis and Characterization of Nanometric Iron and Iron-Titanium Oxides by Mechanical Milling: Electrochemical Properties as Anodic Materials in Lithium Cells. *J. Electrochem. Soc.* **2005**, *152* 1748.
171. Ruttanapun, C.; S. Maensiri, Effects of spin entropy and lattice strain from mixed-trivalent $\text{Fe}^{3+}/\text{Cr}^{3+}$ on the electronic, thermoelectric and optical properties of delafossite $\text{CuFe}_{1-x}\text{Cr}_x\text{O}_2$ (x = 0.25, 0.5, 0.75). *J. Phys. D: Appl. Phys.* **2015**, *48*, 16.
172. Doi, A.; Nomura, M.; Obukuro, Y.; Maeda, R.; Obata, K.; Matsushima, S.; Kobayashi, K., Characterization of Ti-doped CaFe_2O_4 prepared from a malic acid complex 2014 *Ceram Soc Jpn* *122* (1422):175-178.
173. Pannunzio Miner, E. V.; De Paoli, J. M.; Alonso, J. A.; García-Hernández, M.; Sánchez, R. D.; Carbonio, R. E., Ferrimagnetic order in the insulating $\text{Sr}_3\text{Fe}_2\text{ReO}_9$ double perovskite. *Physica B: Condensed Matter* **2007**, *398* (2), 397-400.

174. Zhao, Q.; Liu, M.; Dai, J.; Deng, H.; Yin, Y.; Zhou, L.; Yang, J.; Hu, Z.; Agrestini, S.; Chen, K.; Pellegrin, E.; Valvidares, M.; Nataf, L.; Baudelet, F.; Tjeng, L. H.; Yang, Y.-f.; Jin, C.; Long, Y., High-Pressure Synthesis and Ferrimagnetic Ordering of the B-Site-Ordered Cubic Perovskite $\text{Pb}_2\text{FeOsO}_6$. *Inorg. Chem.* **2016**, *55* (19), 9816-9821.
175. Feng, H. L.; Arai, M.; Matsushita, Y.; Tsujimoto, Y.; Guo, Y.; Sathish, C. I.; Wang, X.; Yuan, Y.-H.; Tanaka, M.; Yamaura, K., High-Temperature Ferrimagnetism Driven by Lattice Distortion in Double Perovskite $\text{Ca}_2\text{FeOsO}_6$. *J. Am. Chem. Soc.* **2014**, *136* (9), 3326-3329.
176. Lin, Q.; Greenblatt, M.; Caspi, E. a. N.; Avdeev, M., Crystallographic and magnetic properties of CaLaMnMoO_6 double perovskite. *J. Solid State Chem.* **2006**, *179* (7), 2086-2092.
177. Mezzadri, F.; Delmonte, D.; Orlandi, F.; Pernechele, C.; Calestani, G.; Solzi, M.; Lantieri, M.; Spina, G.; Cabassi, R.; Bolzoni, F.; Fittipaldi, M.; Merlini, M.; Migliori, A.; Manuel, P.; Gilioli, E., Structural and magnetic characterization of the double perovskite $\text{Pb}_2\text{FeMoO}_6$. *J. Mater. Chem. C* **2016**, *4* (7), 1533-1542.
178. Cheng, X.; Fabbri, E.; Nachtegaal, M.; Castelli, I. E.; El Kazzi, M.; Haumont, R.; Marzari, N.; Schmidt, T. J., Oxygen Evolution Reaction on $\text{La}_{1-x}\text{Sr}_x\text{CoO}_3$ Perovskites: A Combined Experimental and Theoretical Study of Their Structural, Electronic, and Electrochemical Properties. *Chem. Mater.* **2015**, *27*, 7662-7672.
179. Pizzini, S., Physical Chemistry of Semiconductor Materials and Processes, John Wiley & Sons Ltd, West Sussex, United Kingdom. **2015**.
180. Asenath-Smith, E.; Lokuhewa, I. N.; Mixture, S. T.; Edwards, D. D., p-Type thermoelectric properties of the oxygen-deficient perovskite $\text{Ca}_2\text{Fe}_2\text{O}_5$ in the brownmillerite structure. *J. Solid State Chem.* **2010**, *183* (7), 1670-1677.
181. A. Belik, A.; Matsushita, Y.; Katsuya, Y.; Tanaka, M.; Kolodiaznyy, T.; Isobe, M.; Takayama-Muromachi, E., Crystal structure and magnetic properties of 6H-SrMnO_3 . **2011**, *84*, 094438.
182. Liu, T.; Yang, X.; Ma, C.; Hao, X.; Liang, X.; Liu, F.; Liu, F.; Yang, C.; Zhu, H.; Lu, G., CeO_2 -based mixed potential type acetone sensor using MMnO_3 (M: Sr, Ca, La and Sm) sensing electrode. *Solid State Ionics* **2018**, *317*, 53-59.
183. Ryu, J.; O'Hayre, R.; Lee, H., Structural analysis and electrochemical properties of cobalt-doped $\text{Sr}_{0.9}\text{Ce}_{0.1}\text{MnO}_{3-\delta}$ cathode for IT-SOFCs. *J. Mater. Res.* **2014**, *29*, 2667-2672.
184. Zhu, Z.-L.; Gu, J.-H.; Jia, Y.; Hu, X., A comparative study of electronic structure and magnetic properties of SrCrO_3 and SrMoO_3 . *Physica B: Condensed Matter* **2012**, *407*, 1990-1994.
185. Zhang, W.; Meng, J.; Zhang, X.; Zhang, L.; Liu, X.; Meng, J., Co-incorporating enhancement on oxygen vacancy formation energy and electrochemical property of $\text{Sr}_2\text{Co}_{1+x}\text{Mo}_{1-x}\text{O}_{6-\delta}$ cathode for intermediate-temperature solid oxide fuel cell. *Solid State Ionics* **2018**, *316*, 20-28.
186. Gorodea, I. A., Influence of the B-site cation nature on crystal structure and magnetic properties of Ca_2BMO_6 (B = Cr, La, Sm) double perovskite. *Acta Chemica Iasi* **2014**, *22*, 145-154.
187. Hosaka, Y.; Ichikawa, N.; Saito, T.; Manuel, P.; Khalyavin, D.; Atfield, J. P.; Shimakawa, Y., Two-Dimensional Charge Disproportionation of the Unusual High Valence State Fe^{4+} in a Layered Double Perovskite. *J. Am. Chem. Soc.* **2015**, *137* (23), 7468-7473.
188. Ganesanpotti, S.; Tassel, C.; Hayashi, N.; Goto, Y.; Bouilly, G.; Yajima, T.; Kobayashi, Y.; Kageyama, H., Charge Disproportionation and Magnetoresistivity in a Double Perovskite with Alternate Fe^{4+} (d^4) and Mn^{4+} (d^3) Layers. *Eur. J. Inorg. Chem.* **2014**, *2014* (15), 2576-2581.
189. Chan, T. S.; Liu, R. S.; Hu, S. F.; Lin, J. G., Structure and physical properties of double perovskite compounds Sr_2FeMO_6 (M=Mo, W). *Mater. Chem. Phys.* **2005**, *93*, 314-319.
190. Sayani, M.; Sebastiaan van, D., Pulsed laser deposition of $\text{La}_{1-x}\text{Sr}_x\text{MnO}_3$: thin-film properties and spintronic applications. *J. Phys. D: Appl. Phys.* **2014**, *47*, 034010.
191. Cui, L.; Yang, L., Magnetic and transport properties of the double perovskite $\text{Sr}_2\text{FeMnO}_6$. *Adv. Mater. Res.* **2012**, *393-395*, 157-160.

192. Markiewicz, E.; Bujakiewicz-Koronska, R.; Budziak, A.; Kalvane, A.; Nalecz, D. M., Impedance spectroscopy studies of SrMnO₃, BaMnO₃ and Ba_{0.5}Sr_{0.5}MnO₃ ceramics. *Phase Transitions* **2014**, *87*, 1060-1072.
193. Töpfer, J.; Pippardt, U.; Voigt, I.; Kriegel, R., Structure, nonstoichiometry and magnetic properties of the perovskites Sr_{1-x}Ca_xMnO_{3-δ}. *Solid State Sci.* **2004**, *6*, 647-654.
194. Aschauer, U.; Pfenninger, R.; Selbach, S. M.; Grande, T.; Spaldin, N. A., Strain-controlled oxygen vacancy formation and ordering in CaMnO₃. *Phys. Rev. B* **2013**, *88*, 054111.
195. Singh, Y., Electrical Resistivity Measurements: a Review. *Int. J. Modern Phys.: Conference Series* **2013**, *22*, 745–756.
196. Wang, J.; Gao, Y.; Chen, D.; Liu, J.; Zhang, Z.; Shao, Z.; Ciucci, F., Water Splitting with an Enhanced Bifunctional Double Perovskite. *ACS Catal.* **2018**, *8*, 364-371.
197. Jin, C.; Cao, X.; Zhang, L.; Zhang, C.; Yang, R., Preparation and electrochemical properties of urchin-like La_{0.8}Sr_{0.2}MnO₃ perovskite oxide as a bifunctional catalyst for oxygen reduction and oxygen evolution reaction. *J. Power Sources* **2013**, *241*, 225-230.
198. May, K. J.; Carlton, C. E.; Stoerzinger, K. A.; Risch, M.; Suntivich, J.; Lee, Y. L.; Grimaud, A.; Shao Horn, Y., Influence of oxygen evolution during water oxidation on the surface of perovskite oxide catalysts. *J. Phys. Chem. Lett.* **2012**, *3*, 3264-3270.
199. Malkhandi, S.; Trinh, P.; Manohar, A. K.; Jayachandrababu, K. C.; Kindler, A.; Surya Prakash, G. K.; Narayanan, S. R., Electrocatalytic activity of transition metal oxide-carbon composites for oxygen reduction in alkaline batteries and fuel cells. *J. Electrochem. Soc.* **2013**, *160*, 943-952.
200. Liang, Y.; Li, Y.; Wang, H.; Zhou, J.; Wang, J.; Regier, T.; Dai, H., Co₃O₄ nanocrystals on graphene as a synergistic catalyst for oxygen reduction reaction. *Nat. Mater.* **2011**, *10*, 780-786.
201. Mohamed, R.; Cheng, X.; Fabbri, E.; Levecque, P.; Kötz, R.; Conrad, O.; Schmidt, T. J., Electrocatalysis of perovskites: the influence of carbon on the oxygen evolution activity. *J. Electrochem. Soc.* **2015**, *162*, 579-586.
202. Fabbri, E.; Nachttegaal, M.; Cheng, X.; Schmidt Thomas, J., Superior bifunctional electrocatalytic activity of Ba_{0.5}Sr_{0.5}Co_{0.8}Fe_{0.2}O_{3-δ}/carbon composite electrodes: insight into the local electronic structure. *Adv. Energy Mater.* **2015**, *5*, 1402033.
203. Hona, R. K.; Ramezanipour, F., Remarkable Oxygen-Evolution Activity of a Perovskite Oxide from the Ca_{2-x}Sr_xFe₂O_{6-δ} Series. *Angew. Chem. Int. Ed.* **2019**, *58*, 2060-2063.
204. Zhu, Y.; Zhou, W.; Chen, Z. G.; Chen, Y.; Su, C.; Tadó Moses, O.; Shao, Z., SrNb_{0.1}Co_{0.7}Fe_{0.2}O_{3-δ} perovskite as a next-generation electrocatalyst for oxygen evolution in alkaline solution. *Angew. Chem. Int. Ed.* **2015**, *54*, 3897-3901.
205. Singh, A.; Roy, S.; Das, C.; Samanta, D.; Maji, T. K., Metallophthalocyanine-based redox active metal-organic conjugated microporous polymers for OER catalysis. *Chem. Commun.* **2018**, *54*, 4465-4468.
206. Pan, Y.; Chen, Y.; Li, X.; Liu, Y.; Liu, C., Nanostructured nickel sulfides: phase evolution, characterization and electrocatalytic properties for the hydrogen evolution reaction. *RSC Advances* **2015**, *5*, 104740-104749.
207. Oh, S.; Kim, H.; Kwon, Y.; Kim, M.; Cho, E.; Kwon, H., Porous Co-P foam as an efficient bifunctional electrocatalyst for hydrogen and oxygen evolution reactions. *J. Mater. Chem. A* **2016**, *4*, 18272-18277.
208. Zhang, W.; Zhang, X.; Chen, L.; Dai, J.; Ding, Y.; Ji, L.; Zhao, J.; Yan, M.; Yang, F.; Chang, C.-R.; Guo, S., Single-Walled Carbon Nanotube Induced Optimized Electron Polarization of Rhodium Nanocrystals To Develop an Interface Catalyst for Highly Efficient Electrocatalysis. *ACS Catal.* **2018**, *8*, 8092-8099.

209. Zhu, Y.; Zhou, W.; Yu, J.; Chen, Y.; Liu, M.; Shao, Z., Enhancing Electrocatalytic Activity of Perovskite Oxides by Tuning Cation Deficiency for Oxygen Reduction and Evolution Reactions. *Chem. Mater.* **2016**, *28*, 1691-1697.
210. Song, F.; Hu, X., Ultrathin cobalt–manganese layered double hydroxide Is an efficient oxygen evolution catalyst. *J. Am. Chem. Soc.* **2014**, *136*, 16481-16484.
211. Moir, J.; Soheilnia, N.; O'Brien, P.; Jelle, A.; Grozea, C. M.; Faulkner, D.; Helander, M. G.; Ozin, G. A., Enhanced hematite water electrolysis using a 3D antimony-doped tin oxide electrode. *ACS Nano* **2013**, *7*, 4261-4274.
212. Shinagawa, T.; Garcia-Esparza, A. T.; Takanabe, K., Insight on Tafel slopes from a microkinetic analysis of aqueous electrocatalysis for energy conversion. *Sci. Rep.* **2015**, *5*, 13801.
213. Ranaweera, C. K.; Zhang, C.; Bhoyate, S.; Kahol, P. K.; Ghimire, M.; Mishra, S. R.; Perez, F.; Gupta, B. K.; Gupta, R. K., Flower-shaped cobalt oxide nano-structures as an efficient, flexible and stable electrocatalyst for the oxygen evolution reaction. *Mater. Chem. Front.* **2017**, *1*, 1580-1584.
214. Joya, K. S.; Ul Ain Babar, N.; Gilani, S. R.; Yasmeen, F.; Sarfaraz, M.; Ikram, S.; Colak, S. G.; Ocakoglu, K.; Ince, M., Heterogeneous Electrocatalysts for Efficient Water Oxidation Derived from Metal Phthalocyanine. *Chem. Select* **2018**, *3*, 11357-11366.
215. Lv, X.; Zhu, Y.; Jiang, H.; Yang, X.; Liu, Y.; Su, Y.; Huang, J.; Yao, Y.; Li, C., Hollow mesoporous NiCo₂O₄ nanocages as efficient electrocatalysts for oxygen evolution reaction. *Dalton Trans.* **2015**, *44*, 4148-4154.
216. Yang, Y.; Jiang, Y.; Wang, Y.; Sun, Y., Photoinduced decomposition of BaFeO₃ during photodegradation of methyl orange. *J. Mol. Catal. A: Chem.* **2007**, *270* (1), 56-60.
217. Reehuis, M.; Ulrich, C.; Maljuk, A.; Niedermayer, C.; Ouladdiaf, B.; Hoser, A.; Hofmann, T.; Keimer, B., Neutron diffraction study of spin and charge ordering in SrFeO_{3-δ}. *Phys. Rev. B* **2012**, *85* (18), 184109.
218. Zou, X. D.; Hovmoller, S.; Parras, M.; Gongalez-Calbet, J. M.; Vallet-Regi, M.; Grenier, J. C., The Complex Perovskite-Related Superstructure Ba₂Fe₂O₅ Solved by HREM and CIP. *Acta Cryst.* **1993**, *A49*, 27-35.
219. Clemens, O.; Gröting, M.; Witte, R.; Perez-Mato, J. M.; Loho, C.; Berry, F. J.; Kruk, R.; Knight, K. S.; Wright, A. J.; Hahn, H.; Slater, P. R., Crystallographic and Magnetic Structure of the Perovskite-Type Compound BaFeO_{2.5}: Unrivalled Complexity in Oxygen Vacancy Ordering. *Inorg. Chem.* **2014**, *53* (12), 5911-5921.
220. Ruttanapun, C.; Maensiri, S., Effects of spin entropy and lattice strain from mixed-trivalent Fe³⁺/Cr³⁺ on the electronic, thermoelectric and optical properties of delafossite CuFe_{1-x}Cr_xO₂ (x = 0.25, 0.5, 0.75). *J. Phys. D: Appl. Phys.* **2015**, *48* (49), 495103.
221. Schmidt, M.; Campbell, S. J., Crystal and Magnetic Structures of Sr₂Fe₂O₅ at Elevated Temperature. *J. Solid State Chem.* **2001**, *156* (2), 292-304.
222. Parras, M.; Fournes, L.; Grenier, J. C.; Pouchard, M.; Vallet, M.; Calbet, J. M.; Hagenmuller, P., Structural aspects and Mössbauer resonance investigation of Ba₂Fe₂O₅. *J. Solid State Chem.* **1990**, *88* (1), 261-268.
223. Bhosale, D. R.; Yusuf, S. M.; Kumar, A.; Mukadam, M. D.; Patil, S. I., High oxide ion conductivity below 500°C in the garnets La_xY_{3-x}Fe₅O_{12+δ}. *Phys. Rev. Mater.* **2017**, *1* (1), 015001.
224. Winter, M.; Besenhard, J. O.; Spahr, M. E.; Novák, P., Insertion Electrode Materials for Rechargeable Lithium Batteries. *Adv. Mater.* **1998**, *10*, 725-763.
225. Clemm, C.; Sinai, C.; Ferkinghoff, C.; Dethlefs, N.; Nissen, N. F.; Lang, K. In *Durability and cycle frequency of smartphone and tablet lithium-ion batteries in the field*, Electronics Goes Green (EGG), 2016; pp 1-7.
226. Sharma, N.; Shaju, K. M.; Subba Rao, G. V.; Chowdari, B. V. R., Mixed oxides Ca₂Fe₂O₅ and Ca₂Co₂O₅ as anode materials for Li-ion batteries. *Electrochim. Acta* **2004**, *49*, 1035-1043.

227. Sharma, N.; Shaju, K. M.; Subba Rao, G. V.; Chowdari, B. V. R., Sol-gel derived nanocrystalline CaSnO_3 as high capacity anode material for Li-ion batteries. *Electrochem. Commun.* **2002**, *4*, 947-952.
228. Aurbach, D.; Nimberger, A.; Markovsky, B.; Levi, E.; Sominski, E.; Gedanken, A., Nanoparticles of SnO produced by sonochemistry as anode materials for rechargeable lithium batteries. *Chem.Mater.* **2002**, *14*, 4155-4163.
229. Carreon, M. L.; Thapa, A. K.; Jasinski, J. B.; Sunkara, M. K., The capacity and durability of amorphous silicon nanotube thin film anode for lithium ion battery applications. *ECS Electrochem. Lett.* **2015**, *4*, A124-A128.
230. Reddy, M. V.; Subba Rao, G. V.; Chowdari, B. V. R., Metal oxides and oxysalts as anode materials for Li ion batteries. *Chem. Rev.* **2013**, *113*, 5364-5457.
231. Kam, K. C.; Doeff, M. M., Electrode Materials for Lithium Ion Batteries. *Material Matters* **2012**, *7*, n4.
232. Flandrois, S.; Simon, B., Carbon materials for lithium-ion rechargeable batteries. *Carbon* **1999**, *37*, 165-180.
233. Fu, R.; Zhou, X.; Fan, H.; Blaisdell, D.; Jagadale, A.; Zhang, X.; Xiong, R., Comparison of lithium-ion anode materials using an experimentally verified physics-based electrochemical model. *Energies* **2017**, *10*, 2174.
234. Winter, M.; Besenhard, J. O., Electrochemical lithiation of tin and tin-based intermetallics and composites. *Electrochim. Acta* **1999**, *45*, 31-50.
235. Mishra, A.; Mehta, A.; Basu, S.; Malode, S. J.; Shetti, N. P.; Shukla, S. S.; Nadagouda, M. N.; Aminabhavi, T. M., Electrode Materials for Lithium-ion Batteries. *Mater. Sci. Energy Technol.* **2018**, *1*, 182-187.
236. Courtney, I. A.; McKinnon, W. R.; Dahn, J. R., On the aggregation of tin in SnO composite glasses caused by the reversible reaction with lithium. *J. Electrochem. Soc.* **1999**, *146*, 59-68.
237. Mohamedi, M.; Lee, S. J.; Takahashi, D.; Nishizawa, M.; Itoh, T.; Uchida, I., Amorphous tin oxide films: preparation and characterization as an anode active material for lithium ion batteries. *Electrochim. Acta* **2001**, *46*, 1161-1168.
238. Behm, M.; Irvine, J. T. S., Influence of structure and composition upon performance of tin phosphate based negative electrodes for lithium batteries. *Electrochim. Acta* **2002**, *47*, 1727-1738.
239. Laruelle, S.; Grugeon, S.; Poizot, P.; Dollé, M.; Dupont, L.; Tarascon, J.-M., On the origin of the extra electrochemical capacity displayed by MO/Li cells at low potential. *J. Electrochem. Soc.* **2002**, *149*, 627-634.
240. Obrovac, M. N.; Dunlap, R. A.; Sanderson, R. J.; Dahn, J. R., The electrochemical displacement reaction of lithium with metal oxides. *J. Electrochem. Soc.* **2001**, *148*, 576-588.
241. Poizot, P.; Laruelle, S.; Grugeon, S.; Dupont, L.; Tarascon, J. M., Nano-sized transition-metal oxides as negative-electrode materials for lithium-ion batteries. *Nature* **2000**, *407*, 496.
242. Yang, Z.; Choi, D.; Kerisit, S.; Rosso, K. M.; Wang, D.; Zhang, J.; Graff, G.; Liu, J., Nanostructures and lithium electrochemical reactivity of lithium titanites and titanium oxides: A review. *J. Power Sources* **2009**, *192*, 588-598.
243. Yi, T. F.; Jiang, L. J.; Shu, J.; Yue, C.-B.; Zhu, R. S.; Qiao, H. B., Recent development and application of $\text{Li}_4\text{Ti}_5\text{O}_{12}$ as anode material of lithium ion battery. *J. Phys.Chem. Solids* **2010**, *71*, 1236-1242.
244. Sharma, Y.; Sharma, N.; Subba Rao, G. V.; Chowdari, B. V. R., Nanophase ZnCo_2O_4 as a High Performance Anode Material for Li-Ion Batteries. *Adv. Funct. Mater.* **2007**, *17*, 2855-2861.
245. Yang, Y.; Zhao, Y.; Xiao, L.; Zhang, L., Nanocrystalline ZnMn_2O_4 as a novel lithium-storage material. *Electrochem. Commun.* **2008**, *10*, 1117-1120.

246. Yang, J. B.; Zhou, X. D.; Chu, Z.; Hikal, W. M.; Cai, Q.; Ho, J. C.; Kundaliya, D. C.; Yelon, W. B.; James, W. J.; Anderson, H. U.; Hamdeh, H. H.; Malik, S. K., Charge disproportionation and ordering in $\text{La}_{1/3}\text{Sr}_{2/3}\text{FeO}_{3-\delta}$. *J. Phys.: Condens. Matter* **2003**, *15*, 5093.
247. Zhao, K.; Chen, J.; Li, H.; Zheng, A.; He, F., Effects of Co-substitution on the reactivity of double perovskite oxides $\text{LaSrFe}_{2-x}\text{Co}_x\text{O}_6$ for the chemical-looping steam methane reforming. *J. Energy Institute* **2018**, 1-10.
248. Gupta, R. P.; Sen, S. K., Calculation of multiplet structure of core p -vacancy levels. *Phys. Rev.B* **1975**, *12*, 15-19.
249. Gupta, R. P.; Sen, S. K., Calculation of multiplet structure of core p-vacancy Levels. . *Phys. Rev. B* **1974**, *10*, 71-77.
250. Grosvenor, A. P.; Kobe, B. A.; Biesinger, M. C.; McIntyre, N. S., Investigation of multiplet splitting of Fe 2p XPS spectra and bonding in iron compounds. *Surf. Interface Anal.* **2004**, *36*, 1564-1574.
251. Biesinger, M. C.; Payne, B. P.; Grosvenor, A. P.; Lau, L. W. M.; Gerson, A. R.; Smart, R. S. C., Resolving surface chemical states in XPS analysis of first row transition metals, oxides and hydroxides: Cr, Mn, Fe, Co and Ni. *Appl. Surf. Sci.* **2011**, *257*, 2717-2730.
252. McIntyre, N. S.; Zetaruk, D. G., X-ray photoelectron spectroscopic studies of iron oxides. *Anal.Chem.* **1977**, *49*, 1521-1529.
253. Lin, Y.-M.; Abel, P. R.; Heller, A.; Mullins, C. B., $\alpha\text{-Fe}_2\text{O}_3$ Nanorods as Anode Material for Lithium Ion Batteries. *J. Phys. Chem. Lett.* **2011**, *2*, 2885-2891.
254. Zhang, J.; Wang, B.; Zhou, J.; Xia, R.; Chu, Y.; Huang, J., Preparation of advanced CuO nanowires/functionalized graphene composite anode material for lithium ion batteries. *Materials* **2017**, *10*, 72.
255. Chen, X.; Bi, Q.; Sajjad, M.; Wang, X.; Ren, Y.; Zhou, X.; Xu, W.; Liu, Z., One-dimensional porous silicon nanowires with large surface area for fast charge–discharge lithium-ion batteries. *Nanomaterials* **2018**, *8*, 285.
256. Dharmasena, R.; Thapa, A. K.; Hona, R. K.; Jasinski, J.; Sunkara, M. K.; Sumanasekera, G. U., Mesoporous TiO_2 coating on carbon–sulfur cathode for high capacity Li–sulfur battery. *RSC Advances* **2018**, *8*, 11622-11632.
257. Kim, I. T.; Magasinski, A.; Jacob, K.; Yushin, G.; Tannenbaum, R., Synthesis and electrochemical performance of reduced graphene oxide/maghemite composite anode for lithium ion batteries. *Carbon* **2013**, *52*, 56-64.
258. Xu, X.; Wan, Y.; Sha, Y.; Deng, W.; Xue, G.; Zhou, D., Nanoporous iron oxide@carbon composites with low carbon content as high-performance anodes for lithium-ion batteries. *RSC Adv.* **2015**, *5*, 89092-89098.
259. Chaudhari, N. K.; Kim, M.-S.; Bae, T.-S.; Yu, J.-S., Hematite ($\alpha\text{-Fe}_2\text{O}_3$) nanoparticles on vulcan carbon as an ultrahigh capacity anode material in lithium ion battery. *Electrochim. Acta* **2013**, *114*, 60-67.
260. Zhang, X.; Liu, H.; Petnikota, S.; Ramakrishna, S.; Fan, H. J., Electrospun Fe_2O_3 –carbon composite nanofibers as durable anode materials for lithium ion batteries. *J. Mater. Chem. A* **2014**, *2*, 10835-10841.
261. Liang, J.; Xiao, C.; Chen, X.; Gao, R.; Ding, S., Porous $\gamma\text{-Fe}_2\text{O}_3$ spheres coated with N-doped carbon from polydopamine as Li-ion battery anode materials. *Nanotechnology* **2016**, *27*, 215403.
262. Ping, Q.; iXu, B.; Ma, X.; Tian, J.; Wang, B., An iron oxyborate Fe_3BO_5 material as a high-performance anode for lithium-ion and sodium-ion batteries. *Dalton Trans.* **2019**, *48*, 5741-5748.
263. Oh, H.-D.; Lee, S.-W.; Kim, S.-O.; Lee, J. K., Facile synthesis of carbon layer-entangled Fe_2O_3 clusters as anode materials for improved Li-ion batteries. *J. Power Sources* **2013**, *244*, 575-580.

264. Chu, S.; Majumdar, A., Opportunities and challenges for a sustainable energy future. *Nature* **2012**, *488*, 294-303.
265. Mallouk, T. E., Divide and conquer. *Nat. Chem.* **2013**, *5*, 362-263.
266. Suntivich, J.; May, K. J.; Gasteiger, H. A.; Goodenough, J. B.; Shao-Horn, Y., A perovskite oxide optimized for oxygen evolution catalysis from molecular orbital principles. *Science* **2011**, *334*, 1383-1385.
267. Turner, J. A., Sustainable Hydrogen Production. *Science* **2004**, *305*, 972-974.
268. Walter, M. G.; Warren, E. L.; McKone, J. R.; Boettcher, S. W.; Mi, Q.; Santori, E. A.; Lewis, N. S., Solar Water Splitting Cells. *Chem. Rev.* **2010**, *110*, 6446-6473.
269. Gray, H. B., Powering the planet with solar fuel. *Nat. chem.* **2009**, *1*, 7.
270. Service, R. F., Hydrogen Cars: Fad or the Future? *Science* **2009**, *324*, 1257-1259.
271. Hamdani, M.; Singh, R. N.; Chartier, P., Co₃O₄ and Co- Based Spinel Oxides Bifunctional Oxygen Electrodes *Int. J. Electrochem. Sci.* **2010**, *5*, 556 - 577.
272. Li, Y.; Gong, M.; Liang, Y.; Feng, J.; Kim, J.-E.; Wang, H.; Hong, G.; Zhang, B.; Dai, H., Advanced zinc-air batteries based on high-performance hybrid electrocatalysts. *Nat. Commun.* **2013**, *4*, 1805.
273. Lee, Y.; Suntivich, J.; May, K. J.; Perry, E. E.; Shao-Horn, Y., Synthesis and activities of rutile IrO₂ and RuO₂ nanoparticles for oxygen evolution in acid and alkaline solutions. *J. Phys. Chem. Lett.* **2012**, *3*, 399-404.
274. Frame, F. A.; Townsend, T. K.; Chamousis, R. L.; Sabio, E. M.; Dittrich, T.; Browning, N. D.; Osterloh, F. E., Photocatalytic Water Oxidation with Nonsensitized IrO₂ Nanocrystals under Visible and UV Light. *J. Am. Chem. Soc.* **2011**, *133*, 7264-7267.
275. He, D.; He, G.; Jiang, H.; Chen, Z.; Huang, M., Enhanced durability and activity of the perovskite electrocatalyst Pr_{0.5}Ba_{0.5}CoO_{3-δ} by Ca doping for the oxygen evolution reaction at room temperature. *Chem. Commun.* **2017**, *53*, 5132-5135.
276. Kanan, M. W.; Nocera, D. G., In situ formation of an oxygen-evolving catalyst in neutral water containing phosphate and Co²⁺. *Science* **2008**, *321*, 1072-1075.
277. Park, H. W.; Lee, D. U.; Zamani, P.; Seo, M. H.; Nazar, L. F.; Chen, Z., Electrospun porous nanorod perovskite oxide/nitrogen-doped graphene composite as a bi-functional catalyst for metal air batteries. *Nano Energy* **2014**, *10*, 192-200.
278. Han, B.; Grimaud, A.; Giordano, L.; Hong, W. T.; Diaz-Morales, O.; Yueh-Lin, L.; Hwang, J.; Charles, N.; Stoerzinger, K. A.; Yang, W.; Koper, M. T. M.; Shao-Horn, Y., Iron-Based Perovskites for Catalyzing Oxygen Evolution Reaction. *J. Phys. Chem. C* **2018**, *122*, 8445-8454.
279. Berggren, J., Refinement of the crystal structure of dicalcium ferrite, Ca₂Fe₂O₅. *Acta Chem. Scand.* **1971**, *25*, 3616-3624.
280. Tong, X.; Yang, P.; Wang, Y.; Qin, Y.; Guo, X., Enhanced photoelectrochemical water splitting performance of TiO₂ nanotube arrays coated with an ultrathin nitrogen-doped carbon film by molecular layer deposition. *Nanoscale* **2014**, *6*, 6692-6700.
281. Lu, X.; Zhao, C., Highly efficient and robust oxygen evolution catalysts achieved by anchoring nanocrystalline cobalt oxides onto mildly oxidized multiwalled carbon nanotubes. *J. Mater. Chem. A* **2013**, *1*, 12053-12059.
282. Bu, Y.; Gwon, O.; Nam, G.; Jang, H.; Kim, S.; Zhong, Q.; Cho, J.; Kim, G., A highly efficient and robust cation ordered perovskite oxide as a bifunctional catalyst for rechargeable zinc-air batteries. *ACS Nano* **2017**, *11*, 11594-11601.
283. Matsumoto, Y.; Sato, E., Electrocatalytic properties of transition metal oxides for oxygen evolution reaction. *Mater. Chem. Phys.* **1986**, *14*, 397-426.

284. Tavakkoli, M.; Kallio, T.; Reynaud, O.; Nasibulin, A. G.; Sainio, J.; Jiang, H.; Kauppinen, E. I.; Laasonen, K., Maghemite nanoparticles decorated on carbon nanotubes as efficient electrocatalysts for the oxygen evolution reaction. *J. Mater. Chem. A* **2016**, *4*, 5216-5222.
285. Jung, S.; McCrory, C. C. L.; Ferrer, I. M.; Peters, J. C.; Jaramillo, T. F., Benchmarking nanoparticulate metal oxide electrocatalysts for the alkaline water oxidation reaction. *J. Mater. Chem. A* **2016**, *4*, 3068-3076.
286. Lu, B.; Cao, D.; Wang, P.; Wang, G.; Gao, Y., Oxygen evolution reaction on Ni-substituted Co_3O_4 nanowire array electrodes. *Int. J. Hydrogen Energy* **2011**, *36*, 72-78.
287. Lee, J. G.; Hwang, J.; Hwang, H. J.; Jeon, O. S.; Jang, J.; Kwon, O.; Lee, Y.; Han, B.; Shul, Y.-G., A new family of perovskite catalysts for oxygen-evolution reaction in alkaline media: BaNiO_3 and $\text{BaNi}_{0.83}\text{O}_{2.5}$. *J. Am. Chem. Soc.* **2016**, *138*, 3541-3547.
288. Petrie, J. R.; Cooper, V. R.; Freeland, J. W.; Meyer, T. L.; Zhang, Z.; Lutterman, D. A.; Lee, H. N., Enhanced bifunctional oxygen catalysis in strained LaNiO_3 perovskites. *J. Am. Chem. Soc.* **2016**, *138*, 2488-2491.
289. Zhang, B.; Lui, Y. H.; Zhou, L.; Tang, X.; Hu, S., An alkaline electro-activated Fe-Ni phosphide nanoparticle-stack array for high-performance oxygen evolution under alkaline and neutral conditions. *J. Mater. Chem. A* **2017**, *5*, 13329-13335.
290. Konkena, B.; Junge Puring, K.; Sinev, I.; Piontek, S.; Khavryuchenko, O.; Dürholt, J. P.; Schmid, R.; Tüysüz, H.; Muhler, M.; Schuhmann, W.; Apfel, U.-P., Pentlandite rocks as sustainable and stable efficient electrocatalysts for hydrogen generation. *Nat. Commun.* **2016**, *7*, 12269.
291. Chen, Y.; Yu, G.; Chen, W.; Liu, Y.; Li, G.-D.; Zhu, P.; Tao, Q.; Li, Q.; Liu, J.; Shen, X.; Li, H.; Huang, X.; Wang, D.; Asefa, T.; Zou, X., Highly Active, Nonprecious Electrocatalyst Comprising Borophene Subunits for the Hydrogen Evolution Reaction. *J. Am. Chem. Soc.* **2017**, *139*, 12370-12373.
292. Adolphsen, J. Q.; Sudireddy, B. R.; Gil, V.; Chatzichristodoulou, C., Oxygen Evolution Activity and Chemical Stability of Ni and Fe Based Perovskites in Alkaline Media. *J. Electrochem. Soc.* **2018**, *165*, 827-835.
293. Hona, R. K.; Ramezanipour, F., Structure-dependence of electrical conductivity and electrocatalytic properties of $\text{Sr}_2\text{Mn}_2\text{O}_6$ and $\text{CaSrMn}_2\text{O}_6$. *J. Chem. Sci.* **2019**, *131*, 109.

CURRICULUM VITAE

Ram Krishna Hona

Address: 2241 Arthur Ford Ct. Apt 3
Louisville, KY 40217
Phone: 5022917880
Email: ramkhona@gmail.com

Education	School year
GPA	
Doctor of Philosophy: Chemistry	2019
3.92	
University of Louisville, Louisville, KY, USA Research: Solid state material science	
Master of Science: Chemistry	2014
3.9	
New Mexico State University, Las Cruces, NM, USA	
Thesis: Reverse micellar effect on the electron transfer reaction within the ion pair	
[Co(NH) ₃ 5H ₂ O] ³⁺ /[Fe(CN) ₆] ⁴⁻	
Master of Science: Chemistry	1997
Division	1 st
Tribhubvan University, Kathmandu, Nepal	
Bachelor of Science: Biology and Chemistry	1995
1 st Division	
Tribhubvan University, Kathmandu, Nepal	

Peer reviewed publications

1. Hona R. K., and Ramezanipour, F., Remarkable oxygen-evolution activity of oxygen-deficient perovskites, Ca₂Fe₂O_{6-δ}, CaSrFe₂O_{6-δ}, and Sr₂Fe₂O_{6-δ}: correlations with defect-order and electrical conductivity, *Angew. Chem. Int. Ed.* 2019, 58, 2060–2063 (DOI: [10.1002/anie.201813000](https://doi.org/10.1002/anie.201813000))
2. Hona RK, Huq A, Mulmi S and Ramezanipour, F., Transformation of structure, electrical conductivity, and magnetism in AA'Fe₂O_{6-δ}, A = Sr, Ca and A' = Sr *Inorg. Chem.* 2017, 56, 9716–24 (DOI: [10.1021/acs.inorgchem.7b01228](https://doi.org/10.1021/acs.inorgchem.7b01228))
3. Hona R. K., Huq A. and Ramezanipour, F., Unraveling the role of structural order in the transformation of electrical conductivity in Ca₂FeCoO_{6-δ}, CaSrFeCoO_{6-δ},

- and $\text{Sr}_2\text{FeCoO}_{6-\delta}$ *Inorg. Chem.* 2017, 56, 14494–505 (DOI: [10.1021/acs.inorgchem.7b02079](https://doi.org/10.1021/acs.inorgchem.7b02079))
4. Mulmi S., Hona R. K., Jasinski J. B. and Ramezanipour, F., Electrical Conductivity of $\text{Sr}_{2-x}\text{Ca}_x\text{FeMnO}_5$ ($x=0, 1, 2$) *J. Solid State Electrochem.* 2018, 22, 2329–38 (doi.org/10.1007/s10008-018-3947-6)
 5. Hona R. K., Huq A. and Ramezanipour, F., Magnetic structure of $\text{CaSrFeCoO}_{6-\delta}$: correlations with structural order *Mater. Res. Bull.* 2018, 106, 131–6 (doi.org/10.1016/j.materresbull.2018.05.030)
 6. Hona, R. K.; Ramezanipour, F., Variation in electrical conductivity of $\text{A}_2\text{Fe}_2\text{O}_5$ ($\text{A} = \text{Sr}, \text{Ba}$): the role of structural order. *Mater. Res. Express* 2018, 5, 076307 (doi.org/10.1088/2053-1591/aad10e)
 7. Hona, R. K.; Ramezanipour, F., Disparity in electrical and magnetic properties of isostructural oxygen-deficient perovskites $\text{BaSrCo}_2\text{O}_{6-\delta}$ and $\text{BaSrCoFeO}_{6-\delta}$. *J. Mater. Sci.- Mater. Electron.* 2018, 29, 13464-13473 (doi.org/10.1007/s10854-018-9471-8)
 8. Dharmasena R., Thapa A. K., Hona R.K., Mesoporous TiO_2 coating on carbon–sulfur cathode for high capacity Li–sulfur battery *RSC Adv.*, 2018, 8, 11622–11632 (DOI: [10.1039/c8ra01380b](https://doi.org/10.1039/c8ra01380b))
 9. Hona R. K., Huq A. and Ramezanipour, F., Electrical properties of the ordered oxygen-deficient perovskite $\text{Ca}_2\text{Fe}_{0.5}\text{Ga}_{1.5}\text{O}_5$. *IONICS*, 2019, 25, 1315–1321, (doi.org/10.1007/s11581-018-2759-0)
 10. Hona R. K., and Ramezanipour, F., Improved Electrical Conductivity in a Disordered Oxygen-Deficient Perovskite, $\text{BaSrFe}_2\text{O}_{6-\delta}$, *J. mater. Sci.*, 2019, 167, 69-74 (doi.org/10.1016/j.poly.2019.04.018)
 11. Hona R. K., and Ramezanipour, F., Charge Transport Properties of Oxygen-Deficient Perovskites, $\text{Ca}_2\text{FeGaO}_{6-\delta}$ and $\text{CaSrFeGaO}_{6-\delta}$: The Effect of Defect-Order, *J. mater. Sci.* 2019, 238, 121924, (doi.org/10.1016/j.matchemphys.2019.121924)
 12. Hona R. K., and Ramezanipour, F., *Electrical Conductivity and Electrocatalytic activity of $\text{Sr}_2\text{Mn}_2\text{O}_6$ and $\text{CaSrMn}_2\text{O}_6$* , *J. Chem. Sci.* 2019, 131, 109

Conference presentations

1. Poster presentation: RE3 workshop; renewable energy and energy efficiency 2017, Louisville KY
Title: Effect of Ca incorporation on crystal structure, magnetism and electrical properties of $\text{Sr}_{2-x}\text{Ca}_x\text{Fe}_2\text{O}_{6-\delta}$.
2. Poster presentation: SERMACS 2017, Charlotte
Title: Variation in crystal structure, magnetism and electrical conductivity of Ca-doped $\text{Sr}_2\text{Fe}_2\text{O}_{6-\delta}$.
3. Oral presentation: 2017 Ohio inorganic week, OSU, Ohio
Title: Study of crystal structure, magnetic and electrical properties of $\text{CaSrFe}_2\text{O}_{6-\delta}$.

4. Oral presentation: UofL GRADtalks Brown Bag Series 2018, April 3-5, February, Louisville, KY
Title: Impact of the Ordering of Oxygen Vacancies on the Crystal Structure & Functional Properties in Oxygen Deficient Perovskites
5. Oral presentation: Graduate Student Regional Research Conference (GSRRC), UofL., Louisville KY 2018
Title: Role of Ca in the Crystal Structure of $\text{CaSrFe}_2\text{O}_{6-\delta}$ and Its Electrical and Magnetic Properties
6. Oral presentation: 2018 Glass City Chemistry Conference (Regional ACS), Toledo, OHIO
(invited speaker)
Title: Effect of Structural order on the electrical conductivity of $\text{Sr}_{2-x}\text{Ca}_x\text{Fe}_2\text{O}_5$ ($x = 0$ and 1).
7. Oral presentation: UofL GRADtalks Brown Bag Series 2018, November, Louisville, KY
Title: Oxygen Deficient Perovskites: Effect of vacancy order on structure and conductivity.
8. Oral presentation: UofL (Graduate Student Regional Research Conference) GSRRC 2019 February 27-28.
Title: $\text{Sr}_2\text{Fe}_2\text{O}_{6-\delta}$ as an anode electrode for Li-ion battery.
9. Oral Presentation: Spring 2019 ACS national meeting, Orlando, Florida (March 31-April 4)
Title: Effect of vacancy order on the structure and charge-transport of oxygen deficient perovskites.

Skills/Knowledge

Material synthesis: Design new materials of different composition by conventional solid state synthesis, solgel, co-precipitation method, thermal energy control for the material synthesis.

Material characterization: Scanning electron microscope (SEM), X-ray diffractometer (XRD), Powder Neutron diffraction (PNRD), ultraviolet visible (UV-Vis) spectroscopy, thermogravimetric analysis (TGA), differential scanning calorimetry (DSC), stopped flow fluorescence spectroscopy.

Functional Property measurement: 2 probe and 4- probe conductivity measurement, Impedance spectroscopy for conductivity. Physical property measurement system for magnetism and Neutron diffraction analysis for magnetism.

Li-ion battery works: New material synthesis for electrode. Coin cell assembly inside and outside the glove box. Battery testing and analysis.

Computer programs: MS office, GSAS, Origin, EIS, Fullprof, Mercury, Dimond, Zview, Jade, Machine Learning.

Electrocatalytic water splitting: Electrocatalyst synthesis and its activity analysis for oxygen evolution, hydrogen evolution by water splitting.

Pseudo capacitance: measurement and analysis.

Material Sensing property measurement: For different gases at various temperatures.

Reverse micelles: Design the reverse micelles of different sizes and reaction kinetics study.

Air sensitive glove box reaction: Organo-metallic reaction for crystal growth, CV running.

Rewards and Achievements:

As an undergraduate and graduate student

- Frederick and Eileen Coulston award for Spring with amount of \$ 453 (NMSU) 2012-2013
- Travel Award from GNAS in UofL 2018

As a professional

- Western New Mexico State University, NM, USA 2014
 - Principal of Global College (Nepal) 2009
 - Principal of Lalitpur College (Nepal) 2008
 - Head of the department of mathematics and science 2006
- 2008
Sainik School (Nepal)
 - Honor in Sainik Mahavidhyalaya as one of the best Chemistry faculty 2008
 - Lecturer in Tribhuvan University (Nepal) 1997-
2006
-

Reviewer

Science Journal of Chemistry (SJC)

Journal of Materials Science and Chemical Engineering (MSCE)

References:

1. Dr. Farshid Ramezanipour (My research adviser)
Assistant professor, chemistry department, University of Louisville
KY, USA
farshid.ramezanipour@louisville.edu, 502-852-7061 (office)
2. Dr. Arjun Kumar Thapa (He trained me for Li-ion battery work)
Battery R & D manager, Conn center for renewable energy research,
University of Louisville, KY, USA
arjun.thapa@louisville.edu, 5025958075 (mobile)
3. Dr. Ming Yu
My research seminar and thesis defense committee member,
Professor, Physics Department, University of Louisville, KY, USA
m0yu0001@louisville.edu, (502) 852-0931 (office)